

August 2, 2019

Docket No. 52-048

U.S. Nuclear Regulatory Commission  
ATTN: Document Control Desk  
One White Flint North  
11555 Rockville Pike  
Rockville, MD 20852-2738

**SUBJECT:** NuScale Power, LLC Submittal of “NuScale Comprehensive Vibration Assessment Program Measurement and Inspection Plan Technical Report,” TR-0918-60894, Revision 1

**REFERENCE:** Letter from NuScale Power LLC, to Nuclear Regulatory Commission, “NuScale Power, LLC Submittal of “NuScale Power, LLC Submittal of ‘NuScale Comprehensive Vibration Assessment Program Measurement and Inspection Plan Technical Report,’ TR-0918-60894, Revision 0,” dated December 7, 2018 (ML18341A337)

NuScale Power, LLC (NuScale) hereby submits Revision 1 of the “NuScale Comprehensive Vibration Assessment Program Measurement and Inspection Plan Technical Report” (TR-0918-60894).

Enclosure 1 contains the proprietary version of the report titled “NuScale Comprehensive Vibration Assessment Program Measurement and Inspection Plan Technical Report.” NuScale requests that the proprietary version be withheld from public disclosure in accordance with the requirements of 10 CFR § 2.390. The enclosed affidavit (Enclosure 3) supports this request. Enclosure 1 has also been determined to contain Export Controlled Information. Enclosure 2 contains the nonproprietary version of the report.

This letter makes no regulatory commitments and no revisions to any existing regulatory commitments.

If you have any questions, please contact Marty Bryan at 541-452-7172 or at mbryan@nuscalepower.com.

Sincerely,



Thomas A. Bergman  
Vice President, Regulatory Affairs  
NuScale Power, LLC

**Distribution:** Samuel Lee, NRC, OWFN-8H12  
Gregory Cranston, NRC, OWFN-8H12  
Marieliz Vera, NRC, OWFN-8H12

Enclosure 1: “NuScale Comprehensive Vibration Assessment Program Measurement and Inspection Plan Technical Report,” TR-0918-60894-P, Revision 1, proprietary version

Enclosure 2: “NuScale Comprehensive Vibration Assessment Program Measurement and Inspection Plan Technical Report,” TR-0918-60894-NP, Revision 1, nonproprietary version

Enclosure 3: Affidavit of Thomas A. Bergman, AF-0719-66346

**Enclosure 1:**

NuScale Comprehensive Vibration Assessment Program Measurement and Inspection Plan Technical Report, TR-0918-60894-P, Revision 1, proprietary version

**Enclosure 2:**

NuScale Comprehensive Vibration Assessment Program Measurement and Inspection Plan Technical Report, TR-0918-60894-NP, Revision 1, nonproprietary version

---

Licensing Technical Report

# **NuScale Comprehensive Vibration Assessment Program Measurement and Inspection Plan Technical Report**

August 2019

Revision 1

Docket No.: 52-048

## **NuScale Power, LLC**

1100 NE Circle Blvd., Suite 200

Corvallis, Oregon 97330

[www.nuscalepower.com](http://www.nuscalepower.com)

© Copyright 2019 by NuScale Power, LLC

---

## Licensing Technical Report

### **COPYRIGHT NOTICE**

This report has been prepared by NuScale Power, LLC and bears a NuScale Power, LLC, copyright notice. No right to disclose, use, or copy any of the information in this report, other than by the U.S. Nuclear Regulatory Commission (NRC), is authorized without the express, written permission of NuScale Power, LLC.

The NRC is permitted to make the number of copies of the information contained in this report that is necessary for its internal use in connection with generic and plant-specific reviews and approvals, as well as the issuance, denial, amendment, transfer, renewal, modification, suspension, revocation, or violation of a license, permit, order, or regulation subject to the requirements of 10 CFR 2.390 regarding restrictions on public disclosure to the extent such information has been identified as proprietary by NuScale Power, LLC, copyright protection notwithstanding. Regarding nonproprietary versions of these reports, the NRC is permitted to make the number of copies necessary for public viewing in appropriate docket files in public document rooms in Washington, DC, and elsewhere as may be required by NRC regulations. Copies made by the NRC must include this copyright notice and contain the proprietary marking if the original was identified as proprietary.

---

## Licensing Technical Report

### **Department of Energy Acknowledgement and Disclaimer**

This material is based upon work supported by the Department of Energy under Award Number DE-NE0008820.

This report was prepared as an account of work sponsored by an agency of the United States Government. Neither the United States Government nor any agency thereof, nor any of their employees, makes any warranty, express or implied, or assumes any legal liability or responsibility for the accuracy, completeness, or usefulness of any information, apparatus, product, or process disclosed, or represents that its use would not infringe privately owned rights. Reference herein to any specific commercial product, process, or service by trade name, trademark, manufacturer, or otherwise does not necessarily constitute or imply its endorsement, recommendation, or favoring by the United States Government or any agency thereof. The views and opinions of authors expressed herein do not necessarily state or reflect those of the United States Government or any agency thereof.

---

# Licensing Technical Report

## CONTENTS

<b>Abstract</b> .....	<b>1</b>
<b>Executive Summary</b> .....	<b>2</b>
<b>1.0 Introduction</b> .....	<b>3</b>
1.1 Purpose .....	3
1.2 Scope .....	3
1.3 Abbreviations.....	4
<b>2.0 Background</b> .....	<b>8</b>
2.1 Measurement Plan Overview .....	8
<b>3.0 Benchmark Testing</b> .....	<b>10</b>
3.1 Steam Generator Inlet Flow Restrictor Benchmark Testing.....	10
3.2 TF-1 and TF-2 Benchmark Testing for Turbulence .....	40
3.3 TF-2 Benchmark Testing for Fluid Elastic Instability.....	142
3.4 TF-3 Build-out Modal Testing.....	170
<b>4.0 Validation Methodology</b> .....	<b>202</b>
4.1 Use of Test Data .....	202
4.2 Methodology .....	202
4.3 Validation Approach and Uncertainty Analysis .....	204
4.4 Evaluation Process.....	208
4.5 Evaluation Procedures .....	209
4.6 Experimental Bias Considerations.....	224
4.7 Expected Results and Validation Range of Experimental Results .....	226
4.8 Summary .....	227
<b>5.0 Validation Tests</b> .....	<b>229</b>
5.1 TF-3 Validation Test.....	229
5.2 CNTS Main Steam Line Branch Connections Validation Testing .....	328
5.3 Steam Generator Inlet Flow Restrictor Validation Testing .....	345
<b>6.0 Initial Startup Measurement Testing</b> .....	<b>361</b>
6.1 Regions of Interest and FIV Mechanisms.....	361
6.2 FIV Detection Methodology .....	367
6.3 Sensor Considerations .....	370
6.4 Annotated Drawings .....	391

Licensing Technical Report

**7.0 Inspection Program .....394**

    7.1 Inspection Methodology ..... 394

    7.2 Inspection Procedure ..... 395

    7.3 Pre- and Post-Initial Startup Testing Inspection..... 395

**8.0 Summary and Conclusions .....402**

**9.0 References .....403**

    9.1 Referenced Documents.....403

**Appendix A. TF-3 Instrumentation Plan .....405**

**Appendix B. TF-2 FEI Spectral Plots by Test Series (0 - 300 Hz) .....414**

**Appendix C. TF-2 FEI Spectral Plots by Flow Rate (0 - 300 Hz) .....425**

**Appendix D. TF-2 FEI Spectral Plots by Test Series (0 - 1000 Hz) .....438**

**Appendix E. TF-2 FEI Spectral Plots by Flow Rate (0 - 1000 Hz) .....449**

**Appendix F. TF-2 FEI Content within Frequency Ranges of Interest.....462**

**Appendix G. TF-2 FEI Frequency-Specific Amplitudes versus Flow Rate .....470**

**Appendix H. TF-3 Build-out Testing Frequency Response Function Calculations.....477**

**TABLES**

Table 1-1 Abbreviations .....4

Table 1-2 Definitions .....5

Table 2-1 Analysis program verification testing and inspections .....9

Table 3-1 Steam generator inlet flow restrictor design options ..... 13

Table 3-2 Average and maximum root mean square vibration results..... 19

Table 3-3 Reynolds similitude values.....38

Table 3-4 Steam generator tube displacements .....38

Table 3-5 Fluid conditions for each test case analyzed .....44

Table 3-6 Cross-section geometry .....46

Table 3-7 Adjusted material properties summary .....51

Table 3-8 Sensor positions and nearest node numbers .....63

Table 3-9 Full bundle modal analysis results for TF0001 case .....66

Table 3-10 Full bundle modal analysis results for TF0002 case .....67

Table 3-11 Full bundle modal analysis results for TF0007 case .....68

Table 3-12 Single tube modal analysis results for sliding TF0001 case .....74

Table 3-13 Single tube modal analysis results for sliding TF0002 case .....75

Table 3-14 Single tube modal analysis results for sliding TF0007 case .....76

Table 3-15 Single tube modal analysis results pinned TF0001 case .....77

Table 3-16 Single tube modal analysis results pinned TF0001 case .....78

Table 3-17 Single tube modal analysis results pinned TF0001 case .....79

Table 3-18 X-direction modal analysis results for mesh sensitivity study using single tube model, sliding TF0001 case .....86



## Licensing Technical Report

Table 3-19	Y-direction modal analysis results for mesh sensitivity study using single tube model, sliding TF0001 case .....	87
Table 3-20	Z-direction modal analysis results for mesh sensitivity study using single tube model, sliding TF0001 case .....	88
Table 3-21	Major mode comparison between full bundle and single tube models .....	89
Table 3-22	Applicable TF-2 test cases .....	98
Table 3-23	TF-1 secondary side PSDs used .....	100
Table 3-24	Giraudeau PSD correlation empirical constants .....	103
Table 3-25	Placement of strain gauge instrumentation.....	147
Table 3-26	Test conditions and file names for fluid elastic instability data acquisition .....	148
Table 3-27	Summary of applied processing parameters .....	153
Table 3-28	Dynamic root mean square strains measured during TF-2 fluid elastic instability tests.....	158
Table 3-29	Dynamic peak strains measured during TF-2 fluid elastic instability tests .....	159
Table 3-30	Dynamic peak strains by test series (average and maximum) .....	160
Table 3-31	Dynamic peak strains by flow rate (average and maximum) .....	161
Table 3-32	Relative comparison of content within frequency ranges of interest (0-10 Hz inclusive), sorted by test series .....	162
Table 3-33	Relative comparison of content within frequency ranges of interest (excludes 0-10 Hz), sorted by test series.....	163
Table 3-34	Relative comparison of content within frequency ranges of interest (excludes 0-10 Hz), sorted by test series.....	164
Table 3-35	Acquisition parameters for time and frequency domain .....	173
Table 3-36	Group B, span C (5) accelerometers .....	178
Table 3-37	Group C, multi-span .....	181
Table 3-38	Energy transfer across spans .....	183
Table 3-39	End span (A and AD) frequency response function summary .....	185
Table 3-40	Support and tube frequency response function summary .....	188
Table 3-41	Frequency response function summary per group .....	200
Table 4-1	SG Test Model Inputs.....	210
Table 4-2	SG Tube Inputs to TB Margin Calculation.....	211
Table 4-3	SG Tube TB Margin Uncertainty Method .....	212
Table 4-4	Steam generator test model inputs .....	213
Table 4-5	Steam generator tube inputs to vortex shedding margin calculation: method B ...	214
Table 4-6	Steam generator tube vortex shedding margin uncertainty method: method B ...	215
Table 4-7	Steam generator tube inputs to vortex shedding margin calculation: method A ...	216
Table 4-8	Steam generator tube vortex shedding margin uncertainty method: method A ...	216
Table 4-9	Fluid elastic instability analysis input parameter types .....	218
Table 4-10	Steam generator tube inputs to fluid elastic instability safety margin calculation ..	219
Table 4-11	Steam generator tube fluid elastic instability margin uncertainty method .....	220
Table 4-12	Decay heat removal system steam pipe inputs to acoustic resonance margin calculation .....	223
Table 4-13	Decay heat removal system steam pipe acoustic resonance margin uncertainty method .....	223
Table 4-14	Summary of components and flow induced vibration analysis validation methods .....	228
Table 5-1	Summary of tests .....	229
Table 5-2	Tube array design geometry .....	231

## Licensing Technical Report

Table 5-3	Helical steam generator tube array details .....	232
Table 5-4	TF-3 test facility operating conditions .....	232
Table 5-5	Instrumented tubes (accelerometers and strain gauges).....	234
Table 5-6	Instrumented tubes (accelerometers only).....	234
Table 5-7	Instrumented tubes (strain gauges only).....	235
Table 5-8	Accelerometers placement for instrumented tube #1 .....	236
Table 5-9	Accelerometers placement for instrumented tube #2.....	236
Table 5-10	Accelerometers placement for instrumented tube #3.....	237
Table 5-11	Accelerometers placement for instrumented tube #4.....	237
Table 5-12	Accelerometers placement for instrumented tube #5.....	238
Table 5-13	Accelerometers placement for instrumented tube #6.....	238
Table 5-14	Tube strain gauge placements.....	239
Table 5-15	Steam generator tube support accelerometer .....	239
Table 5-16	Other pressure and temperature instrumentation .....	240
Table 5-17	Partial-tube array modal tests .....	242
Table 5-18	Steady-state flow flow-induced vibration tests .....	247
Table 5-19	Vortex shedding test points <sup>1, 2</sup> .....	248
Table 5-20	Fluid elastic instability flow tests .....	249
Table 5-21	Mass correction for vessels .....	261
Table 5-22	Pivot vs. fixed dry modal results for Columns 9 and 13 in x-direction (horizontal).....	270
Table 5-23	Pivot vs. fixed dry modal results for Columns 9 and 13 in y-direction (vertical) .....	271
Table 5-24	Pivot vs. fixed dry modal results for Columns 9 and 13 in z-direction (horizontal).....	272
Table 5-25	Dry vs. wet modal results for pivot boundary conditions in y-direction .....	277
Table 5-26	Dry vs. wet modal results for fixed boundary conditions in y-direction .....	278
Table 5-27	Fine vs. coarse mesh modal results for pivot boundary conditions in x-direction .....	280
Table 5-28	Fine vs. coarse mesh modal results for pivot boundary conditions in y-direction .....	281
Table 5-29	Fine vs. coarse mesh modal results for pivot boundary conditions in z-direction .....	282
Table 5-30	Fine vs. coarse mesh modal results for fixed boundary conditions in x-direction .....	283
Table 5-31	Fine vs. coarse mesh modal results for fixed boundary conditions in y-direction .....	284
Table 5-32	Fine vs. coarse mesh modal results for fixed boundary conditions in z-direction .....	285
Table 5-33	Top 5 participating modes in y-direction for Column 11 tubes.....	286
Table 5-34	Summary of full bundle model results.....	292
Table 5-35	Design and Nominal values for input uncertainty assessment .....	302
Table 5-36	FEI Measurement Uncertainties .....	304
Table 5-37	Test Distortions for FEI.....	305
Table 5-38	FEI Input and Measurement Uncertainties .....	306
Table 5-39	FEI Testing Biases .....	306
Table 5-40	Expected and Validation Range of Results for FEI .....	307
Table 5-41	VS Design Analysis and Nominal Values – Method A.....	311

## Licensing Technical Report

Table 5-42	VS Measurement Uncertainties .....	311
Table 5-43	Test Distortions for VS .....	313
Table 5-44	VS Input and Measurement Uncertainties .....	313
Table 5-45	VS Testing Biases .....	313
Table 5-46	Expected and Validation Range of Results for VS .....	314
Table 5-47	Best estimate pre-test prediction response.....	322
Table 5-48	LHS results .....	326
Table 5-49	Total uncertainty in the mean square response .....	326
Table 5-50	Upper limit in measured mean square response to validate design analysis .....	326
Table 5-51	Summary of input uncertainties .....	326
Table 5-52	Summary of pivot boundary condition measurement uncertainties .....	327
Table 5-53	Summary of fixed boundary condition measurement uncertainties .....	327
Table 5-54	Fatigue usage due to impact stress .....	327
Table 5-55	Measurements and sensors.....	332
Table 5-56	Input and measurement uncertainties.....	344
Table 5-57	Expected and allowable results for acoustic resonance and second order shear layers .....	345
Table 5-58	Range of possible radial clearances between inlet flow restrictor and tube wall.....	349
Table 5-59	Range of flow conditions for steam generator inlet flow restrictor tests .....	350
Table 5-60	SG IFR flow test matrix .....	358
Table 6-1	NPM initial startup test regions and susceptible FIV mechanisms .....	361
Table 6-2	FIV Mechanisms, Predicted Responses, and Detection Methods for NPM.....	372
Table 6-3	Comparison of Standard Strain and Fiber Optic Sensors .....	376
Table 6-4	Environmental Conditions by Region.....	379
Table 6-5	Typical Parameters for Common Sensor Types.....	379
Table 6-6	Recommended Sensor Locations .....	384
Table 6-7	Optional Sensor Locations .....	386
Table 7-1	Pre- and post-initial startup testing inspection locations .....	396
Table F-1	Amplitude of spectral content between 0 – 10 Hz.....	463
Table F-2	Amplitude of spectral content between 0-10 Hz (excluding test series G).....	464
Table F-3	Amplitude of spectral content between 16-28 Hz .....	465
Table F-4	Amplitude of spectral content between 35-55 Hz .....	466
Table F-5	Amplitude of spectral content between 70-85 Hz .....	467
Table F-6	Amplitude of spectral content between 140-160 Hz .....	468
Table F-7	Amplitude of spectral content between 10-300 Hz .....	469
Table H-1	Testing matrix.....	478

## FIGURES

Figure 3-1	Center flow orifice restrictor design.....	11
Figure 3-2	Threaded fastener design .....	12
Figure 3-3	Stepped solid annular design.....	12
Figure 3-4	Steam generator inlet flow restrictor test facility schematic .....	16
Figure 3-5	Test assembly .....	17
Figure 3-6	Device 1 root mean square acceleration at 110 percent Reynolds similitude and below.....	20
Figure 3-7	Device 2 and 3 root mean square acceleration .....	21

## Licensing Technical Report

Figure 3-8	Device 4-5 root mean square acceleration at 110 percent Reynolds similitude and below.....	22
Figure 3-9	Device 6 root mean square acceleration at 110 percent Reynolds similitude and below.....	22
Figure 3-10	Test 6C1 acceleration .....	23
Figure 3-11	Device 7-10 root mean square acceleration at 110 percent Reynolds similitude and below.....	24
Figure 3-12	Test 10C4 acceleration .....	25
Figure 3-13	Device 11-12 root mean square acceleration at 110 percent Reynolds similitude and below.....	25
Figure 3-14	Test 1A4 (150 percent) acceleration .....	29
Figure 3-15	Test 1A4 (150 percent) frequency .....	29
Figure 3-16	Test 8A1 acceleration.....	30
Figure 3-17	Test 8A1 frequency .....	30
Figure 3-18	Test 8B2 Reynolds similitude of 100 percent acceleration.....	31
Figure 3-19	Test 8B2 Reynolds similitude of 100 percent frequency .....	31
Figure 3-20	Test 9A3 Reynolds similitude of 100 percent acceleration.....	32
Figure 3-21	Test 9A3 Reynolds similitude of 100 percent frequency .....	32
Figure 3-22	Test 9C3 acceleration .....	33
Figure 3-23	Test 9C3 frequency .....	33
Figure 3-24	Test 10A1 Reynolds similitude of 100 percent acceleration.....	34
Figure 3-25	Test 10A1 Reynolds similitude of 100 percent frequency .....	34
Figure 3-26	Test 11C2 acceleration.....	35
Figure 3-27	Test 11C2 frequency .....	35
Figure 3-28	Test 12B1 acceleration.....	36
Figure 3-29	Test 12B1 frequency .....	36
Figure 3-30	Steam generator tube displacement.....	39
Figure 3-31	TF-2 test specimen assembly drawing .....	42
Figure 3-32	TF-2 full bundle geometry and mesh .....	43
Figure 3-33	TF-2 full bundle geometry and mesh close-up.....	44
Figure 3-34	Naming system for various tube support sections .....	45
Figure 3-35	Neglected steam and feedwater piping.....	47
Figure 3-36	Neglected shift of header position and change in tube inclination angle .....	48
Figure 3-37	Neglected longitudinal ribs.....	48
Figure 3-38	Neglected internal structures .....	49
Figure 3-39	Separate plates that are modeled as single monolithic plate.....	50
Figure 3-40	Coordinate systems. global cartesian and global cylindrical shown from global isometric view .....	52
Figure 3-41	Radial coupling between barrels and tube supports .....	53
Figure 3-42	Diagram of screw interface between barrels and tube supports.....	54
Figure 3-43	Tube to tube support coupling (column 5 tubes shown) .....	55
Figure 3-44	Tube supports to thick slab coupling.....	56
Figure 3-45	Header to header attachment plate coupling .....	57
Figure 3-46	Displacement constraint on radial cantilever plate.....	58
Figure 3-47	Primary fluid regions for hydrodynamic effects on barrels. Front view on left, top view on right.....	59
Figure 3-48	Internal barrel and external barrel remote points for hydrodynamic coupling .....	60
Figure 3-49	External barrel and vessel nodes for hydrodynamic coupling.....	62

## Licensing Technical Report

Figure 3-50	Boundary conditions for single tube model .....	64
Figure 3-51	Fundamental mode for TF0001 case (full assembly rocking mode) .....	69
Figure 3-52	Mode 3 for TF0001 case (tube bundle twisting mode).....	70
Figure 3-53	Highest x-participating mode for TF0001 case (tube bundle shifting along x-axis) .....	71
Figure 3-54	Highest y-participating mode for TF0001 case (tube beam mode).....	72
Figure 3-55	Fundamental mode for single tube sliding TF0001 case (breathing mode).....	80
Figure 3-56	Highest x-participating mode for single tube sliding TF0001 case (tube sliding through supports with beam mode) .....	81
Figure 3-57	Highest y-participating mode for single tube sliding TF0001 case (beam mode) ...	82
Figure 3-58	Fundamental mode and highest y-participating mode for single tube pinned TF0001 case (beam mode).....	83
Figure 3-59	Highest x-participating mode for single tube pinned TF0001 case (high order beam mode).....	84
Figure 3-60	Mesh size comparison for mesh sensitivity analysis.....	85
Figure 3-61	Breathing/twisting mode comparison between single tube and full bundle models .....	90
Figure 3-62	Highest y-participating mode comparison between single tube and full bundle models (sliding/shifting and beam mode) .....	91
Figure 3-63	Highest x-participating mode comparison between single tube and full bundle models (beam mode) .....	92
Figure 3-64	Block diagram of the vibration analysis methodology .....	93
Figure 3-65	Block diagram of the ANSYS solution sequence .....	94
Figure 3-66	Strain versus temperature ranges for the TD, TF, and TW tests.....	106
Figure 3-67	Strain gauge data for a case with secondary side boiling .....	107
Figure 3-68	TF0004_0769 column 5 lower strain sensor with pinned boundary conditions ....	108
Figure 3-69	TF0004_0769 column 5 upper strain sensor with pinned boundary conditions ....	109
Figure 3-70	TF0004_0773 column 5 lower strain sensor with pinned boundary conditions ....	110
Figure 3-71	TF0004_0773 column 5 upper strain sensor with pinned boundary conditions ....	111
Figure 3-72	TF0004_0773 column 5 lower strain sensor with sliding boundary conditions .....	112
Figure 3-73	TF0004_0773 column 5 upper strain sensor with sliding boundary conditions ....	113
Figure 3-74	TF0003_0762 column 5 lower strain sensor with pinned boundary conditions ....	114
Figure 3-75	TF0003_0762 column 5 upper strain sensor with pinned boundary conditions ....	115
Figure 3-76	TF0007_0777 column 1 lower strain sensor with pinned boundary conditions ....	116
Figure 3-77	TF0007_0777 column 3 lower strain sensor with pinned boundary conditions ....	117
Figure 3-78	TF0007_0777 column 3 upper strain sensor with pinned boundary conditions ....	118
Figure 3-79	TF0007_0777 column 5 lower strain sensor with pinned boundary conditions ....	119
Figure 3-80	TF0007_0777 column 5 upper strain sensor with pinned boundary conditions ....	120
Figure 3-81	TF0007_0781 column 5 lower strain sensor with pinned boundary conditions ....	121
Figure 3-82	TF0007_0781 column 5 upper strain sensor with pinned boundary conditions ....	122
Figure 3-83	TF0007_0781 column 5 lower strain sensor with pinned boundary conditions and the TF-1 PSD .....	124
Figure 3-84	TF0007_0781 column 5 upper strain sensor with pinned boundary conditions and the TF-1 PSD .....	125
Figure 3-85	TF0007_0781 column 5 unfiltered strain sensor up to 600 Hz .....	126
Figure 3-86	TF0007_0781 column 5 lower strain sensor with pinned boundary conditions and the Au-Yang/Jordan PSD .....	127

## Licensing Technical Report

Figure 3-87	TF0007_0781 column 5 lower strain sensor with pinned boundary conditions and more mode combinations.....	128
Figure 3-88	TF0007_0781 column 5 lower strain sensor with pinned boundary conditions and fine mesh .....	129
Figure 3-89	TF0007_0781 column 5 lower strain sensor with pinned boundary conditions and $\{\{\quad\}\}^{2(a),(c)}$ damping.....	130
Figure 3-90	Test case geometry.....	132
Figure 3-91	Displacement spectrum comparison for test case 1 .....	133
Figure 3-92	Displacement spectrum comparison for test case 2 .....	134
Figure 3-93	Displacement spectrum comparison for test case 3 .....	135
Figure 3-94	Displacement spectrum comparison for test case 4 .....	136
Figure 3-95	Bending strain spectrum comparison for test case 1 .....	137
Figure 3-96	Bending strain spectrum comparison for test case 2 .....	138
Figure 3-97	Bending strain spectrum comparison for test case 3 .....	139
Figure 3-98	Bending strain spectrum comparison for test case 4 .....	140
Figure 3-99	Tube axisymmetric model mesh .....	141
Figure 3-100	Tube axisymmetric model mesh .....	142
Figure 3-101	TF-2 Fluid-heated test section tubing column scheme .....	143
Figure 3-102	TF-2 Tube support detail.....	144
Figure 3-103	Placement of strain gauges on tube coils (typical).....	146
Figure 3-104	Placement of strain gauges on tube coils (S1101-1 and S1101-2 shown).....	146
Figure 3-105	Example of average variations in strain gauge signals.....	152
Figure 3-106	Overall power spectral density content comparison – column-3, side strain gauges (top=S07, bottom=S05) .....	157
Figure 3-107	Scatter plot of peak dynamic strain versus flow rate.....	165
Figure 3-108	Spectral comparison, 0-50 Hz, datasets D5 versus G5, Column-3 sensors... ..	166
Figure 3-109	Spectral comparison, 0-50 Hz, datasets D6 versus G6, Column-5 sensors... ..	167
Figure 3-110	General layout of helical coil steam generator prototype for vibration testing.....	172
Figure 3-111	Typical single, long span vertical; frequency response function (blue) and coherence (orange) .....	176
Figure 3-112	Frequency response function response for roving accelerometer along single span (mass loading).....	176
Figure 3-113	Lower frequency response (below 25 Hz); frequency response function (blue) and coherence (orange).....	177
Figure 3-114	Coherence only for test 1C-1Z (horizontal/1Z and vertical/3Y direction) .....	179
Figure 3-115	Impact location effects on Span C (left: mid-span; right: near end of span) ...	179
Figure 3-116	Coherence only for test 2A-EfwZ (vertical and horizontal direction).....	182
Figure 3-117	2A-EfwZ energy transfer across spans.....	184
Figure 3-118	Coherence only 5A-5Z (horizontal and vertical direction).....	186
Figure 3-119	Support/tube testing configuration .....	187
Figure 3-120	Coherence for test “Sup-103 + Col-12, Span E tub 1+5+9, impact 1-X” .....	189
Figure 3-121	Global polynomial curve fit of frequency response functions (top frequency response function magnitude, bottom imaginary magnitude on log-scale) ....	190
Figure 3-122	Half-power damping estimations over the frequency response function groups.....	191
Figure 3-123	Peak damping values ( $\{\{\quad\}\}^{2(a),(c)}$ :1C-1Y-left and $\{\{\quad\}\}^{2(a),(c)}$ :1A-3Z-right).....	191

## Licensing Technical Report

Figure 3-124	Amplitude-dependent damping from three time histories (raw): exponential fit – blue; log dec – red .....	193
Figure 3-125	Amplitude-dependent damping from three time histories (averaged): exponential fit – blue; log dec – red.....	194
Figure 3-126	Amplitude-dependent damping from pull test: exponential fit – blue; log dec – red.....	195
Figure 3-127	Amplitude-dependent damping: pull pest – black and grey; impact tests – red and blue .....	195
Figure 3-128	1C-1Z, Span C, 5 accelerometers (frequency response function, axial-red, vertical-green, horizontal-blue) .....	197
Figure 3-129	Mode shape for 1C-1Z at {{ }} <sup>2(a),(c)</sup> .....	197
Figure 3-130	Mode shape for 1C-1Z at {{ }} <sup>2(a),(c)</sup> .....	198
Figure 3-131	Mode shape for 1C-1Z at {{ }} <sup>2(a),(c)</sup> .....	198
Figure 3-132	Mode shape for 1C-1Z at {{ }} <sup>2(a),(c)</sup> .....	199
Figure 3-133	Comparison of mode shapes between 1C-1Z ({{ }} <sup>2(a),(c)</sup> ) and 1A-5Z ({{ }} <sup>2(a),(c)</sup> ) using modal assurance criteria.....	199
Figure 5-1	Coordinate systems shown from global isometric view .....	251
Figure 5-2	Numbering system for circumferential positions (CSYS 0 shown).....	252
Figure 5-3	Representative tubes for individual tube models .....	253
Figure 5-4	Boundary condition locations (column 13 shown).....	254
Figure 5-5	TF-3 full bundle model geometry .....	256
Figure 5-6	TF-3 full bundle model mesh .....	257
Figure 5-7	Tube and tube support mesh .....	258
Figure 5-8	Modeled vessel mass (left), and top head mass volume (right).....	260
Figure 5-9	Fixed boundary condition at bottom edge of full bundle model.....	262
Figure 5-10	Tube to tubesheet coupling: steam tubesheet (top), feedwater tubesheet (bottom).....	263
Figure 5-11	Tube support to steam generator support coupling: upper connection (top), lower connection (bottom).....	264
Figure 5-12	Tube to tube support coupling.....	265
Figure 5-13	Various views of tube support to tube support coupling.....	266
Figure 5-14	Column 9 tube support to inner vessel coupling .....	267
Figure 5-15	Column 13 tube support to outer vessel coupling.....	268
Figure 5-16	Fundamental mode for Column 13 dry pivot case (breathing mode).....	273
Figure 5-17	Mode with highest y-direction (vertical) mass participation for Column 13 dry pivot case (beam mode) .....	274
Figure 5-18	Fundamental mode for Column 13 dry fixed case (beam mode of transition bend).....	275
Figure 5-19	Mode with highest y-direction mass participation for Column 13 dry fixed case (beam mode).....	276
Figure 5-20	Maximum strain intensity locations for Column 11, tube 1, pivot case, dominant vertical modes.....	287
Figure 5-21	Maximum strain intensity locations for Column 11, tube 1, fixed case, dominant vertical modes.....	288
Figure 5-22	Maximum strain intensity locations for Column 11, tube 16, pivot case, dominant vertical modes .....	289
Figure 5-23	Maximum strain intensity locations for Column 11, tube 16, fixed case, dominant vertical modes .....	290

## Licensing Technical Report

Figure 5-24	Fundamental mode for full bundle pivot case (breathing mode).....	293
Figure 5-25	Mode with highest x-direction mass participation for full bundle pivot case (rocking mode).....	294
Figure 5-26	Mode with highest y-direction mass participation for full bundle pivot case (tube beam mode).....	295
Figure 5-27	Entire specimen squeezing mode for full bundle fixed case .....	296
Figure 5-28	Tube fundamental mode for full bundle fixed case (beam mode of transition bend).....	297
Figure 5-29	Tube mode with highest y-direction mass participation for full bundle fixed case (tube beam mode).....	298
Figure 5-30	Twisting mode for full tube bundle fixed (no circ) case .....	299
Figure 5-31	Flow Rates and Validation Ranges for TF-3 .....	308
Figure 5-32	FEI Stability Map with TF-3 Test Conditions .....	309
Figure 5-33	Nominal design analysis column 21 tube B RMS displacement (in).....	320
Figure 5-34	Nominal design analysis column 21 tube B displacement response (in) at maximum location .....	321
Figure 5-35	Best estimate test column 11 tube A, fixed, RMS displacement (in).....	322
Figure 5-36	Best estimate test column 11 tube B, fixed, RMS displacement (in).....	323
Figure 5-37	Best estimate test column 11 tube A, pivot, RMS displacement (in).....	324
Figure 5-38	Best estimate test column 11 tube B, pivot, RMS displacement (in).....	325
Figure 5-39	Containment system steam line 2 and CNTS main steam line branch connections.....	330
Figure 5-40	Drawing of decay heat removal system junctions to containment system main steam pipe .....	338
Figure 5-41	Steam generator tube inlet flow restrictor and mounting plate.....	347
Figure 5-42	Dimensions of inlet flow restrictor and flow restrictor bolt .....	348
Figure 5-43	Preload conditions (not to scale).....	357
Figure 6-1	Recommended and Optional Measurement Locations (Table 4-5, Table 4-6).....	391
Figure 6-2	Recommended and Optional Measurement Locations (Table 4-5, Table 4-6).....	392
Figure 6-3	Recommended and Optional Measurement Locations (Table 4-5, Table 4-6).....	393
Figure 7-1	Lower reactor pressure vessel comprehensive vibration assessment program inspection locations.....	398
Figure 7-2	Upper reactor pressure vessel comprehensive vibration assessment program inspection locations.....	399
Figure 7-3	Steam generator and downcomer comprehensive vibration assessment program inspection locations .....	400
Figure 7-4	Steam line comprehensive vibration assessment program inspection locations.....	401
Figure A-1	Column 11 tube 1 instrumented tube .....	405
Figure A-2	Column 11 tube 16 instrumented tube .....	406
Figure A-3	Column 9 tube 15 instrumented tube .....	407
Figure A-4	Column 9 tube 16 instrumented tube .....	408
Figure A-5	Column 12 tube 1 instrumented tube .....	409
Figure A-6	Column 12 tube 2 instrumented tube .....	410
Figure A-7	Column 11 tube 2 instrumented tube .....	411
Figure A-8	Column 11 tube 15 instrumented tube .....	412
Figure A-9	Instrumentation summary .....	413
Figure B-1	Test condition A, channel set 1 .....	415



## Licensing Technical Report

Figure B-2	Test condition A, channel set 2 .....	416
Figure B-3	Test condition B, channel set 1 .....	417
Figure B-4	Test condition B, channel set 2 .....	418
Figure B-5	Test condition C, channel set 1 .....	419
Figure B-6	Test condition C, channel set 2 .....	420
Figure B-7	Test condition D, channel set 1 .....	421
Figure B-8	Test condition D, channel set 2 .....	422
Figure B-9	Test condition G, channel set 1 .....	423
Figure B-10	Test condition G, channel set 2 .....	424
Figure C-1	Nominal primary-side flow rate of 114 kg/s, channel set 1 .....	426
Figure C-2	Nominal primary-side flow rate of 114 kg/s, channel set 2 .....	427
Figure C-3	Nominal primary-side flow rate of 143 kg/s, channel set 1 .....	428
Figure C-4	Nominal primary-side flow rate of 143 kg/s, channel set 2 .....	429
Figure C-5	Nominal primary-side flow rate of 173 kg/s, channel set 1 .....	430
Figure C-6	Nominal primary-side flow rate of 173 kg/s, channel set 2 .....	431
Figure C-7	Nominal primary-side flow rate of 201 kg/s, channel set 1 .....	432
Figure C-8	Nominal primary-side flow rate of 201 kg/s, channel set 2 .....	433
Figure C-9	Nominal primary-side flow rate of 230 kg/s, channel set 1 .....	434
Figure C-10	Nominal primary-side flow rate of 230 kg/s, channel set 2 .....	435
Figure C-11	Nominal primary-side flow rate of 263 kg/s, channel set 1 .....	436
Figure C-12	Nominal primary-side flow rate of 263 kg/s, channel set 2 .....	437
Figure D-1	Test condition A, channel set 1 .....	439
Figure D-2	Test condition A, channel set 2 .....	440
Figure D-3	Test condition B, channel set 1 .....	441
Figure D-4	Test condition B, channel set 2 .....	442
Figure D-5	Test condition C, channel set 1 .....	443
Figure D-6	Test condition C, channel set 2 .....	444
Figure D-7	Test condition D, channel set 1 .....	445
Figure D-8	Test condition D, channel set 2 .....	446
Figure D-9	Test condition G, channel set 1 .....	447
Figure D-10	Test condition G, channel set 2 .....	448
Figure E-1	Nominal primary-side flow rate of 114 kg/s, channel set 1 .....	450
Figure E-2	Nominal primary-side flow rate of 114 kg/s, channel set 2 .....	451
Figure E-3	Nominal primary-side flow rate of 143 kg/s, channel set 1 .....	452
Figure E-4	Nominal primary-side flow rate of 143 kg/s, channel set 2 .....	453
Figure E-5	Nominal primary-side flow rate of 173 kg/s, channel set 1 .....	454
Figure E-6	Nominal primary-side flow rate of 173 kg/s, channel set 2 .....	455
Figure E-7	Nominal primary-side flow rate of 201 kg/s, channel set 1 .....	456
Figure E-8	Nominal primary-side flow rate of 201 kg/s, channel set 2 .....	457
Figure E-9	Nominal primary-side flow rate of 230 kg/s, channel set 1 .....	458
Figure E-10	Nominal primary-side flow rate of 230 kg/s, channel set 2 .....	459
Figure E-11	Nominal primary-side flow rate of 260 kg/s, channel set 1 .....	460
Figure E-12	Nominal primary-side flow rate of 260 kg/s, channel set 2 .....	461
Figure G-1	Dynamic strain, 0-10 Hz versus flow rate .....	471
Figure G-2	Dynamic strain, 16-28 Hz versus flow rate .....	472
Figure G-3	Dynamic strain, 35-55 Hz versus flow rate .....	473
Figure G-4	Dynamic strain, 70-85 Hz versus flow rate .....	474
Figure G-5	Dynamic strain, 140-160 Hz versus flow rate .....	475

---

## Licensing Technical Report

Figure G-6	Dynamic strain, 10-300 Hz versus flow rate .....	476
Figure H-1	315-12-1-C-5 (5y) .....	479
Figure H-2	zSgle tube 1sec .....	479
Figure H-3	1A-1Y .....	480
Figure H-4	1A-1Z .....	480
Figure H-5	1A-3Z .....	481
Figure H-6	1A-5Z .....	481
Figure H-7	1C-1Y .....	482
Figure H-8	1C-1Z .....	482
Figure H-9	1C-5Z .....	483
Figure H-10	1E-1Y .....	483
Figure H-11	1E-1Z .....	484
Figure H-12	1E-5Z .....	484
Figure H-13	2A-CmsZ .....	485
Figure H-14	2A-EfwZ .....	485
Figure H-15	2A-EmsZ .....	486
Figure H-16	2A-GfwZ .....	486
Figure H-17	2C-CmsZ .....	487
Figure H-18	2C-EfwZ .....	487
Figure H-19	2C-EmsZ .....	488
Figure H-20	2C-GfwZ .....	488
Figure H-21	3C-EmsZ .....	489
Figure H-22	4A-2Z .....	490
Figure H-23	4A-3Z .....	490
Figure H-24	5A-2Z .....	491
Figure H-25	5A-4Y .....	491
Figure H-26	5A-5Z .....	492
Figure H-27	5A-Support Z .....	492
Figure H-28	Sup-103+col-12 span E, Tube 1, 5, 9 impact 1x .....	493
Figure H-29	Sup-103+col-12 span E, Tube 1, 5, 9 impact 1Z .....	493
Figure H-30	Supp-to-tube 103 span-E FW-X .....	494
Figure H-31	Supp-to-tube 103 span-E FW-X on plate .....	494

## **Abstract**

The NuScale Comprehensive Vibration Assessment Program (CVAP) includes the requirement for individual analytical, measurement, and inspection programs. The NuScale CVAP design analysis program is documented in the NuScale Comprehensive Vibration Assessment Program Analysis Technical Report, TR-0716-50439 (Reference 9.1.4).

In accordance with Regulatory Guide 1.20, the results of the analysis program serve as the basis for the choice of components and areas to be monitored in the measurement and inspection programs, in order to validate the implementation of the CVAP design analysis program. This technical report provides the details associated with the CVAP measurement and inspection program plans.

---

## Executive Summary

This report provides the details of the NuScale Comprehensive Vibration Assessment Program (CVAP) measurement and inspection programs. These programs consist of benchmark testing and analysis, validation analysis and testing, an instrumentation plan to detect large amplitude vibration during initial startup testing, and inspection of components screened as susceptible to flow induced vibration (FIV) before and after initial startup testing.

This report provides pre-test prediction results for CVAP testing of the NuScale Power Module (NPM) components that have design analyses and are part of the measurement program. The primary goal of the testing is to validate that detrimental effects do not occur during limiting operating conditions.

Following the completion of each test, post-test analyses are performed to complete the validation effort. Assessments are also performed based on the initial startup testing and inspection observations. Combined with the benchmarking efforts, the measurement and inspection work scope validates the FIV screening and predictive analyses in the NuScale Comprehensive Vibration Assessment Program Analysis Technical Report, TR-0716-50439.

## 1.0 Introduction

### 1.1 Purpose

The purpose of this technical report is to describe the scope of the NuScale Comprehensive Vibration Assessment Program (CVAP) measurement and inspection programs.

This report explains the basis for the components assessed in these programs, the details associated with the planned testing and inspections, and how the results are used to validate the CVAP design analysis program.

This report demonstrates how the measurements are used to confirm the adequacy of the design analysis, including the predicted safety margins.

### 1.2 Scope

The NuScale CVAP addresses components exposed to primary or secondary coolant flow in the NuScale Power Module (NPM) through the design analysis and measurement and inspection programs. The scope of this report is the measurement and inspection programs.

The measurement program consists of two components. The first is benchmarking the design analysis using test data that is not fully prototypic, but is applicable to susceptible components and aspects of the design analysis and overall validation approach. The second component of the measurement program is prototypic validation testing. This testing is informed from the design analysis and for components with the lowest predicted safety margins. Validation testing is performed either at specially designed test facilities, to permit higher quality and quantity collection of test data, and the ability to operate above licensing basis limits where the onset of strongly-coupled flow induced vibration (FIV) phenomena is predicted to occur, or on the first NPM during initial startup testing.

The inspection program includes components that meet the screening criteria for any FIV mechanism. Details associated with the testing scope, extent of inspections, and inspection acceptance criteria are provided in this report.

An outline and description of the scope of this report are provided below:

- **Benchmarking Testing:** benchmarking testing was performed for the steam generator inlet flow restrictor (SG IFR), and to assess turbulence and fluid elastic instability (FEI) for the SG tube bundle in the TF-1 and TF-2 test programs. The benchmark test data was used to justify aspects of the design analysis and provide confidence that the validation testing is sufficient to validate the conclusions of the design analysis program.
- **Validation Methodology:** the validation methodology provides a framework for selecting the aspects of the design analysis program that need to be validated, and to establish or confirm that the experiment design provides sufficient data to validate the necessary aspects of the design analysis program. Pre-test prediction calculations

implement the validation methodology. These calculations confirm the adequacy of the experimental scope, identify optimal test conditions and locations for sensors, and determine a range of expected and allowable experimental results, considering uncertainties and biases, that validate the design analysis.

- **Validation Testing:** this section discusses the test design for three validation tests: TF-3, steam generator inlet flow restrictor (SG IFR) and the decay heat removal system (DHRS). Testing details including the test geometry, testing conditions, test matrix, and sensor types and locations are identified. Pre-test predictions based on the experimental design assess applicable uncertainties and biases, and provide the range of expected and allowable experimental results that validate the design analysis.
- **Measurements during Initial Startup Testing:** this section identifies sensors that are temporarily installed during initial startup testing to monitor for large amplitude vibrations. The monitoring locations include the SG, in-core instrument guide tubes (ICIGTs) and control rod drive (CRD) shafts in the upper plenum region, and the connection of the upper and lower riser assemblies.
- **Inspections:** the NuScale CVAP requires inspection of each NPM component that screens for an FIV mechanism. This report provides details related to the inspection procedures and inspection locations, features, examination methods, and acceptance criteria.

### 1.3 Abbreviations

Table 1-1 Abbreviations

<b>Term</b>	<b>Definition</b>
APDL	ANSYS parametric design language
AR	acoustic resonance
ASME	American Society of Mechanical Engineers
CNTS	containment system
CRD	Control rod drive
CSYS	coordinate system
CVAP	Comprehensive Vibration Assessment Program
DAS	data acquisition system
DC	Average
DHRS	decay heat removal system
DSA	dynamic signal analysis
FEI	fluid elastic instability
FFT	fast Fourier transform
FIV	flow-induced vibration
FRF	frequency response function
FW	feedwater
HCSG	helical coil steam generator
ICIGT	in-core instrument guide tubes
IFR	inlet flow restrictor

Term	Definition
LFI	leakage flow instability
LHS	Latin hypercube sampling
MAC	modal acceptance criteria
MI	mineral insulated
MS	main steam
MSIV	main steam isolation valve
MSS	main steam system
NPM	NuScale Power Module
OD	outer diameter
OM	Operations and Maintenance
PSD	power spectral density
RMS	root mean square
RPV	reactor pressure vessel
ROTY	rotation in Y direction
ROTZ	rotation in Z direction
SIET	Sperimentiamo le Tue Idee
SG	steam generator
SNR	signal-to-noise ratio
TB	turbulent buffeting
TEEAR	test equipment error and accuracy report
URHR	upper riser hanger ring
UX	displacement in X direction
UY	displacement in Y direction
UZ	displacement in Z direction
VS	vortex shedding
VT	visual test

Table 1-2 Definitions

Term	Definition
Acoustic resonance	A phenomenon where an acoustic wave is generated at a frequency that coincides with the natural frequency of a confining structure.
Bias	In design analysis, bias is the difference between a best estimate and conservative parameter. In an experiment, bias is another term for a test distortion, i.e., a feature of the test that is different from the design analysis condition.
Confidence Interval	The probability that the true value lies within the specified limits.
Critical instrument	An instrument whose proper function is required in order to accomplish the objectives of the test campaign.
“dry” tube	Refers to a tube exposed to air (not submerged in liquid). It is understood that for the TF-3 testing described in this document the inside of the tubes is dry; liquid is excluded from the inside of the tubes.
Expanded Uncertainty	An estimate of the plus-or-minus limits of total error, with a defined level of confidence (usually 95%).

Term	Definition
Fatigue Usage Factor	Ratio of the number of vibration cycles anticipated during the lifetime of the component to the allowable cycles.
Fixed boundary condition	For the “fixed” boundary condition, the local UX, UY, UZ, ROTY, and ROTZ are constrained, but twisting about the tube axis is still free.
Gap or Pitch Velocity ( $V_{gap}$ )	Local velocity to which tubes are subject to, for flow in a closely pack tube array. This velocity is developed based on the overall flow area blocked by tubes (and supports as applicable). Calculated based on ASME N-1331.1 guidance of the approach flow velocity multiplied by the ratio of the tube pitch divided by the pitch minus the diameter.
General visual	<p>Method: This level of inspection is made with direct, assisted, or remote visual methods. A mirror may be used to enhance visual access to exposed surfaces in the inspection area. This level of inspection is made under normally available lighting conditions such as hangar lighting, flashlight, or drop-light, and may require removal or opening of access panels. Stands, ladders or platforms may be required to gain proximity to the area being checked.</p> <p>Criteria: A visual examination of an interior or exterior area, installation, or assembly to detect general mechanical and structural condition of components and their supports, and to detect surface discontinuities and imperfections. General mechanical and structural condition of components is verified by parameters such as clearances, settings, and physical displacements. Abnormally positioned components, such as misalignment of supports or a pipe outside a pipe hanger, are noted for closer examination. The inspection includes an observation of the condition of the material surfaces, including welds, within the inspection area to detect surface discontinuities and imperfections, such as a loss of integrity at bolted or welded connections, loose or missing parts, debris, cracks, corrosion, erosion, discoloration, and geometric discontinuities, such as gouges, chips, or dents.</p>
Long span	Based on arrangement of the SG tube supports in the NuScale design, lengths of helical tubing that span beneath each steam plenum are 64 degree arcs. These lengths of tubing are generically referred to as “long” spans.
Lower riser section	Reactor internal components from the upper core plate to the upper riser section.
Monte Carlo	Monte Carlo simulations provide statistical results to problems by performing repeated calculations with randomized input variables, and analyzing the trends in the output data.
Pivot boundary condition	For the “pivot” boundary condition, only the local UY and UZ are constrained, which allows for a tube to pivot about any direction, as well as sliding along its axis.
Pre-Test Analysis	The effort to model the test apparatus and assess input, numerical, and measurement uncertainties to inform the expected range of experimental results suitable for validation.
Propagation of Uncertainty	A test, for example, may report measured values for density ( $\rho$ ) and velocity ( $V$ ), in addition to their respective uncertainties. A validation analysis calculates dynamic pressure ( $\frac{1}{2} \rho V^2$ ), so its uncertainty



Term	Definition
	must be estimated by propagating the uncertainty of density and velocity.
Reflector block	The reflector sits inside the core barrel and is made of sections referred to as reflector blocks.
Sensitivity coefficient	The instantaneous rate of change in the result due to a change in a parameter.
Short span	Based on arrangement of the SG tube supports in the NuScale design, lengths of helical tubing that span between each steam plenum are only 26-degree arcs. These lengths of tubing are generically referred to as “short” spans.
SG plenum	There are eight SG plenums (four steam and four feedwater (FW)). The plenums contain the SG tube sheets.
Sliding boundary condition	For the “sliding” boundary condition, the local UY, UZ, ROTY, and ROTZ are constrained, but twisting about the tube axis is left free, as is displacement along the tube axis.
S-N Curve	Plot of stress (S) against the number of cycles to fatigue failure (N), sometimes called “endurance limit.”
Standard uncertainty	For a dispersion of values about a mean value, the standard uncertainty is the estimated standard deviation.
Strouhal number	A dimensionless frequency associated with vortex shedding (VS).
TF-1	Test facility designed to study the effects of secondary side boiling in HCSG tubes. Dynamic pressure measurements collected during flow testing.
TF-2	Test facility designed to study primary and secondary flows in HCSG tubes, and heat transfer. Strain gauge measurements were collected during flow testing.
TF-3	Test facility design to study fluid elastic instability, VS, and turbulence due to primary side flow in HCSG tubes. Testing consists of modal testing in air and in water, and primary side flow testing with extensive instrumentation to detect vibration.
Tube “light” or “heavy”	In reference to the mass of the tube, a “light” case implies the inside of the tube is filled with steam and the added mass on the primary side has a water density based on hot RCS temperature conditions. A “heavy” case implies the inside of the tube is filled with FW and the exterior fluid is at a cold RCS temperature.
Uncertainty	Relating to the presence of an unknown error in a measured quantity or a model calculation.
Upper riser section	Reactor vessel internals (RVI) components from the lower riser section to the top of the riser.
Validation	The process of determining the degree to which a model is an accurate representation of the real world from the perspective of the intended uses of the model.
“wet” tube	Refers to a tube submerged in liquid. It is understood that for the TF-3 testing described in this document the inside of the tubes are dry; liquid is excluded from the inside of the tubes. The frequency of a wet tube is shifted from the frequency of a dry tube based on consideration of the effect of the surrounding fluid displaced.

## 2.0 Background

This report describes the scope of the NuScale CVAP measurement and inspection programs. The following sections provide an overview of the components that require testing to validate the design analysis, per the NuScale Comprehensive Vibration Assessment Program Analysis Technical Report, TR-0716-50439 (Reference 9.1.4). The methodology used to account for uncertainty and bias to demonstrate the test design meets validation objectives is described. Additionally, existing benchmark testing is used to supplement the measurement program validation of the design analysis.

### 2.1 Measurement Plan Overview

The analysis program includes a list of FIV phenomena and a list of components that could be subjected to these phenomena. Due to the low primary coolant flow rates and passive safety designs, many regions of the NPM are not susceptible to FIV and do not meet FIV screening criteria. For NPM components or structures that meet the screening criteria for a phenomenon, analysis is performed to confirm whether the structure or component is susceptible to the FIV phenomena. For the NPM components that are evaluated for turbulent buffeting (TB), the vibrational amplitude and stresses are determined.

For phenomena with the exception of TB, the FIV mechanisms are characteristic of a strong fluid-structure coupling system. The NPM components are designed with sufficient margin of safety to the potential onset of these FIV phenomena. Turbulent buffeting occurs when a component is subject to turbulent flow, which is the dominant flow condition of the primary and secondary coolant. For TB, the fluid-structure coupling is weak and results in low amplitudes of vibration. Provided the impact stresses and fatigue usage are not detrimental to the component or structure over the design life, the acceptance criteria for this source of flow excitation are met.

Per Section 2.2 of Regulatory Guide 1.20 (Reference 9.1.5), the purpose of the measurement program is:

*“... to verify the structural integrity of the reactor internals, determine the margin of safety associated with steady-state and anticipated transient conditions for normal operation, and confirm the results of the vibration analysis.”*

The results of the measurement program are used to validate FIV analysis inputs, results, and the margins of safety. Due to the first-of-a-kind (prototype) NPM design, component screening analysis errs on the side of including potentially susceptible components, even when they could be excluded based on engineering judgment or precedent. This is an approach that minimizes the risk of failing to analyze a significant component. Compared to the existing pressurized water reactor and boiling water reactor designs, the natural circulation design of the NPM is inherently less susceptible to FIV due to the lower primary coolant velocities. Based on these factors, FIV analysis results demonstrate that many components have large margins of safety. The margin of safety is the means by which structural integrity is assured. Therefore, when a margin of safety is sufficiently large, validation by testing is not necessary. The scope of the measurement program is determined based on the results of the analysis program, as summarized in Table 2-1.

Table 2-1 Analysis program verification testing and inspections

Component	Susceptible Mechanisms	Mechanisms with less than 100% Safety Margin	Prototype Testing	
			Test Facility	Initial Startup
CNTS main steam line branch connections	AR	AR	-	CNTS steam piping testing
SG helical tubing	FEI, VS, TB	FEI, VS, TB	TF-3 testing	-
SG tube inlet flow restrictors	LFI, TB	LFI	SG IFR testing	-

Where,

AR = acoustic resonance,  
 CNTS = containment system,  
 SG= steam generator,  
 FEI = fluid elastic instability,  
 VS = vortex shedding, and  
 LFI = leakage flow instability.

Each prototype test used to validate a safety margin less than 100 percent considers applicable uncertainties and biases in the pre-test prediction to ensure that the test design meets the objective of validating the design analysis safety margin.

### 3.0 Benchmark Testing

In the NuScale CVAP, benchmark testing is used to justify important aspects of the design analysis. Benchmarking supplements literature and industry accepted methods to provide confidence that the measurements taken during the validation program do not produce unanticipated results requiring modifications to the design analysis methods.

Four sets of test data are used for benchmarking: TF-1, TF-2, SG IFR testing, and TF-3 Build-out modal testing.

#### 3.1 Steam Generator Inlet Flow Restrictor Benchmark Testing

The SG IFR is designed to provide a pressure loss at the entrance of each SG tube. The pressure loss is necessary to prevent density wave oscillations from forming in the SG tubes, which could result in undesirable steam outlet conditions and thermal fatigue. The primary design parameter associated with the SG IFR is the hydraulic performance of the device, specifically the loss coefficient. Other significant considerations for the component design include manufacturability, ease of removal for inspection of SG tubes, and vibration performance.

The purpose of this test was to inform the design of the SG IFR component. The SG IFR is considered susceptible to leakage FIV and TB. The SG IFR is the only NPM component that is susceptible to leakage FIV. As such, analytical predictions are not performed for this mechanism as a part of the CVAP design analysis program. Instead, acceptable performance is demonstrated with testing. Design analysis is performed for turbulence. Testing to support the CVAP is planned for leakage flow. The preliminary testing discussed herein provides confidence that future testing of the final SG IFR design will demonstrate acceptable FIV performance.

This section summarizes the preliminary designs that were tested and the outcome of the testing. The test data was evaluated to determine when vibration was present. Spectral analysis of the acceleration data was performed to characterize the frequency of the vibration for tests in which vibration was higher than expected. Additionally, this report compares similar designs tested to the final SG IFR design and provides recommendations to be considered for the CVAP SG IFR testing to provide improved vibration data.

##### 3.1.1 Steam Generator Inlet Flow Restrictor Design Options Tested

Three different restrictor design options were tested: a center flow orifice restrictor, annular flow orifice restrictors, and annular flow stepped restrictors. Figure 3-1 shows the center orifice design, which does not insert inside of the SG tube. Figure 3-2 shows the threaded design and Figure 3-3 shows the stepped design.

The center flow orifice restrictor design consists of individual orifice inserts that are mounted on a plate upstream of each tube inlet and seated at each tube inlet. The flow travels through the center of the restrictor directly into the tube. For this design, there is potential for bypass flow to occur where the restrictor is seated on the SG tube. This region

represents a narrow, annular flow path and at higher bypass flow rates could, produce a sufficient differential pressure to generate leakage flow instability (LFI).

The annular designs are inserted in the tube and achieve the pressure loss through the reduced flow area they generate. The two annular flow restrictors are threaded and stepped designs. The threaded design is essentially a bolt. The desired form loss is achieved by specifying a thread diameter and insertion length. Of the designs tested, this arrangement has the least susceptibility to LFI because the restrictor is the most rigid [shorter insertion length and larger average outer diameter (OD)] and does not produce a diverging flow path.

The stepped design consists of a solid rod with a series of stepped cylinders along the length. The desired loss coefficient is obtained by varying the total number of stepped sections inserted into the tube, the step OD, and the spacing between steps. Designs that provide two to five steps inserted were tested. Two different step ODs (0.510 and 0.515 inches) and two different step spacing values (0.50 inch and 0.75 inch) were investigated.

{{

}}<sup>2(a),(c),ECI</sup>

Figure 3-1 Center flow orifice restrictor design

{{

}}<sup>2(a),(c),ECI</sup>

Figure 3-2 Threaded fastener design

{{

}}<sup>2(a),(c),ECI</sup>

Figure 3-3 Stepped solid annular design

The SG tube inner diameter in the test is {{ }}<sup>2(a),(c),ECI</sup> inch for the first {{ }}<sup>2(a),(c),ECI</sup> inches to simulate the inner diameter of the portion of the tube that is hydraulically expanded in the FW plenum tubesheet. The tubesheet length is shorter in the test design compared to the final design. This does not affect the hydraulic performance or vibration of the restrictor device. It does affect the measured accelerations since a portion of the tube containing the restrictor is unsupported due to the shorter tubesheet length compared to the final design. Stainless steel type 304 is used in lieu of Alloy 690.

An accelerometer was installed on the outside of the tube during testing to allow collection of vibration test results. The accelerometer was affixed to the tube with a threaded hex nut, located approximately 1.75 inches from the mounting plate. This location is adjacent to the inserted flow restrictor. The location of the accelerometer is shown in Figure 3-5.

For the threaded and stepped designs, a range of insertion lengths were tested to meet thermal hydraulic test needs. Results show the effect of insertion length and pressure drop on vibration for these designs.

Table 3-1 provides a description of the tested devices. The measured loss coefficients are provided to indicate the relative pressure loss each device provides.

Table 3-1 Steam generator inlet flow restrictor design options

Device Type	Device Number	Measured Loss Coefficient	Nominal Length (inch)	Nominal Inner Diameter (inch)
Center orifice	1	{{ }}		{{ }} <sup>2(a),(c),ECI</sup>
			<b>Insertion Length (inch)</b>	<b>Thread Type</b>
Threaded fastener	2	{{ }}	{{ }} <sup>2(a),(c),ECI</sup>	ASME B1.1-2003 ½"-13 UNC-2A
	3	{{ }}	{{ }} <sup>2(a),(c),ECI</sup>	
			<b>Insertion Length (inch)</b>	<b>Step Spacing &amp; Outer Diameter</b>
Stepped annular	4	{{ }}		{{ }} <sup>2(a),(c),ECI</sup>
	5	{{ }}		{{ }} <sup>2(a),(c),ECI</sup>
	6	{{ }}		{{ }} <sup>2(a),(c),ECI</sup>
	7	{{ }}		{{ }} <sup>2(a),(c),ECI</sup>
	8	{{ }}		{{ }} <sup>2(a),(c),ECI</sup>
	9	{{ }}		{{ }} <sup>2(a),(c),ECI</sup>
	10	{{ }}		{{ }} <sup>2(a),(c),ECI</sup>
	11	{{ }}		{{ }} <sup>2(a),(c),ECI</sup>

Device Type	Device Number	Measured Loss Coefficient	Nominal Length (inch)	Nominal Inner Diameter (inch)
	12	{{		}} <sup>2(a),(c),ECI</sup>

### 3.1.1.1 Comparison of Preliminary Designs Tested to Final Design

The final SG IFR design is a five-step design, with a step OD of {{}}<sup>2(a),(c),ECI</sup> inches, and steps that are {{}}<sup>2(a),(c),ECI</sup> inches long and spaced {{}}<sup>2(a),(c),ECI</sup> inches apart. Including the alignment cone, the insertion length is {{}}<sup>2(a),(c),ECI</sup> inches. Device 6 is the most similar to the final design, because it is a stepped design with the same number of steps and the most similar insertion length and step dimensions. The differences between Device 6 and the final SG IFR design are summarized below.

The distance between steps and the step length in the SG IFR design is {{}}<sup>2(a),(c),ECI</sup> inches. In the test configuration, a step spacing of {{}}<sup>2(a),(c),ECI</sup> inches was used for tests 4-10 and {{}}<sup>2(a),(c),ECI</sup> inches was used for tests 11-12. While these dimensions bound the dimension of the final design, no device provided the exact step spacing. The test design provided a step length of {{}}<sup>2(a),(c),ECI</sup> inches, which is less than the final design of {{}}<sup>2(a),(c),ECI</sup> inches.

Similar dimensional differences in the length and diameter of the alignment cone (located at the end of the flow restrictor) also exist. In the tested design, the alignment cone length is {{}}<sup>2(a),(c),ECI</sup> inches and the end width is {{}}<sup>2(a),(c),ECI</sup> inches. In the final design the length is {{}}<sup>2(a),(c),ECI</sup> inches and the end width is {{}}<sup>2(a),(c),ECI</sup> inches. The minor dimensional differences in the alignment cone are relevant for leakage FIV because the alignment cone provides a diverging flow path, which has been shown to increase the susceptibility of a component to leakage FIV.

Lastly, there are construction differences. In the final design, the flow restrictor consists of a bolt with a threaded alignment cone that attaches to the end. The stepped flow restrictor has an inner diameter {{}}<sup>2(a),(c),ECI</sup> inches larger than the OD of the bolt. It is held in place by compression provided by the mounting plate and the washer and hex head nut. In the tested configuration, the flow restrictor assembly is a single, solid element. In the final design, the compression provided by the nut and the gap between the bolt and flow restrictor could introduce operational biases and uncertainties that are investigated to ensure they do not affect vibration for a bounding range of compression and alignment conditions.

### 3.1.1.2 Steam Generator Inlet Flow Restrictor Test Conditions

The tests are performed at a nominal ambient temperature of 70 degrees Fahrenheit, and a range of 60 degrees Fahrenheit to 120 degrees Fahrenheit is allowed. Each test is run with a fixed FW inlet pressure that is nominally 100 psia, with an allowed range of 80 to 150 psia. Steady-state test conditions are established for five minutes before starting the test. During the test, fluid conditions are controlled to ±1 percent of the target pressure, ±2 degrees Fahrenheit for temperature and ±2 percent of the target flow rate.



A total of 15 restrictors were manufactured and tested. This value is based on three restrictors for each device type, including the different step spacing and OD for the step design. Testing three different copies of the nominally identical restrictor quantifies the effect of differences due to manufacturing tolerances and fit-up on the flow testing results. Tests were conducted in one of the four FW plenum assemblies. The four assemblies are provided for efficiency because each time a restrictor is replaced, the test loop needs to be drained. The test identification value is based on the device number (Table 3-1), the device copy (A, B, C), and the plenum number (1-4).

Tests were performed at flow rates that provided Reynolds similitude of approximately 1 percent, 15 percent, 50 percent, 90 percent, 100 percent and 110 percent. Cavitation checks were also performed for select devices at the highest Reynolds flow condition by increasing the inlet pressure.

Misalignment tests were also performed for Devices 3 and 6. In these tests, the device was installed such that it was in contact with the SG tube wall. Flow rates for 15 percent and 100 percent Reynolds similitude were tested.

### 3.1.1.3 Test Facility Overview

The overall facility design consists of a test loop that connects to a header with four, parallel test assemblies. Each assembly consists of a FW plenum, flow restrictor device, and SG tube. Only one assembly was tested at a time. The ball valves were used to isolate the test assemblies that were not in use. The test fluid was tap water filtered by a 1 micron filter installed between the two pumps. Valves downstream of the second pump are used to adjust the system pressure and a valve downstream of the test apparatus is used to regulate flow rate.

A schematic of the test facility design is provided in Figure 3-4.

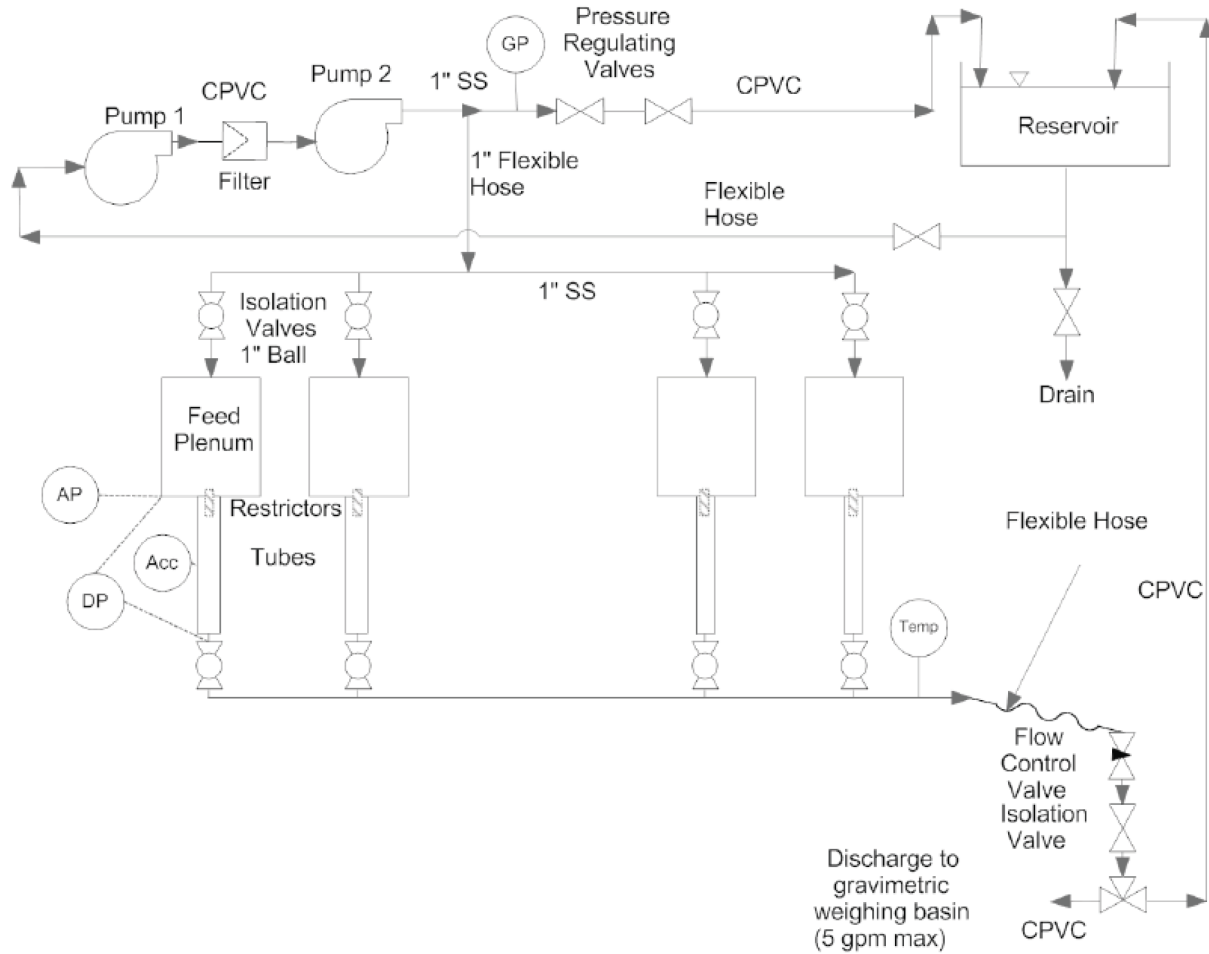


Figure 3-4 Steam generator inlet flow restrictor test facility schematic

The FW plenum is four-inch, schedule 40 pipe. It contains two sets of perforated plates to straighten the flow before it arrives at the restrictor mounting plate. The FW plenum provides absolute pressure measurement, a tap for differential pressure measurement from the plenum to downstream of the flow restrictor in the SG tube, and an accelerometer on the exterior of the SG tube. The FW plenum and nearby test loop components are shown in Figure 3-5.

Additionally, the test facility contains scales used in the gravimetric flow rate determination, a data acquisition system (DAS) to process instrument signals, and a boroscope that was used to visually inspect the inside of the SG tubes.

{

}}<sup>2(a),(c)</sup>

Figure 3-5 Test assembly

#### 3.1.1.4 Testing Procedure

The testing procedure consisted of installing the restrictor devices to be tested into each test assembly, and performing instrument and DAS functional checks. Next, the system is filled with water and air is vented.

Before starting flow testing, the DAS was set to continuously record instrument signals. Flow is started and aligned to the assembly to be tested. Because gravimetric flow rate measurement was used, the flow testing consisted of setting the flow to achieve the expected differential pressure associated with the 50 percent Reynolds similitude flow condition. The test conditions at approximately 50 percent flow were then used to calculate the test value for the restrictor loss coefficient. Differential pressures for the remaining Reynolds similitude flow rates (15 percent, 90 percent, 100 percent and 110 percent) were calculated using the experimentally determined restrictor loss coefficient. Then, the remaining flow tests were executed in the test loop by adjusting the flow control valve. Based on this approach, differences exist between the target and actual flow rates achieved for each Reynolds similitude case. This is acceptable because data was collected over a range of flow rates that spanned the prototypic secondary flow conditions. Gravimetric flow rate provided the actual, average flow rate at the conclusion of each test. In addition to the flow rates noted above, restrictor devices were tested at low flow rates, near 1 percent Reynolds similitude. Also, Devices 1, 3, 6, 7 and 10 were checked for

cavitation by increasing the inlet pressure at the 110 percent flow rate condition. A cavitation number was determined for each type of restrictor design. Higher inlet pressures provide more stability to cavitation; therefore, cavitation is not a concern in the final design since normal operating pressure is much greater than the test pressure conditions.

When the four installed assemblies had been tested, the loop was drained to permit installation of the next set of orifice devices. Visual inspections of the tubes were completed using the boroscope to assess if there was visible damage due to vibration of the restrictor device.

### 3.1.1.5 Assessment of Root Mean Square Vibration Results

The accelerometer results for each device and flow rate condition were evaluated to confirm which devices and flow rate conditions result in levels of tube vibration that may indicate the presence of leakage flow instability. The test data is provided in three formats: continuous save files, dynamic signal analysis (DSA) files, and select data files. The continuous save files contain accelerometer measurements and root mean square (RMS) acceleration values that are averaged, both over 0.5 second intervals. The DSA files contain the dynamic signal from the 4000 Hz accelerometer over 30 seconds. The select data files contain the overall averages of the acceleration and RMS acceleration for each flow rate condition tested. The average RMS acceleration and maximum acceleration values are used to demonstrate the devices and flow conditions where leakage flow instability may be indicated.

Vibration levels, at which there is a possibility of leakage flow instability, typically occurred at the highest flow rate tested. Only Device 1A was flow tested at approximately 150 percent Reynolds similitude. Other devices had a maximum flow test at Reynolds similitude of approximately 110 percent.

Table 3-2 was generated by determining the tests with the highest average RMS acceleration values and highest maximum acceleration values. The table provides the 10 tests with the highest average RMS acceleration values. Additionally, the absolute value of the maximum acceleration was determined for each test at the Reynolds similitude 110 percent case and at a lower similitude condition, if the highest average RMS vibration occurred there. Three tests have high maximum acceleration values (judged to be greater than about 75 dg) but normal average RMS acceleration values (judged to be less than about 30 dg): test 6C1, 10C4, and 11C2. These three tests are also included in the table to provide explanation of the test results.

Table 3-2 Average and maximum root mean square vibration results

Device Description	Device Number	Device	Plenum Tested	Approximate Reynolds Percentage	Average RMS Acceleration (dg)	Maximum Acceleration (dg)
Center orifice	1	A	4	150	{{	}} <sup>2(a),(c)</sup>
Stepped annular OD 0.510 inch Space 0.5 inch	6	C	1	110	{{	}} <sup>2(a),(c)</sup>
Stepped annular OD 0.515 inch Space 0.5 inch	7	A	1	Note (2)	{{	}} <sup>2(a),(c)</sup>
	7	B	4	Note (2)	{{	}} <sup>2(a),(c)</sup>
	8	A	1	110	{{	}} <sup>2(a),(c)</sup>
	8	B	2	100	{{	}} <sup>2(a),(c)</sup>
	9	A	3	100	{{	}} <sup>2(a),(c)</sup>
	9	C	3	110	{{	}} <sup>2(a),(c)</sup>
	10	A	1	100	{{	}} <sup>2(a),(c)</sup>
	10	C	4	110	{{	}} <sup>2(a),(c)</sup>
Stepped annular OD 0.515 inch Space 0.75 inch	11	C	2	110	{{	}} <sup>2(a),(c)</sup>
	12	B	1	110	{{	}} <sup>2(a),(c)</sup>
	12	B	1	90	{{	}} <sup>2(a),(c)</sup>

- Notes: (1) Maximum acceleration for Device 1 tested at 110% is {{ }}<sup>2(a),(c)</sup> dg; average acceleration is {{ }}<sup>2(a),(c)</sup> dg for test 1A4.
- (2) DSA and select data files are not provided for Device 7. The continuous save file is used to determine acceleration values; however, there is not enough information in that file to correlate the period of vibration to a specific flow rate case. It is assumed that the values reported in this table correspond to the 110% Reynolds similitude flow test.
- (3) These values are the maximum reported in the continuous save file, which is an average of the 4000 Hz readings each half second. Therefore, these are not true maximum values like the others in this table.
- (4) A select data file was not provided for this test; therefore, an average RMS acceleration is calculated using the continuous save file.
- (5) High acceleration due to functional tap test during the flow testing.

The center orifice design experienced significant vibration at the 150 percent Reynolds similitude condition. At and below 110 percent, the average RMS accelerations remained below 3 dg for the center orifice configurations and flow rates tested as shown in Figure 3-6. This device was located in the FW plenum rather than the SG tube, where the accelerometer is mounted. Therefore, the sensed vibration in and around the restrictor is higher than was transmitted to and measured at the tube. If significant TB or leakage FIV were present, this would be transmitted to the tube. The low accelerations in Figure 3-6 show that the device performed acceptably at and below 110 percent Reynolds similitude. The RMS accelerations generally increase with increasing flow rate, and represent the acceleration of the tube itself due to turbulent, annular flow.

{{

}}<sup>2(a),(c)</sup>

Figure 3-6 Device 1 root mean square acceleration at 110 percent Reynolds similitude and below

Devices 2 and 3 are the threaded annular design. This design did not experience significant vibration at or below the maximum flow rate tested of 110 percent Reynold similitude. Tests 3A2, 3A3, 3B2, 3B3, 3C3 and 3C4 shown in Figure 3-7 represent flow testing with the restrictor misaligned. In this testing, the restrictor was mounted such that it was touching the inside of the tube. The measured accelerations are higher for the misaligned tests, but are still low, which suggests that the turbulent excitation does not cause high levels of vibration even when contact occurs for the threaded annular design. Overall, the accelerations measured for Devices 2 and 3 are higher than for Device 1 due to the higher velocities in the tube and the location of the restrictor adjacent to the accelerometer rather than in the FW plenum.

{{

}}<sup>2(a),(c)</sup>

Figure 3-7 Device 2 and 3 root mean square acceleration

Devices 4, 5 and 6 represent the stepped annular design with the smaller step spacing and smaller step OD. The OD of the step is {{ }}<sup>2(a),(c)</sup> inches and the spacing between steps is {{ }}<sup>2(a),(c)</sup> inch. Device 4 has three steps inserted into the SG tube, Device 5 has four steps inserted, and Device 6 has five steps inserted. Average RMS vibration levels were low, as shown in Figure 3-8 and Figure 3-9. The misaligned cases for Device 6 did not have significantly higher acceleration results compared to the cases where the device was properly aligned. Only two devices (5B2 and 5C2) saw average RMS accelerations near {{ }}<sup>2(a),(c)</sup> dg at the 110 percent Reynolds similitude condition, and maximum accelerations for these cases remained below {{ }}<sup>2(a),(c)</sup> dg. Case 6C1 had intermittent high acceleration readings. The time history acceleration for this test is shown in Figure 3-10. While the cause of the intermittent increases in acceleration readings is not known, the maximum accelerations are less than {{ }}<sup>2(a),(c)</sup> dg and do not indicate a vibration concern.

{{

}}<sup>2(a),(c)</sup>

Figure 3-8 Device 4-5 root mean square acceleration at 110 percent Reynolds similitude and below

{{

}}<sup>2(a),(c)</sup>

Figure 3-9 Device 6 root mean square acceleration at 110 percent Reynolds similitude and below



{{

}}<sup>2(a),(c)</sup>

Figure 3-10 Test 6C1 acceleration

The final two sets of stepped annular restrictors, with the larger step OD of {{ }}<sup>2(a),(c)</sup> inches, experienced the highest vibration levels, as shown in Figure 3-11 and Figure 3-13. Time history results are not available for Device 7, but 7A1 and 7B4 experienced vibration in excess of what can be attributed to fluid turbulence alone. Tests 8A1, 9A3 and 9C3 also experienced vibration. The average and maximum accelerations for Tests 8B2, 9A3 and 10A1 at Reynolds similitude of 100% are higher than the reported accelerations at 110 percent, although other device and plenum numbers for devices 8, 9 and 10 tested at 110% conditions also have similar or higher average and maximum acceleration results.

{{

}}<sup>2(a),(c)</sup>

Figure 3-11 Device 7-10 root mean square acceleration at 110 percent Reynolds similitude and below

Test 10C4 has a high maximum acceleration, which is due to a functional test where the SG tube is lightly tapped with a screwdriver to test the accelerometer. This is evident in the acceleration readings near 7.5 seconds in Figure 3-12.

{{

}}<sup>2(a),(c)</sup>

Figure 3-12 Test 10C4 acceleration

{{

}}<sup>2(a),(c)</sup>

Figure 3-13 Device 11-12 root mean square acceleration at 110 percent Reynolds similitude and below



$$\Delta f = \frac{1}{n\Delta T} = \frac{f_s}{n} \quad \text{Equation 3-2}$$

$$\Delta f_w = 2f_0\zeta_0 \quad \text{Equation 3-3}$$

Where,

- $\Delta f$  = Frequency resolution (Hz),
- $n$  = Sample block size (-),
- $\Delta T$  = Sampling interval (s),
- $f_s$  = Sampling frequency (Hz),
- $\Delta f_w$  = Resonant peak half width (Hz),
- $f_0$  = Un-damped natural frequency (Hz), and
- $\zeta_0$  = Damping (-).

Spectral analyses of the devices that experienced vibration are performed using Microsoft Excel. A Fourier transform of the time history results is performed to determine if there is a dominant vibration frequency. The Fourier analysis function is used from the Data Analysis Toolpak. To use the function, the input range is specified as the  $2^k$  values of the acceleration history. The fast Fourier transform (FFT) outputs  $2^k$  complex number values. The magnitude of each value is obtained per Equation 3-4, and the associated frequency for the  $n^{\text{th}}$  value is per Equation 3-5.

$$FFT_{mag} = \frac{2 * IMABS(FFT_{complex})}{2^k} \quad \text{Equation 3-4}$$

$$f_n = \frac{nf_s}{2^k} \quad \text{Equation 3-5}$$

Where,

- $FFT_{mag}$  = FFT Amplitude (-),
- $IMABS(FFT_{complex})$  = Magnitude of complex number (-),
- $k$  = Integer that determines sample block size (-),

$f_n$	=	Frequency for $n^{\text{th}}$ FFT amplitude (Hz),
$n$	=	Zero to maximum sample block size (-), and
$f_s$	=	Sampling frequency (Hz).

The amplitude associated with each frequency is calculated for up to 4000 Hz for each test; however, the plots display the first 500 Hz for clarity. If LFI were present in the acceleration data, it would coincide with the fundamental mode of the restrictor device, which is approximately  $\{ \{ \} \}^{2(a),(c)}$ . Spectral results between 500 Hz and 4000 Hz were reviewed and amplitudes are similar to the results below 500 Hz that are shown in the spectral plots in the body of this report.

The tests with the highest acceleration results (not attributed to tap testing or an anomalous reading) are 1A4 at Reynolds similitude of 150 percent, 8A1 at Reynolds similitude of 110%, 8B2 at Reynolds similitude of 100 percent, 9A3 at Reynolds similitude of 100 percent, 9C3 at Reynolds similitude of 110%, 10A1 at Reynolds similitude of 100 percent, 11C2 at Reynolds similitude of 110%, and 12B1 at Reynolds similitude of 110%. There are no noticeable vibration signatures in the acceleration versus time plots. Additionally, the spectral analysis does not indicate there is a dominant frequency for any of these tests. This suggests that the accelerations that were seen were random in nature and are not vibration due to leakage flow instability. Leakage FIV would have a frequency signature that is similar to that of the vibrating component, because it is a strongly-coupled FIV phenomenon.

Because the acceleration measurement is taken at the tube and not on the device itself, noise could result and obscure the device signature. Additionally, when high vibrations were experienced they tended to be significantly higher than the vibration levels at the next tested flow condition, which is indicative of onset of a leakage flow instability rather than the gradual increase in vibration due to a turbulent response. It is concluded that the higher vibration seen in these tests is due to contact between the restrictor and the tube due to random vibration caused by TB. Further testing and analysis will confirm or refute this. It should also be noted that the instances of high vibration occurred at flow rates in excess of the design licensing basis flow conditions, so the vibrations discussed in this report correspond to operating conditions that are beyond design basis. Maximum design flow velocities in the NuScale design correspond to the results below Reynolds similitude of 50% in these tests. Acceleration and amplitude graphs for these tests are provided in Figure 3-14 through Figure 3-29.

{{

}}<sup>2(a),(c)</sup>

Figure 3-14 Test 1A4 (150 percent) acceleration

{{

}}<sup>2(a),(c)</sup>

Figure 3-15 Test 1A4 (150 percent) frequency

{{

}}<sup>2(a),(c)</sup>

Figure 3-16 Test 8A1 acceleration

{{

}}<sup>2(a),(c)</sup>

Figure 3-17 Test 8A1 frequency



{{

}}<sup>2(a),(c)</sup>

Figure 3-18 Test 8B2 Reynolds similitude of 100 percent acceleration

{{

}}<sup>2(a),(c)</sup>

Figure 3-19 Test 8B2 Reynolds similitude of 100 percent frequency

{{

}}<sup>2(a),(c)</sup>

Figure 3-20 Test 9A3 Reynolds similitude of 100 percent acceleration

{{

}}<sup>2(a),(c)</sup>

Figure 3-21 Test 9A3 Reynolds similitude of 100 percent frequency

{{

}}<sup>2(a),(c)</sup>

Figure 3-22 Test 9C3 acceleration

{{

}}<sup>2(a),(c)</sup>

Figure 3-23 Test 9C3 frequency

{{

}}<sup>2(a),(c)</sup>

Figure 3-24 Test 10A1 Reynolds similitude of 100 percent acceleration

{{

}}<sup>2(a),(c)</sup>

Figure 3-25 Test 10A1 Reynolds similitude of 100 percent frequency

{{

}}<sup>2(a),(c)</sup>

Figure 3-26 Test 11C2 acceleration

{{

}}<sup>2(a),(c)</sup>

Figure 3-27 Test 11C2 frequency

{{

}}<sup>2(a),(c)</sup>

Figure 3-28 Test 12B1 acceleration

{{

}}<sup>2(a),(c)</sup>

Figure 3-29 Test 12B1 frequency



Table 3-3 Reynolds similitude values

Location	Temperature (°F)	Pressure (psia)	Velocity (in./s)	Reynolds Number
In tube, normal operating	300	525	{{	}} <sup>2(a),(c)</sup>
At constriction, normal operating			}} <sup>2(a),(c)</sup>	
In tube, minimum test condition	60	80	{{	}} <sup>2(a),(c)</sup>
At constriction, minimum test condition			}} <sup>2(a),(c)</sup>	
In tube, maximum test condition	120	150	{{	}} <sup>2(a),(c)</sup>
At constriction, maximum test condition			}} <sup>2(a),(c)</sup>	

The acceleration results were integrated to provide the displacement at the sensor location. In this test, the accelerometers were located on the exterior of the SG tube, downstream of where the tube exits the tube sheet. The source of vibration is from the turbulent flow inside the tube, and in the case of higher acceleration results, due to the restrictor impacting the tube wall. For the misaligned cases, the restrictor was directly in contact with the SG tube inner wall. For aligned cases, the radial clearance between the restrictor and the tube outer wall is {{ }}<sup>2(a),(c)</sup> inch for the stepped design.

The SG tube displacement is calculated by double integration of the acceleration time history. The integration is performed numerically using the midpoint rule. Table 3-4 provides the maximum displacements for select tests, and Figure 3-30 plots the displacements at the beginning of each test run. Note that because only a portion of the time history is plotted, the maximum displacements in Table 3-4 are higher than the data shown in Figure 3-30. The observed displacements of the tube are smaller than the radial clearance between the restrictor and the tube wall. This is expected as the tube displacement is a result of the vibration of the restrictor. For the test case most similar to the final design and tested at velocities 180 percent to 450 percent of the licensing basis secondary side flow rate, the maximum displacement is {{ }}<sup>2(a),(c)</sup>.

Table 3-4 Steam generator tube displacements

Test	Test Description	Maximum Displacement (inch)
1A4	Threaded design Highest flow velocity (Reynolds of 150%) and accelerations	{{ }} <sup>2(a),(c)</sup>
6C1	Stepped design Reynolds of 110%, design is most similar to final design	{{ }} <sup>2(a),(c)</sup>
8A1	Stepped design Highest maximum accelerations for stepped design Reynolds number 110%	{{ }} <sup>2(a),(c)</sup>
8B2	Stepped design Moderate accelerations Reynolds number 100%	{{ }} <sup>2(a),(c)</sup>



}}

}}<sup>2(a),(c)</sup>

Figure 3-30 Steam generator tube displacement

### 3.1.1.7 Considerations for Future Regulatory Guide 1.20 Testing

The test program for the vibration testing for the SG IFR design demonstrated that for the range of designs tested, LFI is not a concern, and while impact between the restrictor device and the tube occurred between approximately {{  
}}<sup>2(a),(c)</sup> of the normal operating velocities, vibration levels characteristic of impact were not observed at normal operating velocities.

The following items were considered in the development of the CVAP SG IFR testing:

- Modal testing should be performed to confirm the frequencies of the restrictor in the test apparatus structure. Due to differences associated with the test assembly compared to the plant design, this could alter the natural frequency seen at the accelerometer.
- A longer sampling time further improves the frequency resolution. The test should provide real time frequency analysis of the accelerometer readings, considering the entire length of the test data.

- Accelerometers should be placed in more than one location for each assembly to provide redundancy in the measurements and a measure of experimental uncertainty. Direct measurement of restrictor vibration should be made, but if that is not possible, predictions of the expected tube vibration due to turbulent or leakage flow impact from the restrictor should be performed to inform optimal sensor placement locations and interpretation of real time frequency results during the test.
- Predicted reduced flow velocities (which are a function of flow velocity and structural frequency) should be determined for the SG IFR final design and the test velocities chosen considering these values.
- The testing should be long enough to achieve a minimum of 1 million vibration cycles assuming the restrictor is vibrating at its fundamental frequency. Using these results, an adequate inspection frequency for the component design life can be determined in advance of the Regulatory Guide 1.20 inspections following initial startup testing.

### 3.1.1.8 Conclusions

Based on the lack of vibration signatures in the acceleration results and no dominant frequency peaks in the spectral analysis, these initial test results demonstrate that LFI and TB are not a concern for these designs.

Some designs, when tested at the highest Reynolds similitude conditions, experienced increased vibration due to contact between the restrictor and SG tube. The contact appears to have resulted from turbulence or a leakage flow response; however, these higher accelerations were only observed at beyond-design-basis flow velocity conditions. The testing duration combined with the measured acceleration levels were not long enough to produce degradation of the restrictor or the SG tube. High levels of vibration were not present at the lower Reynolds similitude conditions, where the velocity is similar to the velocity present at normal operating conditions. The vibration that was observed would be characteristic of operating at approximately {{  
}}<sup>2(a),(c)</sup> flow conditions in terms of the fluid velocities. Therefore, while small differences exist between the tested and final SG IFR designs and improvements are recommended for future CVAP Regulatory Guide 1.20 testing, the initial testing provides a level of confidence that the SG IFR design does not experience leakage FIV or degradation due to turbulence at normal operating design conditions in the plant.

Validation testing is planned to confirm the final SG IFR design is not susceptible to vibration in accordance with Regulatory Guide 1.20. See Section 5.3 for a discussion of the requirements for the SG IFR validation testing.

## 3.2 TF-1 and TF-2 Benchmark Testing for Turbulence

### 3.2.1 TF-2 Modal Analysis

This section analyzes the modal response of the TF-2 steam generator (SG) test specimen. The TF-2 test specimen is a full-scale representation of columns 1 through 5 of the NPM SG. This calculation is based on the SIET Helical Coil Steam Generator Test Program – Fluid Heated Test Facility Design.

This section applies only to the TF-2 test specimen design and not the NPM design. A full bundle model as well as single tube models are used in the analysis. Both models are run for three test conditions, each with unique fluid temperatures and pressures that represent the test conditions. The single tube model is run for two sets of boundary conditions.

The results generated in this section are:

- Modal frequencies, mass participations, and mode shapes for the full bundle and single tube models for significant modes.
- Mode shape text files for three tubes of interest for the full bundle and single tube models for modes (up to 160 Hz for full bundle and up to 600 Hz for single tube).
- A mesh sensitivity analysis to validate the mesh size used in the models.

### 3.2.1.1 Model Overview

The TF-2 global assembly drawing is shown in Figure 3-31, with major components labeled. The ANSYS model explicitly models these major components except the vessel, which is modeled as rigid nodes. The TF-2 model is shown in Figure 3-32 and Figure 3-33. The model details are described in the following sections.

{{

}}<sup>2(a),(c)</sup>

Figure 3-31 TF-2 test specimen assembly drawing

{{

}}<sup>2(a),(c)</sup>

Figure 3-32 TF-2 full bundle geometry and mesh

{{

}}<sup>2(a),(c)</sup>

Figure 3-33 TF-2 full bundle geometry and mesh close-up

### 3.2.1.2 Test Cases

The model was run for three test cases. Each test case is for a different set of primary and secondary fluid conditions. These temperatures and pressures were measured directly from the sensors in the test specimen during the tests and are summarized in Table 3-5.

Table 3-5 Fluid conditions for each test case analyzed

Case	Primary Side		Secondary Side		Notes
	P <sub>avg</sub> (psi)	T <sub>avg</sub> (°F)	P <sub>avg</sub> (psi)	T <sub>avg</sub> (°F)	
TF0001	{{				drained secondary side
TF0002					filled secondary side (liquid)
TF0007				}} <sup>2(a),(c)</sup>	boiling secondary side (liquid and steam)

### 3.2.1.3 Geometry

The geometry of the TF-2 full bundle model includes:

- Tube coil geometry
- Header geometry
- Tube support geometry
- Assembly view
- Barrels and plates geometry
- Cross-section geometry

Multiple cross-sections are used for the beam elements in the model. The geometry values and source references are listed in Table 3-6. The tube support regions that have cutouts use a representative rectangular cross-section that has equivalent bending stiffness as the detailed geometry. A diagram explaining the naming system for the tube support sections is shown in Figure 3-34.

{{

}}<sup>2(a),(c)</sup>

Figure 3-34 Naming system for various tube support sections

Table 3-6 Cross-section geometry

Design Model Name	Dimensions (inches)	Dimensions (mm)
tube	{{	
header		
wide_end		
wide_transition		
wide_middle		
narrow_end		
narrow_middle		
tab		}} <sup>2(a),(c)</sup>

Details of the TF-2 assembly were simplified to reduce model and mesh complexity. These modifications have negligible impact on mass, stiffness, and thus the overall results of the analysis. Minor simplifications include neglecting small features such as fillets, fasteners, and instrumentation. The larger simplifications are listed below.

- Neglected steam and feedwater piping: Steam and feedwater piping extend from the headers and exit the vessel (see Figure 3-35). The numerous pipe bends do not contribute to the stiffness of the assembly.



{{

}}<sup>2(a),(c)</sup>

Figure 3-35 Neglected steam and feedwater piping

- Neglected shifted headers: In order to avoid interferences between the tubes and headers, the headers are shifted axially (see Figure 3-36). This causes the first and last wrap of a given tube column to have an increased inclination angle. This design aspect has negligible effect on the overall behavior of the bundle. The sensors on the instrumented tubes are also located in the main helix of the bundle, not on these first and last wraps, meaning that slight changes to the end condition of the tubes do not affect the measured results. Therefore, a constant nominal inclination angle is used for the tubes throughout the bundle.

{{

}}<sup>2(a),(c)</sup>

Figure 3-36 Neglected shift of header position and change in tube inclination angle

- Neglected longitudinal ribs: There are six longitudinal ribs that run along the bottom 1/3<sup>rd</sup> of the external barrel (indicated in Figure 3-37. These ribs are not included in the model.

{{

}}<sup>2(a),(c)</sup>

Figure 3-37 Neglected longitudinal ribs

- Neglected internal structures: Inside the bundle are a series of pipes/conduit as well as a ladder (see Figure 3-38). These structures were neglected.

{{

}}<sup>2(a),(c)</sup>

Figure 3-38 Neglected internal structures

- Merging of upper plate and lower plate: At the bottom of the tube bundle is a pair of plates called “upper plate” and “lower plate” that bolt together (see Figure 3-39). These plates were merged into a single plate in the model.

---

 {{
}}<sup>2(a),(c)</sup>

Figure 3-39 Separate plates that are modeled as single monolithic plate

During fabrication, the radial and azimuthal positions of the headers were re-positioned slightly to avoid interferences with the tubes. The radial positioning of the headers is a negligible change, but the azimuthal position change was incorporated into the model, as this affects the lengths of the end segments of the tubes.

#### 3.2.1.4 Mesh

The tubes were meshed with BEAM189 elements, which include midside nodes. The element length is set to 8.3 inches, which gives {{ }}<sup>2(a),(c)</sup> between two sets of supports that are 90° apart. There is an additional element between the two immediately adjacent supports spaced 2 inches from each other. The tube mesh is shown in Figure 3-32 and Figure 3-33.

The tube supports are meshed with BEAM188 elements which do not include midside nodes. Midside nodes are not necessary due to the small element size of less than 1 in. The tube support mesh is shown in Figure 3-32 and Figure 3-33.

The barrels and “thick slabs” are meshed with SHELL281 elements which include midside nodes. This mesh is shown in Figure 3-32 and Figure 3-33.

Primary fluid mass is modeled with MASS21 elements and FLUID38 elements. Remote points, which are used to couple the FLUID38 elements to the barrels, use TARGE170 and CONTA175 elements.

### 3.2.1.5 Materials

Relevant components in the TF-2 test assembly are made of Type 304 stainless steel.

The elastic modulus of barrels, headers, and tube supports is taken at the primary fluid temperature. The elastic modulus of the tubes is taken at the average of the primary and secondary fluid temperatures.

Densities of the materials for the tubes and tube supports were adjusted to account for the hydrodynamic mass (displaced primary fluid mass) as well as the contained secondary fluid mass in the tubes. For the TF0007 case which has boiling inside the tubes, the steam region of the tubes was assigned a different density than the liquid region.

The material property values are summarized in Table 3-7.

Table 3-7 Adjusted material properties summary

Case	Barrels and Headers		Tube Supports		Tubes	
	E (10 <sup>6</sup> psi)	ρ (lbm/in <sup>3</sup> )	E (10 <sup>6</sup> psi)	ρ (lbm/in <sup>3</sup> )	E (10 <sup>6</sup> psi)	ρ (lbm/in <sup>3</sup> )
TF0001	{{					
TF0002						
TF0007						}} <sup>2(a),(c)</sup>

### 3.2.1.6 Coordinate Systems and Circumferential Numbering

Three different coordinate systems types were used in this evaluation. They are described below and in Figure 3-40. Note that the coordinate systems are located at global zero, but are shown at different locations in the figure for clarity. The figure shows images of the TF-2 full bundle model, but the coordinate systems apply to the individual tube models as well.

- Global Cartesian coordinate system: X and Z are horizontal directions, and Y points vertically upward.
- Global cylindrical coordinate system: X is the radial direction, Y is the circumferential direction, and Z points vertically upward.
- Local coordinate systems: Twenty unique local Cartesian coordinate systems are used for coupling tubes to tube supports. There are four coordinate systems for each column of tubes, one at each tube support group. From the perspective of the interface, the local X is along the tube’s axis and Z points radially inward toward the center of the bundle. The local Y axis is perpendicular to these two, and is angled away from the global vertical direction by the tube’s inclination angle (approximately 14°).

{{

}}<sup>2(a),(c)</sup>

Figure 3-40 Coordinate systems, global cartesian and global cylindrical shown from global isometric view

### 3.2.1.7 Boundary Conditions

This section explains the various boundary conditions and constraint equations used in the TF-2 full bundle model to couple the components together.

Nodes along the height of the external barrel are coupled to the outermost tube supports. Nodes along the height of the internal barrel are coupled to the innermost tube supports. The nodes are coupled in the radial direction only (UX) of global cylindrical coordinate system. A visualization of the constraint equation coupling is shown in Figure 3-41.

{{

}}<sup>2(a),(c)</sup>

Figure 3-41 Radial coupling between barrels and tube supports

This connection represents the interface between a series of screws and studs that penetrate the barrels and contact the tube supports to hold them in place. The studs are welded to the tube supports and pass through a large clearance hole in the barrels where they are fastened with a nut. This allows the tube supports to be pulled radially by the stud. The large clearance hole does not provide any vertical or circumferential restraint on the stud. The screws are located beneath each stud and pass through a nut that is welded to

the barrels. However, the screw only pushes on the flat part of the tube support and thus does not provide any vertical or circumferential support. A diagram of this is shown in Figure 3-42.

{{

}}<sup>2(a),(c)</sup>

Figure 3-42 Diagram of screw interface between barrels and tube supports

The tube nodes are coupled to the “tab” nodes of the tube supports at each interface. The local UX, UY, and UZ of the local coordinate systems are coupled. A visualization of the constraint equation coupling is shown in Figure 3-43.



---

{{

}}<sup>2(a),(c)</sup>

Figure 3-43 Tube to tube support coupling (column 5 tubes shown)

This connection represents the tubes sitting in the cutouts of the tube supports. The tube axial direction (local UX) is coupled to represent the high friction at the interface (no sliding). Since there are two supports closely spaced, it only takes a slight amount of axial misalignment of the supports to create high friction forces at the tube support. The fact that most supports carry tubes on both sides of the support also contributes to the high amount of interlocking in the assembly.

The nodes at the ends of the tube supports are coupled to corresponding nodes on the upper and lower thick slabs. The six degrees of freedom are coupled using the global coordinate system. A visualization of the constraint equation coupling is shown in Figure 3-44. Note that the figure shows the upper region coupling, although the bottom region is identical.

{{

}}<sup>2(a),(c)</sup>

Figure 3-44 Tube supports to thick slab coupling

Nodes on the header attachment plates are coupled to the nearest nodes on the headers. The six degrees of freedom are coupled using the global coordinate system. A visualization of the constraint equation coupling is shown in Figure 3-45.

{{

}}<sup>2(a),(c)</sup>

Figure 3-45 Header to header attachment plate coupling

The entire assembly is supported with a displacement boundary condition at the edge of the radial cantilever plate that extends outward from the external barrel, as shown in Figure 3-46. Displacements are constrained, but no rotations are constrained. This simulates the cantilever plate resting on the ledge inside the test vessel.

}}

}}<sup>2(a),(c)</sup>

Figure 3-46 Displacement constraint on radial cantilever plate

The following connections are made through conformal meshes and therefore no constraint equations are required.

- Header attachment plates to interior barrel
- Exterior barrel and interior barrel to thick slabs
- Exterior barrel and interior barrel to bottom plate

### 3.2.1.8 Primary Fluid Hydrodynamic Effect on Barrels

The hydrodynamic effect on the tubes and tube supports is incorporated by adding the displaced primary fluid mass back onto those components. However, the effect on the barrels is more complicated. There are three fluid regions that impact the barrels: the fluid cylinder inside the internal barrel, the fluid annulus between the internal and external barrels (fluid annulus 1), and the fluid annulus between the external barrel and the vessel (fluid annulus 2). These regions are shown in Figure 3-47. The hydrodynamic effect on these regions occurs in the horizontal directions only, as the vertical direction is not contained, and primary fluid is free to flow.

---

{{

}}<sup>2(a),(c)</sup>

Figure 3-47 Primary fluid regions for hydrodynamic effects on barrels. Front view on left, top view on right

The contained fluid inside the internal barrel (fluid cylinder) is modeled by calculating the contained fluid mass and scoping it to the walls of the internal barrel in the horizontal directions only.

To ensure the mass is distributed evenly, the mass applied to each node is weighted by the area apportioned to the given node relative to the total apportioned area of all nodes. The mass is applied via MASS21 elements using the X and Z direction real constants only.

The hydrodynamic coupling between the interior and exterior barrels is accomplished using FLUID38 elements. These elements have two nodes, each node representing the centerline of the concentric cylinders. The elements require three geometric inputs, inner radius, outer radius, and cylinder height. A material with the density of the fluid is also applied to the element.

For the TF-2 ANSYS model, the barrels are sectioned along their heights into seven similarly sized regions. Each region of each barrel contains a remote point that is scoped to a circumferential edge at the center of the region. The pair of remote point pilot nodes for a given region serve as the two nodes for the FLUID38 element. For example, region 1 of the internal barrel has its pilot node connected to the pilot node of region 1 of the external barrel via the FLUID38 element. A visualization of the remote points and FLUID38

coupling is shown in Figure 3-48. Note that the remote point scoping skips the nodes on the barrels that are part of the barrels to tube supports coupling to avoid potential over-constraint.

{{

}}<sup>2(a),(c)</sup>

Figure 3-48 Internal barrel and external barrel remote points for hydrodynamic coupling

Because fluid annulus 1 is also the region containing the tubes and tube supports, the actual amount of fluid is less than the nominal volume of the annulus. To correct for this,

the volume of the tubes and tube supports is subtracted from the nominal annulus volume, and new effective diameters are determined. Note that the volumes of the headers and thick slabs were deemed negligible.

The hydrodynamic fluid coupling between the external barrel and the vessel is also modeled using FLUID38 elements. The thick vessel is considered rigid compared to the rest of the TF-2 test assembly and is not explicitly modeled. Instead, seven nodes are created at the same locations as the seven external barrel remote points. These seven “vessel nodes” have all degrees of freedom set to zero to simulate the vessel rigidity. The vessel nodes are connected to the external barrel pilot nodes through an additional set of FLUID38 elements. A visualization of the remote points, vessel nodes, and FLUID38 coupling is shown in Figure 3-49.

{{

}}<sup>2(a),(c)</sup>

Figure 3-49 External barrel and vessel nodes for hydrodynamic coupling

Because fluid annulus 2 does not contain any large obstructions in the annulus, the nominal dimensions for the annular region are used.



### 3.2.1.9 Instrumented Tubes

There are three tubes instrumented with strain gages. To aid in downstream calculations, the nodes on the tubes nearest to the strain gages are determined. A summary of the sensor positions used to determine the nearest node numbers are presented in Table 3-8. The node numbers of the nearest nodes are included in the table as well.

Table 3-8 Sensor positions and nearest node numbers

Col	Tube	Sensor Name	Node Num	Elev (m)	Elev (in)	Radial Pos (mm)	Radial Pos (in)	Azimuth (°)
1	20	S1101	86192	{{				
		S1102	78712					
3	21	S3101	19559					
		S3102	19501					
5	11	S5101	99520					
		S5102	106811					}} <sup>2(a),(c)</sup>

### 3.2.1.10 Single Tube Model

A single tube model was created from the full bundle model. This single tube model contains the three individual instrumented tubes listed in Table 3-8. Other components are suppressed. The model is shown in Figure 3-50.

Note that since the single tube model doesn't contain the barrels or vessel, the fluid-structure interaction and hydrodynamic mass on these components will not be present to interact with the tubes. The purpose of this is to benchmark the applicability of the single tube modal analysis results when trying to emulate the behavior of the full bundle.

The tube supports are retained in the model, but for visualization purposes only, specifically when viewing results. The tube support nodes are fixed, and the bodies are assigned a zero density material to prevent them from having any effect in the model. See Figure 3-55 for an example.

The single tube model has boundary conditions applied directly to nodes on the tubes to simulate the interaction with the headers and tube supports. The header connection has degrees of freedom fixed to simulate the weld. The tube support connections are run for two different cases: sliding and pinned. The sliding case has the local UY and UZ constrained. The pinned case has the local UX, UY, and UZ constrained. These boundary conditions are shown in Figure 3-50.

Other model details are identical to the full bundle model.

{{

}}<sup>2(a),(c)</sup>

Figure 3-50 Boundary conditions for single tube model

### 3.2.1.11 Modal Analysis – Full Bundle Model

Modal analysis up to 160 Hz was performed for the TF-2 full bundle model for the three fluid condition cases described in Section 3.2.1.2. The top 20 participating modes for each

case are presented in Table 3-9 through Table 3-11. The highest participating mode in each direction is highlighted in yellow.

Visualizations of major modes are shown in Figure 3-51 through Figure 3-54. These modes are shown for the TF0001 case only for brevity. The other cases have similar modes but with slightly shifted frequencies.

---

Table 3-9 Full bundle modal analysis results for TF0001 case

{{

}}<sup>2(a),(c)</sup>

Table 3-10 Full bundle modal analysis results for TF0002 case

{{

}}<sup>2(a),(c)</sup>

Table 3-11 Full bundle modal analysis results for TF0007 case

{{

}}<sup>2(a),(c)</sup>

{{

}}<sup>2(a),(c)</sup>

Figure 3-51 Fundamental mode for TF0001 case (full assembly rocking mode)

{{

}}<sup>2(a),(c)</sup>

Figure 3-52 Mode 3 for TF0001 case (tube bundle twisting mode)



{{

}}<sup>2(a),(c)</sup>

Figure 3-53 Highest x-participating mode for TF0001 case (tube bundle shifting along x-axis)

{{

}}<sup>2(a),(c)</sup>

Figure 3-54 Highest y-participating mode for TF0001 case (tube beam mode)

### 3.2.1.12 Modal Analysis – Single Tube Model

Modal analysis was performed for the TF-2 single tube model for the three fluid condition cases described in Section 3.2.1.2 and the two boundary condition cases described in Section 3.2.1.10. The top 20 participating modes up to 600 Hz for each case are presented in Table 3-12 through Table 3-17. The highest participating mode in each direction is highlighted in yellow.

Visualizations of major modes are shown in Figure 3-55 through Figure 3-59. Only TF0001 case modes are shown. The other cases have similar mode shapes but with slightly shifted frequencies. Also, since the tubes do not interact with each other, only one tube participates for a given mode, and only the participating tube is shown in the figures. For all instances, the column 5 tube is shown since it has the largest mass and lowest frequencies.

Table 3-12 Single tube modal analysis results for sliding TF0001 case

{{

}}<sup>2(a),(c)</sup>

Table 3-13 Single tube modal analysis results for sliding TF0002 case

{{

}}<sup>2(a),(c)</sup>

Table 3-14 Single tube modal analysis results for sliding TF0007 case

{{

}}<sup>2(a),(c)</sup>

Table 3-15 Single tube modal analysis results pinned TF0001 case

{{

}}<sup>2(a),(c)</sup>

Table 3-16 Single tube modal analysis results pinned TF0001 case

{{

}}<sup>2(a),(c)</sup>



Table 3-17 Single tube modal analysis results pinned TF0001 case

{{

}}<sup>2(a),(c)</sup>

{{

}}<sup>2(a),(c)</sup>

Figure 3-55 Fundamental mode for single tube sliding TF0001 case (breathing mode)

{{

}}<sup>2(a),(c)</sup>

Figure 3-56 Highest x-participating mode for single tube sliding TF0001 case (tube sliding through supports with beam mode)

{{

}}<sup>2(a),(c)</sup>

Figure 3-57 Highest y-participating mode for single tube sliding TF0001 case (beam mode)

{{

}}<sup>2(a),(c)</sup>

Figure 3-58 Fundamental mode and highest y-participating mode for single tube pinned TF0001 case (beam mode)

{{

}}<sup>2(a),(c)</sup>

Figure 3-59 Highest x-participating mode for single tube pinned TF0001 case (high order beam mode)

### 3.2.1.13 Mesh Sensitivity Analysis

A mesh sensitivity analysis was performed for the single tube model using the sliding TF0001 case. A fine mesh of 2.0 inches is compared to the nominal mesh size of 8.3 inches, which is shown in Figure 3-60. Both meshes use BEAM189 elements with midside nodes.

The mesh sensitivity results for the top 20 participating modes in each direction are presented in Table 3-18 through Table 3-20.

Agreement of frequency and mass participation is shown between the two mesh sizes, which validates the use of the nominal mesh. For modes below 160 Hz (the upper bound in the full bundle model), the percent error in frequency is less than  $\{\{ \quad \}^{2(a),(c)}$ , and the percent error in effective mass ratio is less than  $\{\{ \quad \}^{2(a),(c)}$  (most modes under  $\{\{ \quad \}^{2(a),(c)}$ ). The percent error increases with higher frequencies, as the higher order modes are increasingly difficult to represent with the coarser mesh, although the coarse mesh is still acceptable.

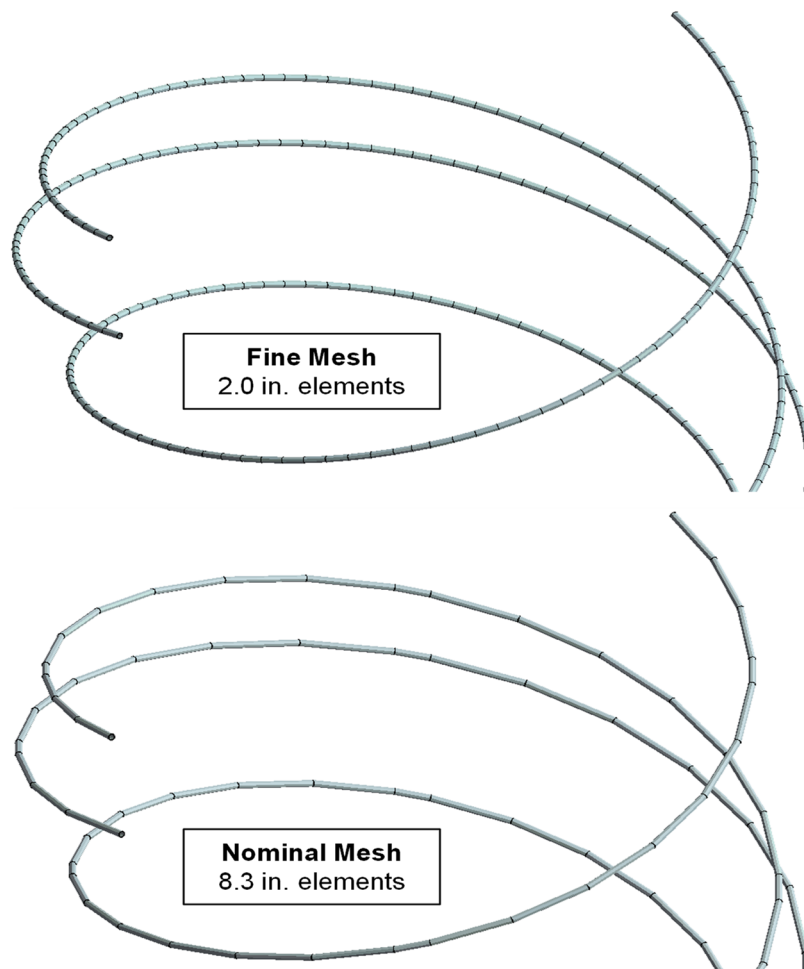


Figure 3-60 Mesh size comparison for mesh sensitivity analysis

---

Table 3-18 X-direction modal analysis results for mesh sensitivity study using single tube model, sliding TF0001 case

{{

}}<sup>2(a),(c)</sup>



Table 3-19 Y-direction modal analysis results for mesh sensitivity study using single tube model, sliding TF0001 case

{{

}}<sup>2(a),(c)</sup>

Table 3-20 Z-direction modal analysis results for mesh sensitivity study using single tube model, sliding TF0001 case

{{

}}<sup>2(a),(c)</sup>

### 3.2.1.14 Modal Analysis Results Discussion

This discussion compares the full bundle modal results to the single tube results for the TF0001 case. The purpose of this is to determine the applicability of the single tube results when trying to emulate the behavior of the full bundle. Table 3-21 summarizes the major mode comparison between the models. Figure 3-61 through Figure 3-63 compare the mode shapes of similar modes. In these figures, bodies are hidden except the instrumented tube in column 5, in order to help identify similar modes between models.

Table 3-21 Major mode comparison between full bundle and single tube models

Full Bundle Freq. (Hz)	Single Tube Freq. (Hz)	Mode Type	Comparison Figure
{{		Full assembly rocking mode. Not applicable to single tube model (either case)	n/a
		Breathing/twisting mode. Not applicable to single tube pinned case.	Figure 3-62
		Highest x-participating mode. Tube or bundle shifting or sliding along x-axis, with beam mode. Not applicable to single tube pinned case.	Figure 3-63
	$\}}^{2(a),(c)}$	Highest y-participating mode. Tube beam mode. Applicable to single tube sliding and pinned cases.	Figure 3-64

The single tube models do not appropriately characterize the behavior of the full bundle model, as they cannot adequately account for the flexibility of the tube supports. Although the tubes are “pinned” to the tube supports in the full bundle model, the sliding case of the single tube model does a better job at emulating the full bundle behavior, as the sliding action of the tube somewhat simulates the flexibility in the tube supports. The pinned case of the single tube model cannot capture this behavior whatsoever. For the major horizontal shifting/sliding mode, the single tube sliding model is about  $\}}^{2(a),(c)}$  higher in frequency than the full bundle model.

The single tube pinned case can characterize the pure tube beam modes as well as the sliding case, as the flexibility of the tube supports is less important in these modes. The major vertical mode is  $\}}^{2(a),(c)}$  higher in frequency in the single tube model (both cases) than the full bundle model.

The twisting/breathing mode of the full bundle model is somewhat captured by the single tube sliding model. The single tube model breathing mode is  $\}}^{2(a),(c)}$  higher in frequency than the lowest twisting mode of the full bundle model, but this full bundle mode has low mass participation, and is not in the top 20 participating modes for any of the directions. However, this breathing mode is only  $\}}^{2(a),(c)}$  lower in frequency than another twisting mode of the full bundle model with a similar mode shape. This full bundle mode has higher mass participation, although it is in the horizontal direction whereas the single tube mode has the mass participation in the vertical direction.

{{

}}<sup>2(a),(c)</sup>

Figure 3-61 Breathing/twisting mode comparison between single tube and full bundle models

{{

}}<sup>2(a),(c)</sup>

Figure 3-62 Highest y-participating mode comparison between single tube and full bundle models (sliding/shifting and beam mode)

{{

}}<sup>2(a),(c)</sup>

Figure 3-63 Highest x-participating mode comparison between single tube and full bundle models (beam mode)

### 3.2.2 TF-1 and TF-2 Vibration Analysis

This section includes analysis of the TB vibrations in the instrumented TF-2 tubes during the test set investigating fluid elastic instability. The analytical results are compared to the TF-2 strain gauge data to provide further basis for the validity of the analytical approach to TB vibrations.

The methodology for determining the structural response spectra due to turbulent buffeting is based on the acceptance integral methodology. See Figure 3-64 for an overview of the solution sequence. First ANSYS is used to run a modal analysis on the TF2 structural model (see Figure 3-65). This information provides the required structural properties. The loading on the structure is quantified by pressure PSDs. Separate PSDs are used for the primary and secondary sides. The spatial distribution of the PSDs are characterized by a coherence function. With the mode information, pressure PSDs, and coherence functions, the acceptance integrals are calculated. The acceptance integrals represent the contribution to the response from different mode combinations.

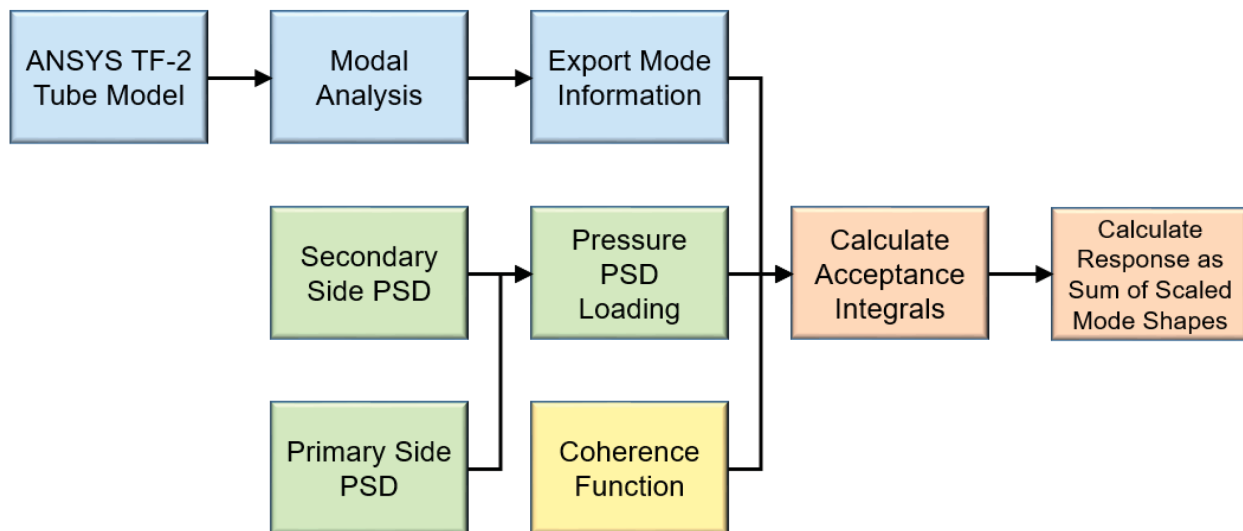


Figure 3-64 Block diagram of the vibration analysis methodology

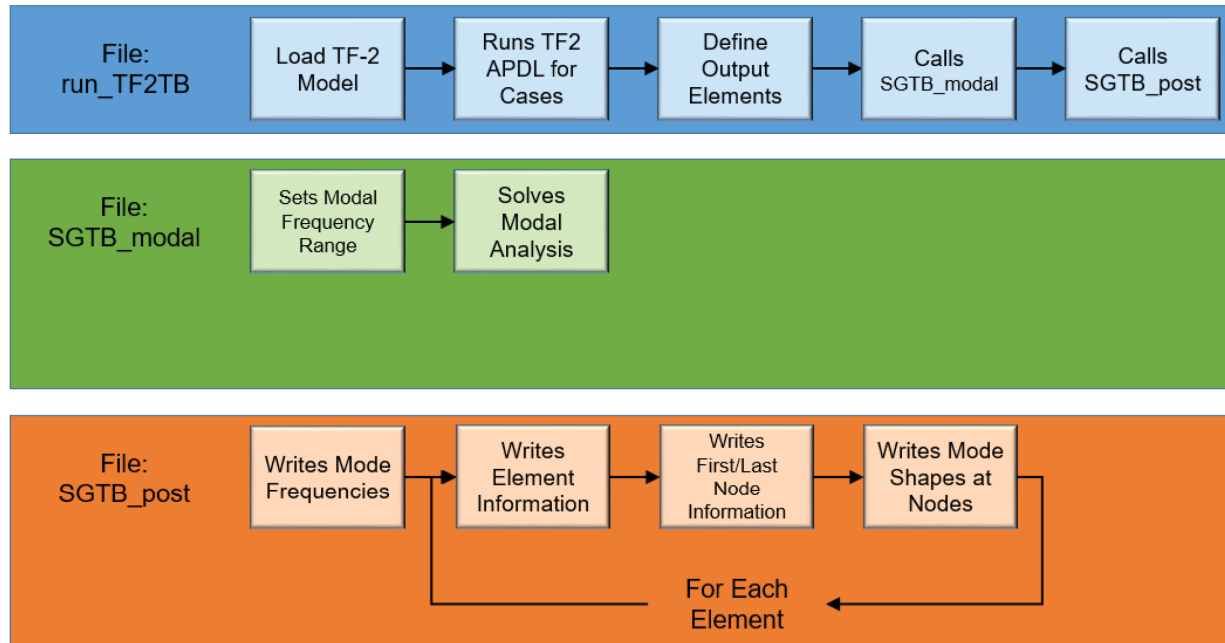


Figure 3-65 Block diagram of the ANSYS solution sequence

### 3.2.2.1 Turbulent Buffeting Response

The response spectra due to turbulent buffeting (Equation 3-8) is calculated using the acceptance integral methodology. Equation 3-8 is simplified to be a single summation instead of split into two summations. The acceptance integral, Equation 3-9, is related to how the energy added to a particular mode by the pressure PSDs is transferred between modes. Equation 3-10 is the modal transfer function which describes how vibrations are transferred between modes. Using the default option in ANSYS, the mode shapes are normalized based on the mass matrix. This normalization causes the generalized mass in Equation 3-10 to be unity.

$$S_y(\vec{x}, \omega) = AS_p(\omega) \sum_{\alpha} \sum_{\beta} \psi_{\alpha} H_{\alpha}(\omega) H_{\beta}^*(\omega) \psi_{\beta} J_{\alpha\beta}(\omega) \quad \text{Equation 3-8}$$

$$J_{\alpha\beta}(\omega) = \frac{1}{A} \int_A \int_A \psi_{\alpha} \left[ \frac{S_p(x', x'', \omega)}{S_p(x', \omega)} \right] \psi_{\beta} dx' dx'' \quad \text{Equation 3-9}$$

$$H_{\alpha}(\omega) = \frac{1}{m_{\alpha} [\omega_{\alpha}^2 - \omega^2 + i\zeta_{\alpha} \omega_{\alpha} \omega]} \quad \text{Equation 3-10}$$

where:

$$\begin{aligned} S_y(\vec{x}, \omega) &= \text{Displacement response spectra (in}^2\text{/Hz)} \\ \vec{x} &= \text{Location on structure} \end{aligned}$$



$\omega$	=	Frequency (rad/s)
$A$	=	Surface area (in <sup>2</sup> )
$\alpha$ or $\beta$	=	Mode index
$\psi_\alpha$ or $\psi_\beta$	=	Displacement mode shape (in/in)
$H_\alpha$ or $H_\beta$	=	Modal transfer function shape (in/lbf)
$J_{\alpha\beta}(\omega)$	=	Acceptance integral (in <sup>2</sup> )
$S_p(x', x'', \omega)$	=	Cross spectral density of pressure between two locations (psi <sup>2</sup> /Hz)
$S_p(x', \omega)$	=	Power spectral density of pressure at a single location (psi <sup>2</sup> /Hz)
$m_\alpha$	=	Generalized mass (lbf-s <sup>2</sup> /in)
$\omega_\alpha$	=	Modal frequency (rad/s)
$\zeta_\alpha$	=	Modal damping ratio (-)

Rearranging the equations above provides the following three equations for the displacement response spectra, acceptance integral, and modal transfer function. The frequencies are converted to be in units of Hz for convenience. This form of the acceptance integral becomes a factor for the mode shapes in Equation 3-11. This step allows the acceptance integral to be calculated once and then used multiple times to calculate the response due to turbulent buffeting for variables other than displacement, such as strain.

$$S_y(\vec{x}, f) = \sum_{\alpha} \sum_{\beta} \psi_{\alpha} \psi_{\beta} A_{\alpha\beta}(f) \quad \text{Equation 3-11}$$

$$A_{\alpha\beta}(f) = \int_A \int_A H_{\alpha}(f) H_{\beta}^*(f) \psi_{\alpha} S_p(x', x'', f) \psi_{\beta} dx' dx'' \quad \text{Equation 3-12}$$

$$H_{\alpha}(f) = \frac{1}{m_{\alpha} 4\pi^2 [f_{\alpha}^2 - f^2 + i\zeta_{\alpha} f \omega_{\alpha}]} \quad \text{Equation 3-13}$$

where:

$A_{\alpha\beta}(\omega)$	=	Redefined acceptance integral (in <sup>2</sup> /Hz)
$f$	=	Frequency (Hz)

Equation 3-14 replaces the displacement mode shapes with strain mode shapes. Due to using beam elements in ANSYS, the strain mode shapes are bending strain in two directions and the axial strain. As the cross spectral density of the turbulent pressure is generally not available, the cross spectral density is replaced with known quantities using the definition of the coherence function in Equation 3-16. The form of the coherence function is further discussed in Section 3.2.2.1.5.

$$S_{\phi}(\vec{x}, f) = \sum_{\alpha} \sum_{\beta} \phi_{\alpha} \phi_{\beta} A_{\alpha\beta}(f) \quad \text{Equation 3-14}$$

$$A_{\alpha\beta}(f) =$$

$$\int_A \int_A H_{\alpha}(f) H_{\beta}^*(f) \psi_{\alpha} \Gamma(x', x'', f) \sqrt{S_p(x', f) S_p(x'', f)} \psi_{\beta} dx' dx'' \quad \text{Equation 3-15}$$

$$\Gamma(x', x'', f) = \frac{S_p(x', x'', f)}{\sqrt{S_p(x', f) S_p(x'', f)}} \quad \text{Equation 3-16}$$

where:

- $S_{\phi}(\vec{x}, f)$  = Strain response spectra (1/Hz)
- $\phi_{\alpha}$  or  $\phi_{\beta}$  = Strain mode shape (in/in<sup>2</sup>)
- $\Gamma(x', x'', f)$  = Coherence function defined in Section 3.2.2.1.5 (-)

The acceptance integral shown in Equation 3-15 includes two area integrals. Those integrals are not calculated analytically. Instead, the integrals are evaluated numerically by two summations over the elements that make up the tube.

The transfer functions are factored out of the summations as they are not location dependent. The displacement mode shape and PSDs are approximated as being constant over an element. This approximation is appropriate because the mode shapes vary over larger length scales than a single element. The displacement mode shapes and surface areas are vectors and are combined with the dot product operator to get the portion of the pressure acting on the surface area in the direction of the mode shape.

$$A_{\alpha\beta}(f) =$$

$$H_{\alpha}(f) H_{\beta}^*(f) \sum_i^{elems} \sum_j^{elems} \Gamma(x_i, x_j, f) \sqrt{S_p(x_i, f) S_p(x_j, f)} (\overline{\psi_{i,\alpha} \cdot \overline{A}_i}) (\overline{\psi_{j,\beta} \cdot \overline{A}_j}) \quad \text{Equation 3-17}$$

Acceptance integrals are not calculated for the possible combinations of alpha and beta mode indices. The mode combinations that do not significantly contribute to the summations in Equation 3-14 are eliminated. The mode combination significance is shown in Equation 3-18. The relative mode combination significance is calculated by normalizing by a hypothetical mode at the largest frequency of interest combined with itself. Acceptance integrals are calculated only for those mode combinations with a relative significance above 0.1. This ensures that all combinations of modes with themselves are included as well as any large cross-modal combinations. A sensitivity on the threshold for significant mode combinations is provided in Section 3.2.2.2.5.

$$\sigma_{\alpha\beta} = \max |H_{\alpha}(f)H_{\beta}^*(f)| \quad \text{Equation 3-18}$$

$$\sigma_{\alpha\beta,rel} = (m_{\alpha} 8\pi^2 \zeta_{\alpha} f_{max}^2)^2 \sigma_{\alpha\beta} \quad \text{Equation 3-19}$$

where:

$$\begin{aligned} \sigma_{\alpha\beta} &= \text{Mode combination significance (in}^2/\text{lb}f^2) \\ \sigma_{\alpha\beta,rel} &= \text{Relative mode combination significance (-)} \\ f_{max} &= \text{Maximum frequency of interest (Hz)} \end{aligned}$$

As beam elements are used in the tube model, the PSDs can be applied in the element y and z directions. The orientation node (node L) is on the element x-z plane. The ANSYS input file sets the location of the orientation node so that the element z direction is radially outward from the global vertical axis and the element y direction is offset from the global vertical axis by the tube inclination angle.

### 3.2.2.1.1 Pressure Power Spectral Densities

With the ANSYS structural model providing the structural information, the next input required for calculating the acceptance integrals is the pressure PSD. The pressure PSD is the input to the system that causes vibrations. As turbulence is a nondeterministic phenomenon, the forcing function cannot be represented exactly. Instead a PSD is used to provide a distribution of how the input pressure varies across the range of frequencies.

### 3.2.2.1.2 Primary Side PSD

The pressure fluctuations on the outside of the tubes is modeled with a PSD for cross-flow in a tube bundle and repeated in Equation 3-22 below. The stored factor on the frequency converts a frequency to the reduced frequency. The stored factor on the pressure converts the normalized pressure PSD to the pressure PSD.

The flow area along with the primary side density are used to calculate the velocity. The primary side density is calculated with the hot primary side temperature.

$$\begin{aligned} F < 0.1 & \quad \overline{G_p}(f) = 0.01 \\ 0.1 < F \leq 0.4 & \quad \overline{G_p}(f) = 0.2 \\ F > 0.4 & \quad \overline{G_p}(f) = 5.3 \times 10^{-4} F^{-3.5} \end{aligned} \quad \text{Equation 3-20}$$

$$F = \frac{f D_h}{v_f} \quad \text{Equation 3-21}$$

$$G_p = \overline{G_p} \frac{1}{4} \rho^2 v_f^3 D_h \quad \text{Equation 3-22}$$

where:

- $F$  = Reduced frequency (-)
- $\overline{G_p}(f)$  = Normalized pressure PSD (-)
- $G_p(f)$  = Pressure PSD (psi<sup>2</sup>/Hz)
- $f$  = Frequency (Hz)
- $D_h$  = Hydraulic diameter (in)
- $\rho$  = Fluid density (lbf-s<sup>2</sup>/in<sup>4</sup>)
- $v_f$  = Free stream velocity(in/s)

### 3.2.2.1.3 Secondary Side PSDs

For the cases listed in Table 3-22, the secondary side is either quiescent fluid, single phase moving liquid, or moving liquid boiling to vapor. For the cases of quiescent fluid, no secondary side PSD is applied as there is no turbulence to cause pressure fluctuations. For the cases with moving fluid, a secondary side PSD is applied based on either established literature or the measurements from the TF-1 test data.

The inlet quality, heat flux, and secondary side pressure are used to find the TF-1 test that most closely matches the conditions of each TF-2 test. Table 3-23 below lists each TF-2 case, the secondary side conditions for that case, and the TF-1 case that most closely matches the conditions. TF-2 cases with no secondary side flow are marked as N/A as no TF-1 PSD is applicable.

Table 3-22 Applicable TF-2 test cases

Case Name	Model Case	Primary Flow (kg/s)	Primary Temp. (°F)	Primary Press. (psia)	Secondary Side Temp. (°F)	Total Secondary Side Flow (kg/s)
TF0001_0751	1	}}				
TF0001_0752						
TF0001_0753						
TF0001_0754						
TF0001_0755						
TF0001_0757						
TF0002_0744	2					}} <sup>2(a),(c)</sup>
TF0002_0745						
TF0002_0746						
TF0002_0747						
TF0002_0748						
TF0002_0750						

Case Name	Model Case	Primary Flow (kg/s)	Primary Temp. (°F)	Primary Press. (psia)	Secondary Side Temp. (°F)	Total Secondary Side Flow (kg/s)
TF0003_0759	2	{{				
TF0003_0761						
TF0003_0762						
TF0003_0763						
TF0003_0764						
TF0003_0766						
TF0004_0767	2					
TF0004_0768						
TF0004_0769						
TF0004_0770						
TF0004_0771						
TF0004_0773						
TF0005_0786	3					
TF0006_0784	3					
TF0006_0844						
TF0007_0777	3					
TF0007_0778						
TF0007_0779						
TF0007_0781						}} <sup>2(a),(c)</sup>

Table 3-23 TF-1 secondary side PSDs used

TF-2 Case Name	TF-1 Case Used	Secondary Side Flow (kg/s) <sup>1</sup>
TF0001_0751	N/A	}}
TF0001_0752		
TF0001_0753		
TF0001_0754		
TF0001_0755		
TF0001_0757		
TF0002_0744		
TF0002_0745		
TF0002_0746		
TF0002_0747		
TF0002_0748		
TF0002_0750		
TF0003_0759	TA0070	
TF0003_0761		
TF0003_0762		
TF0003_0763		
TF0003_0764		
TF0003_0766		
TF0004_0767	N/A	
TF0004_0768		
TF0004_0769		
TF0004_0770		
TF0004_0771		
TF0004_0773		
TF0005_0786	TD0023	
TF0006_0784	TD0024	
TF0006_0844		
TF0007_0777	TD0048	}} <sup>2(a),(c)</sup>
TF0007_0778		
TF0007_0779		
TF0007_0781		

1: The flow rates in the last column are for all five tube columns

Each TF-1 case has five sensor measurements, and thus five PSDs, from the active coil (tube). The PSDs from the five sensors are averaged to get a representative PSD for the entire length of tube. This averaging is acceptable as the PSDs do not vary significantly with elevation.

The PSDs show a noise floor at {{ }}<sup>2(a),(c)</sup>. The noise is removed from the PSD by subtracting {{ }}<sup>2(a),(c)</sup> from the tube averaged PSD. After this subtraction, any values less than 1.0e-12 are increased to 1.0e-12 to prevent values of zero or less in future computations. These processed TF-1 PSDs are output for use in the strain response PSD calculations.

The TF-1 PSDs contain a large amount of low frequency excitation in the  $\{ \dots \}^{2(a),(c)}$  range. There is also another peak in excitation between  $\{ \dots \}^{2(a),(c)}$ . The high frequency of this secondary peak is the reason why the turbulent buffeting analyses using the TF-1 PSDs are run out to 600 Hz.

As an alternative to the TF-1 PSDs, PSDs can be implemented from open literature. Two PSDs are required to cover the single phase and two phase regions of the tube. The single phase Chen PSD is shown in Equation 3-20 (from page 233 of Reference 9.1.12) and the single phase Au-Yang/Jordan PSD in Equation 3-26 (from page 236 of Reference 9.1.11). The Chen PSD is used by default while the Au-Yang/Jordan PSD is used to evaluate the sensitivity of the results to the selected PSD.

$$S < 5.0 \quad \overline{G}_p(f) = \frac{0.272 \times 10^{-5}}{S^{0.25}} \quad \text{Equation 3-23}$$

$$S \geq 5.0 \quad \overline{G}_p(f) = \frac{22.75 \times 10^{-5}}{S^3}$$

$$S = \frac{2\pi f D_h}{v_f} \quad \text{Equation 3-24}$$

$$G_p = \overline{G}_p \rho^2 v_f^3 D_h \quad \text{Equation 3-25}$$

where:

- $S$  = Reduced frequency (-)
- $\overline{G}_p(f)$  = Normalized pressure PSD (-)
- $G_p(f)$  = Pressure PSD (psi<sup>2</sup>/Hz)
- $f$  = Frequency (Hz)
- $D_h$  = Hydraulic diameter (in)
- $\rho$  = Fluid density (lbf-s<sup>2</sup>/in<sup>4</sup>)
- $v_f$  = Free stream velocity(in/s)

$$F < 1.0 \quad \overline{G}_p(f) = 0.155e^{-3.0F} \quad \text{Equation 3-26}$$

$$F \geq 1.0 \quad \overline{G}_p(f) = 0.027e^{-1.26F}$$

$$F = \min\left(5.0, \frac{f R_h}{v_f}\right) \quad \text{Equation 3-27}$$

$$G_p = \overline{G}_p \rho^2 v_f^3 R_h \quad \text{Equation 3-28}$$

where:

$F$	=	Reduced frequency (-)
$\overline{G}_p(f)$	=	Normalized pressure PSD (-)
$G_p(f)$	=	Pressure PSD (psi <sup>2</sup> /Hz)
$f$	=	Frequency (Hz)
$R_h$	=	Hydraulic radius (in)
$\rho$	=	Fluid density (lbf-s <sup>2</sup> /in <sup>4</sup> )
$v_f$	=	Free stream velocity(in/s)

For the two-phase region, the correlations by Giraudeau from Reference 9.1.13 are implemented. These correlations are force PSDs of two-phase fluids around 90° elbows. Giraudeau found that the force PSD on an elbow is caused by the changes in the mass flux through the tube due to turbulent two-phase flow. The helical tube will experience similar behavior in the two phase region.

The Giraudeau correlations are based on Equations 17, 19, 20, and 21 from Reference 9.1.13, repeated below in Equation 3-29, Equation 3-30, Equation 3-31, and Equation 3-32. The five empirical constants that go into the Giraudeau PSD are defined in Table 1 of the reference and Table 3-24 below. The constants are defined for four void fractions. When the actual void fraction in the tube is between the tabulated values, linear interpolation is used. As a two-phase PSD, the Giraudeau correlation is only used when the void fraction is between 0.05 and 0.99.

The Giraudeau PSD is a force PSD on a 90° elbow. To convert the force PSD to a pressure PSD, it is divided by the area of the element squared. Also, each element only sweeps out a portion of a 90° bend. Therefore, the PSD is also multiplied by the square root of one minus the cosine of the angle swept out by the element. This factor ensures that the sum of all force vectors on elements that make up a 90° bend sum to the appropriate value. The Giraudeau PSD is for flow around an elbow and is therefore, only applied radially on the tube. The single phase PSD is also applied in the two-phase region. The single phase PSD is insignificant compared to the Giraudeau PSD in the radial direction, but provides excitation in the vertical direction.

$$\bar{f} < \bar{f}_0 \quad \bar{\Phi} = k_1 \bar{f}^{m_1} \quad \text{Equation 3-29}$$

$$\bar{f} \geq \bar{f}_0 \quad \bar{\Phi} = k_2 \bar{f}^{m_2}$$

$$\bar{\Phi} = \frac{\Phi}{(\rho j^2 D^2) D_h} W e^{0.8} \quad \text{Equation 3-30}$$

$$\bar{f} = \frac{f D_h}{j} \quad \text{Equation 3-31}$$

$$W e = \frac{\rho j^2 D_h}{\sigma} \quad \text{Equation 3-32}$$



where:

- $\bar{f}$  = Reduced frequency (-)
- $\bar{\Phi}$  = Normalized force PSD (-)
- $\Phi$  = Force PSD (lbf<sup>2</sup>/Hz)
- $f$  = Frequency (Hz)
- $D_h$  = Hydraulic diameter (in)
- $\rho_l$  = Liquid density (lbf-s<sup>2</sup>/in<sup>4</sup>)
- $j$  = Mixture velocity (in/s)
- $We$  = Weber number (-)
- $\sigma$  = Surface tension (lbf/in)

Table 3-24 Giraudeau PSD correlation empirical constants

Void Fraction	$\bar{f}_0$	$k_1$	$k_2$	$m_1$	$m_2$
{}					
					$\}}^{2(a),(c)}$

### 3.2.2.1.4 Fluid Conditions for PSDs

The fluid conditions on the secondary side change significantly over the height of tube due to the heating and boiling of the secondary side coolant. To more accurately calculate the local PSD at each element in the tube, elevation dependent fluid properties are required. The local fluid conditions are generated using the results of an NRELAP5 model of the TF-2 test facility.

The NRELAP5 results are steady state and do not show the temperature oscillations discussed in Section 3.2.2.2.1.

### 3.2.2.1.5 Coherence Function

Coherence is a measure of the degree of relationship between two signals. In turbulence, coherence is used to measure how pressure fluctuations are related between two different points in a flow. The response of the structure is different if the pressure fluctuations occur in phase and with the full magnitude compared to pressure fluctuations that occur with phase offsets and different magnitudes.

In Equation 3-33, the first exponential is based on the correlation length which decreases the coherence as the two points are separated by more distance. Distances far apart tend to have pressure fluctuations that are not well correlated as turbulent eddies interact and dissipate. The second exponential is based on the convective velocity of the flow. This term adds a phase offset to the coherence based on the time it takes a turbulent eddy to

travel the distance between the two points. This calculation uses the free stream velocity for the convective velocity.

Due to the exponential behavior of the coherence function, the element size in the ANSYS model may not be fine enough to capture the rapid changes in coherence. To overcome this issue, additional points are added within each element when calculating the element coherence. The coherence at these additional points is calculated and an average value is used for the overall element coherence. The number of additional points is selected to give an average spacing of 0.125 in as smaller spacing was shown to have a negligible effect on the results (see Section 3.2.2.2.6).

$$C(f, \bar{x}_1, \bar{x}_2) = \exp\left(-\frac{|\bar{x}_1 - \bar{x}_2|}{\lambda}\right) \exp\left(-\frac{2\pi i f (\bar{x}_{1,y} - \bar{x}_{2,y})}{v}\right) \quad \text{Equation 3-33}$$

where:

$C(f, \bar{x}_1, \bar{x}_2)$	=	Coherence function (-)
$f$	=	Frequency (Hz)
$\bar{x}_1$	=	Point location 1 (in)
$\bar{x}_2$	=	Point location 2 (in)
$\lambda$	=	Correlation length (in)
$v$	=	Convective velocity (in/s)

### 3.2.2.1.6 Response Power Spectral Densities

With the response PSD calculated using Equation 3-14, the mean square response can be calculated as the integral of the response PSD. The RMS response is the square root of the mean square response. The crossing frequency is a measure of the average frequency that the strain switches direction (compression/tension) and can be calculated using Equation 3-34.

$$f_c = \sqrt{\frac{\int_0^{\infty} f^2 S_{\phi}(f) df}{\int_0^{\infty} S_{\phi}(f) df}} \quad \text{Equation 3-34}$$

where:

$f_c$	=	Crossing frequency (Hz)
$f$	=	Frequency (Hz)
$S_{\phi}(f)$	=	Strain response PSD (in/in/Hz)

These equations require many levels of summations which are implemented in a series of scripts.

### 3.2.2.2 Calculation Body

#### 3.2.2.2.1 Strain Gauge Data Limitations

The strain gauge data is available as described in Section 3.2. The data extends up to 300 Hz. Extended data up to 1000Hz is also available, but does not have the same filtering of electrical noise as the 300 Hz data. The top sensors for column 1 were not functional. Therefore, data from those sensors are not presented. Additionally, the data shows a noise floor around  $\{\{ \quad \} \}^{2(a),(c)} \mu\epsilon^2/\text{Hz}$ . This noise floor creates a threshold below which direct comparisons to the analytical approach are not possible. However, it is possible to infer that any analytical result that is above the noise floor must bound the actual vibration response in the test facility.

The TF-2 test facility has flow restrictor orifices at the inlet of the tubes. These restrictor orifices are not prototypic and have a lower loss coefficient compared to the NuScale design. There are differential pressure sensors located on select tubes to measure the pressure drop across the inlet flow restrictors which is related to the flow rate through the orifice. The differential pressure instruments indicate that for the FEI tests with boiling secondary side flow, there are significant oscillations in flow.

Additional investigation of the available outer diameter temperature sensors shows that there are also significant temperature fluctuations caused by the boiling region inside the tubes moving up and down. The temperature fluctuations occur every  $\{\{ \quad \} \}^{2(a),(c)}$  seconds depending on the test conditions. The temperature data is sampled for at least 50 seconds at approximately 1 Hz while the strain gauge data is sampled for 5 seconds at 5000 Hz.

Figure 3-66 below correlates the maximum range of strain for a set of sensors (column 3 lower top and side sensors for example) to the maximum temperature range for the nearest outer diameter temperature sensors (pair of intrados and extrados sensors). The ranges are calculated as the difference between the minimum and maximum values from the signal time histories. The results in Figure 3-66 show a somewhat linear trend indicating that larger recorded temperature ranges correspond to larger recorded strain ranges.

The comparison is limited by two factors. First, the temperature sensors and strain gauges are not located in the same location. The temperature sensors are nearby, within ~4 ft of tubing, but may not be representative of the temperature changes at the strain gauges. In some cases, the temperature sensors are not in the same tube as the strain gauges and a nearby tube in the same column is used. The second limitation is the duration and frequencies of measurements. The temperature data is collected for a long duration at low frequency and the strain data is collected for a short duration at a high frequency. The two data streams are collected through different systems and may not start at exactly the same time. Therefore, it is not possible to determine what temperature oscillations were occurring during the time the strain data was collected. Due to the  $\{\{ \quad \} \}^{2(a),(c)}$  period of temperature oscillations, the five second strain data may not have coincided with the full range of temperature oscillations. This limitation provides justification for why the outlier points are lower than the trend.

Section 3.2.2.5 describes a simplified ANSYS model of a tube that shows how temperature fluctuations correspond to strains in the tube. The results indicate that thermal strain is generated at a rate of  $\{\{ \quad \}^{2(a),(c)} \mu\epsilon/^\circ\text{C}$  which corresponds well to the trend in Figure 3-66 with a slight under prediction. The under prediction could be due to the assumption of unrestrained thermal expansion in the ANSYS model or differences in material properties compared to the test.

{{

$\}^{2(a),(c)}$

Figure 3-66 Strain versus temperature ranges for the TD, TF, and TW tests

Figure 3-67 below is an example of the strain gauge data for a test case with boiling on the secondary side flow. The largest strains occur at frequencies below  $\{\{ \quad \}^{2(a),(c)}$ . As shown in Figure 4-1, the low frequency temperature fluctuations correspond to the low frequency strain fluctuations. Due to the limited frequency of the temperature data, no direct conclusions can be made about the thermal strain in the  $\{\{ \quad \}^{2(a),(c)}$  range.

While no direct comparisons are possible, the conclusion that the  $\{\{ \quad \}^{2(a),(c)}$  strains are due to thermal strains fits the trends in the TF-2 data. The low frequency strains occur only in cases with secondary side flow and are largest in cases with two-phase secondary side flow. The low frequency strains also only occur in sensors that are near sensors that show temperature oscillations. In Figure 3-67, the lower sensors have low frequency oscillations while the upper sensors show no low frequency strains.

{{

}}<sup>2(a),(c)</sup>

Figure 3-67 Strain gauge data for a case with secondary side boiling

The thermal strains detected in TF-2 are not prototypic of the NuScale design. The design of the SG inlet flow restrictors is such that the inlet pressure loss stabilizes the flow at full power. A stable flow would not have such large thermal strains. Therefore, no attempt is made to match the analytical results to the strain data less than {{ }}<sup>2(a),(c)</sup>.

Without the strain data attributed to thermal oscillations, the TF-2 strain gauge data is predominately made up of noise at around {{ }}<sup>2(a),(c)</sup>. There are a few peaks that may be distinguishable from the noise but there does not seem to be a repeatable trend in those peaks. While the noise in the strain data prevents any quantitative comparison for analytical results below the noise level, any analytical results that are above the noise level are bounding with respect to the test data.

### 3.2.2.2.2 Comparison of Analysis Results to Test Data

The following sections compare the analytical results using the acceptance integral method to the strain test data from TF-2. As described in Section 3.2.2.2.1, the strain data has low frequency content caused by thermal strains. No comparison is attempted for the strain data below {{ }}<sup>2(a),(c)</sup>.

### 3.2.2.2.1 Cases without Secondary Side Flow

Three TF-2 FEI test series had no secondary side flow, TF0001, TF0002, and TF0004. Of those test series, TF0004 is selected for detailed discussion here because it represents the most bounding cases. TF0004 has stagnant liquid on the secondary side and the primary side is at slightly elevated temperatures. Both of these factors contribute to lower modal frequencies and increasing responses.

TF0004\_0769 matches best with the maximum design flow for the actual NuScale SG. TF0004\_0773 scales to approximately 150% of maximum design flow.

Figure 3-68 and Figure 3-69 below show the strain response for the lower and upper sensors of column 5 for TF0004\_0769 with the pinned boundary condition. The analytical results are mostly below the noise floor of the strain sensors. The peak just below  $\{\{ \}^{2(a),(c)}$  is due to the first modes of the tubes. The increased response between  $\{\{ \}^{2(a),(c)}$  is due to the increased pressure input from the primary flow PSD in Equation 3-20. The top of tube sensors show higher response than the side sensors due to mode shapes being predominately in the vertical direction compared to the radial direction.

$\{\{$

$\}^{2(a),(c)}$

Figure 3-68 TF0004\_0769 column 5 lower strain sensor with pinned boundary conditions

{{

}}<sup>2(a),(c)</sup>

Figure 3-69 TF0004\_0769 column 5 upper strain sensor with pinned boundary conditions

Figure 3-70 and Figure 3-71 below show the strain response for the lower and upper sensors of column 5 for TF0004\_0773 with the pinned boundary condition. The responses are generally larger due to the much larger primary flow rate. The higher flow rate also extends the region of higher pressure PSD content to coincide with the first mode frequencies which amplifies the first mode.

{{

}}<sup>2(a),(c)</sup>

Figure 3-70 TF0004\_0773 column 5 lower strain sensor with pinned boundary conditions



---

{{

}}<sup>2(a),(c)</sup>

Figure 3-71 TF0004\_0773 column 5 upper strain sensor with pinned boundary conditions

Figure 3-72 and Figure 3-73 below show the strain response for the lower and upper sensors of column 5 for TF0004\_0773 with the sliding boundary condition. The responses are significantly larger than the pinned boundary condition and the response is shifted to lower frequencies. The lower frequency peaks are the sliding modes.

The large low frequency oscillations occurring with the sliding boundary condition are orders of magnitude higher than the strain gauge noise floor and orders of magnitude higher than the pinned boundary condition. The pinned boundary condition already predicts larger responses than the strain gauge data and is therefore conservative. The sliding boundary condition responses are overly conservative. The remainder of the comparison focus on the pinned boundary condition as it is found to be a better match to the test data.

{{

}}<sup>2(a),(c)</sup>

Figure 3-72 TF0004\_0773 column 5 lower strain sensor with sliding boundary conditions

{{

}}<sup>2(a),(c)</sup>

Figure 3-73 TF0004\_0773 column 5 upper strain sensor with sliding boundary conditions

### 3.2.2.2.2 Cases with Single Phase Secondary Flow

The TF0003 test series have single phase secondary side flow. The {{ }}<sup>2(a),(c)</sup> kg/s of flow through the 252 tubes in TF-2 is comparable to the feedwater flow rate for the NuScale design at 100% power. However, the NuScale design would have boiling in the tubes while these tests are all single phase liquid.

Figure 3-74 and Figure 3-75 below are from TF0003\_0762 which has a comparable primary side flow rate to TF0004\_0769. Therefore, the main difference in test conditions between the plots below and Figure 3-68 and Figure 3-69 is the moving secondary side liquid. The results are nearly identical which indicates that the secondary side single phase PSD is insignificant compared to the primary side tube bundle PSD.

The moving single phase fluid creates some minor temperature fluctuations that create some detectable strain above the noise for less than {{ }}<sup>2(a),(c)</sup> Hz.

{{

}}<sup>2(a),(c)</sup>

Figure 3-74 TF0003\_0762 column 5 lower strain sensor with pinned boundary conditions

---

{{

}}<sup>2(a),(c)</sup>

Figure 3-75 TF0003\_0762 column 5 upper strain sensor with pinned boundary conditions

### 3.2.2.2.3 Cases with Two Phase Secondary Flow

Of the tests with two phase secondary side flow, TF0007\_0777 is most representative of the NuScale design at full power and maximum design flow. However, due to thermal power limitations in the TF-2 test facility, the secondary side flow is much lower than the actual NuScale design.

The results for all three instrumented columns are shown in Figure 3-76 through Figure 3-80. The upper sensors for column 1 are not shown as they were not functional during the test. In general, the analytical results overpredict the test data. The resonance peaks for the first tube modes are an order of magnitude higher than the noise floor of the test data. The lower sensors of columns 1 and 3 show some low frequency response which is due to the two phase pressure PSD. The upper sensors do not show that same response as the two phase region is near the bottom of the tube. The location of the two phase region tends to excite modes near the bottom of the tube.

{{

}}<sup>2(a),(c)</sup>

Figure 3-76 TF0007\_0777 column 1 lower strain sensor with pinned boundary conditions

{{

}}<sup>2(a),(c)</sup>

Figure 3-77 TF0007\_0777 column 3 lower strain sensor with pinned boundary conditions

{{

}}<sup>2(a),(c)</sup>

Figure 3-78 TF0007\_0777 column 3 upper strain sensor with pinned boundary conditions



{{

}}<sup>2(a),(c)</sup>

Figure 3-79 TF0007\_0777 column 5 lower strain sensor with pinned boundary conditions

{{

}}<sup>2(a),(c)</sup>

Figure 3-80 TF0007\_0777 column 5 upper strain sensor with pinned boundary conditions

For comparison, the column 5 results for TF0007\_0781 are shown below. The higher primary flow rate in this test causes overall higher responses. Besides the thermal strain content, the test data does not show any clear peaks above the noise floor. The analytical results are orders of magnitudes higher than the test data.

{{

}}<sup>2(a),(c)</sup>

Figure 3-81 TF0007\_0781 column 5 lower strain sensor with pinned boundary conditions

{{

}}<sup>2(a),(c)</sup>

Figure 3-82 TF0007\_0781 column 5 upper strain sensor with pinned boundary conditions

### 3.2.2.2.3 TF-1 Secondary Side PSD Sensitivity

Additional cases are run to assess how well the results using the TF-1 pressure PSD data matches with the TF-2 strain data. The TF-1 data also has some different features compared to the literature PSDs that require explanation.

Figure 3-83 and Figure 3-84 below show the strain results for a typical case upper and lower sensors. The TF-1 pressure PSD has a large amount of low frequency content ({{ }}<sup>2(a),(c)</sup>) which increases the analytical response greatly. While this result matches the TF-2 test data better for the lower sensor (Figure 3-83), the comparison is worse for the upper sensor (Figure 3-84). Section 3.2.2.2.1 discusses that the low frequency strains in the TF-2 test data are due to thermal strains caused by unsteady fluid temperatures in the test. When accounting for the thermal strain, the TF-1 results significantly overpredict the low frequency strain response.

The TF-1 facility used piston pumps to supply feedwater to the flow. The TF-1 pressure data less than about {{ }}<sup>2(a),(c)</sup> is attributed to the pumping frequency. This interpretation is corroborated by the available pressure data from the feedwater inlet. While the feedwater inlet pressure is sampled at a much lower frequency, the data shows oscillations that are consistent with the low frequency portion of the pressure PSDs measured inside the tube. This indicates that the low frequency pressure data is caused

a phenomenon that affects the whole test loop, like the piston pumps, and not just the tubes.

The other important feature of the TF-1 PSDs is the broad spectral peak around {{ }}<sup>2(a),(c)</sup>. One analysis of the test data describes this peak as being due to bubble formation in the flow. While that explanation is reasonable, it does not entirely fit the data. When present, the spectral peak appears in all pressure sensors of the active tube. The peak also appears in the adiabatic cases which have two-phase flow at approximately constant quality. The {{ }}<sup>2(a),(c)</sup> peak is greatly reduced in magnitude for the diabatic cases with low electrical power and with high subcooling. Explanations other than bubble formation are possible, but without a clear explanation for the {{ }}<sup>2(a),(c)</sup> peak, it is conservative to assume that it is a real phenomenon.

The TF-1 cases are run for frequencies less than 600 Hz. Looking at the response results for frequencies greater than 300 Hz, the strain content is on the order of {{ }}<sup>2(a),(c)</sup> and the displacement content is on the order of {{ }}<sup>2(a),(c)</sup>. Both of these results are not large enough to be significant. Even if the {{ }}<sup>2(a),(c)</sup> peak is a phenomenon applicable to the NuScale design, it will not have a significant impact.

The strain gauge data up to 300 Hz shown in Figure 3-83 and Figure 3-84 has been cleaned up to remove electrical interference among other things. Figure 3-85 shows the strain gauge data out to 600 Hz without the same processing. The response in the data around {{ }}<sup>2(a),(c)</sup> is consistent with the noise floor and does not show any indication that the {{ }}<sup>2(a),(c)</sup> pressure data measured in TF-1 is manifested in the strain response for TF-2.

{{

}}<sup>2(a),(c)</sup>

Figure 3-83 TF0007\_0781 column 5 lower strain sensor with pinned boundary conditions and the TF-1 PSD

{{

}}<sup>2(a),(c)</sup>

Figure 3-84 TF0007\_0781 column 5 upper strain sensor with pinned boundary conditions and the TF-1 PSD

{{

}}<sup>2(a),(c)</sup>

Figure 3-85 TF0007\_0781 column 5 unfiltered strain sensor up to 600 Hz

#### 3.2.2.2.4 Au-Yang Secondary Side PSD Sensitivity

In order to assess the sensitivity of the results to the single phase PSD on the secondary side, additional cases are run using the Au-Yang/Jordan PSD described in Equation 3-26. The Au-Yang/Jordan PSD is developed to bound highly turbulent single phase flows. Figure 3-87 shows that the responses are significantly higher with the Au-Yang/Jordan PSD compared to the Chen PSD in Figure 3-79. The differences are particularly large around the modes near {{ }}<sup>2(a),(c)</sup>.

The Au-Yang/Jordan PSD adds response which results in strains higher than the noise floor of the test data. The test data does not show the same peaks and therefore, the Au-Yang/Jordan PSD is only adding conservatism with respect to the test data. The Chen PSD is better match to the test data.



---

{{

}}<sup>2(a),(c)</sup>

Figure 3-86 TF0007\_0781 column 5 lower strain sensor with pinned boundary conditions and the Au-Yang/Jordan PSD

### 3.2.2.2.5 Mode Combination Significance Sensitivity

To aid in the efficient computation of the response spectra, only the most significant of the possible mode combinations are used. The significance criteria is described in Equation 3-18 and Equation 3-19. The selected significance threshold is 0.1, but a sensitivity is run using a value of 0.01.

Using TF0007\_0781 column five with the pinned boundary condition as an example, the threshold of 0.1 uses the 1683 most significant mode combinations out of 4753 possible combinations. The threshold of 0.01 uses the 3682 most significant combinations. Figure 3-87 shows the results using the threshold of 0.01. The results are largely the same as those in Figure 3-81. The RMS strain amplitudes are within a fraction of a percent for

the x and y directions. The z direction results are within approximately one percent which is acceptable.

{{

}}<sup>2(a),(c)</sup>

Figure 3-87 TF0007\_0781 column 5 lower strain sensor with pinned boundary conditions and more mode combinations

#### 3.2.2.2.6 Coherence Integral Mesh Sensitivity

The numerical solution of the acceptance integrals includes a term for the coherence which is a combination of a decreasing exponential and a sinusoid as shown in Equation 3-33. Since this function can change on length scales smaller than the finite elements, a mesh sensitivity is performed to show that the selected size of 0.125 inch is appropriate for the acceptance integral calculation.

To assess the mesh sensitivity, cases are run with the mesh size reduced by a factor of two. Figure 3-88 below shows fine mesh results which is not noticeably different from Figure 3-81 with the larger mesh size. The calculated RMS strain amplitudes from the two mesh sizes are less than half a percent different which is acceptably small.

---

{{

}}<sup>2(a),(c)</sup>

Figure 3-88 TF0007\_0781 column 5 lower strain sensor with pinned boundary conditions and fine mesh

### 3.2.2.2.7 Damping Sensitivity

To investigate the effect of damping on the results, additional cases are included with a damping of {{ }}<sup>2(a),(c)</sup>. Figure 3-89 below shows the same overall trend as Figure 3-81, but with overall smaller response near resonance. This damping sensitivity study is inconclusive with respect to what damping provides a better match to the TF-2 test data. This sensitivity study does show that damping would have needed to be significantly larger to move the resonance peaks below the noise level in the strain gauge data.

{{

}}<sup>2(a),(c)</sup>

Figure 3-89 TF0007\_0781 column 5 lower strain sensor with pinned boundary conditions and {{ }}<sup>2(a),(c)</sup> damping

### 3.2.2.3 Results and Conclusions

#### 3.2.2.3.1 TF-2 Low Frequency Strains

Analysis of the TF-2 test data shows that the low frequency strains mainly due to temperature oscillations caused by secondary side flow oscillations. The limitations of the duration and frequency of the TF-2 test data prevent a direct comparison, but the trends indicate that low frequency strains occur when nearby temperature sensors also show low frequency temperature oscillations. Simple ANSYS model described in Section 3.2.2.5 provides further indication that the magnitude of the low frequency strains corresponds well to the magnitude of the temperature changes.

The temperature oscillations in the TF-2 test facility are not prototypic of the NuScale design. The SG inlet flow restrictors in the NuScale design are provided to limit the magnitude of secondary side flow oscillations. With an understanding of the low frequency strains, the higher frequency strains in the data are categorized as noise. This indicates that strains due to vibrations in the tests were lower than the noise floor for the higher frequencies.

### 3.2.2.3.2 TF-1 PSDs

Cases run using the TF-1 measured pressure PSDs show that the TF-1 PSD is overly bounding. Noise in the TF-1 PSD and low frequency pressure oscillations, potentially caused by the piston pumping frequency of the facility create challenges in using the TF-1 PSDs. The combination of the Chen single phase PSD and the Giraudeau two phase PSD provides a better match to the TF-2 test data.

The TF-1 pressure PSDs show a peak near  $\{\{ \quad \quad \quad \} \}^{2(a),(c)}$ . There is currently no conclusive physical explanation for this peak. Therefore, the data is assumed to be realistic and included in an analysis. The responses in strain and displacement due to the  $\{\{ \quad \quad \quad \} \}^{2(a),(c)}$  peak are not significant. The reduced impact of these high frequency pressure oscillations is due to the natural decrease in the modal transfer function at higher frequency inputs.

### 3.2.2.3.3 Sensitivity Studies

Sensitivities studies on the mode significance threshold and mesh size indicate that the values used in this analysis are appropriate. A lower threshold or a smaller mesh size did not significantly affect the conclusions in this calculation.

A sensitivity on the secondary side single phase PSD shows that using the bounding Au-Yang/Jordan PSD is overly bounding and compares worse to the test data compared to the Chen PSD.

A damping sensitivity showed that the resonance peaks are sensitive to damping as expected. Based on the noise in the TF-2 strain data, no conclusive comparison is possible about what damping was actually present in the test.

### 3.2.2.3.4 Vibration Analysis

Discounting the thermal strains in the TF-2 test data, there are no clear resonance peaks in the data. The data is dominated by a noise floor around  $\{\{ \quad \quad \quad \} \}^{2(a),(c)}$ . This noise floor corresponds to small strains, on the order of  $\{\{ \quad \quad \quad \} \}^{2(a),(c)}$  RMS. The actual strains in the TF-2 facility are washed out by the noise floor and therefore are less than or equal to the noise floor. As the noise floor corresponds to small responses, it can also be concluded that the TB vibrations in the test facility are small even for scaled primary flow rates that are much higher than in the NuScale design.

The peak responses in the analytical results for all cases have responses at or above the noise floor in the data. The cases where the highest response is expected, highest primary and secondary flow rates, show analytical peak responses orders of magnitude higher than the test data. The shape of the analytical results matches typical responses to turbulent excitations with the majority of the response clustered around the lowest modal frequencies. Assuming that the actual vibration signal in the TF-2 facility is of similar shape, the comparison of the peaks in the analytical results to the lack of peaks above the noise floor in the test data indicates that the analytical approach is bounding compared to the test data.

The analytical results indicate that the primary PSD and the two phase secondary PSD are the most significant inputs. The primary PSD drives the largest resonance peaks at the low frequency tube modes. The two phase PSD is larger in magnitude, but acts at frequencies well below the tube fundamental frequency. The two phase PSD is also local to the lower portion of the tube which only excites modes in the same area.

### 3.2.2.4 Acceptance Integral Implementation Validation

To validate the implementation of the acceptance integral method several test cases are used to compare the methodology to the Random Vibration module in ANSYS Mechanical. ANSYS has the capability to calculate the response spectra due to PSD excitation, but has limitations on what types of coherence can be used. ANSYS can do fully correlated PSDs, PSDs correlated by a phase offset, and spatially correlated PSDs. The spatial correlation is limited to a linear ramp between fully correlated and zero correlation at two distances.

Figure 3-90 below shows the geometry used for the test cases. The beam is straight and aligned in the positive x direction starting from the origin. The beam is 60 in long and meshed with one inch elements. All three translational degrees of freedom are set to zero on the left end and the y and z direction translations are set to zero on the right end.

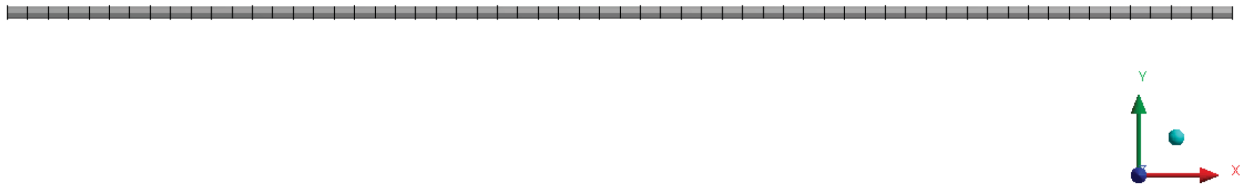


Figure 3-90 Test case geometry

An arbitrary pressure PSD is applied to the beam in the y and z directions. The first test case uses a fully correlated PSD. In order to use the phase offset or spatial correlation options in ANSYS, the pressure PSD must be converted to a force PSD. The equivalent force PSD yields also the same results as the original pressure PSD. The four test cases are as follows:

1. "Full" – Fully correlated force PSD
2. "Wave" – Force PSD correlated by a phase offset due to an x direction velocity of 600 in/s
3. "Spat" – Force PSD with spatial correlation (fully correlated for points within 5 in and uncorrelated for points greater than 10 in away)
4. "Half" – Force PSD on the left half of the beam with spatial correlation (fully correlated for points within 1 in and uncorrelated for points greater than 3 in away)

The same four test cases are executed using the acceptance integral methodology. The results are compared for a point at  $x = 25$  inches. The resulting RMS values are within 0.6

percent for displacement and within two percent for bending strain. Spectra for the four cases for displacement and bending strain are shown in Figure 3-91 through Figure 3-98.

{{

}}<sup>2(a),(c)</sup>

Figure 3-91 Displacement spectrum comparison for test case 1

{{

}}<sup>2(a),(c)</sup>

Figure 3-92 Displacement spectrum comparison for test case 2



{{

}}<sup>2(a),(c)</sup>

Figure 3-93 Displacement spectrum comparison for test case 3

{{

}}<sup>2(a),(c)</sup>

Figure 3-94 Displacement spectrum comparison for test case 4

{{

}}<sup>2(a),(c)</sup>

Figure 3-95 Bending strain spectrum comparison for test case 1

{{

}}<sup>2(a),(c)</sup>

Figure 3-96 Bending strain spectrum comparison for test case 2

{{

}}<sup>2(a),(c)</sup>

Figure 3-97 Bending strain spectrum comparison for test case 3

{

}}<sup>2(a),(c)</sup>

Figure 3-98 Bending strain spectrum comparison for test case 4

### 3.2.2.5 Tube Thermal Strain Model

To get an approximate measure of how temperature fluctuations would induce strain in the tubes, a simplified axisymmetric model of the tube is developed in ANSYS. Figure 3-99 shows the model and mesh. The thermal boundary conditions are selected based on estimates from the NRELAP5 cases. However, the exact boundary conditions are not critical as the purpose is to understand how much strain is generated for a given change in outer diameter temperature. An axisymmetric model is used for its simplicity and efficiency. Modeling the curvature of the tube is not critical to get an estimate of the effect of temperature on strain.

The inner and outer wall heat transfer coefficients are 15 kW/m<sup>2</sup>-K and 12 kW/m<sup>2</sup>-K respectively. The inner wall fluid temperature is 420°F and oscillates as a square wave with an amplitude of 40°F zero to peak and a frequency of 0.1Hz. The square wave was selected to represent the quick fluid temperature change when going from saturated conditions to single phase conditions. The precise frequency is not important as the temperatures reach an approximate steady state after only a few seconds.

The structural boundary conditions include a fixed boundary condition in the vertical direction at the lower edge and a constraint that the nodes on the upper edge have the same y coordinate. These boundary conditions emulate a situation where the tube is

allowed to grow unrestrained in the vertical direction. This modeling choice is an approximation as there will be some resistance to lengthening of the tube which may result in additional strains. Figure 3-100 shows the resulting strain time history due to the temperature changes. The strain change occurs over about a one second period out of a 10 second cycle which would be captured by only some of the five second sets of strain data.

The strain plot in Figure 3-100 occurs for a 28°F temperature change on the outer diameter of the tube. Therefore, a strain range of  $\{\{ \dots \}^{2(a),(c)}$  on the outer diameter of the tube corresponds to a temperature change of  $\{\{ \dots \}^{2(a),(c)}$ . This rate is important because it relates two measured quantities from the TF-2 test, temperature and strain on the outer diameter of the tube.

$\{\{$

$\}^{2(a),(c)}$

Figure 3-99 Tube axisymmetric model mesh

---

 {{

 }}<sup>2(a),(c)</sup>

Figure 3-100 Tube axisymmetric model mesh

### 3.3 TF-2 Benchmark Testing for Fluid Elastic Instability

In the process of benchmarking the thermal-hydraulic performance of the prototypic HCSG, NuScale commissioned Sperimentiamo le Tue Idee (SIET) to construct and test two separate test specimens. Test Facility #1 (TF-1) utilized electric direct heating of several individual helical coil tubes to investigate thermal hydraulic behavior within the secondary-side (HCSG tubes). Test Facility #2 (TF-2) was a more-complex specimen, consisting of a 5-column, partially-prototypic HCSG assembly inserted into a test vessel and operated at a range of conditions, with variations in both primary- and secondary-side parameters. Given that it represents a smaller version of the ultimate fully-prototypic design, TF-2 was used to obtain a limited sample of data to characterize the response of individual HCSG tubes to various flow conditions. These measurements were accomplished by affixing axially-oriented strain gauges to the outside of specific tubes. During testing, TF-2 was subjected to both normal and above-normal operating conditions, including a series of cases wherein primary flow rates were increased to approximately {{ }}<sup>2(a),(c)</sup> of normal operating maximum to assess whether FEI) excitation of the HCSG tubing is feasible.

This section provides a detailed analysis of the strain gauge measurements obtained from TF-2 during FEI testing conditions, including the methodology, results, relevant observations, and the ultimate conclusion that the onset of FEI was not observed in any of the tests. While the TF-2 test was not fully-prototypic, the measurements and subsequent results presented herein are used in conjunction with other testing program results to validate the HCSG CVAP design analysis.



### 3.3.1 TF-2 Test Design

The primary purpose for fabrication and testing of TF-2 was qualification of the NuScale thermal hydraulic models, and confirmation of fluid property specifications and assumptions. SIET possesses an existing test facility (GEST) with the pressure vessel and associated pumps and equipment necessary to perform high-pressure, high-temperature testing of vessel internal components. A prototypical assembly was created to mimic the as-designed HCSG, with representative tubes of identical OD and pitch. Modifications were made to the end portal designs to simplify manufacturing. The size of the specimen was limited by the size of the GEST vessel, which necessitated using Columns 1-5 (of 21 total) as shown in Figure 3-101. This is less-desirable for the FEI assessment because the inner-most tubes have the lowest reduced velocities and require the highest driving flow to reach the onset point.

{{

}}<sup>2(a),(c)</sup>

Figure 3-101 TF-2 Fluid-heated test section tubing column scheme

Assessment of vibration mechanisms, including FEI, was not taken into consideration during initial scoping activities for the test program. The opportunity to obtain additional, value-added data in support of CVAP benchmarking efforts was acted on once recognized; however, at that stage it was not possible to implement a comprehensive instrumentation configuration for FIV. There were physical and environmental challenges associated with the sensors themselves. In addition, the design and construction of TF-2 did not facilitate use of a fully-prototypic tube support configuration. The actual NuScale design is based on eight tube support columns, which are comprised of interlocking plates with bent extruded tabs as shown in Figure 3-102. The support columns are arranged in a consistent pattern at azimuths of  $\{\{ \quad \}\}^{2(a),(c)}$ , and so on, such that the longest unsupported span of the HCSG tubing is  $\{\{ \quad \}\}^{2(a),(c)}$ .

$\{\{$

$\}\}^{2(a),(c)}$

Figure 3-102 TF-2 Tube support detail

Conversely, TF-2 was fabricated with four support columns (at  $\{\{ \quad \}\}^{2(a),(c)}$ ), for an effective span length of  $\{\{ \quad \}\}^{2(a),(c)}$ . This is beneficial for the FEI assessment because, compared to the fully-prototypic support configuration, the longer spans result in lower frequencies. The TF-2 supports restrain motion in a similar fashion as the tabbed supports in the fully-prototypic design. For either configuration, the interface at each tab/guide approximates a pinned connection. The presence of multiple tabs in close proximity serves to reduce rotation about the support column and constrains the significant modes to individual bending of the unsupported spans. Minor differences in thermal expansion between the tubing, tube supports, reactor pressure vessel (RPV) riser,

and RPV wall cumulatively result in the tubing being pinned tightly against one side of the supports, further supporting the above determination on modal constraints. Variations in support interface rigidity may introduce variations in localized static strains within individual tubing spans.

Given the preceding discussion, the natural frequencies and mode shapes of the TF-2 tubing are not expected to match those from NuScale's fully-prototypic design models, including the FEI analysis. In order to facilitate comparison and evaluation of the resulting data, NuScale generated modal predictions for several single tube configurations within TF-2. Because the corresponding NuScale modal analysis has not been finalized as of issuance of this report, the corresponding mode shapes and frequencies presented herein are treated as an assumption. Given the geometry and support arrangement of the helical array, there are a number of modes, many with similar, closely-spaced frequencies and response profiles. The frequencies that are of interest based on mass participation are provided in Section 3.2.1.14.

Section 3.2.1.14 and Table 3-21 discuss the frequencies that are expected to provide significant contribution to potential tubing movements based on ANSYS modal analysis of the TF-2 test specimen. The TF-2 models were generated in a global/cartesian coordinate system, wherein the Y-direction is vertical and the X- and Z-directions are either axial to or perpendicular with the tubing, depending on azimuth.

The in-vessel instruments were exposed to a fluid environment over the full range of operating parameters, which restricts the applicable sensors to a small range. Also, there were physical challenges in terms of limited space to install or affix sensors in the space between the inner (annual) and outer walls. Given these challenges, SIET chose to employ Kyowa strain gauges (Model KHC-20-120-G9-16), which are affixed to the tubing by capacitive discharge welding. These sensors have been deployed for in-vessel measurements of boiling water reactor steam dryers. The noise floor is quite high compared with 350Ω strain gauges, which have a higher gauge resistance and improved signal-to-noise ratio.

The indicated strain gauges were installed in pairs at six different locations (12 total sensors). Columns 1, 3, and 5 were chosen to represent the range of available geometries within TF-2. For each column, strain gauges were installed on one select tube, at a "Lower" and an "Upper" location. These locations were generally 1½ helical turns from the respective FW or steam plenums. At each location, one strain gauge was installed on the tube extrados (side) and another was installed on the top. Both strain gauges were oriented axially. Refer to Figure 3-103 for a schematic illustrating the placement of strain gauges at each location and Figure 3-104 for a photograph of the sensors installed at the lower location of Column-1. Table 3-25 summarizes channel and location information for the installed strain gauges.

Because the actual damage mechanism associated with FEI is excessive tube motion leading to adverse wear and impacting, it is important to understand how measured strains relate to actual tube displacements. This relationship varies depending on sensor placement and support configuration.

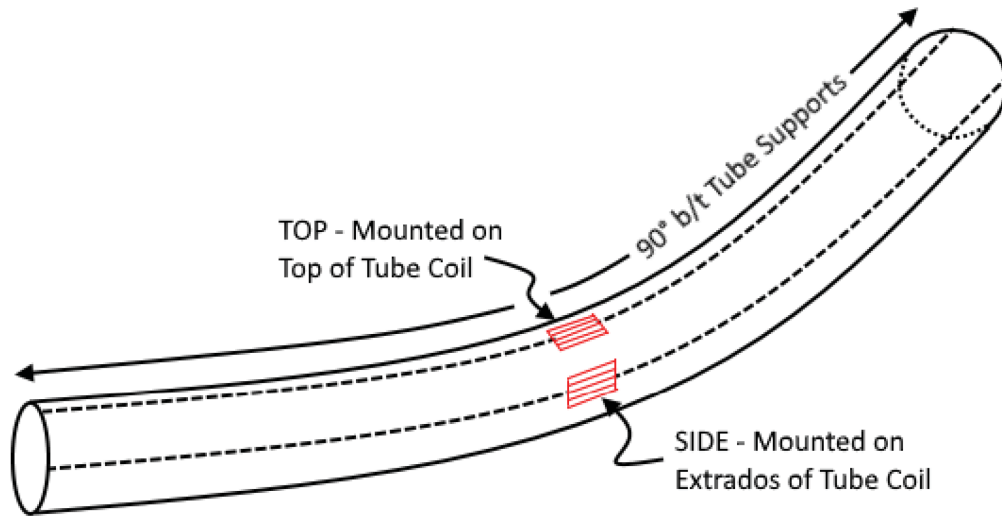


Figure 3-103 Placement of strain gauges on tube coils (typical)

{{

}}<sup>2(a),(c)</sup>

Figure 3-104 Placement of strain gauges on tube coils (S1101-1 and S1101-2 shown)

Table 3-25 Placement of strain gauge instrumentation

Sensor Description		Sensor Placement (General)				Sensor Placement (Specific)				
Name	ID	Column	Tube	Plenum	Position	Elevation (m)	Linear (m)	Azimuth (°)	$\theta/\Delta$ to Nearest Support	
S1101-1	S01	1	20	FW	Side	}}			}} <sup>2(a),(c)</sup>	
S1101-2	S02				Top					
S1102-1	S03			MS	Side	}}				}} <sup>2(a),(c)</sup>
S1102-2	S04				Top					
S3101-1	S05	3	21	FW	Side	}}		}} <sup>2(a),(c)</sup>		
S3101-2	S06				Top					
S3102-1	S07			MS	Side	}}				}} <sup>2(a),(c)</sup>
S3102-2	S08				Top					
S5101-1	S09	5	11	FW	Side	}}		}} <sup>2(a),(c)</sup>		
S5101-2	S10				Top					
S5102-1	S11			MS	Side	}}				}} <sup>2(a),(c)</sup>
S5102-2	S12				Top					

- Notes:
1. The “Plenum” column defines sensor location based on the nearest inlet/outlet – -FW or MS.
  2. Global elevations are measured from a datum several meters below the steam generator.
  3. Linear positions are measured from the inlet (FW) orifice of an individual tube, along its centerline.
  4. Global azimuths are measured from a 0° reference at the inlet (FW) plenum. In this arrangement, tube supports are at global azimuths of {{ }}<sup>2(a),(c)</sup> and so on.
  5. Sensors S03 and S04 (Column-1, Upper/MS Location) were determined to be non-functional upon installation, and the data from these channels is excluded from subsequent analysis hereinafter.

Table 3-26 summarizes the test series, plateaus, and filenames that were selected for further processing, including the applicable steady-state fluid parameters at the time of acquisition. It also presents a shortened alpha-numeric naming convention that is used to identify/discuss specific datasets throughout the remainder of this section. Test series TF0005 and TF0006 did not contain datasets at ramped flow conditions, but only at maximum flow conditions. It is assumed that these datasets are outliers wherein SIET was attempting to establish steady-state flow conditions at elevated temperature and pressure.

Table 3-26 Test conditions and file names for fluid elastic instability data acquisition

Test Series	Primary Side			Secondary Side		Test ID
	Flow (kg/s)	Temp. (°F)	Pres. (psi)	Temp. (°F)	Conditions	
TF0001	114.4	Ambient	{{		}} <sup>2(a),(c)</sup>	A1
	141.7					A2
	172.5					A3
	199.2					A4
	230.5					A5
	263.3					A6
TF0002	113.7	Ambient	{{		}} <sup>2(a),(c)</sup>	B1
	143.3					B2
	174.6					B3
	205.0					B4
	229.5					B5
	262.5					B6
TF0003	113.2	Ambient	{{		}} <sup>2(a),(c)</sup>	C1
	142.2					C2
	175.5					C3
	200.7					C4
	234.5					C5
	263.6					C6
TF0004	113.5	249.9	{{		}} <sup>2(a),(c)</sup>	D1
	145.7					D2
	170.6					D3
	202.0					D4
	232.6					D5
	266.8					D6
TF0005	252.7	580.0	{{		}} <sup>2(a),(c)</sup>	E6
TF0006	260.2	499.9	{{		}} <sup>2(a),(c)</sup>	F6a
	262.3					F6b
TF0007	168.4	449.8	{{		}} <sup>2(a),(c)</sup>	G3
	199.0					G4
	227.0					G5
	256.0					G6

- Notes:
- The indicated temperatures represent inlet values. The secondary-side parameters represent average values across tube columns. Where present, singular values represent an average or nominal value for datasets within a particular test series.
  - The indicated test IDs (right-most column) were assigned to simplify reference to individual datasets or conditions. The 1<sup>st</sup> character (alpha-indicator) refers to a specific test series with consistent primary and secondary side parameters (note: primary flow varies); the 2<sup>nd</sup> character (numeric) is a sequential index increasing with flow rate.

The FEI data files listed in Table 3-26 were reviewed to evaluate waveform (time) and spectral (frequency) content. A consistent processing approach was applied to each of the data files in Table 3-26, to enable like-for-like comparisons. This processing consisted of eliminating spurious signal noise and computing statistics or estimates to inform the FEI evaluation. The general steps and characteristics of the processing script are described below for reference.

- The raw waveform files exhibit variation between datasets and individual channels in terms of average (DC) value(s). Figure 3-105 exemplifies these DC variations by

plotting the raw waveform data for sensors S01, S05, and S09 (one in each column) at the maximum primary flow for each test series (i.e., datasets A6, B6, C6, D6, and G4). These variations were anticipated given the sensor type and configuration, as well as the uncertain boundary conditions on individual tubes when the HCSG assembly is thermally loaded. Given the randomness of the variations, it is not possible to infer meaningful results by comparing the “static” values (DC/average) between datasets or individual channels. Removal of the DC content (by subtracting the average) results in reasonable “dynamic” waveforms, which are comparable between datasets or channels. Thus, the DC content of the waveforms was removed during processing.

- Digital filtering was used to restrict the signal content to the frequency range of interest for the HCSG and to eliminate spurious electrical noise. Filters were based on  $\{\{ \}^{2(a),(c)}$ . The filters were applied in the forward and reverse direction to avoid phase distortion, using the *filtfilt* function in Matlab.
  - If present, FEI excitation within the HCSG is expected to amplify the first-mode bending frequencies of the individual tube columns. These frequencies range from approximately  $\{\{ \}^{2(a),(c)}$  (radial direction) to  $\{\{ \}^{2(a),(c)}$  (vertical direction), depending on the assumed boundary conditions. Given the support configuration and general flexibility of the thin-walled tubes, higher-order modes may also be visible within the data, up to 100 Hz per the modal analysis. For the FEI analysis herein, a digital bandpass filter was used to de-emphasize content outside of the frequency range of interest. Specifically, the filter negates the impact of low-frequency drift and slow oscillations that are visible in many of the unadulterated waveforms.  $\{\{ \}^{2(a),(c)}$ .
  - The TF-1 dynamic pressure data exhibits a notable response peak between  $\{\{ \}^{2(a),(c)}$  within the dynamic pressure data obtained from the secondary-side sensors. Thus, a second or alternate processing run was performed with a bandpass filter range of 5 to 1,000 Hz to evaluate whether the data contains any higher-frequency peaks of interest that align with the TF-1 content. A separate set of processing parameters are applicable to the higher-frequency bandpass, which are referred to as “Run-2” hereinafter. The 3-300 Hz bandpass noted in the previous item is referred to as “Run-1”. Table 3-27 provides a summary of the exact processing/filtering parameters applied during Run-1 and Run-2.
  - The strain gauge signals exhibit some electrical line noise ( $\{\{ \}^{2(a),(c)}$ ) or its multiples ( $\{\{ \}^{2(a),(c)}$ , and so on). In order to delineate content at apparent structural frequencies and normalize overall results between datasets, these electrical frequencies (where present) were removed using bandstop (notch) filters. For each peak, a 6<sup>th</sup>-order filter was applied, with a bandwidth of  $\{\{ \}^{2(a),(c)}$  depending on the amplitude and width of the target frequency. For Run-2, filtering of electrical multiples (i.e.,  $\{\{ \}^{2(a),(c)}$  and higher) introduced additional spectral noise. Thus, the bandstop filters for Run-2 were applied in an identical fashion as Run-1, such that some amount of electrical noise remained present at  $\{\{ \}^{2(a),(c)}$  and above.

- For certain channels, the digital filtering operations produced a “ringing” effect at the beginning and end of the resulting waveform where the digital filters struggle to track the target raw signal from unknown initial conditions. Therefore, before calculating the overall values and frequency transforms for each channel, one-half second of data was truncated from the start and end of each channel’s waveform to remove potential ringing effects. The net effect of this operation is that the overall length of each channel waveform is reduced from 5 seconds (raw) to 4 seconds (processed).
- After these operations were completed, overall values were obtained from the processed waveforms for each channel of each dataset. Values were obtained in terms of RMS, zero-to-peak (0-pk), and peak-to-peak (pk-pk) measures, although only the RMS and 0-pk results will be used in the remainder of this report.
- The processed time domain data was converted to the frequency domain using an FFT algorithm; specifically, the *pwelch* function within Matlab, which calculates the broadband-normalized power spectral density (PSD) of a signal. A frequency resolution (bin width or  $\Delta f$ ) of  $\Delta f = \frac{1}{N \cdot T}$  was applied for all channels, resulting in multiple waveform data blocks of  $T = \frac{1}{\Delta f}$  duration. For the large frequency range in Run-2, a  $\Delta f = \frac{1}{N \cdot T}$  was applied to obtain 1-second data blocks). An overlap of 50 percent was used to increase the number of data blocks in the computation. A Hanning window was used in conjunction with the FFT algorithm to avoid spectral bin leakage due to varying start and end conditions of each block, thereby improving spectral bin resolution. Use of the Hanning window in this manner has a global scaling effect on each block, which in turn requires multiplication by an adjustment factor (1.5) in order for frequency domain amplitudes to match time domain content at specific frequencies. The windowed, scaled FFT results for each block are then linearly averaged to compute the “overall” PSD. This averaging process improves spectral resolution and normalizes the effects of frequency-specific amplitude perturbations. The entire process of resolving the waveform into overlapped blocks, performing the FFT conversion, windowing, scaling, and averaging is self-contained and controlled by the *pwelch* function and its parameter inputs.

For random vibration signals such as those obtained from the TF-2 strain gauges, spectral plots are represented in RMS units to simplify identification and characterization of dominant peaks. Thus, the overall PSDs computed as described in the preceding item were converted to RMS spectra, using the expression in Equation 3-35.

$$S_{rms}(f) = \sqrt{S_{psd}(f) \cdot \Delta f \cdot F_{window}} \quad \text{Equation 3-35}$$

Where,

- $S_{rms}(f)$  = Frequency domain spectral output in terms of RMS value,
- $S_{psd}(f)$  = Frequency domain spectral output in terms of PSD value (i.e., from *pwelch*),
- $\Delta f$  = Spectral resolution or “bin width,” and
- $F_{window}$  = Window adjustment factor (1.5 for Hanning window).



For any signal, Parseval’s theorem holds that the total energy content in the time domain must equal the energy content within the resulting frequency domain. Thus, for the spectra obtained from the frequency domain conversions described above, it is possible to compute an overall RMS value over a specific frequency range using a square-root-of-the-sum-of-the-squares approach. This relationship is expressed in generic form (i.e., for an FFT algorithm without windowing, scaling, and averaging) in Equation 3-36. The integral limits for the spectral term (right-hand side) of Equation 3-36 were modified to reflect a frequency range of interest (i.e.,  $f_{low}$  to  $F_{high}$  instead of 0 to  $F$ ). The expression in Equation 3-36 is applicable to the normalized (single-sided), raw (complex) output of generic FFT algorithms. For this application, use of the *pwelch* function in the manner described above automatically returns a single-sided, magnitude-only (non-complex) spectrum, which is properly scaled for the applied windowing and averaging parameters. Consequently, the expression used to compute overall RMS values from the *pwelch* spectral results was modified for span-specific calculations as shown in Equation 3-37.

$$W_{rms} = \sqrt{\frac{1}{T} \int_0^T [W(t)]^2 \cdot dt} = S_{rms} = \sqrt{\frac{2}{F} \int_0^F [S(f)]^2 \cdot df} \quad \text{Equation 3-36}$$

Where,

- $W_{rms}$  = Time domain RMS measurement from signal waveform,
- $W(t)$  = Discretized time domain waveform, containing “N” number of points,
- $T$  = Period/length of time domain signal(s),
- $dt$  = Difference in time between measurement points (i.e., inverse of sampling rate),
- $S_{rms}$  = Frequency domain RMS measurement from normalized (single-sided) Fourier transform,
- $S(f)$  = Normalized Fourier transform raw output (in complex form),
- $F$  = Maximum discretized frequency of the continuous Fourier transform. For  $N$  waveform points,  $F = N \cdot \Delta f / 2$ , and
- $df$  = Difference in frequency between bins (i.e.,  $\Delta f$ ).

$$S_{rms\_f} = \sqrt{\sum_{f_{low}}^{f_{high}} [S_{psd}(f)]^2 \cdot \Delta f} \cdot \sqrt{\frac{1}{F_{window}}} \quad \text{Equation 3-37}$$

Where,

- $S_{rms\_f}$  = Frequency-band-specific RMS measurement computed from *pwelch* spectrum output,
- $f_{low}$  = Lower bound of the frequency span of interest, and
- $f_{high}$  = Upper bound of the frequency span of interest.

{{

}}<sup>2(a),(c)</sup>

Figure 3-105 Example of average variations in strain gauge signals

Table 3-27 Summary of applied processing parameters

Parameter:	Run-1	Run-2
DC Removal	Yes	Yes
Bandpass Filter	{{	}} <sup>2(a),(c)</sup>
Notch Filters (Electrical Noise)	{{	}} <sup>2(a),(c)</sup>
Waveform Truncation	{{	}} <sup>2(a),(c)</sup>
Frequency Spectra/PSD	{{	}} <sup>2(a),(c)</sup>

- Notes: 1. A nominal value of {{ }}<sup>2(a),(c)</sup> was used for notch filter bandwidth in most cases; the {{ }}<sup>2(a),(c)</sup> setting was applied in select cases where the width of the {{ }}<sup>2(a),(c)</sup> primary electrical noise peak warranted additional reduction of the adjacent frequency bins.
2. The indicated notch filters at {{ }}<sup>2(a),(c)</sup> were only applied when review of the spectra indicated content present at those frequencies.

### 3.3.2 TF-2 FEI Benchmarking Analysis Results

The datasets listed in Table 3-26 were processed and the results collected in intermediate output files, containing summarized overall or statistical values, as well as digitized spectral tables. The intermediate results were then formatted into representative tables and plots for further assessment and interpretation. The list below summarizes the results obtained in this fashion. Unless otherwise explicitly specified, the tables, plots, and summary values specified below were obtained from datasets processed according to the “standard” parameters specified in Run-1 in Table 3-27.

The waveform duration ({{ }}<sup>2(a),(c)</sup>) is short and does not facilitate accurate characterization of frequencies when acquiring random vibration data as is typical of FIV excitation. Specifically, for turbulence or FEI, one can observe variations in the amplitude of response peaks over the course of {{ }}<sup>2(a),(c)</sup> due to minor differences or local effects in the fluid excitation function. The concern is particularly relevant at low frequencies ({{ }}<sup>2(a),(c)</sup>), as there are fewer cycles for the FFT algorithm to attempt to characterize and, if acquisition is triggered during a period of relative “calm,” the response may not be visible.

The overall noise floor of the data, on average  $\{\{ \} \}^{2(a),(c)}$  (PSD units), is higher than desirable for such measurements. This is evident when viewing combined spectral or PSD plots in which the resultant data for the datasets is overlaid. A reference example is provided in Figure 3-106 for several of the Column-3 sensors. As noted previously, this elevated noise is not unexpected given the type of strain gauges used. The increased noise floor does not impact the ability to characterize observable peaks, but obscures minor peaks (in particular for modes that are not excited by the flow conditions). This issue is compounded by the aforementioned short waveform duration.

Table 3-28 and Table 3-29 provide overall values in terms of RMS and 0-pk units. The tables are fitted with data bars to facilitate quick visualization of datasets/channels that fall outside of the norm.

Table 3-30 and Table 3-31 provide summarized overall 0-pk values by test series and primary flow rate, respectively. Average and maximum values are reported for each category and the test series or flow rate with the overall largest value for each channel is summarized at the bottom of the table. These tables help to illustrate whether specific parameters have a marked effect on overall dynamic content.

The FFT outputs were used to create comparison spectral plots for the datasets and channels. The plots were grouped in two different fashions: by test condition and by primary flow rate. Additional notes are as follows:

Datasets E6, F6a and F6b were excluded from these spectral plots. The primary- and secondary-side flow conditions for these datasets are similar to dataset G6, but the spectral data is not a direct match. These datasets appear to be outliers, because flow was not ramped in a similar fashion as test series A-D and G.

Appendix B contains plots from 0-300 Hz arranged by test series, consistent with filters applied according to Run-1. Appendix C plots contain the same 0-300 Hz data arranged by primary flow rate.

Data was also plotted from 0-1,000 Hz, consistent with the bandpass filter applied according to the alternate parameters specified in Run-2 in Table 3-27. Appendix D contains the plots arranged by test series and Appendix E contains the plots arranged by primary flow rate. Datasets within test series G exhibited more content at electrical noise multiples (i.e.,  $\{\{ \} \}^{2(a),(c)}$ , and so on) as compared to prior recordings. It was not possible to filter out the electrical peaks without introducing additional spectral noise, so bandstop filters were limited to multiples between 50 and 300 Hz. Thus, the plots in Appendices D and E exhibit electrical noise peaks at higher multiples (350 Hz and above), specifically for test series G.

The spectral plots were reviewed for frequency content. Most datasets or channels exhibit content at frequencies not predicted within the assumed modal analysis results; in many cases, the amplitude of these peaks is larger than any within the predicted frequency bands. The most-common additional peaks were: 1) a low-frequency response (<10 Hz), 2) a series/group of peaks in the  $\{\{ \} \}^{2(a),(c)}$  range, and 3) another group or set of fairly-sharp peaks in the  $\{\{ \} \}^{2(a),(c)}$  range. Accordingly, the method shown in Equation 3-37 and its accompanying discussion are used to compute frequency-range-

specific RMS values. The results of those computations are provided in tabular form in Appendix F. The frequency ranges that were evaluated are as follows:

- $\{\{ \quad \}\}^{2(a),(c)}$ : Tube breathing mode, plus large responses observed on several channels. Application of the bandpass filter ( $\{\{ \quad \}\}^{2(a),(c)}$  per Table 3-27) served to minimize content at frequencies below  $\{\{ \quad \}\}^{2(a),(c)}$ .
- $\{\{ \quad \}\}^{2(a),(c)}$ : First-mode bending in horizontal plane, visible responses within data.
- $\{\{ \quad \}\}^{2(a),(c)}$ : First-mode bending in vertical plane, visible responses within data.
- $\{\{ \quad \}\}^{2(a),(c)}$ : visible responses within data, predominantly at  $\{\{ \quad \}\}^{2(a),(c)}$  (frequency and amplitude varies by channel and dataset).
- $\{\{ \quad \}\}^{2(a),(c)}$ : visible responses within data.

The observed significant frequencies (above) were compared with potential sources of known excitation within the system. Outside of electrical content, which was removed by filtering, the only other potential source of forced excitation would be vane passing frequency pulsations from the driving pump(s). There were no consistent peaks within the data at  $\{\{ \quad \}\}^{2(a),(c)}$  or multiples thereof.

The data from Table 3-28 and Appendix F was combined in Table 3-32, to create a “consolidated” view of the various frequencies and amplitudes of interest for each dataset and channel. The table was generated by comparing the frequency-bin-specific RMS values from the tables in Appendix F to the overall RMS values from Table 3-28; most of the numbers in the table thus represent a “percentage” of the total signal energy. There is no technical basis for this calculation, as it compares values calculated from a single-sided frequency domain representation to those obtained directly from the raw time domain. As such, the numbers in the table should be treated as representative trends, not an exact measure of fractional energy. Conditional formatting is used to further delineate peaks.

Table 3-33 and Table 3-34 mimic the consolidated view within Table 3-32, but with low-frequency content (0-10 Hz) excluded to highlight changes in response at the presumed tubing response modes. Table 3-33 is sorted by test series and dataset, while Table 3-34 presents the same data sorted by flow rate.

The overall peak dynamic strains from Table 3-29 were plotted versus flow rate to illustrate any escalation of content with increased primary flow. Figure 3-107 provides the resulting plot. Data labels are included for points with overall values greater than  $\{\{ \quad \}\}^{2(a),(c)}$  to help identify datasets where large responses were observed. The plot provides a graphical representation of any non-linear escalation in tubing vibration with flow rate. If one or more resonant responses were present within the range of the TF-2 test series, whether driven by FEI, VS, or TB, it would be evident within Figure 3-107.

The amplitude-versus-flow scatter plot framework in Figure 3-107 was repeated for the frequency-range-specific RMS computations in Appendix F. The resulting plots are provided in Appendix G.

The low-frequency responses observed primarily within test series G (primary conditions at {{ }}<sup>2(a),(c)</sup>, secondary side boiling at {{ }}<sup>2(a),(c)</sup>) were further evaluated by plotting those spectra against their corresponding datasets from test series D ({{ }}<sup>2(a),(c)</sup>). Figure 3-108 provides a comparison for Column-3 (Sensors S05-S08) for Datasets D5 and G5. Figure 3-109 provides a comparison for Column-5 (Sensors S09-S12) for Datasets D6 and G6. From the data, it is evident that the peak frequency of interest is at or near the lower cutoff for the bandpass filter ({{ }}<sup>2(a),(c)</sup>), with the exact response varying somewhat by channel and dataset. The corresponding raw waveforms were superimposed on the spectral plots to further clarify the difference in signals between channels with the low-frequency response component.

{{

}}<sup>2(a),(c)</sup>

Figure 3-106 Overall power spectral density content comparison – column-3, side strain gauges (top=S07, bottom=S05)

Table 3-28 Dynamic root mean square strains measured during TF-2 fluid elastic instability tests

{{

}}<sup>2(a),(c)</sup>

Note: 1. The blue data bars reflect a common scale across datasets/channels, from 0 to the maximum value listed in the table ({{ }}<sup>2(a),(c)</sup> from dataset G4, channel S10).



Table 3-29 Dynamic peak strains measured during TF-2 fluid elastic instability tests

{{

}}<sup>2(a),(c)</sup>

Note: 1. The blue data bars reflect a common scale across datasets/channels, from 0 to the maximum value listed in the table ({{ }}<sup>2(a),(c)</sup> from dataset G3, channel S06).

Table 3-30 Dynamic peak strains by test series (average and maximum)

{{

}}<sup>2(a),(c)</sup>

- Notes
1. Values in the table represent the average or maximum across datasets within the indicated test series.
  2. The **blue** data bars represent a common scale across the average values, from 0 to the maximum value listed in the table ({{ }}<sup>2(a),(c)</sup>).
  3. The **yellow** data bars represent a common scale across the maximum values, from 0 to the overall maximum listed in the table ({{ }}<sup>2(a),(c)</sup>).
  4. The **green** data bars represent a common scale across the maximum values, from 0 to the overall maximum listed in the table ({{ }}<sup>2(a),(c)</sup>).
  5. The summary rows at the bottom of the table indicate the test series during which the highest average, maximum, and standard deviation values were observed within individual datasets.

Table 3-31 Dynamic peak strains by flow rate (average and maximum)

{{

}}<sup>2(a),(c)</sup>

- Notes:
1. Flow rates listed above represent an average of the values listed in Table 3-26 for applicable datasets. For example, the first value ({{ }}<sup>2(a),(c)</sup> is the average flow rate for Datasets A1, B1, C1 and D1; the last value ({{ }}<sup>2(a),(c)</sup> is the average for Datasets A6, B6, C6, D6 and G4.
  2. Values in the table represent the average or maximum across datasets within the indicated test series.
  3. The blue, yellow and green data bars are as-described in the footnotes to Table 3-30.
  4. The summary rows at the bottom of the table indicate the flow rates at which the highest average, maximum, and standard deviation values were observed within individual datasets.

Table 3-32 Relative comparison of content within frequency ranges of interest (0-10 Hz inclusive), sorted by test series

{{

- Notes:
1. Values listed in the "Overall" columns were obtained from Table 3-28 (i.e., in units of  $\mu\epsilon$ -RMS).
  2. The values in the colored columns were obtained by dividing the frequency-bin-specific RMS energy by the overall value, and thus represent an effective percentage of total signal energy within the given spectral band(s). **These values should not be treated as absolutes; they are for trending/comparison purposes only.**
  3. The conditional formatting/highlights are frequency-bin-specific across the channels. For example, within the {{ }}<sup>2(a),(c)</sup> bin, formatting is applied over the range from the minimum value ({{ }}<sup>2(a),(c)</sup> from dataset G6, channels S09 and S10) to the maximum value ({{ }}<sup>2(a),(c)</sup> from dataset C1, channel S11), which includes 310 values in total (31 datasets x 10 working channels).
  4. The rule(s) for the applied conditional formatting were arrived at through several iterations of parameters, with final selection qualitative in nature. Conditional criteria are as follows:  
 Green = Mean - StdDev  
 Yellow = Mean + StdDev  
 Red = Mean + StdDev x 3

}}<sup>2(a),(c)</sup>

Table 3-33 Relative comparison of content within frequency ranges of interest (excludes 0-10 Hz), sorted by test series

{{

- Notes: 1. Values listed in the "Overall  $\{\{\}^{2(a),(c)}$ " columns were obtained from Table F-7 (i.e.,  $\{\{\}^{2(a),(c)}$  inclusive, in units of  $\mu\epsilon$ -RMS).
- 2. Other footnotes from Table 3-32 are applicable herein.

$\}^{2(a),(c)}$

Table 3-34 Relative comparison of content within frequency ranges of interest (excludes 0-10 Hz), sorted by test series

{{

}}<sup>2(a),(c)</sup>

- Notes:
1. Values listed in the "Overall {{{<sup>2(a),(c)</sup>" columns were obtained from Table F-7 (i.e., {{{<sup>2(a),(c)</sup> inclusive, in units of  $\mu\epsilon$ -RMS).
  2. Flow rates listed above represent an average of the values listed in Table 3-26 for applicable datasets, similar to the representation in Table 3-31.
  3. Other footnotes from Table 3-32 are applicable herein.

{{

}}<sup>2(a),(c)</sup>

Figure 3-107 Scatter plot of peak dynamic strain versus flow rate

{{

}}<sup>2(a),(c)</sup>

Figure 3-108 Spectral comparison, 0-50 Hz, datasets D5 versus G5, Column-3 sensors



{{

}}<sup>2(a),(c)</sup>

Figure 3-109 Spectral comparison, 0-50 Hz, datasets D6 versus G6, Column-5 sensors

Observations on the TF-2 data evaluation are summarized below:

- Data was acquired at various primary and secondary-side conditions, as documented in Table 3-26. The length of each waveform recording ( $\{\{ \quad \}^{2(a),(c)}$  seconds) was insufficient to effectively characterize the frequencies of interest given the random variations present in typical FIV data. This concern is most-pronounced at low frequencies.
- Channels S03 and S04 (Column-1, Upper Location) were inoperable for the evaluated test data.
- The sensor locations with respect to the nearest supports (Table 3-25) are not ideal from the standpoint of measuring maximum bending strains; many of the sensors are near the neutral-strain point for a fixed-fixed or pinned-pinned beam. That said, any significant response that is present (such as FEI) should still be plainly visible.
- A mid-span measurement of  $\{\{ \quad \}^{2(a),(c)}$  would represent approximately  $\{\{ \quad \}^{2(a),(c)}$  of displacement for a representative tube. This static deflection correlation may be extended to vibration at a primary driving frequency, such as that which would be expected from significant FEI excitation. As shown in Table 3-29, the peak value observed during FEI testing was  $\{\{ \quad \}^{2(a),(c)}$ , and the average value was below  $\{\{ \quad \}^{2(a),(c)}$ . Furthermore, the reported values represent a composite overall and values at individual frequencies are much lower. The maximum observed single-frequency peak was  $\{\{ \quad \}^{2(a),(c)}$  and on average, the maximum across the datasets and channels was  $\{\{ \quad \}^{2(a),(c)}$ . Reported value applies for frequencies greater than  $\{\{ \quad \}^{2(a),(c)}$ . Responses at low frequencies exhibited significant variation between datasets and it is not possible to establish bounding amplitudes considering the short duration of the recorded waveforms. The low amplitude of individual frequency peaks versus composite overalls suggests that the primary excitation on the TF-2 tubes was broad-band in nature, presumably due to general flow turbulence or buffeting.
  - The resultant value of  $\{\{ \quad \}^{2(a),(c)}$  within the example calculation corresponds to a Displacement/Diameter ratio of approximately  $\{\{ \quad \}^{2(a),(c)}$ , or displacement of  $\{\{ \quad \}^{2(a),(c)}$  in metric units. Comparing these values to several of the aforementioned literature sources, a measured strain of  $\{\{ \quad \}^{2(a),(c)}$  peak falls at the extreme lower end of most published test data.
- RMS frequency spectra were generated to compare the responses on each individual channel with respect to test series or primary flow. The plots contained in Appendices B through E were reviewed for significant content and the following frequencies were consistently observed:
  - $\{\{ \quad \}^{2(a),(c)}$ : low-frequency content that appeared to be present only during test series with secondary-side flow (i.e., C and G). Figure 3-108 and Figure 3-109 contain additional spectral comparisons for select datasets and sensors that exhibited responses in this realm.
  - $\{\{ \quad \}^{2(a),(c)}$ : presumed to be horizontal-plane, first-mode bending.
  - $\{\{ \quad \}^{2(a),(c)}$ : presumed to be first-mode bending about the vertical axis.
  - $\{\{ \quad \}^{2(a),(c)}$ : prominent group of peak(s) present in most datasets; does not specifically match an assumed modal response; may be an upper-order mode.

- $\{\{ \quad \}\}^{2(a),(c)}$  prominent peak present in many datasets; does not specifically match an assumed modal response; may be an upper-order mode.
- None of the observed frequencies align with potential sources of mechanical excitation. Specifically, the tubing does not appear to contain content at the driving pump(s) vane passing frequencies. Therefore, the observed peaks were determined to be structural responses, indicative of first-mode bending, as well as upper-order complex modes.
- Appendices D and E provide spectra plotted to 1,000 Hz. These plots were reviewed and compared against the PSD results from TF-1 to determine whether the notable secondary-side response between  $\{\{ \quad \}\}^{2(a),(c)}$  is also evident in the TF-2 data. Although several peaks are evident at specific frequencies (as noted above), none of the TF-2 data exhibited a broad-band response such as that observed in the TF-1 data. It is concluded that the  $\{\{ \quad \}\}^{2(a),(c)}$  secondary-side response was either not present within TF-2, or present but not strong enough to induce a global structural response of the HCSG tubing.
- Frequency-bin-specific RMS values were computed (Appendix F) and collated (Table 3-32 and Table 3-33) to illustrate where variation exists in the data. Based on review of those tables:
  - The spectral plots do contain evidence of the first-mode bending peaks for the tubing; namely, responses at approximately  $\{\{ \quad \}\}^{2(a),(c)}$  are visible in select plots. The amplitude of these responses is small, typically on the order of  $\{\{ \quad \}\}^{2(a),(c)}$ , indicating that large motions of the tubing center-spans is not occurring.
  - The variation responses within the FEI frequency ranges of interest are somewhat random. In general, the data appears to illustrate a slightly-increasing trend with primary flow, which is expected. In certain cases, the maximum values occurred during datasets with less-than-maximum primary flow. This can be observed from Table 3-34 in the response within the  $\{\{ \quad \}\}^{2(a),(c)}$  band for sensor S07.
  - The low-frequency responses ( $\{\{ \quad \}\}^{2(a),(c)}$ ) are only visibly significant for datasets with secondary-side flow, in particular for test series G (boiling conditions). This is readily-apparent from Table 3-32, but also evident within the overalls (Table 3-28 through Table 3-31) and spectral comparisons (Appendices B and C). Figure 3-108 and Figure 3-109 further illustrate this phenomenon by comparing select datasets and sensors within test series G to corresponding data from test series D (stagnant secondary flow).
    - Review of the raw waveforms (refer to the inlays in Figure 3-108 and Figure 3-109 for examples) suggest that the observed response is a physical effect measured by the strain gauge sensors, not a signal anomaly or sensor malfunction. The effect is consistently apparent within the “lower” sensor locations (those closer to the FW plenum), which suggests that it may be a function of secondary-side excitation. The responses in question were most pronounced within test series G (secondary-side boiling), even compared to test series C (single-phase flow, roughly six times the mass rate as series G), suggesting that the effect is exacerbated by elevated temperatures or fluid phase changes.
    - The truncated  $\{\{ \quad \}\}^{2(a),(c)}$  recordings are insufficient to allow for consistent characterization of the low-frequency responses. For example, it is

unclear whether the large spike observed in S05/S06/S09/S10 near the start of both the G5 and G6 datasets is a one-time or repeating event. Based on the limited data available, it appears that the observed response was generally between  $\{\{ \quad \quad \quad \}^{2(a),(c)}$ .

- The single-tube modal results do not exhibit a frequency below  $\{\{ \quad \quad \quad \}^{2(a),(c)}$ : the fundamental breathing mode of the helix is  $\{\{ \quad \quad \quad \}^{2(a),(c)}$ , which is not expected to be excited by primary-fluid flow. Thus, the observed low-frequency response is likely a combined structural mode of the TF-2 tubing and support configuration.

Based on the data evaluation herein, including the observations above, FEI excitation of the HCSG tubes did not occur throughout the entirety of TF-2 FEI testing. This conclusion is largely based on the lack of amplification of responses within the assumed primary bending mode frequency ranges and is further reinforced by the low levels measured across the entire frequency span of interest. If FEI were present, one would expect to see a significant increase or emergence of sharp peaks in the first-mode bending frequency range ( $\{\{ \quad \quad \quad \}^{2(a),(c)}$ ). Table 3-33 shows that the actual FEI data contains no such amplification; values generally trend upward with flow, but in some cases even decrease at the maximum primary flow rates. Figure 3-107 plots the data from TF-2 and it is clear that an exponential increase in vibration levels at higher flow rates was not observed, as would be the case if the critical velocity were reached. Furthermore, the points at which elevated vibration levels were observed at elevated flow rates can be correlated to the low-frequency, secondary-side effect noted above. Even after accounting for a sub-optimal test setup (TF-2 size limited to Columns 1-5, i.e., shortest spans,  $\{\{ \quad \quad \quad \}^{2(a),(c)}$  recording length, and sensor locations), the lack of first-mode response escalation indicates the fully-prototypic HCSG design is not susceptible to FEI excitation within its normal operating parameters.

### 3.4 TF-3 Build-out Modal Testing

For CVAP validation testing, NuScale has elected to construct the prototypic test facility (TF-3) with five tube columns of identical geometry as Columns 9 through 13 of the fully-prototypic design.

At the time of the build-out modal testing, TF-3 was partially constructed, with two tube columns complete: Column-13 (outermost) and Column-12. Each column is divided into four plenums, each of which contains sixteen 304/316 stainless steel tubes (64 total tubes per column). The spacing and overlap of the tubes are such that access to the Column-13 tubes is extremely limited; therefore, the in-situ testing was focused on the accessible Column-12 tubes. The HCSG was positioned in a horizontal orientation that could be manipulated to adjust the relative position and azimuth of the tubes, plenums, and supports. Each tube has a  $\{\{ \quad \quad \quad \}^{2(a),(c)}$  OD and  $\{\{ \quad \quad \quad \}^{2(a),(c)}$  wall thickness. Tube spans between supports for Column-12 are approximately  $\{\{ \quad \quad \quad \}^{2(a),(c)}$  (long span) and  $\{\{ \quad \quad \quad \}^{2(a),(c)}$  (short span), with an approximate tubing weight of  $\{\{ \quad \quad \quad \}^{2(a),(c)}$ .

Testing was targeted at the accessible Column-12 tubes, ranging from the “bottom” of the HCSG (denoted Span A, FW inlet) to the “top” (Span AD, MS outlet). The in-situ testing was primarily a discovery task, intended to inform approach and parameters for future

regimented testing. As such, emphasis was placed on testing a multitude of span, support, and sensor variations, with less emphasis on repeatability and like-for-like comparisons between spans. Nonetheless, efforts were focused toward consistent, accurate determination of the following variables:

1. Modal parameter estimations including
  - a. Natural frequency
  - b. Damping
  - c. Mode shape(s)
2. Excitation methods
3. Effects of boundary conditions
4. Measurement and signal fidelity

A general overview of the HCSG test setup is shown in Figure 3-110, with annotations detailing terminology used throughout the remainder of this report. The sensing chain used for acquisition and analysis is documented in Table H-1.

The general nomenclature used for the test IDs includes a group to identify the sensor(s) azimuth and plenum (accounting for rotation of the pressure vessel), spans, identified as segments between supports (starting with Span A/FW plenum and progressing through Span AD/MS plenum), and the general impact location/direction. These references were modified slightly throughout testing to capture varying conditions and lessons learned, and are specifically denoted in the notes below the tables and figures herein.

The individual tests were categorized into six groups by the unique test configuration. These configurations represent unique tubes, spans, and/or components that were tested and can be summarized by the following:

- A. Single Spans – Single Accelerometer
- B. Span C – (5) Accelerometers
- C. Multi-span (C through G) – Single Accelerometer per Span
- D. Plenum transitions Span A (FW-side) and Span AD (MS-side) – Multiple Accelerometers
- E. Support and Tube Testing
- F. Support Only

Note: the testing conducted as part of Group E included characterization of responses from both support(s) and tubing. Upon further analysis, these responses offered sufficient characterization of lower-frequency modes impacting the supports, such that the Group F tests could be regarded as redundant. Therefore, the Group F data is not analyzed further.

{{

}}<sup>2(a),(c)</sup>

Figure 3-110 General layout of helical coil steam generator prototype for vibration testing

### 3.4.1 Data Acquisition and Test Methods

Modal testing to characterize the HCSG tubing and support parameters was conducted n impulse excitation from an instrumented hammer with various accelerometer configurations to measure the ensuing response(s). The vibration data was recorded primarily in the frequency domain and for select tests, in the time domain. The following acquisition parameters were used:

Table 3-35 Acquisition parameters for time and frequency domain

Domain	No. Samples	Resolution	Ending Time	Linear Averages
Time (sec)	{{			}} <sup>2(a),(c)</sup>
Frequency (Hz)	{{			}} <sup>2(a),(c)</sup>

During the acquisitions, a force (impact hammer) and exponential window for the input was applied. The force window value was assigned unity over the leading five percent of the time record following the initial impulse trigger, followed by a cosine taper to zero for the remainder of the time record (eliminating noise). An exponential window was also applied and set to unity (identical to that applied to the response accelerometers) for the frequency domain calculations. Because the exponential window was set to 1.0 at the end of the acquisition (i.e., no amplitude effect), no corrections for damping are needed as the force/input signal was unaltered for the period of application. Frequency response functions (FRFs) were calculated by the Fourier spectrum of the acceleration response divided by the Fourier spectrum of the excitation force (impact hammer). Four FRF averages from four separate impacts were used to calculate these results; this number of averages was determined experimentally, and represents the best compromise for maintaining consistency of response peaks while reducing noise at non-responsive frequencies.

The acquisition duration (typically 4 seconds) and tube damping resulted in a reduction of amplitude to {{ }}<sup>2(a),(c)</sup> of the maximum imparted response. This is sufficient to reduce window leakage in FFT computations. Leakage is a signal processing bias error due to the limited definition of a periodic waveform or transient over the sampling period. The error is leaked across spectral lines and over the entire frequency range representing noise and reducing signal-to-noise ratio of the measurement. Given the limited time available, windowing was not completely optimized during this initial testing. Future testing should apply an exponential fit that can be used to define a time constant/end value of the exponential window to improve the overall signal-to-noise ratio (especially for less predominant modes).

A soft hammer tip with a mass extender was used for excitation. The soft tip is used to spread the force energy (pulse width) over a longer time and excite lower frequencies. The combination of hammer tip and impulse energy (mass extender, impact velocity) describe the force input used for modal parameter estimation. Any changes to these variables will affect modal parameter estimation.

Spectral coherence was calculated for each FRF, estimating the relation between two signals (input/hammer vs. the response). These values range from zero to one over the frequency range of interest, where one represents a perfect correlation. Values less than one can be attributed to several factors:

- Anti-resonance locations or locations where the FRF value is close to zero
- Resonance locations (FRF peaks) where the effect of leakage is pronounced. Note windowing reduces leakage and does not eliminate it.

- The measured response contains contributions caused by extraneous noise, non-linearity, or other forces not contained in the measurement input.
- Impact locations/directions were slightly altered between averages.

The coherence metric was used to define various useable frequency ranges for the analysis groups; generally, values greater than  $\{\{ \quad \}^{2(a),(c)}$  were considered acceptable.

Modal parameters, especially when used for analytical modes, are considered global structure properties. However, the tube and HCSG support structure has a combination of local and global modes. The local modes or those specific to a span have difficulty transferring across a sufficiently stiff boundary. These modes typically require local excitation and measurement to characterize, similar to the single span testing. For multi-span, tube and component testing, the stiffness of this boundary or tightness of supports change between each span and each support from fixed to relatively free. This results in varying levels of energy transfer across these boundaries and the measurement of both local and global modes between supports, tubes, and spans.

Mass loading of the structure can affect modal parameter estimation. The weight of an individual accelerometer used for this testing is  $\{\{ \quad \}^{2(a),(c)}$  ounces and the cable is  $\{\{ \quad \}^{2(a),(c)}$  (not including conductor). This compares to about  $\{\{ \quad \}^{2(a),(c)}$  percent mass loading across a long span for a single accelerometer (most tests herein) and between  $\{\{ \quad \}^{2(a),(c)}$  percent for five accelerometers (depending on the cable length left suspended). This effect will be discussed further when using multiple accelerometers to characterize a mode.

### 3.4.2 Analytically Predicted Modes

Section 5.1.2 contains a summary of modal predictions for Columns 9 and 13 (innermost and outermost of the TF). These modes are summarized below for comparison to the ensuing results presented herein. The lower end of the range represents the frequency for Column 9 and the upper end of the range is the frequency for Column 13.

- Highest mass participation in the vertical direction
  - $\{\{ \quad \}^{2(a),(c)}$  (pinned boundary conditions)
  - $\{\{ \quad \}^{2(a),(c)}$  (fixed boundary conditions)
- Highest mass participation in the horizontal direction
  - $\{\{ \quad \}^{2(a),(c)}$  (pinned boundary conditions)
  - $\{\{ \quad \}^{2(a),(c)}$  (fixed boundary conditions)

For the in-situ testing that was conducted, there is good agreement for the first predominant mode in the vertical direction, which is more closely approximated by a fixed boundary condition (generally reported herein in the  $\{\{ \quad \}^{2(a),(c)}$  range). Similarly, the predominant horizontal mode from testing was most often present in the  $\{\{ \quad \}^{2(a),(c)}$  range.



### 3.4.3 Frequency Response Function Analysis

Table H-1 summarizes testing parameters, sensor locations, and configurations used during the acquisition. FRF calculations from 0-400 Hz for each group of tests is provided in Figure H-1 through Figure H-31 of Appendix H. The following sub-sections discuss the FRF results for each of the groups.

#### Group A: Single Span – Single Accelerometer

On the first day, several initial tests were conducted on individual tubes, altering various acquisition parameters to identify an acceptable set for repeat testing. A typical acquisition is as demonstrated in Figure 3-111 for these tests. A subset of tests was selected for this group to illustrate the analysis over a simplified number of responses.

A single long span (Span C, first long span after FW plenum) was tested, with the resulting FRF shown in Figure 3-111. The FRF and coherence is overlaid to demonstrate a spurious response (highlighted in yellow) along with the evident response peaks ( $\{\{ \}^{2(a),(c)}$ , highlighted in gray). The FRF response is also slightly skewed, especially at the lower frequency peak. Both effects are indications of non-linearity. This is also likely an effect of multiple closely-spaced modes, as detailed in Group B test responses (refer to the following section).

Another test was conducted to enhance the resolution of mode shapes using a roving response test and Maxwell's reciprocity. Twelve roving FRF measurements along a single span are shown in Figure 3-112 using a single impact location. The use of reciprocity and roving to define a mode shape assumes the structure is dynamically symmetric. The combination of mass loading (albeit to a lower extent) and non-linearity negated the principals assumed for reciprocity, with the peaks shifting between measurements. For this reason, roving response tests were not used for further analysis, and are not recommended for any subsequent testing.

Use of non-tubing impact excitation locations (e.g., supports) and reduced acquisition periods (i.e., one second) allowed for further characterization of lower frequency modes. The reduction in the acquisition period (from  $\{\{ \}^{2(a),(c)}$ ) reduces the averaged noise (if present) in the signals and computed FRFs, but also adversely affects the frequency resolution (increased bin sizes from  $\{\{ \}^{2(a),(c)}$ ), which, in turn, affects the accuracy of damping calculations in the frequency domain such as half-power. As shown in Figure 3-113, a  $\{\{ \}^{2(a),(c)}$  mode (normally where low coherence prevents characterization) was captured using a smaller time window to reduce the noise following the transient. It is not clear if the removal of the ring supports for this test also affected the improved coherence at lower frequencies. The discussion of Group E will also describe the lower modes excited from support locations.

The variation of responses along spans is evident throughout the testing where various modes became difficult to excite repeatedly. Variation was mainly attributed to the boundary conditions (HCSG support tightness ranged from fixed to some variety of pinned), impact energy (direction/magnitude), and non-linearity. Not all modes were excited and in general the lower frequency modes (below  $\{\{ \}^{2(a),(c)}$ ) were the most difficult to excite consistently.

{{

}}<sup>2(a),(c)</sup>

Figure 3-111 Typical single, long span vertical; frequency response function (blue) and coherence (orange)

{{

}}<sup>2(a),(c)</sup>

Figure 3-112 Frequency response function response for roving accelerometer along single span (mass loading)

{{

}}<sup>2(a),(c)</sup>

Figure 3-113 Lower frequency response (below 25 Hz); frequency response function (blue) and coherence (orange)

**Group B: Span C – Five Accelerometers**

This group of tests entailed instrumentation of one span (Span C, first long span after FW plenum) with five equally-spaced accelerometers. The span was rotated during the tests from a bottom-azimuth orientation (4:00-5:00), to the side (2:30-3:30), and the top (11:30 to 12:30). The primary purpose of this test group was to determine the effects of varying boundary conditions based on vessel rotation/azimuth (i.e., compression applied by support rings), and allow for improved mode shape characterization by multiple accelerometer locations.

Generally, there were three frequency response ranges of interest: {{  
}}<sup>2(a),(c)</sup>. Rotation of the RPV or HCSG caused a slight shift among the responses. Shifts within the FRF peaks were mostly bounded within {{  
}}<sup>2(a),(c)</sup> (depending on the mode). The lower frequency modes (between {{  
}}<sup>2(a),(c)</sup>) were predominantly in the vertical direction, while the largest-amplitude FRF responses were in the horizontal direction (between {{  
}}<sup>2(a),(c)</sup>). The location of the impact (near each end and mid-span A summary of the FRF results during this testing are shown in Table 3-36 and the FRFs are plotted for each test in Appendix H, Figure H-3 through Figure H-13.

Impact locations mid-span produced improved characterization for the first predominant mode and impact locations near the ends of the span offered the best characterization across the upper modes. The latter is demonstrated by a mid-span and end-impact for tests 1A-3Z and 1A-5Z. Additionally, the direction of the impact improves the

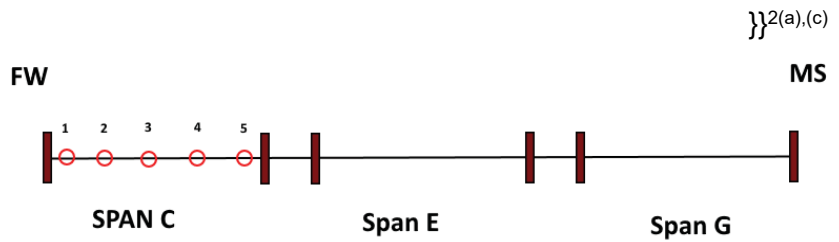
characterization for predominant horizontal and vertical modes, however, both impact directions result in detecting the same modes. The improved characterization is a result of a majority of the overall energy imparted into the tube directed along the impact axis (e.g., y-vertical, z-horizontal), resulting in a higher signal-to-noise ratio of the responses for modes predominant in the impact direction.

The coherence between the input and output were generally calculated above 0.9 over the frequency range of  $\{\{ \}^{2(a),(c)}$  as shown in Figure 3-114 (below).

Table 3-36 Group B, span C (5) accelerometers

$\{\{$

Notes: 1. Test ID references "azimuth of Span C, 1A 6:00, 1C-3:00, 1E-12:00"-sensor (1, 2, 3, 4, 5) impacted and direction (y-vertical, z-horizontal).



{{

}}<sup>2(a),(c)</sup>

Figure 3-114 Coherence only for test 1C-1Z (horizontal/1Z and vertical/3Y direction)

{{

}}<sup>2(a),(c)</sup>

Figure 3-115 Impact location effects on Span C (left: mid-span; right: near end of span)

Note for Figure 3-115: Both impacts measured all five locations and the impact was imparted in the horizontal direction at two locations, midspan (location 3) and near the support (sensor location 5).

### Group C: Multi-span (C through G) – Single Accelerometer per Span

This group of tests entailed instrumentation/characterization of five spans (C, D, E, F, and G), each with a single accelerometer mounted mid-span. Spans D and F represent a “short” span ( $\{\{ \quad \}^{2(a),(c)}\}$ ) whereas Spans C, E, and G are “long” spans ( $\{\{ \quad \}^{2(a),(c)}\}$ ). The set of spans was also rotated from an azimuth where Span C was orientated at 06:00 (BDC) and Span G was at 12:00 (TDC) to where Span C was oriented at 09:00 and Span G was at 03:00. The primary purpose of this group of testing was to determine the effects of changing boundary conditions through rotation and the variations in local modal parameters between like spans.

Generally, two modes were present in the first orientation ( $\{\{ \quad \}^{2(a),(c)}\}$ ). Excitation was limited to the longer tubes with no consistent presence or dominating frequency between the long spans and short spans. These frequencies increased ( $\{\{ \quad \}^{2(a),(c)}\}$ ) during rotation elevating to ( $\{\{ \quad \}^{2(a),(c)}\}$ ). Both lower modes were clearly responding for each long span with the lower mode mostly clearly represented from Span E impacts. It is unclear if the two modes were influenced by boundary conditions as the end conditions were quite similar among the spans. The lower modes ( $\{\{ \quad \}^{2(a),(c)}\}$ ) were predominant in the vertical direction for this testing.

The next set of predominant modes was at ( $\{\{ \quad \}^{2(a),(c)}\}$ ); these also shifted by 2 Hz after the rotation. The last set of modes near ( $\{\{ \quad \}^{2(a),(c)}\}$ ) (predominant within a group of closely spaced modes) was shifted by approximately ( $\{\{ \quad \}^{2(a),(c)}\}$ ) upon rotation. The mid-span location demonstrated primarily vertical predominant modes over these upper frequency ranges.

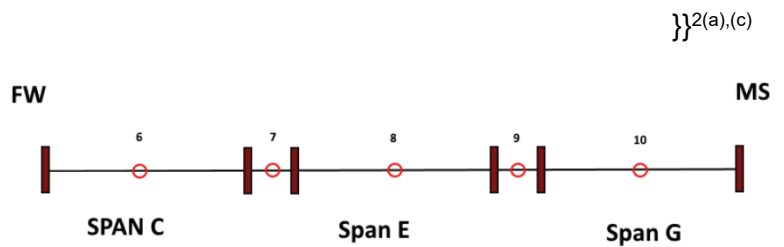
A separate test was also conducted within Span E (3C-EmsZ), where tubes 2, 6, 10, and 14 were tested with single mid-span accelerometers, impacting tube 6. The first mode frequencies ranged from ( $\{\{ \quad \}^{2(a),(c)}\}$ ). A single tube excitation was effective in exciting the first mode in adjacent tubes, albeit with elevated noise and elevated modes were no longer discernable.

A summary of the FRF results during this testing are shown in Table 3-37 and the FRFs are plotted for each test in Appendix H, Figure H-13 through Figure H-21.

Table 3-37 Group C, multi-span

{{

Notes: 1. Test ID references  
“azimuth of Spans, 2A (C-12:00, G-6:00), 2C (C-9:00, G-3:00), 3C (E-12:00)”-“Impacted Span on FW or MS side of span in the z-horizontal direction).”



The coherence between the input and output were generally calculated above  $\{\{ \quad \}\}^{2(a),(c)}$  over the frequency range of  $\{\{ \quad \}\}^{2(a),(c)}$ , as exemplified by Figure 3-116.

$\{\{$

$\}\}^{2(a),(c)}$

Figure 3-116 Coherence only for test 2A-EfwZ (vertical and horizontal direction)

The majority of FRF peaks are present not only in one FRF or span, but across each of the individual spans, even though each span exhibits localized modes (long and short spans). The energy transfer across spans (cross-communication) was investigated using both the FRF magnitude and coherence of the input (hammer) and response signals on each span. From a single test impacting the center span of Span E, two modes were excited ( $\{\{ \quad \}\}^{2(a),(c)}$ ). From this test alone, it is unclear which mode is local to Span E or if both are local. As shown in Table 3-38, the first predominant mode at  $\{\{ \quad \}\}^{2(a),(c)}$  is dominate in Span E (impact location) at more than five times the response (g/lbf) of the other responses, but the peak is present in three out of four of the adjacent spans at a reduced magnitude. This FRF peak occurs on similar span lengths (i.e., Spans C, E, G) at  $\{\{ \quad \}\}^{2(a),(c)}$  of the impacted span's FRF response magnitude, which suggests a similar local mode is present along the spans although not properly excited. For the  $\{\{ \quad \}\}^{2(a),(c)}$  peak there is clearly amplification on Span G (FRF magnitude six times that of Span E) and very slight amplification on Span C (albeit with low coherence) indicating a clear resonance near this frequency for Span G. The presence of local modes specific to a span and the identification of modes cross-communicating from adjacent spans is only clear when analyzing the FRFs across multiple spans in a single test. The ambiguity in response (i.e., multiple closely spaced peak responses at each sensor) is more clearly identified by local exaction to each span while measuring adjacent spans.



Utilizing Figure 3-117 (below), three FRFs for each span are provided for three impact locations (Span E, top left; Span C, top right; Span G, bottom right). All five span responses are plotted for each impact (C, D, E, F, and G) varying by color. Coherence is plotted for the Span E impact test (lower left). From these tests it becomes apparent there are multiple closely-spaced modes between  $\{\{ \quad \}\}^{2(a),(c)}$  which are not easily distinguished in these tests. For Span E, there is a predominant mode at  $\{\{ \quad \}\}^{2(a),(c)}$ . For Span G, the predominant mode is at  $\{\{ \quad \}\}^{2(a),(c)}$ . A comparison of boundary conditions between spans does not explain the differences in the predominant mode responses. The HCSG supports are relatively the same tightness for Span C and Span E (cumulative relative tightness of 5), while Span G was slightly looser (cumulative tightness of 6. Each end of the span was tested by hand to determine the relative tightness of the support on a scale of 0-5, where 0 was nearly a fixed boundary and 5 was very loose. The algebraic sum from each end of the span is reported here as the cumulative tightness.). Although clear peaks in the FRF response can be seen from Spans E and G (whether they were impacted directly or not), The Span C response was much less clear or pronounced and even when impacted directly (upper right plot, Figure 3-117), poor responses were measured. This span would require additional testing to fully characterize the FRF response and it appears the span was not properly excited with cross-communication from modes on Span E and Span G dominating the response. In addition, modes below 140 Hz were not excited on short spans (D and F), which may be because of lack of excitation local to each span (i.e., impacts were only completed on long spans).

Table 3-38 Energy transfer across spans

{{

}}<sup>2(a),(c)</sup>

- Notes: 1. Impact location was on FW side of Span E with responses measured across five spans (C, D, E, F, G) by single mid-span accelerometer. FRF magnitude and coherence are provided for this test across two peak FRF responses at  $\{\{ \quad \}\}^{2(a),(c)}$ . The input/output ratio is the ratio of FRF amplitude from Span E (closest to excitation source) to adjacent span FRF responses to quantify amplification and attenuation.

}}

}}<sup>2(a),(c)</sup>

Figure 3-117 2A-EfwZ energy transfer across spans

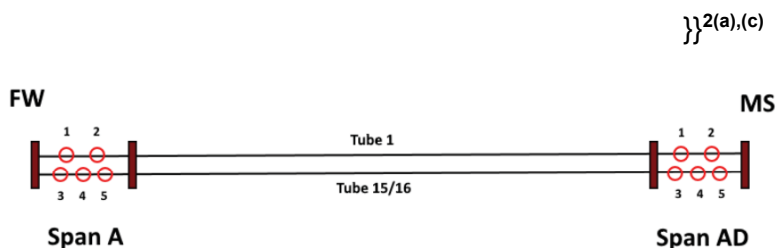
**Group D: End Spans (A and AD) – Multiple Accelerometers**

This group of tests characterized the response of the end spans (transition bends) on both the top and bottom of the HCSG (FW and steam plenums), for the shortest and longest tubes within each of these spans. These spans are fixed on one end (plenum orifice) and supported by the HCSG supports on the other end. The tubes were excited by a hammer impulse on each tube and on the HCSG support. Predominant measured frequencies are summarized in Table 3-39.

Table 3-39 End span (A and AD) frequency response function summary

{{

- Notes: 1. Test ID reference indicates "Span (4A-spanA and 5A-span AD)-"impact sensor and direction." Two sensors were placed on the shorter tube (1) and three sensors were placed on the longer tube span (15 or 16).



Comparing the short sections at each end of the HCSG, the FW side (4A-2Z) shows the predominant responses in the  $\{\{ \quad \quad \quad \}^{2(a),(c)}$  range, whereas the MS side (5A-2Z) shows the first set of predominant frequencies lower ( $\{\{ \quad \quad \quad \}^{2(a),(c)}$  range). This is likely a cause of the boundary conditions where one end is fixed and the other simply-supported end is tighter on the FW side when compared to the MS side. Additionally, the unsupported length of each tube at the transition to the plenums is different, leading to differences in the measured frequencies. A predominant response from the support was also measured at  $\{\{ \quad \quad \quad \}^{2(a),(c)}$  and present on the shorter tube. Using a separate sensor affixed to the support (#6, Test 5A-Support6Z) and impacting that support, the  $\{\{ \quad \quad \quad \}^{2(a),(c)}$  response was clearly evident on the support sensor and through cross-communication was also observed on the shorter tube response (sensors 1 and 2).

Excitation of the support and tube resulted in similar responses in the lower frequency range ( $\{\{ \quad \quad \quad \}^{2(a),(c)}$ ); responses were muted above those frequencies when not directly excited at the tube. The fixed-end on these spans offered very clean responses and high signal-to-noise ratios. All modes were excited in the horizontal direction, which also corresponded to the largest energy response. Coherence between the signals was generally above  $\{\{ \quad \quad \quad \}^{2(a),(c)}$  over the frequencies  $\{\{ \quad \quad \quad \}^{2(a),(c)}$  as shown in Figure 3-118 (below). This coherence plot represents the best input/output relationship among the tests conducted, with a value of nearly 1.0 across the entire frequency range. Also, the plot exhibits little evidence of noise and cross-communication at FRF peaks, and a much more deterministic response below  $\{\{ \quad \quad \quad \}^{2(a),(c)}$ .

{{

}}<sup>2(a),(c)</sup>

Figure 3-118 Coherence only 5A-5Z (horizontal and vertical direction)

Notes: 1. Vertical coherence (4Y, midspan of tube 16) compared with the impact hammer (999Z) and horizontal coherence (5Z, near the first support) compared with impact hammer (999Z).

### Group E: Support and Tube Testing

Group E entailed testing of the HCSG support and tubing as one structure. Seven equally-spaced accelerometers were placed along the vertical axis of a support and mid-span accelerometers were placed on adjacent tubes. This group of tests is unique from other groups in that the support was impacted and used to excite modes within the tubes. In addition, the boundary conditions were unique in that the seven support rings were removed for these tests. The testing configuration is shown in Figure 3-119.

Four tests were conducted, first measuring three adjacent tubes (1, 5, 9) impacting the support in the axial (tube direction) and the horizontal (z-direction). The next two tests instrumented tubes 1, 2, 5, 6, 9, 10, 13, and 14 representing the majority of the sixteen tubes across Span E. In addition, a larger hammer (1 mV/lbf compared to the smaller 5 mV/lbf) was used to excite the tube and support structure. A summary of the FRF results is presented in Table 3-40 for the four tests in this group.

Overall, the signal-to-noise ratio decreased for this testing as the energy transferred through the support to the tubes was as much as two orders of magnitude less than other FRF peaks (FRF peaks on the order of {{ }}<sup>2(a),(c)</sup>). A relatively weak axial tube mode (lowest FRF magnitude of Group E) was detected at {{ }}<sup>2(a),(c)</sup> Hz for the initial axial impact direction (Sup-103 + Col-12, Span E Tub 1+5+9, Impact 1-X) and became less prominent in the second test in the same impact direction (Supp-to-Tube 103 Span E FW-X ) due to elevated noise in the lower frequencies. The FRF magnitude was similar between the support and tube response indicating a global mode. When impacting

in the horizontal direction a  $\{\{ \quad \}\}^{2(a),(c)}$  mode was excited again in the axial direction (Sup-103 + Col-12, Span E Tub 1+5+9, Impact 1-Z) and present in nearly all measurement directions (likely a local mode from the support). In general, axial and horizontal modes were detected at  $\{\{ \quad \}\}^{2(a),(c)}$  across the tests most likely originating as local modes from the support because there was little to no variance for each tube and the magnitude of the FRF response were largest on the support (except for  $\{\{ \quad \}\}^{2(a),(c)}$ ). Most of the tubes tested exhibited predominant vertical modes between  $\{\{ \quad \}\}^{2(a),(c)}$  with some outliers detected up to  $\{\{ \quad \}\}^{2(a),(c)}$ .

Coherence was above  $\{\{ \quad \}\}^{2(a),(c)}$  over the lower frequencies mostly due to the different method of excitation, as shown in Figure 3-120.

$\{\{$

$\}\}^{2(a),(c)}$

Figure 3-119 Support/tube testing configuration

Table 3-40 Support and tube frequency response function summary

{{

}}<sup>2(a),(c)</sup>

{{

}}<sup>2(a),(c)</sup>

Figure 3-120 Coherence for test “Sup-103 + Col-12, Span E tub 1+5+9, impact 1-X”

Notes: 1. Provided in axial (901x-direction), vertical (901y-direction) and horizontal (901z-direction)

### 3.4.4 Damping Estimation

#### 3.4.4.1 Half-power Method for Damping Estimations

A global polynomial curve fit was used to approximate damping using the half-power method. The curve fit was applied over multiple FRFs (all valid sensors per impact test) to calculate a global fit per measurement direction. The fit was applied over discrete frequencies to increase the accuracy of the fit function as shown in Figure 3-121. Figure 3-121 represents the FRF magnitude (g/lbf) in the top plot and the bottom is the imaginary part (log-scale) of the FRF used to identify peaks for fitting. Due to noise within the FRFs, a filter was applied to report damping values greater than {{ }}<sup>2(a),(c)</sup>. The removal of those peaks shifted the average value from {{ }}<sup>2(a),(c)</sup>.

Damping estimations were calculated for each group and represent various FRF peaks. These are plotted in Figure 3-122. The range of damping values is {{ }}<sup>2(a),(c)</sup>. Multiple closely-spaced peaks coupled with non-linear FRF responses resulted in broadening FRF peaks used to calculate damping with the half-power method. This effect is well demonstrated for peak damping values of {{ }}<sup>2(a),(c)</sup> in Figure 3-123.

Based upon the 250 damping values, a 95 percent confidence interval describing the average damping over the reported frequency range using the half-power method is expected to be between {{ }}<sup>2(a),(c)</sup>. Similarly for a 95 percent confidence interval, a single damping value (not an average) from the tube would be expected to fall between {{ }}<sup>2(a),(c)</sup>. Because more impact hammer tests were performed than pull tests, these statistics are skewed towards

representing damping due to small amplitude vibration (TB) rather than the larger amplitude vibration expected from strongly-coupled phenomena such as VS and FEI.

{{

}}<sup>2(a),(c)</sup>

Figure 3-121 Global polynomial curve fit of frequency response functions (top frequency response function magnitude, bottom imaginary magnitude on log-scale)



{{

}}<sup>2(a),(c)</sup>

Figure 3-122 Half-power damping estimations over the frequency response function groups

{{

}}<sup>2(a),(c)</sup>

Figure 3-123 Peak damping values ({{  
}}<sup>2(a),(c)</sup>:1A-3Z-right}}<sup>2(a),(c)</sup>:1C-1Y-left and {{

### 3.4.4.2 Exponential and Log-decrement Methods

In addition of the half-power methods, the exponential and log-decrement methods are also assessed.

#### Exponential Fit

An exponential curve is fitted to subsets of the 45 positive peaks. The exponential fit assumes a decay of the positive peaks in the form of  $e^{-\zeta\omega_{ne}t}$  where  $\zeta$  is the damping ratio,  $\omega_{ne}$  is the estimated natural frequency of the considered data, and  $t$  is time. Subsets of the positive peaks are used to calculate the exponents coefficient. The subsets include

positive peaks in groups of 5, 9, 13, 17, and 21 positive peaks per data block. These are referred to as “runs” in the following text. For each of these runs, an exponential fit is performed starting with the first peak (i.e., 1 of 45) and the exponential coefficient ( $-\zeta\omega_{ne}$ ) recorded. The run is then shifted to the second positive peak (i.e., 2 of 45) to calculate a new exponential coefficient, then the third peak, and so on. The calculated exponential coefficient is divided by the runs corresponding natural frequency estimate to determine a damping ratio estimate. Because the natural frequency may change with amplitude the natural frequency estimate for each run is calculated as

$$\omega_{ne} = \frac{2\pi(N \text{ Cycles})}{\text{Time}_{\text{Peak(Final)}} - \text{Time}_{\text{Peak(Initial)}}} \quad \text{Equation 3-38}$$

By developing a damping ratio estimate at various initial peaks, an amplitude dependent damping ratio estimate can be obtained.

### Logarithmic Decrement

The logarithmic decrement is calculated as:

$$\delta = \frac{1}{N} \ln \left( \frac{x_i}{x_{i+N}} \right) \quad \text{Equation 3-39}$$

where  $\delta$  is the logarithmic decrement,  $x_i$  is a maxima free vibration displacement amplitude (i.e., one of the 45 positive peaks), and  $x_{i+N}$  represents the maxima free vibration displacement amplitude measured  $N$  periods from  $x_i$ . The damping ratio is then written as:

$$\zeta = \frac{\delta}{\sqrt{4\pi^2 + \delta^2}} \quad \text{Equation 3-40}$$

The damping ratio is calculated for an array of initial peaks and subsequent peaks (i.e., the  $N$ s).

The exponential fit and logarithmic decrement damping estimates from three processed displacement time histories are overlaid and shown in Figure 3-124. The three displacement time histories come from the 315-12-1-C-6 (5y) time ({{ }}<sup>2(a),(c)</sup> filter), 2A-EfwZt\_8Y ({{ }}<sup>2(a),(c)</sup> filter), and 2A-GfwZt\_10Y ({{ }}<sup>2(a),(c)</sup> filter) data sets. Note the frequency range of interest for the three data sets centered around {{ }}<sup>2(a),(c)</sup>. The three impact tests are bounded by tube displacements less than 2.5 mils. The majority of oscillations used for damping calculations are less than 1 mil. These amplitude ranges are expected to be most representative of the TB mechanism.

The data shown in Figure 3-124 is the raw data from both the exponential fit and logarithmic decrement. As such, it contains various  $N$  values because each  $N$  value for a time history is associated with an amplitude value. The damping values in Figure 3-124 that are significantly above or below the mean (Figure 3-125) are generally due to low  $N$  values. The negative damping values in both the exponential fit and logarithmic decrement methods (Figure 3-124, Figure 3-126, and Figure 3-127) are attributed to filtering, which resulted in positive peaks having lower displacement amplitudes than the subsequent peaks. The damping ratios greater than 1.5 percent correspond to the amplitudes associated with  $N=1$  and  $N=2$ .

}}

}}<sup>2(a),(c)</sup>

Figure 3-124 Amplitude-dependent damping from three time histories (raw): exponential fit – blue; log dec – red

### 3.4.4.3 Amplitude Dependency

Three vibration mechanisms are prone to the HCSG tube design include buffeting, VS, and FEI. These mechanisms are expected to manifest at differing amplitudes if excited during operation. Ranking the mechanisms from the expected smallest amplitude to the largest: TB, VS, FEI. Amplitude dependency was not a specific focus of the initial testing. The various tests were post-processed into displacement units and a best effort was applied to evaluate the effect of amplitude dependency.

Figure 3-125 shows a processed version of the data from Figure 3-124 where the damping estimates at each amplitude are averaged and then plotted. For example, the 20 logarithmic decrement damping estimates for a given displacement amplitude are averaged together and the average is plotted. There is a clear trend of damping increasing with response amplitude for both methods.

{{

}}<sup>2(a),(c)</sup>

Figure 3-125 Amplitude-dependent damping from three time histories (averaged): exponential fit – blue; log dec – red

While most of the data was collected with an impact hammer one pull test was performed, and the output recorded. The tube was physically displaced by hand, released, and allowed to undergo free vibration.

A plot of displacement amplitude versus damping using the exponential fit and logarithmic decrement methods are shown in Figure 3-126. Figure 3-127 overlays the damping data from the pull test to the damping data to the three previously discussed time histories. Peak displacement responses used for damping are roughly {{ }}<sup>2(a),(c)</sup> mils and represent the largest damping values calculated, up to {{ }}<sup>2(a),(c)</sup>. Figure 3-127 shows that even neglecting the first {{ }}<sup>2(a),(c)</sup> positive peak data points from the pull test (starting near {{ }}<sup>2(a),(c)</sup>), the pull test indicates more damping than the three tests noted above.

{{

}}<sup>2(a),(c)</sup>

Figure 3-126 Amplitude-dependent damping from pull test: exponential fit – blue; log dec – red

{{

}}<sup>2(a),(c)</sup>

Figure 3-127 Amplitude-dependent damping: pull test – black and grey; impact tests – red and blue

### 3.4.5 Mode Shapes

A geometry file of a single tube and HCSG supports was used to evaluate specific mode shapes for Group B (Span C). Group B was chosen because it was unique in providing five measurement locations to fully define mode shapes, whereas other tests specifically focused on FRF responses with a single mid-span location. An overview of the five locations and FRFs used is provided in Figure 3-128. For the mode shapes, points between the measurements were interpolated and the points on the end ( $\{\{\}^2(a),(c)\}$ ) were fixed. There are three frequency regimes of interest near  $\{\{\}^2(a),(c)\}$ . The first mode analyzed is predominant in the vertical direction. The second and third modes are most predominant in the horizontal directions while still contributing slightly in the vertical direction.

The first predominant mode is represented as multiple, closely-spaced peaks within in the FRF. Two modes were chosen to evaluate the mode shapes: 1)  $\{\{\}^2(a),(c)\}$  representing a broad smooth peak, and 2)  $\{\{\}^2(a),(c)\}$  representing a sharp FRF peak. The mode shapes (shown both deflected and non-deflected) are provided in Figure 3-129 and Figure 3-130. These figures show very similar mode shapes between the closely-spaced modes predominant motion in the vertical directions and much less pronounced motion horizontally. In addition, very little motion is occurring in the axial direction. These modes most closely represent the first bending mode of a simply supported or fixed-beam.

The second predominant mode near  $\{\{\}^2(a),(c)\}$  represents the largest FRF response. Again, multiple peaks are present near this mode as closely-spaced modes. A predominant horizontal mode is shown in Figure 3-131. This mode is best characterized as a second bending mode of a beam with the mid-point relatively motionless.

The third predominant mode near  $\{\{\}^2(a),(c)\}$  is one of many peaks between  $\{\{\}^2(a),(c)\}$ . This peak was chosen consistent with its relative response in all directions. The predominant horizontal mode shape is shown in Figure 3-132. The mode is best characterized as a third bending mode of a beam with two inflection points.

Because a single test (1C-1Z) was used to develop the mode shapes, a comparison to another test (1A-5Z) was used to quantify variability. Figure 3-133 shows two mode shapes for qualitative comparison. These shapes are very similar even at two frequencies and two different tests ( $\{\{\}^2(a),(c)\}$ ). A quantitative evaluation using a modal assurance criterion (MAC) value demonstrates very consistent mode shapes (MAC value  $\{\{\}^2(a),(c)\}$ ). A MAC value is a statistical indicator for correlating the complex vectors for nodes pairs between two tests (amplitude and phase). The indicator is most sensitive to large differences and relatively insensitive to small differences in mode shapes making it ideal for use in empirical testing. The numeric correlation is bounded between 0 and 1, with 1 indicating fully consistent mode shapes. A value near 0 indicates the modes are not consistent.

{{

}}<sup>2(a),(c)</sup>

Figure 3-128 1C-1Z, Span C, 5 accelerometers (frequency response function, axial-red, vertical-green, horizontal-blue)

{{

}}<sup>2(a),(c)</sup>

Figure 3-129 Mode shape for 1C-1Z at {{ }}<sup>2(a),(c)</sup>

{{

}}<sup>2(a),(c)</sup>

Figure 3-130 Mode shape for 1C-1Z at {{ }}<sup>2(a),(c)</sup>

{{

}}<sup>2(a),(c)</sup>

Figure 3-131 Mode shape for 1C-1Z at {{ }}<sup>2(a),(c)</sup>



{{

}}<sup>2(a),(c)</sup>

Figure 3-132 Mode shape for 1C-1Z at {{ }}<sup>2(a),(c)</sup>

{{

}}<sup>2(a),(c)</sup>

Figure 3-133 Comparison of mode shapes between 1C-1Z ({{ }}<sup>2(a),(c)</sup>) and 1A-5Z ({{ }}<sup>2(a),(c)</sup>) using modal assurance criteria

### 3.4.6 Build-Out Modal Testing Conclusions

Five groups of tests were completed to characterize frequency response, damping, and mode shapes. The individual test configurations for the tests in this report are summarized in the test matrix in Table H-1.

Local modes for various span lengths and boundary conditions resulted in three predominant modes over a range of frequencies for the majority of tests. The first predominant mode ranged from  $\{\{ \dots \}^{2(a),(c)}$  with one exception in Group A and those in Group E. Excitation of the HCSG support showed measurements on the adjacent tubes to have multiple low-frequency FRF peaks between  $\{\{ \dots \}^{2(a),(c)}$  (these tests had support rings removed). The FRF peaks specific to supports also introduced lower modes between  $\{\{ \dots \}^{2(a),(c)}$  for Group E. Lower modes below  $\{\{ \dots \}^{2(a),(c)}$  were difficult to excite and not present in responses for Groups B, C, and D. A summary of frequency ranges over predominant modes for the testing groups is provided in Table 3-41.

Table 3-41 Frequency response function summary per group

$\{\{$

$\}^{2(a),(c)}$

Modes were excited more clearly within the measured FRFs when excited mid-span for the first predominant mode and near the ends for the second and third predominant modes. The influence of local modes unique to each span and boundary condition in the HCSG creates additional complexity in evaluation and multiple tests may be required to discern specific modes within each span. With impact excitation, the data suggests modes can be excited up to one adjacent span of similar length from the excitation source. Fixed-end conditions, or nearly fixed-end, offer the best location for impact testing and elevated signal-to-noise ratios.

Multiple methods were used to calculate damping with the following trends:

- Half-power method exhibited the largest variance

- Logarithmic decrement can improve variance using the 3<sup>rd</sup> peak and subsequent peaks to calculate
- Half-power generally produced higher estimates when compared to logarithmic decrement
- Logarithmic decrement has issues resolving damping for upper modes ( $\{\{ \}^{2(a),(c)}\}$ ). It is noteworthy that FEI is expected to be predominant for the first-mode bending, or less than  $\{\{ \}^{2(a),(c)}\}$  based on the current testing data and TB and VS are also expected at frequencies below  $\{\{ \}^{2(a),(c)}\}$ .
- Exponential fit produced generally lower damping values than logarithmic decrement with less variance (evident at larger initial tube displacements). Amplitude dependency on damping was observed for both logarithmic decrement and exponential damping estimations and can be summarized as follows:
  - Impact testing was limited to  $\{\{ \}^{2(a),(c)}\}$  of tube displacement with the majority below  $\{\{ \}^{2(a),(c)}\}$ . Damping values generally increased with amplitude ranging from  $\{\{ \}^{2(a),(c)}\}$  with a few points between  $\{\{ \}^{2(a),(c)}\}$ .
  - Pull testing for excitation was limited to  $\{\{ \}^{2(a),(c)}\}$  of initial displacement (single test). Damping values were between  $\{\{ \}^{2(a),(c)}\}$  over the  $\{\{ \}^{2(a),(c)}\}$  range and up to the  $\{\{ \}^{2(a),(c)}\}$  displacement with an exponential fit. The trend and scatter increased for elevated displacements with a maximum damping (logarithmic decrement) of  $\{\{ \}^{2(a),(c)}\}$ .

Mode shapes of Span C characterized the three predominant frequency responses as:

- first-mode bending in the vertical direction
- second-mode bending in the predominantly horizontal direction
- third-mode bending in the predominantly horizontal direction

Impact testing provided good repeatability of FRFs across multiple tests. The mode shapes were also repeatable from various locations (i.e., different span locations) of excitation.

## 4.0 Validation Methodology

The validation methodology provides a framework for selecting the aspects of the design analysis program to be validated and establishes or confirms that the experimental design provides sufficient data to validate the necessary aspects of the design analysis program. Pre-test prediction calculations implement the validation methodology. These calculations confirm the adequacy of the experimental scope. This includes identifying optimal test conditions and locations for sensors, and determining a range of expected and allowable experimental results, considering uncertainties and biases, that validate the design analysis.

### 4.1 Use of Test Data

Every measurement has some minor error, that results in a difference between the measured value and the true value. This difference between the measured and true value is the total error that is comprised of two components: random error and systematic error (Reference 9.1.2). Random error varies randomly in repeated measurements throughout the conduct of a test, whereas the systematic error remains constant, for example due to imperfect calibration or data reduction techniques. Accurate measurement requires minimizing both random and systematic errors. The test data received by NuScale will have with it a test equipment error and accuracy report (TEEAR), which provides the estimated value of expanded uncertainty for each recorded quantity (direct and derived). When each test is complete and the TEEAR uncertainty values are available, they will be substituted for experimental uncertainty ( $u_D$ ) as discussed in Section 4.2.

### 4.2 Methodology

Pre-test predictions develop and apply a series of calculations and finite-element models to generate best estimate and allowable responses for the components in the test. The output of the analyses is compared to prototype test results from the vibration and stress measurement program to validate the analytical approach in the design analyses and the margin of safety. The implementation of this methodology is discussed in detail for individual NPM components in the context of the corresponding FIV analysis method in Sections 4.3, 4.4, 4.5, and 4.6.

This validation process accounts for the fact that model predictions and analytical methods rely on engineering simplifications, and that test results are inevitably affected by practical differences (see Section 4.6) and instrument uncertainty that introduces errors into the validation process.

Equation 4-1 to Equation 4-6 are presented for derivation of the validation approach. Following the logic presented in Section 1-5 of Reference 9.1.2, a predicted value  $S$  is compared to an experiment data value  $D$  for purposes of validation. The comparison error or discrepancy is:

$$E = S - D \quad \text{Equation 4-1}$$

The validation comparison error,  $E$ , incorporates errors from both the analysis and the test, as shown below. The true value of the variable of interest is denoted as  $T$ , so the error in the predicted value,  $\sigma_S$ , is the difference between  $S$  and  $T$ :

$$\sigma_S = S - T \quad \text{Equation 4-2}$$

Similarly, the error in the measured value,  $\sigma_D$ , is the difference between  $D$  and  $T$ :

$$\sigma_D = D - T \quad \text{Equation 4-3}$$

Using Equations 4-1 through 4-3, the validation comparison error  $E$  is expressed as:

$$E = (\sigma_S + T) - (\sigma_D + T) = \sigma_S - \sigma_D \quad \text{Equation 4-4}$$

Knowledge of the true value  $T$  is not known with certainty, so the application of Equation 4-4 is continued through the definition of additional terms. The errors in the predicted value  $S$  are assigned to one of three categories included in the following summation:

$$\sigma_S = \delta_{model} + \delta_{num} + \delta_{input} \quad \text{Equation 4-5}$$

- (i) The error  $\delta_{model}$  due to assumptions and approximations in design analysis
- (ii) The error  $\delta_{num}$  due to the numerical solution of the equations (relevant to complex computer codes, e.g., finite element analysis)
- (iii) The error  $\delta_{input}$  due to variability in the input parameters to the pre-test analysis.

The objective of a validation exercise is to ascertain the magnitude of  $\delta_{model}$  to within an uncertainty range. However, this error can be obscured by errors from the analysis solution scheme and/or the error embedded in the pre-test prediction input parameters, as well as the test result error. Re-arranging Equation 4-5 and using Equation 4-4:

$$\delta_{model} = E + \sigma_D - \delta_{num} - \delta_{input} \quad \text{Equation 4-6}$$

Equation 4-6 is not solved directly. Once a test is complete and measurement data is collected, the sign and magnitude of  $E$  are known from Equation 4-1, but the remaining terms on the right-hand side of Equation 4-6 are not known with certainty. In the Reference 9.1.2 approach, each error term is viewed as a single realization from a parent probability distribution. The standard deviation of each parent population (also called

“standard uncertainty”) corresponding to these errors is taken as  $u_D$ ,  $u_{num}$ , and  $u_{input}$ . Thus, the standard uncertainty associated with the estimate of  $\delta_{model}$  is expressed as a *validation uncertainty* as follows:

$$u_{val} = \sqrt{u_D^2 + u_{num}^2 + u_{input}^2} \quad \text{Equation 4-7}$$

Consequently, Equation 4-6 and the range defined in Equation 4-8, characterize an interval within which  $\delta_{model}$  falls. Therefore, the determination of the validation comparison error  $E$  provides a direct assessment of the prediction error with  $u_{val}$  as the validation standard uncertainty.

$$E \pm u_{val} \quad \text{Equation 4-8}$$

### 4.3 Validation Approach and Uncertainty Analysis

Based on the validation methodology described in Section 4.2, the uncertainty analysis applies the following guidelines, with Equation 4-8 as the basis for the validation exercise in the post-test analysis:

- If the absolute value of the validation comparison error  $E$  is much greater than the validation standard uncertainty  $u_{val}$ , then  $\delta_{model}$  is approximately equal to  $E$  (i.e., it accounts for most of the observed difference between analysis result and test data). In this case, there is an incentive to enhance the accuracy of the analysis to reduce model error.
- If the absolute value of the validation comparison error  $E$  is less than or equal to  $u_{val}$ , then  $\delta_{model}$  is within the “noise level” created by uncertainties in the solution scheme, inputs, and test data used to perform the validation. In this case, there is small benefit to pursuing model improvements to achieve better accuracy.
- If  $u_{val}$  is identified with a particular family of probability distributions, then a confidence interval can be defined. For instance, assuming  $(\delta_{input} + \delta_{num} - \sigma_D)$  is from a Gaussian distribution, the “expanded uncertainty” with 95 percent confidence is  $U_{95} = 2 u_{val}$ . Thus,  $(E \pm U_{95})$  provides an interval in which  $\delta_{model}$  resides about 95 times out of 100.

The following sections provide the detailed methodology for calculating the validation metrics  $E$  and  $u_{val}$  for each of the FIV phenomena examined in the measurement program.  $u_{val}$  is calculated in the pre-test prediction and  $E$  cannot be finalized until the post-test analysis, when errors in the measured values can be assessed.  $u_{val}$  is also used in the pre-test prediction to inform the expected and allowable range of experimental results that validate the design analyses.

### 4.3.1 Propagation of Uncertainties into a Result

Engineering variables of interest are often functions of other variables based on a well-known mathematical relationship. In this validation methodology, the engineering variables of interest are the safety margins associated with the onset of an FIV phenomenon or other FIV results such as the fatigue margin for a SG tube. The effect of random standard uncertainty in the constituent variables, denoted as  $u_{X_i}$ , is approximated by the Taylor series method (Reference 9.1.2). Consider a result  $R$  expressed in terms of the average or assigned values of the independent parameters  $X_i$  that enter into the result. That is,

$$R = f(X_1, X_2, \dots, X_I) \quad \text{Equation 4-9}$$

Where  $I$  signifies the total number of parameters involved in  $R$ . When there is a known mathematical relationship between the result and its parameters, sensitivity coefficients  $\theta_i$  are calculated by partial differentiation (Equation 3-2-2 of Reference 9.1.2):

$$\theta_i = \frac{\partial R}{\partial X_i} \quad \text{Equation 4-10}$$

The absolute standard uncertainty of the result is calculated based on square root sum of squares of each uncertainty term, as follows:

$$u_R = \left[ \sum_{i=1}^I (\theta_i u_{X_i})^2 \right]^{1/2} \quad \text{Equation 4-11}$$

An alternative to partial differentiation by analytical derivation is to use central finite differences. This implies that the sensitivity coefficients are calculated as shown below:

$$\theta_i = \frac{f(\dots, X_i^0 + \Delta X_i^0, \dots) - f(\dots, X_i^0 - \Delta X_i^0, \dots)}{2\Delta X_i^0} \quad \text{Equation 4-12}$$

It is implicit that the sensitivity coefficient in Equation 4-10 is evaluated at the nominal value of the parametric vector. Note that many design analysis input parameters have been biased to be conservative (versus best-estimate or nominal). Therefore, care is taken in the pre-test prediction to use best-estimate inputs in the absolute standard uncertainty calculation to ensure an appropriate range for the expected measurement results is obtained. If using Equation 4-12, a choice is made to set the value of the perturbation size  $\Delta X_i$ . If  $\Delta X_i$  is too large then truncation error is large, so a practically small value is

recommended. It is often useful to set  $\Delta X_i$  equal to the ratio of the variable's standard error to its nominal (mean) value.

### 4.3.2 Calculation of Input Parameter Uncertainty

Based on the guidance in Reference 9.1.2, there are two different approaches for estimating  $u_{input}$ . The approach depends on whether a *local* or *global* view of uncertainty estimation process is followed. In this report, both are presented as valid options because of the diversity in the FIV phenomena and their analytical methods, and to provide flexibility for the analyst when performing pre-test analysis.

#### 4.3.2.1 Local Method

An analysis prediction  $S$  with  $n_p$  uncorrelated input parameters is effectively a result developed from the arithmetic construction or manipulation of the underlying input parameters. Hence, the same uncertainty propagation method discussed in Section 4.3.1 is used to evaluate  $u_{input}$ , namely:

$$u_{input} = \left[ \sum_{i=1}^{n_p} \left( \frac{\partial S}{\partial X_i} u_{X_i} \right)^2 \right]^{1/2} \quad \text{Equation 4-13}$$

where  $u_{X_i}$  is the standard uncertainty in input parameter  $X_i$ . Ideally,  $u_{X_i}$  should come from prior experiments, although engineering judgment may be accepted instead to estimate it or may require validation based on the measurement program results.

#### 4.3.2.2 Global Method

The sensitivity coefficient method presented in the preceding section is termed local sensitivity and uncertainty propagation because the function evaluations are in a narrow (local) neighborhood of the mean parameter value. This approach does not capture highly nonlinear behavior in the input parameter space. For this reason, sampling-based methods using a Monte Carlo technique is used to mitigate the limitation in the local method. Reference 9.1.2 specifies using the Latin Hypercube Sampling (LHS) method to achieve a reasonable number of samples, equivalent to  $n_{LHS} \geq n_p + 1$ , where  $n_p$  is the number of variables in the function being evaluated.

Once the analysis is performed using  $n_{LHS}$  parameter vectors, whose constituent values are paired at random, the mean value and standard deviation from the different parametric runs is calculated using Equation 4-14 and Equation 4-15, respectively (Equations 3-3-1 and 3-3-2 of Reference 9.1.2).



$$\bar{S} = \frac{1}{n_{LHS}} \sum_{i=1}^{n_{LHS}} S_i \quad \text{Equation 4-14}$$

$$u_{input} = \left[ \frac{1}{n_{LHS} - 1} \sum_{i=1}^{n_{LHS}} (S_i - \bar{S})^2 \right]^{1/2} \quad \text{Equation 4-15}$$

The validation exercise that employs the LHS method demonstrates statistical convergence by performing sensitivity runs with an increasing number of samples. In addition, if the distribution function of the input variables is assumed, then sensitivity of  $u_{input}$  to this assumption is explored.

### 4.3.3 Calculation of Mesh Numerical Uncertainty

In some FIV evaluations, the analysis relies on a computer model that is developed using finite-element methods. In this case, the solution process introduces uncertainty in the overall model result due to the fact that discretized equations are used and/or iterative matrix solvers are executed (the latter only for nonlinear systems). Finite element models are used to determine the vibration mode shape and natural frequency in many FIV evaluations. Estimation of numerical uncertainty is not required for hand calculations in which the input parameters are obtained from mathematical or empirical correlations.

The Grid Convergence Index method is a means to estimate the numerical uncertainty that arises from the use of computational grids with different resolution capabilities that aim to output a result  $\varphi$ . Considering three numerical meshes (fine; medium; coarse) to have characteristic cell sizes  $h_1 < h_2 < h_3$ , and refinement factors  $r_{21} = h_2/h_1$  and  $r_{32} = h_3/h_2$ , the order of convergence,  $p$ , is calculated as:

$$p = \frac{\ln(\epsilon_{32}/\epsilon_{21}) + q(p)}{\ln(r_{21})} \quad \text{Equation 4-16}$$

where

$$q(p) = \ln \left( \frac{r_{21}^p - s}{r_{32}^p - s} \right) \quad \{0 \text{ if } r_{21} = r_{32}\} \quad \text{Equation 4-17}$$

$$s = 1 \cdot \text{sign} \left( \frac{\epsilon_{32}}{\epsilon_{21}} \right) \quad \text{Equation 4-18}$$

$$\epsilon_{32} = \varphi_3 - \varphi_2 \text{ (difference in result between coarse and medium mesh)} \quad \text{Equation 4-19}$$

$$\epsilon_{21} = \varphi_2 - \varphi_1 \text{ (difference in result between medium and fine mesh)} \quad \text{Equation 4-20}$$

A uniform and integer mesh refinement factor is used (for example  $r = 2$ ) to implement this method. Numerical uncertainty is then estimated from the Grid Convergence Index, given below, with a factor of safety  $F_s = 3$  (Recommended it for unstructured grid refinement. Also, three grid solutions should be sufficiently conservative):

$$u_{num} = GCI = \frac{F_s |\varphi_1 - \varphi_2|}{r_{21}^p - 1} \quad \text{Equation 4-21}$$

Note that if, for example, the order of the discretization scheme is known to be  $p=2$  (second order), and the medium mesh cell size ( $h_2$ ) is uniformly decreased by half in all directions ( $r=2$ ), then  $u_{num}$  from Equation 4-21 becomes the absolute value of the difference between the result on the fine and medium grid ( $\approx |\varphi_1 - \varphi_2|$ ). For linear modal analysis, this value is small because there is a weak dependence of calculated frequency on grid density.

#### 4.4 Evaluation Process

The overall process for the pre-test prediction and post-test assessments is summarized below. Some values may require assumptions at the time of the pre-test prediction depending on the status of the test design. In the post-test assessment, the uncertainties are confirmed or adjusted as necessary based on the final test design and results.

##### Pre-Test Prediction

1. Using best-estimate input and accounting for experimental biases, calculate safety margin and critical parameters for the test (frequencies, critical or lock-in velocities, and so on).
2. Calculate input, measurement and numerical uncertainties.
3. Using the parameters determined above, quantify the range of allowable test results that adequately validate the design analysis.

These steps provide confidence that considering the experimental biases, and input, measurement and numerical uncertainties, the test design is adequate to validate the design analysis.

## Post-Test Assessment

1. Determine if changes to the expected or allowable range in the pre-test prediction are required based on considerations such as finalization of the test design, confirmation of measurement uncertainties, or the as-tested conditions.
2. Confirm test results match predictions and are within the allowable range for validation.
3. Quantify the validation comparison error and model error to confirm they are acceptable.

These steps complete the validation of the design analysis using the test results. If the modeling error is greater than the validation comparison error, the design analysis is to be updated to decrease modeling error. Additionally, if the test results do not match predictions, the design analysis is to be revised based on the conclusions of the testing.

## 4.5 Evaluation Procedures

### 4.5.1 Turbulent Buffeting of Steam Generator Tube

The method for validating the TB design analysis process by testing measurements is described below.

#### 4.5.1.1 Overview

Consider the results of the test used for validating the TB design analysis to provide the natural frequencies in water ( $f_{n_T}$ ), mode shapes ( $\phi_T$ ), and associated uncertainty ( $u_D$ ). An ANSYS model to simulate the test geometry is developed as described in Section 5.1.2. The model prediction for the vibration modes and natural frequencies are  $\phi_M$ , and  $f_{n_M}$ , respectively. The model results are examined on a column-by-column basis and an appropriate comparison to a corresponding test result is to be made.

##### 4.5.1.1.1 Calculate Model Error in Modal Parameters

Using Equation 4-1, the modeling error is determined as the maximum difference in frequency or mode shape comparison:

$$E_{SG} = \max(|f_{n_M} - f_{n_T}|, |\phi_M - \phi_T|).$$

The comparison may involve more than just the fundamental beam mode.

##### 4.5.1.1.2 Calculate Model Uncertainty

The uncertainty associated with the result from modeling of the SG test is referred to as  $u_{val}$ , and consists of input, numerical, and measurement uncertainties, combined per Equation 4-7, and discussed in the following sections. The analysis ensures that the resultant  $u_{val} \geq |E_{SG}|$ , otherwise the modeling approach should be modified to reduce the error. Engineering judgment may be used to weigh the relative significance of the errors obtained from the comparison of different modes, and among the different SG columns.

This step is dependent on the level of detail in the test data, and whether measured frequencies can be distinguished and matched to their counterparts in the model.

#### 4.5.1.1.2.1 Input Uncertainty

Significant inputs to the analysis of the test configuration are listed in Table 4-1. The sampling technique discussed in Section 4.3.2.2 provides a method to generate a series of model predictions from which an input uncertainty can be estimated (Equation 4-15). Note that sampling of different boundary conditions is not necessary unless the modeling error is much larger than the overall uncertainty ( $u_{val} \ll |E_{SG}|$ ). When evaluating input uncertainty, nominal (best-estimate) values are used, as discussed in Section 4.3.1.

Table 4-1 SG Test Model Inputs

Input Parameter	Basis for Variability
Geometric Dimensions	Manufacturing tolerances will affect the nominal values specified for the model
Mass	The effect of hydrodynamic mass in actual tube bundle may be different than that estimated by formula which is based on a correlation for single flexible tube surrounded by an array of rigid tubes (note: the correlation relies on pitch and diameter)
Boundary Conditions	SG boundary conditions are subject to variability based on considerations such as fit-up with the supports, manufacturing tolerances, compression and thermal expansion. Boundary conditions are expected to be fixed, pivot or a combination. Boundary conditions may vary throughout the tube bundle.

#### 4.5.1.1.2.2 Numerical Uncertainty

The numerical uncertainty in the modal analysis ( $u_{num}$ ) is estimated based on the sensitivity study described in Section 3.2.2.2.3 for the approximate solution of the acceptance integrals. The approximation method is described in Section 3.2.2.1.

#### 4.5.1.1.2.3 Measurement Uncertainty

In the post-test analysis, the measurement data uncertainty is used directly as provided by the test if it is reported for the frequency and mode shape and no other action is required. In the pre-test analysis, a propagation calculation will be performed to obtain  $u_D$  similar to the approach for estimating input uncertainty.

#### 4.5.1.1.3 Estimate Vibration Amplitude Uncertainty

The turbulence-induced RMS displacement is determined analytically using the approach described in Section 3.2.2. The test program shall measure the displacement ( $\bar{y}_{test}$ ), and also quantify its uncertainty as  $u_{Dy}$ . Using Equation 4-1, the prediction error is:  $E_y = \bar{y}_{rx} - \bar{y}_{test}$ .

The parameter of interest is the maximum RMS value of displacement in the two adjacent spans of a support. The input uncertainty in the RMS displacement is determined using the global method described in Section 4.3.2.2. The parameters sampled are the damping

ratio, modal frequencies, and PSD magnitude. The sample standard deviation of the results provides the uncertainty in the RMS displacement.

#### 4.5.1.2 Estimate Uncertainty in Safety Margin for SG Tube in NPM

Margin to the TB acceptance criterion is determined via Equation 4-22 which allows determination of the allowable number of cycles and the fatigue usage due to impact stress. Equation 4-22 is rewritten as Equation 4-23.

$$S_{rms} = c \left( \frac{E^4 M_e f_n^2 \bar{y}_{rms}^2}{D^3} \right)^{1/5} \quad \text{Equation 4-22}$$

$$F(X_1, X_2, X_3, X_4) = \alpha \left( \frac{X_1 X_2^2 X_3}{X_4^3} \right)^{1/5} \quad \text{Equation 4-23}$$

where  $\alpha = \frac{1}{2} c E^{4/5}$ . The input parameters in Equation 4-23 are discussed in Table 4-2, and assigned generic labels. The process in Section 4.3.1 is used to evaluate the effect of uncertainty in the different parameters, as given in Table 4-3.

Table 4-2 SG Tube Inputs to TB Margin Calculation

Temporary Label	Input Parameter	Basis
$X_1$	Effective mass of tube, usually taken as 2/3 the total mass of the two spans $\{ M_e \}$	Total mass includes the mass of the tube metal, secondary fluid, and hydrodynamic mass (virtual mass on primary side). Uncertainty in those contributing factors propagate to the total. A nominal value for effective tube mass is used.
$X_2$	Natural frequency of the tube $\{ f_n \}$	This is obtained using an ANSYS modal analysis. Note that in Reference 1.4.9, the first ten mode frequencies were averaged given their larger relative response to turbulent buffeting compared to higher mode numbers. A nominal value for natural frequency is used.
$X_3$	Maximum mean square vibration amplitude of the tube in the adjacent spans $\{ y_{rms}^2 \}$	This is calculated using a PSD approach, which will be verified to be bounding as part of the SG testing. A nominal vibration amplitude is used.
$X_4$	Outer diameter of the tube $\{ D \}$	Manufacturing tolerances affect the nominal value specified for the calculation. A nominal outer diameter is used.

Table 4-3 SG Tube TB Margin Uncertainty Method

Step	Description	Procedure
$\theta_1$	Analytic derivative of Equation 4-23 with respect to $X_1$	$\frac{\alpha X_1^{-4/5} X_2^{2/5} X_3^{1/5}}{5 X_4^{3/5}}$
$u_{X1}$	Uncertainty in $X_1$	Uncertainty in total tube mass is determined from the uncertainty in secondary fluid density
$\theta_2$	Analytic derivative of Equation 4-23 with respect to $X_2$	$\frac{2\alpha X_1^{1/5} X_2^{-3/5} X_3^{1/5}}{5 X_4^{3/5}}$
$u_{X2}$	Uncertainty in $X_2$	Standard deviation from the mean frequency of the set of vibration modes included in the average
$\theta_3$	Analytic derivative of Equation 4-23 with respect to $X_3$	$\frac{\alpha X_1^{1/5} X_2^{2/5} X_3^{-4/5}}{5 X_4^{3/5}}$
$u_{X3}$	Uncertainty in $X_3$	$u_y$ from Section 4.5.1.1.3
$\theta_4$	Analytic derivative of Equation 4-23 with respect to $X_4$	$\frac{-3\alpha X_1^{1/5} X_2^{2/5} X_3^{1/5}}{5 X_4^{8/5}}$
$u_{X4}$	Uncertainty in $X_4$	Obtain from standard deviation of SG outer diameters as generated by manufacturing tolerances distribution
$u_R$	Equation 4-11. The result is added to / subtracted from the alternating stress in Equation 4-23 evaluated at nominal values	$\sqrt{\theta_1^2 u_{X1}^2 + \theta_2^2 u_{X2}^2 + \theta_3^2 u_{X3}^2 + \theta_4^2 u_{X4}^2}$

## 4.5.2 Vortex Shedding

Consider the results of the test to provide the natural frequency in water ( $f_{n_T}$ ), mode shape ( $\phi_T$ ), and associated uncertainty ( $u_D$ ). An ANSYS model to simulate the test geometry is developed using the same configuration, as well as environment and boundary conditions as the experiment. The model predictions for the fundamental mode natural frequency and mode shape are  $f_{n_M}$  and  $\phi_M$ , respectively.

### 4.5.2.1 Calculate Model Error

Using Equation 4-1, calculate the modeling error based on maximum of different modes:

$$E_{SG_f} = |f_{n_M} - f_{n_T}|,$$

$$E_{SG_\phi} = |\phi_M - \phi_T|,$$

$$E_{SG} = \max(E_{SG_f}, E_{SG_\phi}), \text{ based on normalized values.}$$

The above comparison errors are examined for at least the first mode results. If higher modes are reviewed the same procedure is followed, but the first mode is more limiting to the margin assessment. Also, because  $\phi$  is not a single value but a function of SG height, the maximum difference is used on the basis of a unity normalized mode shape.

#### 4.5.2.2 Calculate Model Uncertainty

The uncertainty associated with the result from modeling of the SG test is referred to as  $u_{val}$ , and consists of input, numerical, and measurement uncertainties, combined per Equation 4-7, and discussed in the following sections. The analysis ensures that the resultant  $u_{val} \geq |E_{SG}|$ , otherwise the modeling approach is to be modified to reduce the error.

##### 4.5.2.2.1 Input Uncertainty

The inputs to the modal analysis of the test configuration are listed in Table 4-4. The sampling method discussed in Section 4.3.2.2 is used to generate a series of model predictions from which an input uncertainty is estimated (Equation 4-15). Note that sampling of different boundary conditions is not necessary unless the modeling error is much larger than the overall uncertainty ( $u_{val} \ll |E_{SG}|$ ).

Table 4-4 Steam generator test model inputs

Input Parameter	Basis for Variability
Geometric Dimensions	Manufacturing tolerances affect the nominal values specified for the model
Mass	Effect of hydrodynamic mass in actual tube bundle is likely different than that estimated by formula, which is based on a correlation for single flexible tube surrounded by an array of rigid tubes (note: the correlation relies on pitch and diameter)
Boundary Conditions	SG boundary conditions are subject to variability based on considerations such as fit-up with the supports, manufacturing tolerances, compression and thermal expansion. Boundary conditions are expected to be fixed, pivot or a combination. Boundary conditions may vary throughout the tube bundle.

##### 4.5.2.2.2 Numerical Uncertainty

The numerical uncertainty in the modal analysis ( $u_{num}$ ) is estimated using the approach discussed in Section 4.3.3 using nominal model inputs.

##### 4.5.2.2.3 Measurement Uncertainty

In the post-test analysis, the measurement data uncertainty is used directly as provided by the test if it is reported for the frequency and mode shape and no other action is required. In the pre-test analysis, a propagation calculation is performed to obtain  $u_D$  (Section 4.1) similar to the approach for estimating input uncertainty.

#### 4.5.2.3 Estimate Uncertainty in Safety Margin for Steam Generator Tube in NuScale Power Module

There are four methods to show acceptable margin to VS lock-in. The three methods applicable to tube arrays are described below for completeness; however, they may not be necessary to execute the pre-test prediction. Method B is described first. Method B

requires that the reduced damping ( $C_{RD}$ ) is greater than the minimum threshold value of 64. The corresponding safety margin is represented using Equation 4-24.

$$SM_{VSB} = \frac{C_{RD}}{64} - 1 = \frac{1}{64} \left[ \frac{4\pi\xi m_{tot} \int_0^{l_{tube}} \phi_1^2(x) dx}{\rho D^2 \int_0^{l_e} \phi_1^2(x) dx} \right] - 1 \quad \text{Equation 4-24}$$

The input parameters in Equation 4-24 are discussed in Table 4-5, and assigned generic labels. The process in Section 4.3.1 is used to determine the analytically predicted allowable range for the safety margin in Equation 4-24 and evaluate the effect of uncertainty in the different parameters. Equation 4-24 is re-written as:

$$SM_{VSB} = \frac{SX_1 X_2 g(X_5, X_7)}{X_3 X_4^2 h(X_6, X_7)} - 1 \quad \text{Equation 4-25}$$

where  $S = \pi/16$ ,  $g$ , and  $h$  are the definite integrals. Table 4-6 shows the details of performing the calculation on Equation 4-25, which is performed separately for the “light” and “heavy” tube cases. The SG mode shape relative magnitude is zero at the beginning and end of the tube, so  $\phi_1(0) = \phi_1(l_{tube}) = 0$ .

Table 4-5 Steam generator tube inputs to vortex shedding margin calculation: method B

Temporary Label	Input Parameter	Basis
$X_1$	Damping ratio in air { $\xi$ }	A nominal value of damping is used. This parameter is measured in a dedicated test, so its uncertainty is propagated.
$X_2$	Total mass of tube { $m_{tot}$ }	Total mass includes the mass of the tube metal, secondary fluid, and hydrodynamic mass (virtual mass on primary side). Uncertainty in those contributing factors propagates to the total. Nominal values for “light” and “heavy” cases are developed.
$X_3$	Fluid density { $\rho$ }	The primary fluid temperature variation along the SG radius and height is a source of uncertainty in the calculation, which assumes a constant value for RCS (cold or hot region).
$X_4$	Tube outer diameter { $D$ }	Manufacturing tolerances affect the nominal value specified for the calculation.
$X_5$	Overall length of tube { $l_{tube}$ }	Manufacturing tolerances affect the nominal value specified for the calculation.
$X_6$	Length of tube subject to cross flow { $l_e$ }	In the design analysis, this is assumed from the lowest elevation to the elevation corresponding to the second tube support, considering both active and inactive supports. Its uncertainty propagates to the margin calculation.



Temporary Label	Input Parameter	Basis
X <sub>7</sub>	Fundamental modal shape { φ <sub>1</sub> }	The free-vibration mode shape of the SG tube is obtained using an ANSYS modal analysis. This parameter includes uncertainty in the modal analysis modeling, considering both the range of possible mode shapes based on boundary conditions and the components of the mode shape that could be excited by cross flow.

Table 4-6 Steam generator tube vortex shedding margin uncertainty method: method B

Step	Description	Procedure
θ <sub>1</sub>	Analytic derivative of Equation 4-25 with respect to X <sub>1</sub>	$\frac{SX_2g(X_5,X_7)}{X_3X_4^2h(X_6,X_7)}$ , where <i>g</i> and <i>h</i> are definite integrals evaluated at the nominal values
u <sub>X1</sub>	Uncertainty in X <sub>1</sub>	Obtain from measurement data of damping ratio in air
θ <sub>2</sub>	Analytic derivative of Equation 4-25 with respect to X <sub>2</sub>	$\frac{SX_1g(X_5,X_7)}{X_3X_4^2h(X_6,X_7)}$ , evaluated at the nominal values
u <sub>X2</sub>	Uncertainty in X <sub>2</sub>	Uncertainty in total tube mass is determined from the uncertainty in secondary fluid density, tube material density, and RCS density (i.e., u <sub>X2</sub> ≈ [u <sub>ps</sub> <sup>2</sup> +u <sub>p690</sub> <sup>2</sup> +u <sub>prcs</sub> <sup>2</sup> ] <sup>0.5</sup> )
θ <sub>3</sub>	Analytic derivative of Equation 4-25 with respect to X <sub>3</sub>	$\frac{-SX_1X_2g(X_5,X_7)}{X_3^2X_4^2h(X_6,X_7)}$ , evaluated at the nominal values
u <sub>X3</sub>	Uncertainty in X <sub>3</sub>	Obtain from RCS density range across SG (uncertainty due to fluid temperature variation)
θ <sub>4</sub>	Analytic derivative of Equation 4-25 with respect to X <sub>4</sub>	$\frac{-2SX_1X_2g(X_5,X_7)}{X_3X_4^3h(X_6,X_7)}$ , evaluated at the nominal values
u <sub>X4</sub>	Uncertainty in X <sub>4</sub>	Obtain from standard deviation of SG outer diameters as generated by manufacturing tolerances distribution
θ <sub>5</sub>	Analytic derivative of Equation 4-25 with respect to X <sub>5</sub>	$\frac{SX_1X_2\phi_1^2(l_{tube})}{X_3X_4^2h(X_6,X_7)} = 0$
u <sub>X5</sub>	Uncertainty in X <sub>5</sub>	Not propagated
θ <sub>6</sub>	Analytic derivative of Equation 4-25 with respect to X <sub>6</sub>	$\frac{SX_1X_2g(X_5,X_7)}{X_3X_4^2\phi_1^2(l_e)}$ , evaluated at the nominal values
u <sub>X6</sub>	Uncertainty in X <sub>6</sub>	Obtain from range of tube length exposed to flow based on tolerances in the configuration of supports and their assumed effectiveness
θ <sub>7</sub>	Sensitivity coefficient is taken as unity because modal analysis is linear	Equate to 1.0 (justified because model uncertainty is expected to be small)
u <sub>X7</sub>	Uncertainty in X <sub>7</sub>	Same as u <sub>val</sub> in Section 4.5.2.2.
u <sub>R</sub>	Equation 4-11	$\sqrt{\theta_1^2u_{X1}^2 + \theta_2^2u_{X2}^2 + \theta_3^2u_{X3}^2 + \theta_4^2u_{X4}^2 + \theta_5^2u_{X5}^2 + \theta_6^2u_{X6}^2 + \theta_7^2u_{X7}^2}$

Uncertainty estimates are also provided for Method A and C.

$$SM_{VSA} = \frac{f_n D}{v \cos \theta S t} - 1 = \frac{X_9 X_{10}}{X_8 \cos \theta X_{11}} - 1 \quad \text{Equation 4-26}$$

Table 4-7 Steam generator tube inputs to vortex shedding margin calculation: method A

Temporary Label	Input Parameter	Basis
$X_8$	velocity { $v$ }	This parameter includes uncertainties in the assumed primary coolant flow velocity.
$X_9$	Natural Frequency { $f_n$ }	This parameter includes uncertainties in the SG tube natural frequency.
$X_{10}$	Tube outer diameter { $D$ }	This parameter includes uncertainties associated with manufacturing tolerances.

Table 4-8 Steam generator tube vortex shedding margin uncertainty method: method A

Step	Description	Procedure
$\theta_8$	Analytic derivative of Equation 4-26 with respect to $X_8$	$\frac{-X_9 X_{10}}{X_8^2 \cos \theta X_{11}}$
$u_{X8}$	Uncertainty in $X_8$	Uncertainty in velocity.
$\theta_9$	Analytic derivative of Equation 4-26 with respect to $X_9$	$\frac{X_{10}}{X_8 \cos \theta X_{11}}$
$u_{X9}$	Uncertainty in $X_9$	Uncertainty in the SG tube frequency.
$\theta_{10}$	Analytic derivative of Equation 4-26 with respect to $X_{10}$	$\frac{X_9}{X_8 X_{11}}$
$u_{X10}$	Uncertainty in $X_{10}$	Uncertainty in tube outer diameter.
$\theta_{11}$	Analytic derivative of Equation 4-26 with respect to $X_{11}$	$\frac{-X_9 X_{10}}{X_8 \cos \theta X_{11}^2}$
$u_{X11}$	Uncertainty in $X_{11}$	Uncertainty in the Strouhal number.
$u_R$	Equation 4-11	$\sqrt{\theta_8^2 u_{X8}^2 + \theta_9^2 u_{X9}^2 + \theta_{10}^2 u_{X10}^2 + \theta_{11}^2 u_{X11}^2}$

Method C uses the same variables as Methods A and B, but with different acceptance criteria limits. Specifically, the reduced damping needs to be greater than 1.2 instead of 64 and the reduced velocity needs to be less than 3.3 instead of 1.0. The reduced velocity limit does not affect the analytic derivatives. The safety margin value can be calculated using Equation 4-26 with 3.3 substituted for the value of 1 from Method A. For the reduced damping, Equation 4-25 can be used with the value of S modified to  $0.3\pi$  instead of  $\pi/16$ . When using Method C, the reduced damping and reduced velocity both are evaluated to determine expected and allowable ranges.

### 4.5.3 Fluid-Elastic Instability of SG Tubes

The method for validating the design analysis process by testing measurements is described below.

#### 4.5.3.1 Calculate Model Error

Model error is quantified at the completion of the post-test analysis per Equation 4-1. For the FEI assessment, model error is calculated for each measured or derived parameter that is a calculation result, such as the frequencies, mode shapes, and pitch velocity. The model error is then compared to the validation standard uncertainty to ensure the validation metric are consistent with the inequality in Equation 4-8.

No estimation of model error is required during the pre-test analysis.

#### 4.5.3.2 Calculate Model Uncertainty

Model uncertainty is comprised of input uncertainty, numerical uncertainty, and measurement uncertainty. These uncertainties are evaluated in the pre-test prediction. Some values require assumptions at the time of the pre-test prediction depending on the status of the test design. In the post-test assessment, the uncertainties are confirmed or adjusted as necessary based on the final test design.

In the pre-test analysis, the predicted uncertainties are used to determine the range of allowable test results that validate the design analysis. See Section 4.7 for additional details regarding this aspect of the pre-test analysis. In the post-test analysis, the range is confirmed using final uncertainty values, and the validation uncertainty is compared to the model error as described in Section 4.5.3.1.

##### 4.5.3.2.1 Input Uncertainty

The effect of input parameter uncertainty on simulation uncertainty is calculated using the local or global methods that are discussed in Sections 4.3.2.1 and 4.3.2.2, respectively. The local method is sufficient for input parameters that are relevant to FEI. If the effects of large differences in the input parameter need to be investigated the global method is to be used.

The categories of inputs relevant for the FEI analysis of the test configuration are listed in Table 4-9. The sampling methods discussed in Section 4.3.2.2 are used to generate a series of predictions from which an input uncertainty can be estimated (Equation 4-15).

In the pre-test analysis, the significant inputs within each category in Table 4-9 are to be considered. Examples of the types of input parameter variability for each category are also identified in the table. The input parameters that are considered in the input uncertainty assessment are to be justified in the pre-test analysis.

Table 4-9 Fluid elastic instability analysis input parameter types

Input Parameter Category	Example Input Parameter Variability
Modal	The effects of as-built conditions and allowed variability in test conditions on the pitch velocity are considered.
Thermal hydraulic	The effect of the following on the pitch velocity are considered: allowed variation in test conditions, calculation methods for determining local velocities, and the effect of as-built conditions on local velocities.
Design	The effect of as-built conditions on the critical velocity are considered.
Empirical	Uncertainties in the empirical correlations used to determine the critical velocity are considered.

#### 4.5.3.2.2 Numerical Uncertainty

Numerical uncertainty is assessed in the pre-test prediction. Completion of testing does not affect the predicted numerical uncertainty.

Numerical uncertainty applies to the modal analysis of the SG tube and the integration of the mode shapes over the length of the tube, which is performed as a summation approximation. The numerical uncertainty in the modal analysis ( $U_{num}$ ) is estimated using the approach discussed in Section 4.3.3 using nominal inputs.

#### 4.5.3.2.3 Measurement Uncertainty

Measurement uncertainty is estimated in the pre-test prediction and a final evaluation is performed in the post-test assessment. Depending on the maturity of the test design at the time of the pre-test prediction, engineering judgment is used to estimate measurement uncertainty values. In this event, appropriate assumptions are made that are reasonable both in terms of the test design and the ability to validate the design analysis. The results of the pre-test prediction are used to identify any changes that need to be incorporated into the detailed test design to accommodate reasonable measurement uncertainty. Open items are established to track the assumption until it has been incorporated.

In the post-test analysis, the measurement data uncertainty is used directly as provided by the test and no other action is required. In the pre-test analysis, a propagation calculation is performed to obtain  $u_D$  (Section 4.1) similar to the approach for estimating input uncertainty.

#### 4.5.3.3 Estimate Uncertainty in Safety Margin

The margin to the onset of FEI is based on the difference between the reduced mode shape weighted mean pitch velocity and the critical velocity, as shown in the following equation. The uncertainties in the modal, thermal hydraulic, design and empirical inputs are evaluated to quantify the effect of each parameter on the design analysis safety margin.

$$SF_{FEI} = \frac{f_i DC \left( \frac{2\pi m' \xi}{\rho D^2} \right)^a}{v \cos(\theta) M_i^{0.5}} - 1 \quad \text{Equation 4-27}$$

The input parameters in Equation 4-27 are discussed in Table 4-10, and assigned generic labels in Equation 4-28.

$$SF_{FEI} = \frac{X_6 X_{9,i} X_7 \left( \frac{2\pi X_3 X_4}{X_5 X_6^2} \right)^{X_8}}{X_1 \cos(\theta) X_{2,i}^{0.5}} - 1 \quad \text{Equation 4-28}$$

The process in Section 4.3.1 is used to determine the effect of input parameter uncertainty on the safety margin value as outlined in Table 4-11.

Table 4-10 Steam generator tube inputs to fluid elastic instability safety margin calculation

Temporary Label	Input Parameter	Basis
$X_1$	velocity	This parameter includes uncertainties in the assumed primary coolant flow velocity.
$X_{2,i}$	modal multiplier	This parameter includes uncertainty in the modal analysis modeling uncertainty, considering both the range of possible mode shapes based on boundary conditions and the components of the mode shape that could be excited by cross flow.
$X_3$	mass	This parameter includes uncertainty in the mass of the tube and the surrounding fluid.
$X_4$	damping	This parameter includes uncertainty, which is finalized when the damping value is measured.
$X_5$	density	This parameter includes uncertainty in the operating temperature of the primary coolant.
$X_6$	tube outer diameter	This parameter includes minor uncertainties in the manufacturing tolerances of the tube.
$X_7, X_8$	Connors' constants	These parameters include uncertainties associated with characterizing the onset of FEI for helical tubes.
$X_{9,i}$	Tube frequency	This parameter includes minor uncertainties in the frequency of the tube.

Table 4-11 Steam generator tube fluid elastic instability margin uncertainty method

Step	Description	Procedure
$\theta_1$	Analytic derivative of Equation 4-28 with respect to $X_1$	$\frac{-X_6 X_{9,i} X_7 \left( \frac{2\pi X_3 X_4}{X_5 X_6^2} \right)^{X_8}}{X_1^2 \cos(\theta) X_{2,i}^{0.5}}$
$u_{X1}$	Uncertainty in $X_1$	Uncertainty in velocity based on differences in primary coolant flow rate, due to considerations such as calculation method and temperature.
$\theta_2$	Analytic derivative of Equation 4-28 with respect to $X_2$	$\frac{-X_6 X_{9,i} X_7 \left( \frac{2\pi X_3 X_4}{X_5 X_6^2} \right)^{X_8}}{2X_1 \cos(\theta) X_{2,i}^{3/2}}$
$u_{X2}$	Uncertainty in $X_2$	Uncertainty in modal multiplier considering differences in tube and fluid mass, material properties and boundary conditions.
$\theta_3$	Analytic derivative of Equation 4-28 with respect to $X_3$	$\frac{X_6 X_{9,i} X_7 X_8 \left( \frac{2\pi X_3 X_4}{X_5 X_6^2} \right)^{X_8}}{X_3 X_1 \cos(\theta) X_{2,i}^{0.5}}$
$u_{X3}$	Uncertainty in $X_3$	Uncertainty in linear mass density considering differences in tube and hydrodynamic mass.
$\theta_4$	Analytic derivative of Equation 4-28 with respect to $X_4$	$\frac{X_6 X_{9,i} X_7 X_8 \left( \frac{2\pi X_3 X_4}{X_5 X_6^2} \right)^{X_8}}{X_4 X_1 \cos(\theta) X_{2,i}^{0.5}}$
$u_{X4}$	Uncertainty in $X_4$	Uncertainty in damping considering the potential range of expected damping at the design analysis condition.
$\theta_5$	Analytic derivative of Equation 4-28 with respect to $X_5$	$\frac{-X_6 X_{9,i} X_7 X_8 \left( \frac{2\pi X_3 X_4}{X_5 X_6^2} \right)^{X_8}}{X_5 X_1 \cos(\theta) X_{2,i}^{0.5}}$
$u_{X5}$	Uncertainty in $X_5$	Uncertainty in density considering the range of potential primary fluid temperatures at the design analysis condition.
$\theta_6$	Analytic derivative of Equation 4-28 with respect to $X_6$	$\frac{-X_{9,i} X_7 (2X_8 - 1) \left( \frac{2\pi X_3 X_4}{X_5 X_6^2} \right)^{X_8}}{X_1 \cos(\theta) X_{2,i}^{0.5}}$
$u_{X6}$	Uncertainty in $X_6$	Deviation of SG outer diameters as generated by manufacturing.
$\theta_7$	Analytic derivative of Equation 4-28 with respect to $X_7$	$\frac{X_{9,i} X_6 \left( \frac{2\pi X_3 X_4}{X_5 X_6^2} \right)^{X_8}}{X_1 \cos(\theta) X_{2,i}^{0.5}}$
$u_{X7}$	Uncertainty in $X_7$	Consider a range of empirical constants appropriate to bound FEI for the helical SG tubes.

Step	Description	Procedure
$\theta_8$	Analytic derivative of Equation 4-28 with respect to $X_8$	$\frac{X_6 X_{9,i} X_7 \left( \frac{2\pi X_3 X_4}{X_5 X_6^2} \right)^{X_8} \ln \frac{2\pi X_3 X_4}{X_5 X_6^2}}{X_1 \cos(\theta) X_{2,i}^{0.5}}$
$u_{X8}$	Uncertainty in $X_8$	Consider a range of empirical constants appropriate to bound FEI for the helical SG tubes.
$\theta_9$	Analytic derivative of Equation 4-28 with respect to $X_9$	$\frac{X_6 X_7 \left( \frac{2\pi X_3 X_4}{X_5 X_6^2} \right)^{X_8}}{X_1 \cos(\theta) X_{2,i}^{0.5}}$
$u_{X9}$	Uncertainty in $X_9$	Uncertainties in the SG tube frequency.
$u_R$	Equation 4-11	$\sqrt{\theta_1^2 u_{X1}^2 + \theta_2^2 u_{X2}^2 + \theta_3^2 u_{X3}^2 + \theta_4^2 u_{X4}^2 + \theta_5^2 u_{X5}^2 + \theta_6^2 u_{X6}^2 + \theta_7^2 u_{X7}^2 + \theta_8^2 u_{X8}^2 + \theta_9^2 u_{X9}^2}$

#### 4.5.4 Acoustic Resonance

The method for validating the design analysis process by testing measurements is described below.

##### 4.5.4.1 Calculate Model Error

Model error is quantified at the completion of the post-test analysis per Equation 4-1. For the acoustic resonance (AR) assessment, model error is calculated for each measured or derived parameter that is a calculation result, such as the acoustic frequencies and velocity. The model error is compared to the validation standard uncertainty to ensure the validation metric are consistent with the inequality in Equation 4-8.

No estimation of model error is required during the pre-test analysis.

##### 4.5.4.2 Calculate Model Uncertainty

Model uncertainty is comprised of input uncertainty, numerical uncertainty, and measurement uncertainty. These uncertainties are evaluated in the pre-test prediction. Some values may require assumptions at the time of the pre-test prediction depending on the status of the test design. In the post-test assessment, the uncertainties are confirmed or adjusted as necessary based on the final test design.

In the pre-test analysis, the predicted uncertainties are used to determine the range of allowable test results that would validate the design analysis. See Section 4.7 for additional details regarding this aspect of the pre-test analysis. In the post-test analysis, the range is confirmed using final uncertainty values, and the validation uncertainty is compared to the model error as described in Section 4.5.4.1.

##### 4.5.4.2.1 Input Uncertainty

The effect of input parameter uncertainty on simulation uncertainty is calculated using the local or global methods that are discussed in Sections 4.3.2.1 and 4.3.2.2, respectively.

The sampling methods discussed in Section 4.3.2.2 are used to generate a series of predictions from which an input uncertainty is estimated (Equation 4-15). The input parameters that are considered in the input uncertainty assessment are to be justified in the pre-test analysis.

#### 4.5.4.2.2 Numerical Uncertainty

There is no numerical uncertainty in the AR calculation method, so this term is zero for the purpose of the pre-test and post-test analyses.

#### 4.5.4.2.3 Measurement Uncertainty

Measurement uncertainty is estimated in the pre-test prediction and a final evaluation is performed in the post-test assessment. Depending on the maturity of the test design at the time of the pre-test prediction, engineering judgment is used to estimate measurement uncertainty values. In this event, appropriate assumptions are made that are reasonable both in terms of the test design and the ability to validate the design analysis. The results of the pre-test prediction are used to identify any changes that need to be incorporated into the detailed test design to accommodate reasonable measurement uncertainty. Open items are established to track the assumption until it has been incorporated.

In the post-test analysis, the measurement data uncertainty is used directly as provided by the test and no other action is required. In the pre-test analysis, a propagation calculation is performed to obtain  $u_D$  (Section 4.1) similar to the approach for estimating input uncertainty.

#### 4.5.4.3 Estimate Uncertainty in Safety Margin

Margin to the AR acceptance criterion of Strouhal number is calculated as follows:

$$SF_{AR} = \frac{cd_i}{(0.62)4(L_v + 0.3d_i)V} - 1 \quad \text{Equation 4-29}$$

The uncertainty in Equation 4-29 is primarily from input parameters and variables that are measured during the startup test at a single location susceptible to AR. Table 4-12 discusses the influential parameters that contribute to the uncertainty in safety margin. The process in Section 4.3.1 is used to determine the analytically predicted allowable range for the safety margin. Hence, Equation 4-29 is re-written as:

$$SF_{AR} = \frac{X_1 X_2}{4(X_3 + 0.3X_2)X_4 X_5} - 1 \quad \text{Equation 4-30}$$

Table 4-13 shows the details of performing the calculation on Equation 4-30.



Table 4-12 Decay heat removal system steam pipe inputs to acoustic resonance margin calculation

Input Parameter	Basis
Speed of sound	In analysis space, the speed of sound is evaluated as a function of steam pressure and temperature in the rigid piping. During NPM steady-state operation and startup testing, the thermodynamic properties of the steam fluctuate about a mean. Accordingly, changes in pressure or temperature are accounted for in the speed of sound.
Local flow velocity at tee in pipe	This input parameter is evaluated from the total secondary mass flow rate, steam density, and flow area of pipe to obtain an average value. During NPM steady-state operation and startup testing it is probable that the local velocity is slightly different due to thermodynamic fluctuations, turbulence, or geometry effects (e.g., effect of upstream elbow).
Length of closed branch pipe	This parameter is measured during construction or in the test setup based on the as-built configuration.
Inside diameter connected to tee junction	This parameter is measured during construction or in the test setup based on the as-built configuration.
Strouhal Number	Specific geometric considerations are used to determine the best-estimate value and uncertainty range for the Strouhal number.

Table 4-13 Decay heat removal system steam pipe acoustic resonance margin uncertainty method

Step	Description	Procedure
$\theta_1$	Analytic derivative of Equation 4-30 with respect to $X_1$	$\frac{0.403X_2}{(X_3 + 0.3X_2)X_4X_5}$
$u_{x1}$	Uncertainty in $X_1$	Uncertainty in the speed of sound is estimated based on the range of possible pressures, temperature and flow rates in the test.
$\theta_2$	Analytic derivative of Equation 4-30 with respect to $X_2$	$\frac{0.403X_1X_3}{(X_3 + 0.3X_2)^2 X_4X_5}$
$u_{x2}$	Uncertainty in $X_2$	Uncertainty in the inner diameter of the cavity piping.
$\theta_3$	Analytic derivative of Equation 4-30 with respect to $X_3$	$\frac{-0.403X_1X_2}{(X_3 + 0.3X_2)^2 X_4X_5}$
$u_{x3}$	Uncertainty in $X_3$	Uncertainty in the length of the cavity.
$\theta_4$	Analytic derivative of Equation 4-30 with respect to $X_4$	$\frac{-0.403X_1X_2}{(X_3 + 0.3X_2)X_4^2 X_5}$
$u_{x4}$	Uncertainty in $X_4$	Uncertainty in the steam flow velocity.
$\theta_5$	Analytic derivative of Equation 4-30 with respect to $X_5$	$\frac{-0.403X_1X_2}{(X_3 + 0.3X_2)X_4 X_5^2}$
$u_{x5}$	Uncertainty in $X_5$	Uncertainty in the Strouhal number.
$u_R$	Equation 4-11	$\sqrt{(\theta_1 u_{x1})^2 + (\theta_2 u_{x2})^2 + (\theta_3 u_{x3})^2 + (\theta_4 u_{x4})^2 + (\theta_5 u_{x5})^2}$

## 4.6 Experimental Bias Considerations

Some of the NuScale CVAP tests are performed on prototypic mockups of the NPM components, as opposed to in-situ with the plant at normal operation. The following tests have reasonable differences from the plant configuration:

- Steam generator FIV testing is performed on a full-size subset of the total number of tubes corresponding to the 9<sup>th</sup> to 13<sup>th</sup> columns of the actual steam generator. Unheated water flow about the tubes (on the outside) provides the excitation forces, and no fluid is present within the tubes (on the inside).

### 4.6.1 Steam Generator Testing

The geometry of the helical coil tubes used in the FIV testing is identical to the components used in the NPM. The boundary conditions in terms of supports and structural interactions (i.e., interfaces with other components) are also similar. The water flow in the reactor primary side is simulated by water entering the lower part of the inner vessel, rising upwards and turning at the top into the annulus to cross the tube bundle in a downward sense. Nonetheless, there are practical considerations that make the test specimen differ from the NPM so those differences are considered. The following features introduce bias into the design analysis that relies on test measurements:

- The circulating water on the exterior of the tubes is at room temperature
- The helical coil tubes are not filled with boiling water, but contain instruments and cables
- The test specimen contains five tube columns instead of twenty-one in the full assembly.

The objective of the testing is to collect data and confirm that VS and FEI are not active, that inputs to the analysis of the different FIV mechanisms (e.g., natural frequency, damping ratio, and so on) are justified, and that vibration amplitude predictions for TB are bounding.

#### 4.6.1.1.1 Approach for Testing and Confirmation of Turbulent Buffeting Characteristics

The natural frequency in water is a parameter in the calculation of safety margin against fatigue from alternating stress induced by random vibrations on the SG tubes, and its uncertainty is accounted for by comparison of simulations and measurements. The simulation accurately models the empty tube and specify the appropriate water temperature as the test to make the comparison valid.

The structural or operating features of the test that deviate from the NPM design result in a different average frequency as determined in the design analysis. Therefore, the modal analysis of the test apparatus is compared to the modal analysis of the NPM to understand any differences.

The effective mass of tube is another parameter that is affected by the test vs. NPM differences. Its influence on vibration appears in the measured frequency and mean square displacement amplitude. As discussed earlier, the pre-test prediction determines the modal characteristics and compares to the design analysis. Lastly, the maximum RMS displacement is a parameter in the safety margin calculation for the design analysis. The methodology uses an upper bound PSD approach from literature, so the expectation is that measured RMS responses are less than in the pre-test prediction (i.e., positive bias).

To comprehensively consider the uncertainty in RMS displacement, the PSD analysis is validated against the recorded dynamic pressure data in the test to confirm that the literature approach is bounding for the HCSG under prototypical NPM velocities. Numerical evaluation of the differences between the literature PSD and the benchmarked PSD from the test is performed to quantify the uncertainty and incorporate any bias.

#### **4.6.1.1.2 Approach for Testing and Confirmation of Vortex Shedding Characteristics**

The signature of VS is a periodic oscillation in the pressure field that translates to a distinct frequency in the PSD. If the frequency of the periodic driving force matches the natural frequency of a tube, then resonance occurs and the amplitude of the vibration becomes significant. Vortex shedding characteristics in terms of the coherent structure of the eddies are strongly dependent on Reynolds number.

The SG testing, although on a subset of the total number of tubes, allows detection of this phenomenon if it occurs for a range of velocities that are considered based on flow rate changes with power in the NPM. The differences relative to the NPM design in terms of circulating water temperature and empty tubes, and their potential impact on VS are considered as follows:

- The water temperature affects the fluid density and viscosity, which influence the Reynolds number (the tube diameter and flow speed are similar to NPM conditions). Therefore, the pre-test prediction evaluates those changes in Reynolds number, and ensures that the test specifies sufficient flow rate changes to cover the possible range of Reynolds number at plant conditions.
- The vibration mode shape and natural frequency of the tube are important parameters that affect the tube's response to periodic flow excitations and potential for phase synchronization. As discussed earlier, the pre-test prediction determines the modal characteristics of the test apparatus and compares to the design analysis.

#### **4.6.1.1.3 Approach for Testing and Confirmation of Fluid Elastic Instability Characteristics**

Fluid elastic instability is an intense vibration regime that causes significant motion and tube wear much greater than vibration caused by turbulence. Analytically, the onset of FEI is determined when the pitch velocity is greater than an empirically established critical velocity (evaluated using Connors' coefficient). In order to comprehensively consider other parameters that may be affected by experimental biases, the following are evaluated:

- The effective pitch velocity is dependent on the vibration mode and natural frequency of the tube. The pre-test prediction determines the modal characteristics of the test apparatus and compares to the design analysis. The comparison ensures that the test specifies sufficient flow rate changes to compensate for any differences that result in a decrease of the reduced pitch velocity in the test relative to the NPM design.
- The critical velocity is dependent on the tube's total mass per unit length (including hydrodynamic mass), damping ratio, and density, which may deviate from the normal operating state. The damping ratio is a measured variable, so its value and associated uncertainty will be used directly in the range of safety margin calculation. The empty tubes provide a positive bias because that reduces the critical velocity (mass is in the numerator), and hydrodynamic mass is approximately 1/10 the metal mass. On the other hand, the test temperature provides a negative bias (density is in the denominator) because the test water density is greater than in the NPM. Therefore, the pre-test prediction compares values of the critical velocity calculated for the test apparatus and the NPM design.

#### 4.7 Expected Results and Validation Range of Experimental Results

The purpose of the pre-test prediction is to calculate the expected experimental results and determine a range of results that are acceptable to validate the design analysis. If the experimental design exactly matches the conditions of the design analysis, and if there were no errors in the experimental measurements or modeling, the experimental result would exactly match the design analysis result.

Distortions exist for most experiments, and the effect of the positive and negative distortion values on the range of validation safety margins and experimental results is determined. For example, testing at a lower pressure than the pressure associated with the limiting design condition is considered a distortion, if pressure affects the results of the analysis. To quantify the effect of the distortion, the design analysis calculation is re-performed, using the standard design analysis methods, at the test pressure and a new safety margin is determined. The difference between the best-estimate safety margin and the safety margin determined at the test pressure is the distortion adjustment. If the testing condition is more limiting than the design analysis condition, the value of the adjustment is positive and increases the validation range. Each distortion is individually calculated and then the safety margins are added together in Equation 4-31.

The input, numerical and measurement uncertainties are calculated based on the guidelines in Section 4.5.1. These uncertainties are calculated in terms of the safety margin and are combined in Equation 4-31.

The effect of the design analysis safety margin, distortions and uncertainties on the allowable range of the safety margin is described by Equation 4-31. The design analysis safety margin is provided as an upper bound to the range to provide a reasonable cutoff for the validation. For the lower bound of the range, the design analysis safety margin is not considered to ensure that even accounting for uncertainties there is positive margin to the onset of the phenomena at normal operating conditions. The expected results for the critical measured parameter should be documented, and a validation range using the result of Equation 4-31 for that parameter should be specified. The expected results for

each measured parameter are documented, and an allowable validation range using the result of Equation 4-31 for that parameter specified.

$$Range_{Upper} = SM_{BE} - \Delta SM_d + SM_{DA} + \Delta SM_u$$

Equation 4-31

$$Range_{Lower} = SM_{BE} - \Delta SM_d - \Delta SM_u$$

Where,

$Range$  = Range of safety margins for validation (%),

$SM_{BE}$  = Best-estimate safety margin (%),

$SM_{DA}$  = Safety margin from the design analysis (%),

$\Delta SM_d$  = Safety margin adjustment from distortions (%), and

$\Delta SM_u$  = Safety margin adjustment from total uncertainty (%).

Note that it could be possible to justify a higher upper bound for the validation range, since an experimental result that falls above the upper bound indicates that there are un-realized conservatisms in the design analysis. Particularly for design analysis results with small safety margins or known, highly conservative inputs, this approach should be considered to determine an alternate upper bound instead of the approach provided in Equation 4-31.

#### 4.8 Summary

The NuScale Power CVAP Measurement Program relies on diverse testing campaigns to verify the structural integrity of NPM components that are evaluated in the Analysis Program to have a margin of safety less than 100 percent. This report provides an approach to validate the analysis methods against the experimental results, and methodologies to quantify bias and uncertainty embodied with the results of the design analyses and the measurement program. Table 4-14 summarizes the components discussed in the body of the report, and their analysis validation approach.

When testing is complete, post-test analysis is performed to assess the experimental results and finalize the validation effort. The pre-test prediction provides a level of confidence in the test design and its ability to validate the design analysis. Any differences between the pre-test predictions and experimental results will be adjudicated in the post-test analysis.

Table 4-14 Summary of components and flow induced vibration analysis validation methods

Component	FIV Mechanism	Validation Test	Margin Relative To	Variables with Uncertainty to be Measured
DHRS Steam Pipe	AR	Initial Startup	Critical Strouhal Number	Speed of sound
				Flow velocity
				Cavity diameter and length
SG	VS	Prototypic	Reduced Damping	Tube diameter and mass
				Mode shapes and natural frequencies
				Damping ratio in air
SG	TB	Prototypic	Impact Fatigue Usage	Tube diameter and mass
				Mode shapes and natural frequencies
				Mean square response
				PSD
SG	FEI	Prototypic	Stability Ratio	Damping ratio in water
				Flow velocity
				Mode shapes and natural frequencies
				Tube diameter and mass
				Damping
				Primary fluid density

## 5.0 Validation Tests

The following sections provide a summary of the validation testing planned for the steam generator, SG IFR, and DHRS steam tee. The test design, as specified in the testing needs document, is discussed for each test. For the SG and DHRS tests, the results of the pre-test prediction calculations are also provided.

### 5.1 TF-3 Validation Test

#### 5.1.1 TF-3 Testing Overview

The general objective of the TF-3 test is to obtain vibration test data for a prototypical NuScale HCSG for validation of FEI, VS, and TB design analyses. The specific test program objectives are:

1. Determine in-air natural frequencies and mode shapes of the HCSG tubes; this includes ability to characterize modes of the tube bundle assembly (synchronized motion of full tube bundle and supports).
2. Determine in-water natural frequencies and mode shapes of the HCSG tubes and supports; this includes ability to characterize modes of the tube bundle assembly (synchronized motion of full tube bundle and supports).
3. Determine in-air and in-water damping values for a range of representative mode frequencies and vibration amplitudes.
4. Obtain data to characterize primary flow dynamic pressure fluctuations, SG tube and tube support vibration amplitudes for a range of primary flow conditions.
5. Obtain high flow rate vibration amplitudes to demonstrate margins to FEI and VS.

The TF-3 test program consists of modal testing during the fabrication process, modal testing on the completed test assembly, and flow testing as shown in Table 5-1.

Table 5-1 Summary of tests

Test	Type
In-air natural frequencies and mode Shape testing (during fabrication)	Partial-tube array
In-air damping tests (during fabrication)	Partial-tube Array
In-air natural frequencies and mode Shape testing	Full-tube Array
In-air damping tests	Full-tube array
In-water natural frequencies and mode Shape testing	Full-tube array
In-water damping tests	Full-tube array
Steady-state flow testing	Full-tube array, flow
VS flow testing	Full-tube array, flow
FEI flow testing	Full-tube array, flow

Individual tube testing is performed during fabrication of the test specimen. Testing is performed following installation of a complete helical column, but before installation of the

next column. Temporary support rings are used during this testing to simulate the restraint provided by the riser in a fully-assembled tube bundle. This testing includes measurements using both permanently-installed and temporarily-mounted accelerometers.

Individual tube testing during assembly allows exploration of the various boundary conditions that may exist. Access limitations exist in a fully-assembled tube bundle array test, both for instrumentation placement and for means to perform excitation of tubes. Single-tube tests allow greater ability to examine variability in boundary conditions between tubes, based on the flexibility to use temporary, removable accelerometers that can be iteratively employed. Permanent sensor arrangement in the tube array cannot be altered once the array is constructed. Performing modal measurements during fabrication allows confirmation that sensor function is as expected.

Tube array testing is performed using a representative tube bundle array, constructed using prototypic supports. Array testing includes in-air modal and damping tests, performed as part of individual tube testing during fabrication of the test specimen. The array testing also includes in-water modal and damping tests and flow testing over the full range of nominal design operating conditions, as well as at FEI and VS on-set conditions. This testing is a comprehensive performance demonstration of the FIV design of the NuScale SG.

A full-array test provides the most prototypic platform to characterize modal frequencies, shapes and damping for the NuScale design. In order to directly evaluate FEI, VS or confirm primary side flow PSDs for the NuScale design, flow testing of a prototypic tube array is necessary.

#### 5.1.1.1 TF-3 Test Specimen

The scope of the TF-3 test is the SG (including tubes and tube support structures) both as a fully-assembled tube array and during the fabrication process at points where full-helical columns are installed. This section identifies the design aspects that must be prototypic.

##### Temporary Supports for Individual Tube Testing during Fabrication

The in-process tube array is used for testing during fabrication; therefore, requirements for the full tube array (described in the following section) apply. The only physical modification for the tube array for this testing is that a temporary support structure is needed to simulate the constraint provided by the riser in a fully assembled tube bundle. This structure is designed to interface with the innermost installed column of tube supports. This structure is adjustable to allow variation in the applied compression and to allow use at various intermediate steps in the specimen fabrication (i.e., be able to be deployed as each column is installed, and so on).

##### Full-Tube Array Testing

Confinement of flow through the SG tube bundle is represented, with a prototypic upper riser (including riser-to-SG-tube-support clearance) and reactor vessel (including vessel-to-SG-tube-support clearances). The full test specimen includes a mechanism to provide



adjustable compression of the tube supports between the riser and the vessel wall. This mechanism is functional (including ability to adjust compression) during testing conditions, including flow testing. Prototypic geometry upstream of the SG is maintained by representing fluid confinement from the outlet of the riser to the inlet of the SG tube bundle. Flow downstream of the SG is maintained as “balanced” annular flow using a pressure drop plate or other feature to remove the effect of any constrictions (transition of flow from an annulus to an exit pipe or plenum) at the outlet of the test fixture.

The design of the SG tube array itself, including tube geometry and length, design of tube supports and physical interfaces between the tubes and tube supports and the riser and vessel (interfaces), is fully prototypic unless otherwise noted below. The only allowable departure from prototypic design geometry is that only helical Columns 9 through 13 are included. This implicitly requires the diameter of the riser and vessel to be scaled accordingly so that prototypic gaps between the riser and vessel, and between the inner and outer tube columns, are maintained. Other minor allowed deviations are described below. The design of tube array test fixture is in accordance with Table 5-2.

Table 5-2 Tube array design geometry

Drawing	Design Elements
Steam generator	<ul style="list-style-type: none"> <li>• SG tube geometry (including OD and wall thickness)</li> <li>• SG tube arrangement (e.g., pitch)</li> </ul>
Feed plenum access port	<ul style="list-style-type: none"> <li>• Feed plenum tube layout</li> <li>• Geometry of vessel and tubesheet</li> </ul>
Steam generator tube supports	<ul style="list-style-type: none"> <li>• SG tube supports</li> </ul>
Upper RPV section	<ul style="list-style-type: none"> <li>• Steam plenum tube sheet layout</li> <li>• Upper and lower SG supports</li> <li>• Upstream SG flow geometry (pressurizer baffle plate)</li> <li>• Downstream SG flow geometry (riser)</li> <li>• Interface between outer column tube supports and the vessel; this implicitly includes maintaining prototypic separation between outermost tube column and vessel</li> </ul>
Reactor vessel internals – upper riser	<ul style="list-style-type: none"> <li>• Interface between inner column tube supports and riser; this implicitly includes maintaining prototypic separation between innermost tube column and riser.</li> <li>• Riser geometry and supports (upstream SG flow geometry)</li> <li>• Downstream SG flow geometry (riser)</li> </ul>

The tubes in the test fixture include the entire helix, transition, and straight lengths. A general summary of tube requirements for this test are provided in Table 5-3. Tube lengths upstream of the shell-side face of the feed plenum and downstream of the shell-side face of the steam plenum are reduced because a reduced number of columns are being tested and this affects the interface with the plenums.

Table 5-3 Helical steam generator tube array details

Helical Column	# of Tubes	Helical Radius (in.)	NuScale Part #	Length (in.)
9	{{			}} <sup>2(a),(c)</sup>
10	{{			}} <sup>2(a),(c)</sup>
11	{{			}} <sup>2(a),(c)</sup>
12	{{			}} <sup>2(a),(c)</sup>
13	{{			}} <sup>2(a),(c)</sup>

The SG tubes for this testing use 304 or 316 stainless steel or other materials as proposed by the supplier and approved by NuScale. The SG tubes are 0.625-inchOD with a 0.050-inch wall thickness.

Test facility operating conditions are provided in Table 5-4.

Table 5-4 TF-3 test facility operating conditions

Parameter	Maximum	Minimum	Nominal
Primary-side temperature <sup>(1)</sup>	{{		}} <sup>2(a),(c)</sup>
Primary-side pressure <sup>(2)</sup>	{{		}} <sup>2(a),(c)</sup>
Primary-side flow	{{		}} <sup>2(a),(c)</sup>
Secondary-side temperature	{{		}} <sup>2(a),(c)</sup>
Secondary-side pressure	{{		}} <sup>2(a),(c)</sup>
Secondary-side flow	{{		}} <sup>2(a),(c)</sup>

Notes:

- (1) Maximum primary-side temperature is based on accommodating heatup due to flow resistance without the need for dedicated cooling. Maximum design temperature may be reduced provided required flow rates are accommodated.
- (2) Maximum primary-side pressure is based on providing margin to accommodate required flow. Maximum design pressure for test fixture or system may be reduced, provided required flow rates are accommodated.
- (3) This volumetric flow corresponds to a gap velocity of {{ }}<sup>2(a),(c)</sup>.
- (4) This volumetric flow corresponds to a gap velocity of {{ }}<sup>2(a),(c)</sup>. Lower minimum flow capacity is acceptable. The minimum flow requirement is based on allowing flexibility in selecting pump and pump controls. Testing at flows less than minimum flow are not planned.

### 5.1.1.2 TF-3 Test Instrumentation and Data Acquisition

The purpose of the TF-3 test is to obtain data on the vibration characteristics of the SG tubes; therefore, most test instrumentation is applied to the SG tubes, with a secondary emphasis on the tube supports and the vessel. Both strain gauges and accelerometers are used to characterize tube vibration amplitudes and associated frequencies:

- PCB Piezotronics (Model number W356A03, 10mV/g sensitivity, 2-5000Hz frequency range) tri-axial accelerometers are used for tube accelerometer instrumentation.

- Strain gauges (HBM 1-LY65-3/350) are used for tube strain gauge instrumentation.

A total of eight tubes selected from Columns 9, 11 and 12 are instrumented. Two tubes are permanently instrumented with strain gauges and accelerometers, four tubes are instrumented with accelerometers only, and two tubes are instrumented with strain gauges only. Based on the potential for varying boundary conditions (fixed, pivot, hybrid of pivot and fixed) for any given tube or span, the general approach for instrumentation is to provide some instrumentation on as many spans as possible to maximize the capability to capture measurements of the full possible range of tube vibration modes.

The total number of instrumented tubes and the distribution of instrumentation among the selected tubes provides a balance between obtaining intensive data for a representative number of tubes (tubes with both strain gauges and accelerometers), having the capability to assess any influence of the types of instrumentation on data obtained (mix of tubes instrumented with only one or both types of instruments), and obtaining data on a broader sample of tubes (spreading total available instrumentation among a greater total number of tubes). There was also a preference to place instrumentation in spans that have an exciter coupling (or are proximate to the coupled spans) and a need to place multiple accelerometers on some spans to better characterize some higher order modes (anti-node(s) occur within the span, not only at supports) that have high relative mass participation factors.

Each of the six instrumented tubes have a maximum of 10 accelerometers based on instrument cable constriction limitations. Accelerometers are placed in locations expected to have the largest vibration magnitude for the most dominant (highest mass participation factor) modes. For three accelerometer-instrumented tubes (one in each instrumented column), two accelerometers are designated for placement at a tube support, to ensure capability to detect rigid body motion. There are accelerometers placed on the tube supports that are paired with the tube accelerometers placed at a support.

Strain gauges are placed in pairs at a given location, with one strain gauge on the tube extrados (oriented along major axis of the tube, on outside of major curvature) and one strain gauge on the "top" of the tube (oriented along major axis of the tube, 90 degrees diametrically offset from extrados). These pairs of placements will characterize the maximum strains associated with tube bending deflections perpendicular to the axis of the tube at a given location. Specific placement of strain gauges is based on locations of maximum predicted strain associated with most dominant tube frequencies (maximum mass participation factor).

Detailed descriptions of the specific instrument locations on each tube are provided in the following sections. The general basis for the selection of the tubes for instrumentation is as follows:

- Column 12. Based on progress of test specimen fabrication, Column 12 and Column 13 have already been fully installed, but no instrumentation was included. It is feasible to remove tube(s) from either end of the row of tubes installed at each of the four plenums in Column 12 to add instrumentation. Instrumentation of any tubes in Column 13 requires extensive disassembly of the specimen and is not practical. Because the

outermost tube column has the highest susceptibility to FEI, two tubes from Column 12 are to be instrumented to provide the capability to characterize FEI.

- Column 11. The center column of the tube bundle is the most removed from the tube bundle interfaces (vessel and riser wall) and should represent the most “nominal” flow conditions. Design of the test specimen included access ports that allow coupling up to four tubes to harmonic exciters. Therefore, four tubes are selected for instrumentation in this column to provide the greatest amount of instrumentation in the most representative column and to allow maximum utilization of the harmonic exciter. The harmonic exciter is the only means of performing modal measurements on tubes in the fully-assembled test specimen.
- Column 9. This is the innermost tube column in the specimen. In order to fully characterize the vibration response of the tube bundle, any potential variations in vibration response due to flow differences along the perimeter (i.e., riser surface) are assessed. Two tubes are selected for instrumentation in this column. Tubes at the bottom periphery of the tube bundle (including the tubes in the innermost column) are potentially susceptible to VS.

A summary of instrumented tubes is provided in the following tables. Figures representing the physical layout of the instruments along each tube are provided in Appendix A.

Table 5-5 Instrumented tubes (accelerometers and strain gauges)

Test Tube #	Tube Part Number	Location Description	Notes
1	A014.1101	Column 11, tube 1 at steam plenum 4 (305.4°)	This corresponds to the position of Instrumented tube N.1.
2	A014.1116	Column 11, tube 16 at steam plenum 2 (144.6°)	This corresponds to the position of Instrumented tube N.16.

Table 5-6 Instrumented tubes (accelerometers only)

Test Tube #	Tube Part Number	Location Description	Notes
3	A014.0915	Column 9 tube 15 at steam plenum 1 (~45°)	To evaluate VS
4	A014.0916	Column 9 tube 16 at steam plenum 1 (~45°)	To evaluate VS
5	A014.1201	Column 12, tube 1 at steam plenum 3 (~225°)	To evaluation limiting location for FEI
6	A014.1202	Column 12, tube 2 at steam plenum 3 (~225°)	To evaluation limiting location for FEI

Table 5-7 Instrumented tubes (strain gauges only)

Test Tube #	Tube Part Number	Location Description	Notes
7	A014.1102	Column 11, tube 2 at steam plenum 4 (307.1°)	This corresponds to the position of Instrumented tube N.2.
8	A014.1115	Column 11, tube 15 at steam plenum 2 (144.3°)	This corresponds to the position of Instrumented tube N.15.

At least ten tri-axial accelerometers, including mounts and adapters suitable to support removable placement at various locations on individual tubes, are available for modal testing to be performed during test specimen fabrication. Removable accelerometer specifications are recommended by the supplier and approved by NuScale. Tri-axial accelerometers are used for permanent instrumentation of the tubes. Higher sensitivity (100 mV/g) is desired for the testing using removable accelerometers.

Instrumented tubes (Columns 9, 11 and 12) contain 3.75 helical turns, which result in a total of 31 tube spans (length of tubing between two adjacent support) for each tube. Based on the non-symmetric placement of the tube supports, spans are alternatively “long” (64-degree arc) and “short” (26-degree arc). The first and subsequent odd-numbered spans are “long” and even-numbered spans are “short.” For the purpose of identifying instrument locations for the test specimen, instrument locations are identified to a specific span, based on numbering that originates at the steam plenum. The steam plenum numbering is based on FW plenum 1 being oriented at 45 degrees with the steam plenum numbering proceeding in a clockwise direction (steam plenum 2 is located at 135 degrees, and so on). For example, Span 1 is a long span and represents the tube span from the FW plenum steam tubesheet to the first support (e.g., steam transition bend). Span 31 is also a long span and represents the span of tubing from the last support to the FW tubesheet.

Likewise, SG tube support circumferential position #1 is designated as corresponding to the tube support located immediately counter-clockwise from steam plenum 1 and SG tube support numbering proceeds in a clockwise manner, such that positions #1 and #2 are on each side of steam plenum 1. Figure A-1 provides a figure illustrating this numbering scheme.

Accelerometer placement is in accordance with the following tables and figures. Figures A-1 through A-6 show physical placements of each accelerometer along the tube length and Figure A-10 provides a composite view of the accelerometer placements.

Table 5-8 Accelerometers placement for instrumented tube #1

Accelerometer	Location	Notes
A1	Span 1 (steam transition), mid-span	Fundamental mode (fixed)
A2	Span 11: mid span	To detect prevalent fixed and pivot lower order modes
A3	Span 14/15 at support	To monitor for rigid body motion of the tube, e.g., movement of the tube due to FIV of the tube support (to which the tube is coupled), so that this can be differentiated from FIV of the tube itself.
A4	Span 15: 1/3 span	Span 15 has harmonic exciter coupling (nozzle N3)
A5	Span 15: 1/2 span	
A6	Span 25: mid span	To detect prevalent fixed and pivot lower order modes
A7	Span 26/27 at support	To monitor for rigid body motion of the tube
A8	Span 27: 1/3 span	To detect higher order modes, proximate
A9	Span 27: 1/2 span	to exciter location
A10	Span 29: mid span	Span 29 has harmonic exciter coupling (nozzle N1), VS susceptible location

Table 5-9 Accelerometers placement for instrumented tube #2

Accelerometer	Location	Notes
A11	Span 1 (steam transition): mid-span	
A12	Span 3: 1/3 span	Span 3 has harmonic exciter coupling (nozzle N4)
A13	Span 3: 1/2 span	
A14	Span 13: 1/3 span	To detect prevalent fixed and pivot higher order modes, proximate to exciter
A15	Span 13: 1/2 span	
A16	Span 15: mid span	Span 15 has harmonic exciter coupling (nozzle N2)
A17	Span 17: mid span	To detect prevalent fixed and pivot lower order modes, proximate to exciter
A18	Span 25: mid span	To detect prevalent fixed and pivot lower order modes, proximate to exciter
A19	Span 26: mid span	To detect response of short spans
A20	Span 27: mid span	To detect prevalent fixed and pivot lower order modes, proximate to exciter

Table 5-10 Accelerometers placement for instrumented tube #3

Accelerometer	Location	Notes
A21	Span 1 (steam transition): mid span	Fundamental beam mode
A22	Span 7: 1/3 span	To monitor for prevalent higher order modes
A23	Span 7: 1/2 span	
A24	Span 11: mid span	To monitor for prevalent first order modes
A25	Span 13: mid span	To monitor for prevalent first order modes
A26	Span 23: 1/3 span	To monitor for prevalent higher order modes
A27	Span 23: 1/2 span	
A28	Span 27: mid span	To monitor for prevalent first order modes
A29	Span 30: mid span	First short span from feed transition, susceptible to VS
A30	Span 31 (feed transition): mid span	VS shedding susceptible location, fundamental mode response (fixed)

Table 5-11 Accelerometers placement for instrumented tube #4

Accelerometer	Location	Notes
A31	Span 7: mid span	
A32	Span 13: 1/3 span	To monitor for prevalent higher order modes
A33	Span 13: 1/2 span	
A34	Span 13/14 at support	To monitor for rigid body motion of the tube
A35	Span 15: mid span	To monitor for prevalent first order modes
A36	Span 21: mid span	To monitor for prevalent first order modes
A37	Span 22/23 at support	To monitor for rigid body motion of the tube
A38	Span 23: mid span	To monitor for prevalent first order modes
A39	Span 29: mid span	First long span from feed transition, susceptible to VS
A40	Span 31 (feed transition): mid span	VS shedding susceptible location, fundamental mode response (fixed)

Table 5-12 Accelerometers placement for instrumented tube #5

Accelerometer	Location	Notes
A41	Span 1 (steam transition): mid span	Fundamental mode (pivot)
A42	Span 5: mid span	
A43	Span 7: 1/3 span	To monitor for higher order modes
A44	Span 7: 1/2 span	
A45	Span 9: mid span	
A46	Span 21: mid span	
A47	Span 22: mid span	To monitor for first order response mode of short span
A48	Span 23: mid span	
A49	Span 29: mid-span	VS shedding susceptible location
A50	Span 31 (feed transition): mid-span	VS shedding susceptible location

Table 5-13 Accelerometers placement for instrumented tube #6

Accelerometer	Location	Notes
A51	Span 1 (steam transition): mid span	Fundamental mode (pivot)
A52	Span 13: mid span	
A53	Span 13/14 at support	To monitor for rigid body motion of the tube
A54	Span 15: 1/3 span	
A55	Span 15: 1/2 span	
A56	Span 21: mid span	
A57	Span 23; 1/3 span	To monitor for higher order modes
A58	Span 23: 1/2 span	
A59	Span 23/24 at support	To monitor for rigid body motion of the tube
A60	Span 25: mid span	

A total of 32 uni-axial strain gauges are mounted on SG tubes as shown in Table 5-14. Appendix A Figures A-1, A-2, A-7, and A-8 show physical placements of each strain gauge along the tube length and Figure A-10 provides a composite view of strain gauge placements. Strain gauge placements are based on measuring strains associated with most prevalent vertical modes. Strain gauges are generally placed in spans that do not include accelerometers. This is both to increase the extent of specimen that contains at least some instrumentation and to minimize potential impact of instrumentation on measurements (heavily concentrating instrumentation in a single span further alters vibration response as compared to a span with no added mass due to instrumentation).



Table 5-14 Tube strain gauge placements

Instrumented Tube #	Strain Gauge Number	Location	Notes
#1, column 11, tube 1	S1, S2	Span 1, at steam plenum tubesheet face	{{ }} <sup>2(a),(c)</sup>
	S3, S4 S5, S6	Span 15, each end, as close as practical to tube support	-
	S7, S8	Span 31, at feed plenum tubesheet	{{ }} <sup>2(a),(c)</sup>
#2, column 11, tube 16	S9, S10	Span 16, mid-span	{{ }} <sup>2(a),(c)</sup>
	S11, S12	Span 17, mid-span	{{ }} <sup>2(a),(c)</sup>
	S13, S14 S15, S16	Span 27, each end, as close as practical to tube support	{{ }} <sup>2(a),(c)</sup>
	S17, S18	Span 11, mid-span	-
#7, column 11, tube 2	S19, S20 S21, S22	Span 13, each end, as close as practical to tube support	{{ }} <sup>2(a),(c)</sup>
	S23, S24	Span 31, at feed plenum tubesheet	{{ }} <sup>2(a),(c)</sup>
	S25, S26 S27, S28	Span 15, each end, as close as practical to tube support	{{ }} <sup>2(a),(c)</sup>
#8, column 11, tube 15	S29, S30	Span 31, at tube support	{{ }} <sup>2(a),(c)</sup>
	S31, S32	Span 31, at tubesheet	{{ }} <sup>2(a),(c)</sup>

There are six SG tube accelerometers (as shown in Table 5-15) that are coincident with a SG tube support. An accelerometer is placed on the corresponding tube support at a location coincident (to the extent practical) with each of these SG tube accelerometers.

Table 5-15 Steam generator tube support accelerometer

SG Tube Accelerometer	Instrumented Tube #	Column	Corresponding SG Tube Support Position (Circumferential)	Radial Tube Support Position (Radial)
A3	1	11	Circumferential position #5	SG tube support between Col 11/12
A7	1	11	Circumferential position #1	SG tube support between Col 11/12
A34	4	9	Circumferential position #6	SG tube support between Col 9/10
A37	4	9	Circumferential position #6	SG tube support between Col 9/10
A53	6	12	Circumferential position #1	SG tube support between Col 12/13
A59	6	12	Circumferential position #7	SG tube support between Col 12/13

Based on Table 5-15, there are a total of four upper and lower SG supports (at circumferential locations #1, #5, #6 and #7) that have corresponding tube accelerometers to monitor for rigid body motions of the SG tube supports. Accelerometers are placed on both the upper and lower SG supports at each of these locations (eight accelerometers).

Likewise, a paired accelerometer is placed on the SG tube support along with each of these accelerometers (eight accelerometers).

Sixteen accelerometers are placed on the vessels to evaluate potential modal responses of the entire test specimen. Based on pre-test modal analysis, depending on the boundary conditions that exist, the vessel shells respond in beam modes  $\{\{ \dots \}^{2(a),(c)}$ , shell modes  $\{\{ \dots \}^{2(a),(c)}$  or torsional modes  $\{\{ \dots \}^{2(a),(c)}$ . Eight inside of the inner vessel (i.e., riser), two sets of four accelerometers (at approximately 1/10, 2/5, 3/5 and 9/10 heights, vertically in-line), offset circumferentially by 90 degrees. Eight outside of primary vessel, two sets of four accelerometers (at approximately 1/10, 2/5, 3/5 and 9/10 height vertically in-line), offset circumferentially by 90 degrees.

The inner wall of the vessel is instrumented with 14 dynamic pressure transducers to characterize a turbulent pressure force PSD for steady flow conditions. Other sensors included in this test are documented in Table 5-16.

Table 5-16 Other pressure and temperature instrumentation

Measurement	Total Number	Description
Temperature	2	Primary-side inlet and outlet temperature
Pressure	5	Primary-side static pressure spaced over height
Differential pressure	4	Primary-side pressure drop spaced over height (pressure drop measurements are developed based on differentials between five pressure instruments)
Flow	2	Primary-side flow

For the purposes of this testing, frequencies up to 500 Hz are of interest; therefore, DAS sampling rates for modal and damping tests are at least 2000 Hz. Lower DAS operating frequencies are permitted for FEI and VS tests (these phenomena are associated with frequencies  $\{\{ \dots \}^{2(a),(c)}$ .

Damping tests require DAS capabilities to provide near real-time calculated damping measurements. This includes the DAS being pre-programmed to determine transfer function(s) for fixed exciter damping tests.

The DAS is capable of measuring both large-amplitude, slow-changing strain (i.e., “static” strain) and low-amplitude, rapid-cycling strain (i.e., “dynamic” strain). Evaluation of the FIV phenomena described herein requires only dynamic strains; however, knowledge of static strain changes and variations throughout testing may be of benefit in understanding boundary conditions at the support interface points. Before each dynamic strain measurement (e.g., damping, modal- or flow-test dataset), the static and average strains are measured to establish a baseline. In order to facilitate accurate measurement of both static and dynamic strains, the DAS includes one of the following features or equivalent

measures to address accurate measurement, as recommended by the testing organization and approved by NuScale:

- Capability to measure with high-range (low-gain) settings for static strains, output the analog (raw) signals, and use separate hardware to measure with low-range (high-gain) settings for dynamic strains (high-gain measurements is zero-centered for ease of data post-processing).
- Capability to auto-balance (null-calibrate) each channel, with procedures or software features to “re-zero” strain signals before each test series dataset (to avoid signal saturation). The DAS must record all such adjustments such that an accurate static strain representation can be reproduced.

### 5.1.1.3 Description of TF-3 Tests

#### 5.1.1.3.1 Partial-Tube Array Testing During Fabrication

In-air mode testing is performed on individual tubes in fully assembled columns during the fabrication process. Testing is performed after each of the columns containing permanently instrumented tubes (Columns 9, 11 and 12) is fully installed, including associated tube supports. Testing is performed with up to three variable levels of compression applied by temporary tube bundle supports. Testing with variable levels of support compression evaluates potential variations in frequency that could result from differences in the boundary conditions between the SG tubes and supports.

Tube excitation using impulse hammer strikes or other means such as a harmonic exciter, is utilized for partial-tube array testing performed during test specimen fabrication. Access to perform impulse tests is precluded once test specimen is fully assembled with the riser installed. Specific requirements for impulse hammer(s) necessary to provide measurable response for the test specimen tubes are provided by the testing services supplier and approved by NuScale.

Fixed point excitation capabilities using a harmonic exciter is provided for instrumented tubes #1, #2, #7 and #8 (column 11) through access nozzles N1, N2, N3, and N4. Fixed point excitation is only used for full-tube array tests (in-air and in-water modal and damping tests). The harmonic exciter is capable of providing a range of displacements and operating over a frequency range of at least 5 to 500 Hz.

Specific tubes and spans to be evaluated for these tests are in accordance with Table 5-17.

Table 5-17 Partial-tube array modal tests

Tube	Column	Description	Extent
Instrumented Tube #5	12	Permanently instrumented	Long spans, any short spans with permanent instrumentation
Instrumented Tube #6	12	Permanently instrumented	10 long spans (including long spans with permanent instrumentation), any short spans with permanent instrumentation
W12	12	Selected during testing based on loosely held tube	Four groups of five spans (long/short/long/short/long) selected to provide one group from near each end (feed and steam plenum tube sheets), and one group from both ~1/3 and ~2/3 of the full length of the test specimen
X12	12	Selected during testing based on tightly held tube	Four groups of five spans (long/short/long/short/long) selected to provide one group from near each end (feed and steam plenum tube sheets), and one group from both ~1/3 and ~2/3 of the full length of the test specimen
Multiple	12	Span(s) selected during testing. The tube segments in the span are evaluated to assess variability in boundary conditions (tubes exhibit frequencies associated with fixed, pivot or hybrid boundary conditions)	2 long spans, mode frequencies only
Instrumented Tube #1	11	Permanently instrumented	All long spans, any short spans with permanent instrumentation
Instrumented Tube #2	11	Permanently instrumented	Ten long spans (including any long spans with permanent instrumentation), any short spans with permanent instrumentation

Tube	Column	Description	Extent
W11	11	Selected during testing based on loosely held tube	Four groups of five spans (long/short/long/short/long) selected to provide one group from near each end (feed and steam plenum tube sheets), and one group from both ~1/3 and ~2/3 of the full length of the test specimen
X11	11	Selected during testing based on tightly held tube	Four groups of five spans (long/short/long/short/long) selected to provide one group from near each end (feed and steam plenum tube sheets), and one group from both ~1/3 and ~2/3 of the full length of the test specimen
Multiple	11		Two long spans, mode frequencies only
Instrumented Tube #3	9	Permanently instrumented	All long spans, any short spans with permanent instrumentation
Instrumented Tube #4	9	Permanently instrumented	Ten long spans (including any long spans with permanent instrumentation), any short spans with permanent instrumentation
W9	9	Selected during testing based on loosely held tube	Four groups of five spans (long/short/long/short/long) selected to provide one group from near each end (feed and steam plenum tube sheets), and one group from both ~1/3 and ~2/3 of the full length of the test specimen
X9	9	Selected during testing based on tightly held tube	Four groups of five spans (long/short/long/short/long) selected to provide one group from near each end (feed and steam plenum tube sheets), and one group from both ~1/3 and ~2/3 of the full length of the test specimen
Multiple	9		Two long spans, mode frequencies only

There are three technical objectives of the modal testing during tube bundle fabrication:

- Reproducibly measure mode frequencies and mode shapes (goal of characterization of up to four mode shapes and frequencies per tube) using impulse excitation.
- Evaluate range of tube modal responses. Based on preliminary modal measurements, a range of frequencies (representing pivot and fixed boundary conditions) are expected.
- Obtain consistent modal measurements for temporary and permanent instrumentation.

Testing is conducted by placing temporary accelerometers, taking measurements and then repeating as necessary to obtain required data. The specific placement of temporary accelerometers to perform this portion of the testing is determined by the test performer as necessary to meet the test objectives.

NuScale provides concurrence that necessary modal measurements have been achieved if less than four modes can be measured for a given tube. For testing Columns 9 and 11, extent of modal testing for tubes W and X may be reduced based on demonstrated consistency of results with tests for other columns and locations in the tube array.

Three-dimensional mode shape functions are developed for as many modes as possible (up to a goal of four), including at least one first-order beam mode for each tube tested. For each individual mode shape and frequency that can be characterized for each variable level of temporary support compression, at least two sets of duplicate measurements are obtained. If divergent results are observed for the duplicate tests, additional test runs may be requested until consistent results are observed. Accelerometers are not required to be re-positioned to obtain duplicate data sets. Mode shapes are defined in a local coordinate system. Locations of removable accelerometers are recorded to within an accuracy of  $\pm 0.002^{(a),(c)}$  inches. Rotational position (e.g., bottom dead center, top dead center, and so on) of each span tested is also recorded to evaluate the impact of the horizontal orientation of the test fixture.

In addition to data from removable accelerometers, data is recorded using permanently installed strain gauges and accelerometers in the tested tubes.

#### 5.1.1.3.2 In-Air Damping Tests

Damping tests are performed on the same individual tubes that are characterized as part of partial tube array fabrication modal testing. This includes testing performed with up to three variable levels of compression applied by temporary tube bundle supports. Tests are performed on tubes in Columns 9, 11 and 12. The extent of damping measurements in each column is based on the number of individual modes that are successfully characterized as part of the partial tube array fabrication modal testing. Damping values for a maximum of four modes for each of four tubes in each column (total of sixteen damping values) are measured. Damping values for each tube and mode are developed using both logarithmic decrement and half-power bandwidth methods. Damping testing includes evaluation of amplitude specific damping.

The specific placement of temporary accelerometers to perform this portion of the testing is determined based on the test objectives. In addition to data from removable accelerometers, data is recorded using permanently installed strain gauges and accelerometers in the tested tubes.

There are two primary objectives of this testing:

- Reproducibly measure damping values for modal frequencies characterized during partial tube array fabrication modal testing. Damping values are determined using at least two methods (logarithmic decrement and half-power bandwidth methods)
- Determine variability in damping values between different tubes and as a function of modal frequency.

Minimum duration of data files is agreed upon by NuScale and the testing services supplier.

Both half power and logarithmic decrement methods are used to determine damping values. For each individual tube and frequency that can be characterized, damping values are obtained using each method. For each damping value measured for each method, a duplicate set of damping values is obtained. If divergent results are observed for the duplicate tests, additional test runs may be requested until consistent results are observed.

Logarithmic decrement and half-power bandwidth methods produce different ranges of damping values (results from each method are not expected to show strong agreement). Therefore, testing objectives are satisfied when reproducible results are produced for each method, even if the results obtained for each method are not in agreement.

#### **5.1.1.3.3 Tube Array Testing: In-Air Natural Frequencies and Mode Shapes**

This testing obtains frequency and mode shape measurements comparable to those observed in the tests during tube bundle fabrication. With the exception of possible limited access for tubes #3 and #4 (Column 9), impulse excitation is not possible for these tests. Therefore, a fixed point exciter is used to measure mode frequencies and mode shapes of only tubes in Column 11 (Instrumented tube #1, #2, #7 and #8).

Initial testing is performed by frequency sweep testing for frequencies between 5 and 500 Hz. Frequency sweep rates are recommended by the testing services supplier and approved by NuScale. Following this initial sweep testing, harmonic sweep testing around frequencies characterized during individual tube testing of Column 11 tubes is performed if broad spectrum sweep testing did not adequately characterize these modes. Measurements are obtained for each tube using excitation at each of the fixed points (two to three points per tube, based on access through N1, N2, N3 and N4). At least two duplicate sets of measurements are obtained for each tube at each discernable modal frequency with excitation from each exciter coupling location.

In addition, excitation in frequency ranges corresponding to any predicted predominant frequencies not characterized during the individual tube testing is performed. This testing is to confirm the boundary conditions (as indicated by observed modal frequencies) in the

fully-assembled tube array are consistent with those during the testing during the fabrication process.

During this testing, it is only necessary to record data for the individual tubes to which excitation is applied. Repetition of some or all tests using altered tube bundle compression forces is performed.

Damping values associated with each individual frequency detected are based on determination of the transfer function (i.e., FRF) for each tube. Excitation for damping tests is performed using the fixed-point exciter system and includes determination of amplitude dependency of damping. Results are obtained for permanently instrumented tubes in Column 11 (instrumented tubes #1, #2, #7 and #8).

#### **5.1.1.3.4 Tube Array Testing: In-Water Natural Frequencies and Mode Shapes**

The objectives, conduct, and necessary data for this testing are identical to the full array in-air natural frequency and mode shape testing, with the exception that the test specimen be maintained full of stagnant water.

The objectives, conduct, and necessary data for this testing are identical to the full array in-air natural damping testing, with the exception that the test specimen be maintained full of stagnant water.

#### **5.1.1.4 TF-3 Steady-State Flow Testing**

These tests are devoted to fully characterizing the vibration amplitudes of the HCSG as function of normal primary flow velocities.

Measurements are also performed with no flow conditions to determine background noise levels. When increasing flow velocity, displacement amplitudes are monitored so that the test can be suspended if the onset of instability is observed. Because flows in this phase of testing are limited to 100 percent normal design flow, no unusual vibration is expected.

The general requirements of this testing are steady flow runs of a minimum of five minutes at each test run, with recording of a dedicated test point data file for a minimum of two minutes at each test run. Once steady flow conditions have been observed for at least three minutes (based on concurrence with the NuScale test engineer, as supported by relevant instrument readings), a minimum of two minutes of data are recorded to a dedicated file for the test point. Minimum testing points are in accordance with Table 5-18.



Table 5-18 Steady-state flow flow-induced vibration tests

Test Run	Flow (gpm)	$V_{gap}$ (ft/s)	Description
1	{{		Baseline
2			
3			25% flow
4			
5			50% flow
6			
7			75% flow
8			
9			100% flow
10		}} <sup>2(a),(c)</sup>	

The PSD functions cover a range of non-dimensional reduced frequencies (frequency\*tube diameter/ $V_{gap}$ ) up to 10. The flow test points in Table 5-20 provide data to validate the design PSD over the prescribed range of reduced frequencies.

Each steady-state flow test run is repeated on a different day from the first test run. If divergent results are observed for the duplicate tests, additional test runs may be requested until consistent results are observed.

#### 5.1.1.5 TF-3 Vortex Shedding Flow Testing

This test is to demonstrate that the SG design is not susceptible to VS phenomena. The VS can cause excessive vibration when alternating vortices are induced at a frequency that is at or near a modal frequency of the structure. The purpose of these tests is to evaluate flow rates which could induce VS at frequencies coincident with modal frequencies of individual tubes at the bottom periphery of the tube bundle by measuring vibration amplitudes that result during these flowrates.

Flow rates necessary to cover the range of VS frequencies are provided in Table 5-19. Vortex shedding may occur when the  $V_{gap}$  is in proximity to a structural frequency (perfect coincidence is not necessary); therefore, testing at only specific points is not sufficient to characterize this phenomena. As there are many closely-spaced modal frequencies of the tubes within part of the range where tube natural frequencies and VS frequencies coincide, the testing approach requires taking sufficient data at flowrates throughout this range to fully demonstrate VS is precluded. It is understood there may be practical limitations with respect to fine adjustment of flow velocities using high-capacity pumps; therefore, the proposed test sequence may be adjusted to facilitate available control capability.

Table 5-19 Vortex shedding test points<sup>1, 2</sup>

Bulk flow (gal/min)	V <sub>gap</sub> (ft/s)	f <sub>s</sub> (Hz)	Basis
{{		}} <sup>2(a),(c)</sup>	Approximate frequency of fundamental tube mode
{{		}} <sup>2(a),(c)</sup>	Approximate frequency of second tube mode
{{		}} <sup>2(a),(c)</sup>	Approximate frequency of third tube mode
{{		}} <sup>2(a),(c)</sup>	
{{		}} <sup>2(a),(c)</sup>	Approximate frequency of fourth tube mode
{{		}} <sup>2(a),(c)</sup>	Closely-spaced modes in this frequency range
{{		}} <sup>2(a),(c)</sup>	Closely-spaced modes in this frequency range
{{		}} <sup>2(a),(c)</sup>	Testing at this level bounds all design conditions with sufficient margin

Note 1: there is some overlap of the VS test conditions, steady-state flow test, and FEI test conditions. A consolidated test matrix that includes common flow conditions that satisfy evaluation of all phenomena may be developed.

Note 2: test points may be adjusted based on results of modal testing to ensure test runs most closely correspond with actual measured structural frequencies of the test array.

The VS tests include a minimum of five minutes of steady-state flow with recording of a dedicated test point data file for a minimum of two minutes at each test point. Once steady flow conditions have been observed for at least three minutes, a minimum of two minutes of data are recorded to a dedicated file for the test point. If large tube displacements (characteristic of VS) are observed, duration of data files may be reduced to prevent possible damage to the test specimen. The VS is associated with the fundamental or other lower frequency modes (less than {{ }}<sup>2(a),(c)</sup>), therefore data acquisition rate may be reduced for this testing. Flowrate changes between test points are controlled such that changes in flowrate do not exceed 10 percent per minute.

Each VS flow test run is repeated on a different day from the first test run. If divergent results are observed for the duplicate tests, additional test runs may be requested until consistent results are observed. Likewise, if any indication of VS occurs during transitions, additional test points are added to examine flow rates intermediate to the test points specified in Table 5-19.

### 5.1.1.6 TF-3 Fluid Elastic Instability Flow Testing

This test is to demonstrate the onset (or lack of) of FEI in the NuScale HCSG to demonstrate design margin. However, the ability to demonstrate the onset of FEI in this test may be impossible for two reasons, 1) it is possible that a helical tube design is immune to FEI phenomena based on unique design features (“de-tuning” based on array including tubes of various frequencies, cannot be synchronously excited in a single mode), and 2) if margin to FEI is significantly larger than predicted, test facility flow rates are inadequate to reach FEI. Based on achieving maximum possible test flow rates without onset of FEI, adequate design margin is demonstrated.

The general requirements of this testing are that steady-state flow runs of five minutes with recording of a dedicated test point data file for a minimum of two minutes at each test point. Once steady flow conditions have been observed for at least three minutes, a minimum of two minutes of data are recorded to a dedicated file for the test point. If large tube displacements are observed, duration of data files may be reduced to prevent possible damage to the test specimen. Fluid elastic instability is associated with the fundamental or other lower frequency modes (less than  $\{\{\}^{2(a),(c)}$  for the NuScale design); therefore, data acquisition rate may be reduced for this testing. Flowrate changes between test points are controlled such changes in flowrate do not exceed 10 percent per minute.

Fluid elastic instability is characterized by synchronized vibration of the tube array at a common frequency (predicted to be between  $\{\{\}^{2(a),(c)}$  for this test specimen). Continuous monitoring of vibration amplitude frequency of available strain gauges and accelerometers is necessary during FEI testing to accurately identify the onset of FEI, if it occurs. If the onset of FEI is observed, flow rates are immediately reduced and concurrence from NuScale obtained before subsequent increases in flow rates.

Minimum testing is in accordance with Table 5-20.

Table 5-20 Fluid elastic instability flow tests

Test Run	Flow (gpm)	$V_{gap}$ (ft/s)	Description
1	$\{\{\}$		
2			
3			Predicted onset of FEI (conservative Connors constants)
4			
5			Predicted onset of FEI (best estimate Connors constants)
6			
7			
-			Additional test points up to maximum flow or onset of FEI, as directed by NuScale
8		$\{\{\}^{2(a),(c)}$	Max flow test, with concurrence of NuScale if no indication of FEI is observed at all previous test points.

Each FEI flow test run is repeated on a different day from the first test run. If divergent results are observed for the duplicate tests, additional test runs may be requested until consistent results are observed.

### 5.1.1.7 TF-3 Results Scope

The Summary Test Report includes the following:

- test description

- list and discussion of test anomalies and test procedure changes
- assessment of test data acceptability
- any relevant data plots or tables

The Final Test Report includes the following:

- raw data
- calculations, including methodology and results summaries
- checksums for the non-encrypted reduced and calculated data sets
- reduced and calculated data in an encrypted file
- instrument calibration certificates
- test readiness inspection report
- completed, filled out, and signed test procedures
- test logs

### 5.1.2 TF-3 Modal Analysis Pre-Test Prediction

This calculation is to predict the modal response of the steam generator TF-3 test specimen. The TF-3 test specimen is a full-scale representation of Columns 9 through 13 of the NuScale power module SG. This calculation supports the TF-3 test program.

This calculation applies only to the TF-3 test specimen design. Individual tube models as well as a TF-3 full-bundle model are used in the analysis.

The type of results generated in this calculation are:

- Modal frequencies, mass participations, and mode shapes for individual tube models of Columns 9, 11, and 13
- Sensitivity studies to determine the effect of different boundary conditions, mesh sizes, and the influence of primary-side water (dry vs wet conditions)
- Recommended strain gauge placement to capture dominant modes of Column 11 tubes
- Mode frequencies and mass participations of the TF-3 full-bundle model compared to the individual tube models

Three different coordinate systems types are used in this calculation for the models. They are described below and pictured in Figure 5-1. Note that all coordinate systems are located at global zero, but are shown at different locations in the figure for clarity. The figure also shows images of the TF-3 full-bundle model, but the coordinate systems apply to the individual models as well.

- Global Cartesian coordinate system: X and Z are horizontal directions, and Y points vertically upward. This is ANSYS coordinate system 0 (CSYS 0).
- Global cylindrical coordinate system: X is the radial direction, Y is the circumferential direction, and Z points vertically upward. This is ANSYS coordinate system 5 (CSYS 5).

- Local coordinate systems: Forty unique local Cartesian coordinate systems are used for coupling tubes to tube supports, one assigned to each of the forty tube supports. From the perspective of the interface, the local X is along the tube axis and Z points radially inward toward the center of the bundle. The local Y axis is perpendicular to these two, and is angled away from the global vertical direction by the tube inclination angle (approximately 13° to 14°). The ANSYS coordinate system number is the column number followed by the tube support number. For example, Column 13, tube support 7 is coordinate system 137 (CSYS 137).

{{

}}<sup>2(a),(c)</sup>

Figure 5-1 Coordinate systems shown from global isometric view

The numbering system for identifying the circumferential positions of the tube supports (as used above in defining CSYS 137), tubesheets, and tube ends is shown in Figure 5-2. This applies to both individual tube models and the full-bundle model. This numbering system is for bookkeeping within the ANSYS models only and does not represent any numbering system used in the TF-3 or SG drawings.

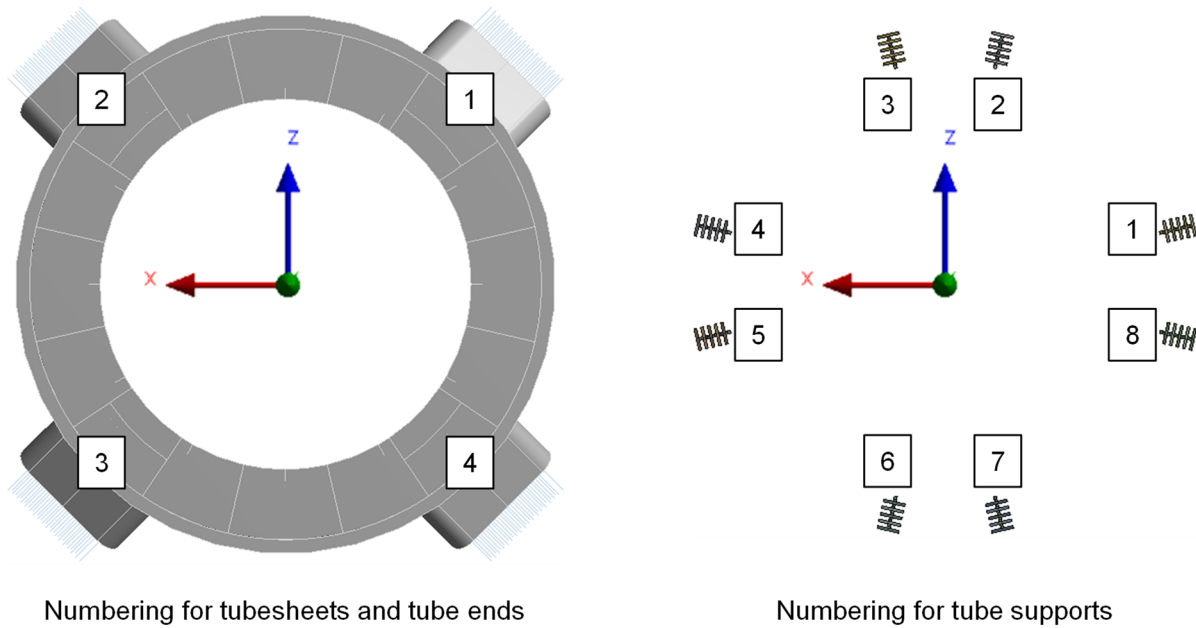


Figure 5-2 Numbering system for circumferential positions (CSYS 0 shown)

### 5.1.2.1 Single-Tube Models

This calculation includes individual tube models for Columns 9, 11, and 13. The model for each column contains the two bounding tubes, one at each end of a row of tubes in the tubesheet. Columns 9, 11 and 13 are shown in Figure 5-3. The tube geometry of the TF-3 test specimen is the same as the tube geometry for the NuScale Power Module SG.

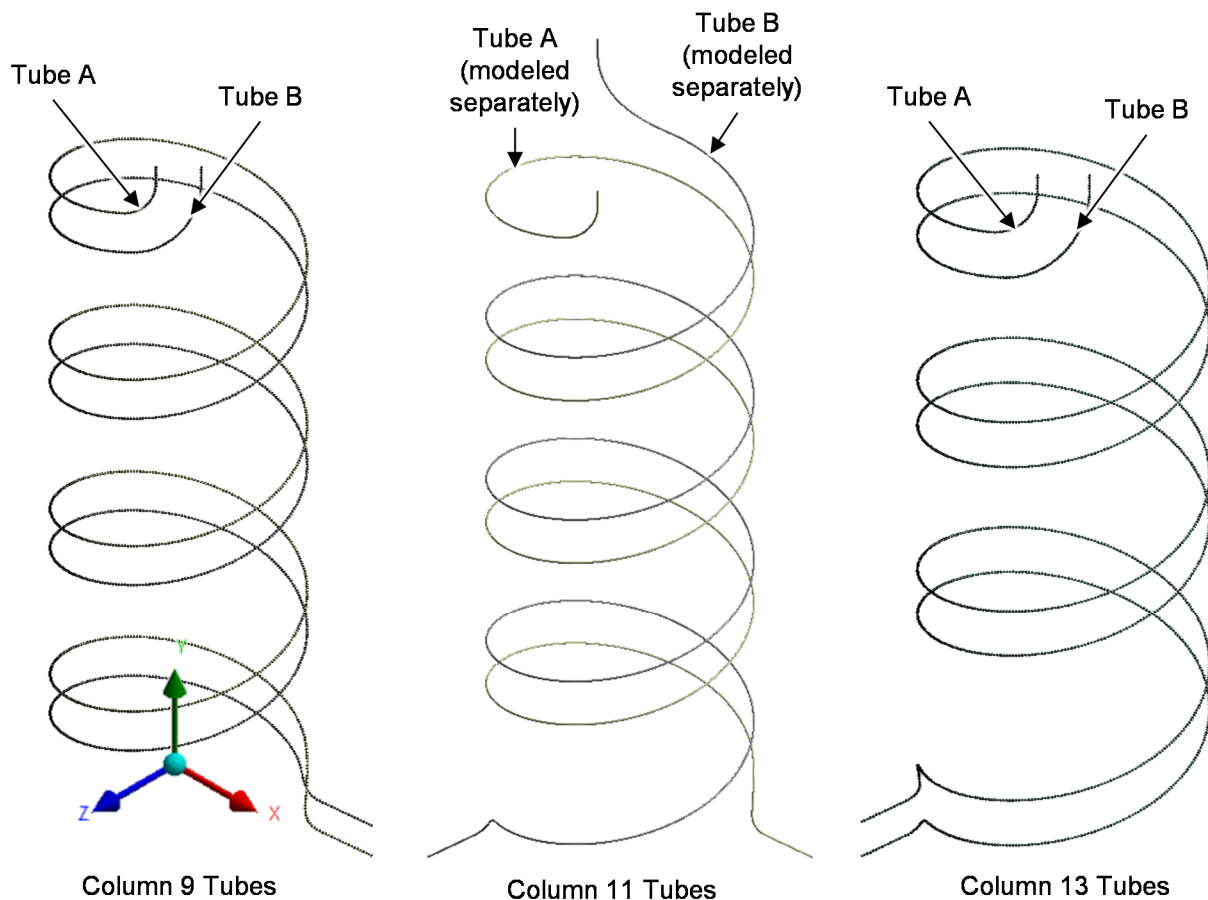


Figure 5-3 Representative tubes for individual tube models

The individual tube models are meshed with 1-inch BEAM188 elements, which do not have midside nodes. The exception to this is in the mesh sensitivity analysis, which uses 12-inch BEAM189 elements with midside nodes (see Section 5.1.2.6).

The tubes are assigned Type 304 stainless steel material properties at 70 degrees Fahrenheit.

For analyzing the test conditions with water on the primary side, the material density is adjusted to account for the displaced water mass of the tube (added mass effect). The effect of the added mass is analyzed in Section 5.1.2.5.

Boundary conditions are applied to the tubes to simulate the connections to the tubesheets and tube supports, which are not explicitly modeled. The edges at the ends of the tubes have all degrees of freedom constrained to simulate the connection where the tubes are inserted and welded to the tubesheets (the inserted length is fixed).

The tube vertices at the tube support interface locations are constrained using the local coordinate system directions. Two combinations of constraints are analyzed: “pivot” and “fixed.” For the “pivot” case, only the local UY and UZ are constrained, which allows for a

tube to pivot about any direction, as well as slide along its axis. For the “fixed” case, the local displacements (UX, UY, UZ), rotation in Y direction (ROTY), and rotation in Z direction (ROTZ) are constrained, but twisting about the tube axis is still free. The additional constraints simulate a condition where the tube supports are pressed together and provide more clamping on the tube. This condition occurs in the NuScale Power Module SG due to thermal expansion differences and/or tolerance stack-up.

These two boundary condition combinations should bound any possible modal behavior. A depiction of the boundary condition locations is shown in Figure 5-4.

{{

}}<sup>2(a),(c)</sup>

Figure 5-4 Boundary condition locations (column 13 shown)



### 5.1.2.2 TF-3 Full Bundle Model

This section describes the TF-3 full bundle model, which explicitly models all tubes, tube supports, and vessels in a single ANSYS model.

Details of the vessels have been simplified to reduce mesh complexity. The top head, bolts, vessel penetrations, cover plates, and small features have been removed. These components have negligible stiffness compared to the major components of the specimen that are modeled. For example, although the top head is stiff, it is negligible compared to the 5-inch thick steam tubesheet to which it attaches. The mass of these components is added back into the model in order to maintain the correct overall mass-to-stiffness ratio.

The TF-3 vessels and tubesheets are modeled using surface bodies at the nominal mid-surface of the thickness. One exception to this is the steam tubesheet, which uses an offset in order to properly interface with the surfaces beneath it, while still maintaining the stiffness at the correct elevation. Also, some stiffener ring elevations were adjusted slightly (less than 0.65 inch) in order to line up with elevations of other components. This avoids skinny elements with poor aspect ratios without affecting overall specimen behavior.

The tubes are made of line bodies with a circular tube cross-section. The inner radius is  $\{\{ \quad \}^{2(a),(c)}$  inch and the outer radius is  $\{\{ \quad \}^{2(a),(c)}$  inch.

The tube supports are made of line bodies with rectangular cross-sections. The cross-section of the main tube support body is  $\{\{ \quad \}^{2(a),(c)}$  inch wide and  $\{\{ \quad \}^{2(a),(c)}$  inch thick. This gives equivalent bending stiffness as the detailed geometry design.

The rectangular cross-section of the tube support tabs has the nominal dimensions of  $\{\{ \quad \}^{2(a),(c)}$  thick.

The geometry of the TF-3 full bundle model is shown in Figure 5-5.

The tubes are meshed with BEAM189 elements, which include midside nodes. The element length is set to 12 inches, which was determined to be adequate as described in Section 5.1.2.6. The tube mesh is shown in Figure 5-6 and Figure 5-7.

The tube supports are meshed with BEAM188 elements that do not include midside nodes. Midside nodes are not necessary due to the small element size of less than 1 inch. The small elements are necessary to characterize the correct spacing between adjacent tabs and between adjacent tube supports. The tube support mesh is shown in Figure 5-6 and Figure 5-7.

The vessels and tubesheets are meshed with SHELL281 elements that include midside nodes. The element size varies between 13 inches for the general shell regions, down to 1 inch at the tubesheet interface with the tubes. The vessels and tubesheet mesh are shown in Figure 5-6.

{{

}}<sup>2(a),(c)</sup>

Figure 5-5 TF-3 full bundle model geometry

{{

}}<sup>2(a),(c)</sup>

Figure 5-6 TF-3 full bundle model mesh

}}

}}<sup>2(a),(c)</sup>

#### Figure 5-7 Tube and tube support mesh

Bodies are assigned material properties for Type 304 stainless steel at 70 degrees Fahrenheit. This is the correct material for most components in the test specimen. It is a simplification of the tubesheet material, any differences in density are compensated by the mass corrections. The tube support tab material uses a stiffer elastic modulus. This arbitrarily stiff value is used to properly couple the moments between the center of the tab and the base of the tab where it connects with the main tube support body. In the true design, the moments are coupled by multiple tabs with significant horizontal spacing, which is not easily achievable in the simplified beam model representation. This simplification only impacts the TF-3 full bundle model where moments are coupled between the tubes and supports (fixed boundary condition).

---

Because many features of the TF-3 specimen have been removed from the model geometry, their masses must be added back to maintain the overall mass of the specimen. This is done by applying distributed masses in ANSYS Workbench Mechanical.

The mass correction is split into two sections: the top head and the shells. The top head mass is calculated by multiplying the detailed head geometry volume by the density for Type 304 stainless steel. The remaining mass that is applied to the shells is the difference between the vessel target mass, and the modeled vessel mass and head mass. This is summarized in Figure 5-8 and Table 5-21. The top head distributed mass is applied to the steam tubesheet surface and the shell mass is applied to the outer vessel surface.

{{

}}<sup>2(a),(c)</sup>

Figure 5-8 Modeled vessel mass (left), and top head mass volume (right)

Table 5-21 Mass correction for vessels

Item Description	Value	Reference
Top head volume (in <sup>3</sup> )	{{ }} <sup>2(a),(c)</sup>	Figure 5-8
Top head density (lbm/in <sup>3</sup> )	{{ }} <sup>2(a),(c)</sup>	Type 304 SS at 70°F
Top head mass to add (lbm)	{{ }} <sup>2(a),(c)</sup>	= top head volume * density
Total target mass for vessels (lbm)	{{ }} <sup>2(a),(c)</sup>	
Modeled vessel mass (lbm)	{{ }} <sup>2(a),(c)</sup>	
Added top head mass (lbm)	{{ }} <sup>2(a),(c)</sup>	calculated top head mass above
Shell mass to add (lbm)	{{ }} <sup>2(a),(c)</sup>	= target mass - modeled vessel mass - top head mass

The mass of the tubes and tube supports do not need correction. The tubes are modeled with their true geometry and the tube supports end up at nearly the correct mass despite having a simplified geometry. The modeled tube support volume is only 1 percent different than the actual volume.

### 5.1.2.3 Boundary Conditions

This section explains the various boundary conditions and constraint equations used in the TF-3 full bundle model to couple the components together. The shell bodies do not require additional coupling to each other, as they share a conformal mesh as a single part. In the following figures, shell thicknesses and beam cross-sections are turned on or off depending on which provides the greatest clarity.

The bottom edge of the TF-3 full bundle model has a fixed boundary condition applied. This simulates the entire specimen bolted to the foundation.

Nodes near the top of each tube are coupled to corresponding nodes on the steam tubesheet. Nodes near the bottom of each tube are coupled to corresponding nodes on the feed tubesheets. All degrees of freedom are coupled at each connection. This simulates the inserted and welded tube in the tubesheet. The coupling is performed using constraint equations written in an ANSYS parametric design language (APDL) command object named "Commands (APDL) – tubes to sheets – tube sups to SG sups." A visualization of the constraint equation coupling is shown in Figure 5-10.

{{

}}<sup>2(a),(c)</sup>

Figure 5-9 Fixed boundary condition at bottom edge of full bundle model



---

{{

}}<sup>2(a),(c)</sup>

Figure 5-10 Tube to tubesheet coupling: steam tubesheet (top), feedwater tubesheet (bottom)

Nodes near the top of each tube support are coupled to corresponding nodes on the upper SG supports. Nodes near the bottom of each tube support are coupled to corresponding nodes on the lower SG supports. For the upper connection, the UX, UY, and UZ of the global cylindrical coordinate system (CSYS 5) are coupled. For the lower connection, the UX and UY of the global cylindrical coordinate system (CSYS 5) are coupled. The coupling is performed using constraint equations written in an APDL command object named "Commands (APDL) – tubes to sheets – tube sups to SG sups." A visualization of the constraint equation coupling is shown in Figure 5-11.

---

{{

}}<sup>2(a),(c)</sup>

Figure 5-11 Tube support to steam generator support coupling: upper connection (top), lower connection (bottom)

Tube nodes are coupled to tube support tab nodes at each interface. For the “pivot” case, the local UY and UZ are coupled. For the “fixed” case, the local UX, UY, UZ, ROTY, and ROTZ are coupled. The coupling is performed using constraint equations written in an APDL command object named “Commands (APDL) – tubes to tube sups.” A visualization of the constraint equation coupling is shown in Figure 5-12.

---

{{

}}<sup>2(a),(c)</sup>

Figure 5-12 Tube to tube support coupling.

The tube support tab tip nodes are coupled to the adjacent tube support back nodes. A given tip node is coupled to two back nodes using a weighted average. For the nominal case, the UX, UY, and ROTZ of the global cylindrical coordinate system (CSYS 5) are coupled. The coupling is performed using constraint equations written in an APDL command object named “Commands (APDL) – tubes sups to tube sups and vessels.”

The supports are only coupled together at certain elevation intervals, approximately every 9 inches. Because the tube support design has pockets machined out of the back, tabs from the adjacent support may protrude into the pocket and not interface with the support. Because of this, the tube support design uses spacers every 18 inches to fill in the pockets and guarantee contact with an adjacent tab. It is also likely that contact will still be made at non-spacer locations, so 9 inches was selected as the interval between sets of constraint equations. A visualization of the constraint equation coupling is shown in Figure 5-13.

{{

}}<sup>2(a),(c)</sup>

Figure 5-13 Various views of tube support to tube support coupling

Using a similar methodology to the section above, the Column 9 tube support tips are coupled to the inner vessel (i.e., riser) and the Column 13 tube support backs are coupled to the outer vessel. Because the mesh of the vessels is much coarser than the tube supports, each vessel node within the region of interest is coupled to the two closest tube support nodes using a weighted average. The same degrees of freedom are coupled as the above section, except for the interface between Column 13 tube supports and the outer vessel, where the moment about the vertical axis is not coupled. This is because the back face of the support does not fully engage with the vessel and the support is free to pivot around the vertical alignment strip welded to the vessel. The coupling is performed using constraint equations written in an APDL command object named “Commands (APDL) – tubes sups to tube sups and vessels.” A visualization of the constraint equation coupling is shown in Figure 5-14 and Figure 5-15.

{{

}}<sup>2(a),(c)</sup>

Figure 5-14 Column 9 tube support to inner vessel coupling

}}

}}<sup>2(a),(c)</sup>

Figure 5-15 Column 13 tube support to outer vessel coupling

#### 5.1.2.4 Modal Analysis – Individual Tube Models

Modal analysis is performed for the individual tube models. These include sensitivity analyses for different boundary conditions, dry vs. wet conditions, and different mesh sizes. It also includes strain gauge placement recommendations based on modal analysis of Column 11.

Modal analysis was performed up to 1000 Hz using the individual tube models to determine the sensitivity to the two sets of boundary conditions, pivot and fixed. The pivot condition has the local UY and UZ constrained at each tube support interface location. The fixed condition has the local UX, UY, UZ, ROTY, and ROTZ constrained.

The analyses were performed for Column 9 and Column 13 individual tube dry models. The tabulated results of the 20 modes with highest mass participation plus the fundamental mode are shown in Table 5-22 through Table 5-24. Results are shown in the global Cartesian coordinate system (CSYS, 0).

The mode shapes of the fundamental mode and highest y-direction mass participation mode are shown in Figure 5-16 and Figure 5-17 for the pivot case, and in Figure 5-18 and Figure 5-19 for the fixed case. Column 13 dry model is used as the example. The mode shapes for modes below 300 Hz are written to text files.

The fixed results show significant increase in the modal frequencies. The fixed results also have the majority of the mass participation above 1000 Hz for the horizontal directions. Column 13 shows similar trends as Column 9, but with reduced frequency.

Table 5-22 Pivot vs. fixed dry modal results for Columns 9 and 13 in x-direction (horizontal)

Column 9 Pivot, X (horiz)			Column 13 Pivot, X (horiz)			Column 9 Fixed, X (horiz)			Column 13 Fixed, X (horiz)		
MODE	FREQ. (HZ)	MASS PARTIC. RATIO, X	MODE	FREQ. (HZ)	MASS PARTIC. RATIO, X	MODE	FREQ. (HZ)	MASS PARTIC. RATIO, X	MODE	FREQ. (HZ)	MASS PARTIC. RATIO, X
1	{{	}} <sup>2(a),(c)</sup>	1	{{	}} <sup>2(a),(c)</sup>	1	{{	}} <sup>2(a),(c)</sup>	1	{{	}} <sup>2(a),(c)</sup>
11	{{	}} <sup>2(a),(c)</sup>	7	{{	}} <sup>2(a),(c)</sup>	17	{{	}} <sup>2(a),(c)</sup>	15	{{	}} <sup>2(a),(c)</sup>
14	{{	}} <sup>2(a),(c)</sup>	11	{{	}} <sup>2(a),(c)</sup>	18	{{	}} <sup>2(a),(c)</sup>	16	{{	}} <sup>2(a),(c)</sup>
15	{{	}} <sup>2(a),(c)</sup>	12	{{	}} <sup>2(a),(c)</sup>	50	{{	}} <sup>2(a),(c)</sup>	44	{{	}} <sup>2(a),(c)</sup>
16	{{	}} <sup>2(a),(c)</sup>	13	{{	}} <sup>2(a),(c)</sup>	51	{{	}} <sup>2(a),(c)</sup>	47	{{	}} <sup>2(a),(c)</sup>
17	{{	}} <sup>2(a),(c)</sup>	14	{{	}} <sup>2(a),(c)</sup>	208	{{	}} <sup>2(a),(c)</sup>	229	{{	}} <sup>2(a),(c)</sup>
18	{{	}} <sup>2(a),(c)</sup>	15	{{	}} <sup>2(a),(c)</sup>	209	{{	}} <sup>2(a),(c)</sup>	230	{{	}} <sup>2(a),(c)</sup>
19	{{	}} <sup>2(a),(c)</sup>	18	{{	}} <sup>2(a),(c)</sup>	263	{{	}} <sup>2(a),(c)</sup>	238	{{	}} <sup>2(a),(c)</sup>
33	{{	}} <sup>2(a),(c)</sup>	19	{{	}} <sup>2(a),(c)</sup>	264	{{	}} <sup>2(a),(c)</sup>	239	{{	}} <sup>2(a),(c)</sup>
61	{{	}} <sup>2(a),(c)</sup>	21	{{	}} <sup>2(a),(c)</sup>	266	{{	}} <sup>2(a),(c)</sup>	248	{{	}} <sup>2(a),(c)</sup>
144	{{	}} <sup>2(a),(c)</sup>	43	{{	}} <sup>2(a),(c)</sup>	265	{{	}} <sup>2(a),(c)</sup>	249	{{	}} <sup>2(a),(c)</sup>
145	{{	}} <sup>2(a),(c)</sup>	52	{{	}} <sup>2(a),(c)</sup>	278	{{	}} <sup>2(a),(c)</sup>	250	{{	}} <sup>2(a),(c)</sup>
147	{{	}} <sup>2(a),(c)</sup>	122	{{	}} <sup>2(a),(c)</sup>	277	{{	}} <sup>2(a),(c)</sup>	253	{{	}} <sup>2(a),(c)</sup>
149	{{	}} <sup>2(a),(c)</sup>	124	{{	}} <sup>2(a),(c)</sup>	279	{{	}} <sup>2(a),(c)</sup>	254	{{	}} <sup>2(a),(c)</sup>
150	{{	}} <sup>2(a),(c)</sup>	127	{{	}} <sup>2(a),(c)</sup>	280	{{	}} <sup>2(a),(c)</sup>	255	{{	}} <sup>2(a),(c)</sup>
213	{{	}} <sup>2(a),(c)</sup>	130	{{	}} <sup>2(a),(c)</sup>	289	{{	}} <sup>2(a),(c)</sup>	320	{{	}} <sup>2(a),(c)</sup>
215	{{	}} <sup>2(a),(c)</sup>	185	{{	}} <sup>2(a),(c)</sup>	290	{{	}} <sup>2(a),(c)</sup>	331	{{	}} <sup>2(a),(c)</sup>
216	{{	}} <sup>2(a),(c)</sup>	186	{{	}} <sup>2(a),(c)</sup>	322	{{	}} <sup>2(a),(c)</sup>	333	{{	}} <sup>2(a),(c)</sup>
231	{{	}} <sup>2(a),(c)</sup>	189	{{	}} <sup>2(a),(c)</sup>	325	{{	}} <sup>2(a),(c)</sup>	334	{{	}} <sup>2(a),(c)</sup>
232	{{	}} <sup>2(a),(c)</sup>	198	{{	}} <sup>2(a),(c)</sup>	326	{{	}} <sup>2(a),(c)</sup>	337	{{	}} <sup>2(a),(c)</sup>
277	{{	}} <sup>2(a),(c)</sup>	199	{{	}} <sup>2(a),(c)</sup>		{{	}} <sup>2(a),(c)</sup>		{{	}} <sup>2(a),(c)</sup>



Table 5-23 Pivot vs. fixed dry modal results for Columns 9 and 13 in y-direction (vertical)

Column 9 Pivot, Y (vert)			Column 13 Pivot, Y (vert)			Column 9 Fixed, Y (vert)			Column 13 Fixed, Y (vert)		
MODE	FREQ. (HZ)	MASS PARTIC. RATIO, Y	MODE	FREQ. (HZ)	MASS PARTIC. RATIO, Y	MODE	FREQ. (HZ)	MASS PARTIC. RATIO, Y	MODE	FREQ. (HZ)	MASS PARTIC. RATIO, Y
1	{{	}} <sup>2(a),(c)</sup>	1	{{	}} <sup>2(a),(c)</sup>	1	{{	}} <sup>2(a),(c)</sup>	1	{{	}} <sup>2(a),(c)</sup>
2	{{	}} <sup>2(a),(c)</sup>	2	{{	}} <sup>2(a),(c)</sup>	3	{{	}} <sup>2(a),(c)</sup>	3	{{	}} <sup>2(a),(c)</sup>
9	{{	}} <sup>2(a),(c)</sup>	16	{{	}} <sup>2(a),(c)</sup>	4	{{	}} <sup>2(a),(c)</sup>	4	{{	}} <sup>2(a),(c)</sup>
20	{{	}} <sup>2(a),(c)</sup>	17	{{	}} <sup>2(a),(c)</sup>	7	{{	}} <sup>2(a),(c)</sup>	7	{{	}} <sup>2(a),(c)</sup>
21	{{	}} <sup>2(a),(c)</sup>	22	{{	}} <sup>2(a),(c)</sup>	8	{{	}} <sup>2(a),(c)</sup>	8	{{	}} <sup>2(a),(c)</sup>
24	{{	}} <sup>2(a),(c)</sup>	23	{{	}} <sup>2(a),(c)</sup>	11	{{	}} <sup>2(a),(c)</sup>	11	{{	}} <sup>2(a),(c)</sup>
25	{{	}} <sup>2(a),(c)</sup>	29	{{	}} <sup>2(a),(c)</sup>	12	{{	}} <sup>2(a),(c)</sup>	12	{{	}} <sup>2(a),(c)</sup>
26	{{	}} <sup>2(a),(c)</sup>	53	{{	}} <sup>2(a),(c)</sup>	31	{{	}} <sup>2(a),(c)</sup>	27	{{	}} <sup>2(a),(c)</sup>
31	{{	}} <sup>2(a),(c)</sup>	119	{{	}} <sup>2(a),(c)</sup>	32	{{	}} <sup>2(a),(c)</sup>	29	{{	}} <sup>2(a),(c)</sup>
60	{{	}} <sup>2(a),(c)</sup>	120	{{	}} <sup>2(a),(c)</sup>	33	{{	}} <sup>2(a),(c)</sup>	31	{{	}} <sup>2(a),(c)</sup>
137	{{	}} <sup>2(a),(c)</sup>	206	{{	}} <sup>2(a),(c)</sup>	35	{{	}} <sup>2(a),(c)</sup>	110	{{	}} <sup>2(a),(c)</sup>
138	{{	}} <sup>2(a),(c)</sup>	207	{{	}} <sup>2(a),(c)</sup>	129	{{	}} <sup>2(a),(c)</sup>	112	{{	}} <sup>2(a),(c)</sup>
139	{{	}} <sup>2(a),(c)</sup>	211	{{	}} <sup>2(a),(c)</sup>	130	{{	}} <sup>2(a),(c)</sup>	136	{{	}} <sup>2(a),(c)</sup>
140	{{	}} <sup>2(a),(c)</sup>	212	{{	}} <sup>2(a),(c)</sup>	134	{{	}} <sup>2(a),(c)</sup>	137	{{	}} <sup>2(a),(c)</sup>
241	{{	}} <sup>2(a),(c)</sup>	213	{{	}} <sup>2(a),(c)</sup>	157	{{	}} <sup>2(a),(c)</sup>	140	{{	}} <sup>2(a),(c)</sup>
242	{{	}} <sup>2(a),(c)</sup>	214	{{	}} <sup>2(a),(c)</sup>	158	{{	}} <sup>2(a),(c)</sup>	141	{{	}} <sup>2(a),(c)</sup>
245	{{	}} <sup>2(a),(c)</sup>	215	{{	}} <sup>2(a),(c)</sup>	161	{{	}} <sup>2(a),(c)</sup>	148	{{	}} <sup>2(a),(c)</sup>
246	{{	}} <sup>2(a),(c)</sup>	334	{{	}} <sup>2(a),(c)</sup>	162	{{	}} <sup>2(a),(c)</sup>	161	{{	}} <sup>2(a),(c)</sup>
389	{{	}} <sup>2(a),(c)</sup>	335	{{	}} <sup>2(a),(c)</sup>	343	{{	}} <sup>2(a),(c)</sup>	300	{{	}} <sup>2(a),(c)</sup>
390	{{	}} <sup>2(a),(c)</sup>	336	{{	}} <sup>2(a),(c)</sup>	344	{{	}} <sup>2(a),(c)</sup>	342	{{	}} <sup>2(a),(c)</sup>
	{{	}} <sup>2(a),(c)</sup>									}} <sup>2(a),(c)</sup>

Table 5-24 Pivot vs. fixed dry modal results for Columns 9 and 13 in z-direction (horizontal)

Column 9 Pivot, Z (horiz)			Column 13 Pivot, Z (horiz)			Column 9 Fixed, Z (horiz)			Column 13 Fixed, Z (horiz)		
MODE	FREQ. (HZ)	MASS PARTIC. RATIO, Z	MODE	FREQ. (HZ)	MASS PARTIC. RATIO, Z	MODE	FREQ. (HZ)	MASS PARTIC. RATIO, Z	MODE	FREQ. (HZ)	MASS PARTIC. RATIO, Z
1	{{	}} <sup>2(a),(c)</sup>	1	{{	}} <sup>2(a),(c)</sup>	1	{{	}} <sup>2(a),(c)</sup>	1	{{	}} <sup>2(a),(c)</sup>
10	{{	}} <sup>2(a),(c)</sup>	12	{{	}} <sup>2(a),(c)</sup>	2	{{	}} <sup>2(a),(c)</sup>	2	{{	}} <sup>2(a),(c)</sup>
14	{{	}} <sup>2(a),(c)</sup>	13	{{	}} <sup>2(a),(c)</sup>	15	{{	}} <sup>2(a),(c)</sup>	13	{{	}} <sup>2(a),(c)</sup>
15	{{	}} <sup>2(a),(c)</sup>	14	{{	}} <sup>2(a),(c)</sup>	16	{{	}} <sup>2(a),(c)</sup>	14	{{	}} <sup>2(a),(c)</sup>
16	{{	}} <sup>2(a),(c)</sup>	15	{{	}} <sup>2(a),(c)</sup>	31	{{	}} <sup>2(a),(c)</sup>	38	{{	}} <sup>2(a),(c)</sup>
17	{{	}} <sup>2(a),(c)</sup>	18	{{	}} <sup>2(a),(c)</sup>	48	{{	}} <sup>2(a),(c)</sup>	42	{{	}} <sup>2(a),(c)</sup>
18	{{	}} <sup>2(a),(c)</sup>	126	{{	}} <sup>2(a),(c)</sup>	49	{{	}} <sup>2(a),(c)</sup>	43	{{	}} <sup>2(a),(c)</sup>
30	{{	}} <sup>2(a),(c)</sup>	128	{{	}} <sup>2(a),(c)</sup>	94	{{	}} <sup>2(a),(c)</sup>	80	{{	}} <sup>2(a),(c)</sup>
146	{{	}} <sup>2(a),(c)</sup>	129	{{	}} <sup>2(a),(c)</sup>	95	{{	}} <sup>2(a),(c)</sup>	227	{{	}} <sup>2(a),(c)</sup>
148	{{	}} <sup>2(a),(c)</sup>	131	{{	}} <sup>2(a),(c)</sup>	206	{{	}} <sup>2(a),(c)</sup>	228	{{	}} <sup>2(a),(c)</sup>
149	{{	}} <sup>2(a),(c)</sup>	139	{{	}} <sup>2(a),(c)</sup>	207	{{	}} <sup>2(a),(c)</sup>	231	{{	}} <sup>2(a),(c)</sup>
213	{{	}} <sup>2(a),(c)</sup>	184	{{	}} <sup>2(a),(c)</sup>	234	{{	}} <sup>2(a),(c)</sup>	238	{{	}} <sup>2(a),(c)</sup>
214	{{	}} <sup>2(a),(c)</sup>	186	{{	}} <sup>2(a),(c)</sup>	235	{{	}} <sup>2(a),(c)</sup>	267	{{	}} <sup>2(a),(c)</sup>
215	{{	}} <sup>2(a),(c)</sup>	187	{{	}} <sup>2(a),(c)</sup>	263	{{	}} <sup>2(a),(c)</sup>	271	{{	}} <sup>2(a),(c)</sup>
217	{{	}} <sup>2(a),(c)</sup>	188	{{	}} <sup>2(a),(c)</sup>	264	{{	}} <sup>2(a),(c)</sup>	277	{{	}} <sup>2(a),(c)</sup>
218	{{	}} <sup>2(a),(c)</sup>	191	{{	}} <sup>2(a),(c)</sup>	267	{{	}} <sup>2(a),(c)</sup>	278	{{	}} <sup>2(a),(c)</sup>
221	{{	}} <sup>2(a),(c)</sup>	200	{{	}} <sup>2(a),(c)</sup>	268	{{	}} <sup>2(a),(c)</sup>	320	{{	}} <sup>2(a),(c)</sup>
222	{{	}} <sup>2(a),(c)</sup>	201	{{	}} <sup>2(a),(c)</sup>	277	{{	}} <sup>2(a),(c)</sup>	326	{{	}} <sup>2(a),(c)</sup>
230	{{	}} <sup>2(a),(c)</sup>	208	{{	}} <sup>2(a),(c)</sup>	278	{{	}} <sup>2(a),(c)</sup>	330	{{	}} <sup>2(a),(c)</sup>
233	{{	}} <sup>2(a),(c)</sup>	235	{{	}} <sup>2(a),(c)</sup>	323	{{	}} <sup>2(a),(c)</sup>	333	{{	}} <sup>2(a),(c)</sup>
234	{{	}} <sup>2(a),(c)</sup>	236	{{	}} <sup>2(a),(c)</sup>	324	{{	}} <sup>2(a),(c)</sup>			}} <sup>2(a),(c)</sup>
	{{										}} <sup>2(a),(c)</sup>

{{

}}<sup>2(a),(c)</sup>

Figure 5-16 Fundamental mode for Column 13 dry pivot case (breathing mode)

{{

}}<sup>2(a),(c)</sup>

Figure 5-17 Mode with highest y-direction (vertical) mass participation for Column 13 dry pivot case (beam mode)

{{

}}<sup>2(a),(c)</sup>

Figure 5-18 Fundamental mode for Column 13 dry fixed case (beam mode of transition bend)

{{

}}<sup>2(a),(c)</sup>

Figure 5-19 Mode with highest y-direction mass participation for Column 13 dry fixed case (beam mode)

### 5.1.2.5 Dry-Wet Sensitivity Analysis

Modal analysis was performed for the tube models in the wet configuration, meaning added mass was included to account for the displaced water on the primary side of the test specimen. No fluid is modeled inside the tubes. The added mass was included by increasing the density of the tube material.

The added mass contributes to a  $\{\{ \}^{2(a),(c)}$  reduction in modal frequencies. Because the added mass is a linear change, the  $\{\{ \}^{2(a),(c)}$  shift applies equally to any frequency of any configuration. The results for the y-direction of Column 13 are presented in Table 5-25 and Table 5-26.

Table 5-25 Dry vs. wet modal results for pivot boundary conditions in y-direction

Dry - Col 13 Pivot, Y (vert)			Wet - Col 13 Pivot, Y (vert)			
MODE	FREQ. (HZ)	MASS PARTIC. RATIO, Y	MODE	FREQ. (HZ)	MASS PARTIC. RATIO, Y	% CHANGE FREQ.
1	$\{\{$	$\}^{2(a),(c)}$	1	$\{\{$		$\}^{2(a),(c)}$
2	$\{\{$	$\}^{2(a),(c)}$	2	$\{\{$		$\}^{2(a),(c)}$
16	$\{\{$	$\}^{2(a),(c)}$	16	$\{\{$		$\}^{2(a),(c)}$
17	$\{\{$	$\}^{2(a),(c)}$	17	$\{\{$		$\}^{2(a),(c)}$
22	$\{\{$	$\}^{2(a),(c)}$	22	$\{\{$		$\}^{2(a),(c)}$
23	$\{\{$	$\}^{2(a),(c)}$	23	$\{\{$		$\}^{2(a),(c)}$
29	$\{\{$	$\}^{2(a),(c)}$	29	$\{\{$		$\}^{2(a),(c)}$
53	$\{\{$	$\}^{2(a),(c)}$	53	$\{\{$		$\}^{2(a),(c)}$
119	$\{\{$	$\}^{2(a),(c)}$	119	$\{\{$		$\}^{2(a),(c)}$
120	$\{\{$	$\}^{2(a),(c)}$	120	$\{\{$		$\}^{2(a),(c)}$
206	$\{\{$	$\}^{2(a),(c)}$	206	$\{\{$		$\}^{2(a),(c)}$
207	$\{\{$	$\}^{2(a),(c)}$	207	$\{\{$		$\}^{2(a),(c)}$
211	$\{\{$	$\}^{2(a),(c)}$	211	$\{\{$		$\}^{2(a),(c)}$
212	$\{\{$	$\}^{2(a),(c)}$	212	$\{\{$		$\}^{2(a),(c)}$
213	$\{\{$	$\}^{2(a),(c)}$	213	$\{\{$		$\}^{2(a),(c)}$
214	$\{\{$	$\}^{2(a),(c)}$	214	$\{\{$		$\}^{2(a),(c)}$
215	$\{\{$	$\}^{2(a),(c)}$	215	$\{\{$		$\}^{2(a),(c)}$
334	$\{\{$	$\}^{2(a),(c)}$	334	$\{\{$		$\}^{2(a),(c)}$
335	$\{\{$	$\}^{2(a),(c)}$	335	$\{\{$		$\}^{2(a),(c)}$
336	$\{\{$	$\}^{2(a),(c)}$	336	$\{\{$		$\}^{2(a),(c)}$
	$\{\{$					$\}^{2(a),(c)}$

Table 5-26 Dry vs. wet modal results for fixed boundary conditions in y-direction

Dry - Col 13 Fixed, Y (vert)			Wet - Col 13 Fixed, Y (vert)			
MODE	FREQ. (HZ)	MASS PARTIC. RATIO, Y	MODE	FREQ. (HZ)	MASS PARTIC. RATIO, Y	% CHANGE FREQ.
1	{{	}} <sup>2(a),(c)</sup>	1	{{	}} <sup>2(a),(c)</sup>	}} <sup>2(a),(c)</sup>
3	{{	}} <sup>2(a),(c)</sup>	3	{{	}} <sup>2(a),(c)</sup>	}} <sup>2(a),(c)</sup>
4	{{	}} <sup>2(a),(c)</sup>	4	{{	}} <sup>2(a),(c)</sup>	}} <sup>2(a),(c)</sup>
7	{{	}} <sup>2(a),(c)</sup>	7	{{	}} <sup>2(a),(c)</sup>	}} <sup>2(a),(c)</sup>
8	{{	}} <sup>2(a),(c)</sup>	8	{{	}} <sup>2(a),(c)</sup>	}} <sup>2(a),(c)</sup>
11	{{	}} <sup>2(a),(c)</sup>	11	{{	}} <sup>2(a),(c)</sup>	}} <sup>2(a),(c)</sup>
12	{{	}} <sup>2(a),(c)</sup>	12	{{	}} <sup>2(a),(c)</sup>	}} <sup>2(a),(c)</sup>
27	{{	}} <sup>2(a),(c)</sup>	27	{{	}} <sup>2(a),(c)</sup>	}} <sup>2(a),(c)</sup>
29	{{	}} <sup>2(a),(c)</sup>	29	{{	}} <sup>2(a),(c)</sup>	}} <sup>2(a),(c)</sup>
31	{{	}} <sup>2(a),(c)</sup>	31	{{	}} <sup>2(a),(c)</sup>	}} <sup>2(a),(c)</sup>
110	{{	}} <sup>2(a),(c)</sup>	110	{{	}} <sup>2(a),(c)</sup>	}} <sup>2(a),(c)</sup>
112	{{	}} <sup>2(a),(c)</sup>	112	{{	}} <sup>2(a),(c)</sup>	}} <sup>2(a),(c)</sup>
136	{{	}} <sup>2(a),(c)</sup>	136	{{	}} <sup>2(a),(c)</sup>	}} <sup>2(a),(c)</sup>
137	{{	}} <sup>2(a),(c)</sup>	137	{{	}} <sup>2(a),(c)</sup>	}} <sup>2(a),(c)</sup>
140	{{	}} <sup>2(a),(c)</sup>	140	{{	}} <sup>2(a),(c)</sup>	}} <sup>2(a),(c)</sup>
141	{{	}} <sup>2(a),(c)</sup>	141	{{	}} <sup>2(a),(c)</sup>	}} <sup>2(a),(c)</sup>
148	{{	}} <sup>2(a),(c)</sup>	148	{{	}} <sup>2(a),(c)</sup>	}} <sup>2(a),(c)</sup>
161	{{	}} <sup>2(a),(c)</sup>	161	{{	}} <sup>2(a),(c)</sup>	}} <sup>2(a),(c)</sup>
300	{{	}} <sup>2(a),(c)</sup>	300	{{	}} <sup>2(a),(c)</sup>	}} <sup>2(a),(c)</sup>
342	{{	}} <sup>2(a),(c)</sup>	342	{{	}} <sup>2(a),(c)</sup>	}} <sup>2(a),(c)</sup>
{{			}} <sup>2(a),(c)</sup>			

### 5.1.2.6 Mesh Sensitivity Analysis

Modal analysis was performed with the Column 13 individual tube dry model to determine the effect of element type and size on modal results. The “fine mesh” uses 1-inch BEAM 188 elements, and the “coarse” mesh uses 12-inch BEAM189 elements.

The purpose of this sensitivity analysis is to ensure the coarse mesh properly characterizes the modal response of the tubes, as this coarse mesh is used in the TF-3 full bundle model to reduce computation time.

The mesh sensitivity results for the top 20 participating modes are presented in Table 5-27 through Table 5-29 for the pivot boundary conditions, and in Table 5-30 through Table 5-32 for the fixed boundary conditions. For the fixed condition, only modes under 400 Hz are shown. Results are shown in the global Cartesian coordinate system (CSYS, 0).

Agreement is shown between the two mesh sizes, validating the use of the coarse mesh in the full bundle model. For modes below 200 Hz, the frequency shift is less than {{  
}}<sup>2(a),(c)</sup>. The frequency shift increases with higher frequencies, but stays under {{  
}}<sup>2(a),(c)</sup> up to 400 Hz. This growing frequency shift is due to the increased



complexity of the mode shapes at higher frequencies, which become harder to represent with the coarse mesh that cannot fully resolve the complex shape. The difference is acceptable for the frequencies of interest.

Some modes show large changes in mass participation between the fine and coarse meshes, but this is typically a case of mass participation shifting from one mode to an adjacent closely spaced mode of a similar mode shape. When looking at comparable sets of modes between the fine and coarse meshes, the sums of the mass participations are similar between the two meshes, validating this explanation. See the mass participation sums at the end of each table. Additionally, the modes with large percent changes between mesh sizes tend to be the modes with low mass participation, so the magnitude of the mass participation change is small.

Table 5-27 Fine vs. coarse mesh modal results for pivot boundary conditions in x-direction

Fine Mesh - Col 13 Pivot, X (horiz)			Coarse Mesh - Col 13 Pivot, X (horiz)			
MODE	FREQ. (HZ)	MASS PARTIC. RATIO, X	MODE	FREQ. (HZ)	MASS PARTIC. RATIO, X	% CHANGE FREQ.
7	{{	}} <sup>2(a),(c)</sup>	7	{{	}} <sup>2(a),(c)</sup>	}} <sup>2(a),(c)</sup>
11	{{	}} <sup>2(a),(c)</sup>	11	{{	}} <sup>2(a),(c)</sup>	}} <sup>2(a),(c)</sup>
12	{{	}} <sup>2(a),(c)</sup>	12	{{	}} <sup>2(a),(c)</sup>	}} <sup>2(a),(c)</sup>
13	{{	}} <sup>2(a),(c)</sup>	13	{{	}} <sup>2(a),(c)</sup>	}} <sup>2(a),(c)</sup>
14	{{	}} <sup>2(a),(c)</sup>	14	{{	}} <sup>2(a),(c)</sup>	}} <sup>2(a),(c)</sup>
15	{{	}} <sup>2(a),(c)</sup>	15	{{	}} <sup>2(a),(c)</sup>	}} <sup>2(a),(c)</sup>
18	{{	}} <sup>2(a),(c)</sup>	18	{{	}} <sup>2(a),(c)</sup>	}} <sup>2(a),(c)</sup>
19	{{	}} <sup>2(a),(c)</sup>	19	{{	}} <sup>2(a),(c)</sup>	}} <sup>2(a),(c)</sup>
21	{{	}} <sup>2(a),(c)</sup>	21	{{	}} <sup>2(a),(c)</sup>	}} <sup>2(a),(c)</sup>
43	{{	}} <sup>2(a),(c)</sup>	-	{{	}} <sup>2(a),(c)</sup>	}} <sup>2(a),(c)</sup>
52	{{	}} <sup>2(a),(c)</sup>	52	{{	}} <sup>2(a),(c)</sup>	}} <sup>2(a),(c)</sup>
122	{{	}} <sup>2(a),(c)</sup>	122	{{	}} <sup>2(a),(c)</sup>	}} <sup>2(a),(c)</sup>
124	{{	}} <sup>2(a),(c)</sup>	124	{{	}} <sup>2(a),(c)</sup>	}} <sup>2(a),(c)</sup>
127	{{	}} <sup>2(a),(c)</sup>	127	{{	}} <sup>2(a),(c)</sup>	}} <sup>2(a),(c)</sup>
130	{{	}} <sup>2(a),(c)</sup>	130	{{	}} <sup>2(a),(c)</sup>	}} <sup>2(a),(c)</sup>
185	{{	}} <sup>2(a),(c)</sup>	185	{{	}} <sup>2(a),(c)</sup>	}} <sup>2(a),(c)</sup>
186	{{	}} <sup>2(a),(c)</sup>	186	{{	}} <sup>2(a),(c)</sup>	}} <sup>2(a),(c)</sup>
-	{{	}} <sup>2(a),(c)</sup>	187	{{	}} <sup>2(a),(c)</sup>	}} <sup>2(a),(c)</sup>
-	{{	}} <sup>2(a),(c)</sup>	188	{{	}} <sup>2(a),(c)</sup>	}} <sup>2(a),(c)</sup>
189	{{	}} <sup>2(a),(c)</sup>	-	{{	}} <sup>2(a),(c)</sup>	}} <sup>2(a),(c)</sup>
198	{{	}} <sup>2(a),(c)</sup>	198	{{	}} <sup>2(a),(c)</sup>	}} <sup>2(a),(c)</sup>
199	{{	}} <sup>2(a),(c)</sup>	199	{{	}} <sup>2(a),(c)</sup>	}} <sup>2(a),(c)</sup>
	{{					}} <sup>2(a),(c)</sup>

Table 5-28 Fine vs. coarse mesh modal results for pivot boundary conditions in y-direction

Fine Mesh - Col 13 Pivot, Y (vert)			Coarse Mesh - Col 13 Pivot, Y (vert)			
MODE	FREQ. (HZ)	MASS PARTIC. RATIO, Y	MODE	FREQ. (HZ)	MASS PARTIC. RATIO, Y	% CHANGE FREQ.
1	{{	}} <sup>2(a),(c)</sup>	1	{{	}} <sup>2(a),(c)</sup>	}} <sup>2(a),(c)</sup>
2	{{	}} <sup>2(a),(c)</sup>	2	{{	}} <sup>2(a),(c)</sup>	}} <sup>2(a),(c)</sup>
-	{{	}} <sup>2(a),(c)</sup>	13	{{	}} <sup>2(a),(c)</sup>	}} <sup>2(a),(c)</sup>
16	{{	}} <sup>2(a),(c)</sup>	16	{{	}} <sup>2(a),(c)</sup>	}} <sup>2(a),(c)</sup>
17	{{	}} <sup>2(a),(c)</sup>	17	{{	}} <sup>2(a),(c)</sup>	}} <sup>2(a),(c)</sup>
22	{{	}} <sup>2(a),(c)</sup>	22	{{	}} <sup>2(a),(c)</sup>	}} <sup>2(a),(c)</sup>
23	{{	}} <sup>2(a),(c)</sup>	23	{{	}} <sup>2(a),(c)</sup>	}} <sup>2(a),(c)</sup>
-	{{	}} <sup>2(a),(c)</sup>	28	{{	}} <sup>2(a),(c)</sup>	}} <sup>2(a),(c)</sup>
29	{{	}} <sup>2(a),(c)</sup>	29	{{	}} <sup>2(a),(c)</sup>	}} <sup>2(a),(c)</sup>
53	{{	}} <sup>2(a),(c)</sup>	53	{{	}} <sup>2(a),(c)</sup>	}} <sup>2(a),(c)</sup>
119	{{	}} <sup>2(a),(c)</sup>	119	{{	}} <sup>2(a),(c)</sup>	}} <sup>2(a),(c)</sup>
120	{{	}} <sup>2(a),(c)</sup>	120	{{	}} <sup>2(a),(c)</sup>	}} <sup>2(a),(c)</sup>
206	{{	}} <sup>2(a),(c)</sup>	206	{{	}} <sup>2(a),(c)</sup>	}} <sup>2(a),(c)</sup>
207	{{	}} <sup>2(a),(c)</sup>	207	{{	}} <sup>2(a),(c)</sup>	}} <sup>2(a),(c)</sup>
-	{{	}} <sup>2(a),(c)</sup>	210	{{	}} <sup>2(a),(c)</sup>	}} <sup>2(a),(c)</sup>
211	{{	}} <sup>2(a),(c)</sup>	211	{{	}} <sup>2(a),(c)</sup>	}} <sup>2(a),(c)</sup>
212	{{	}} <sup>2(a),(c)</sup>	-	{{	}} <sup>2(a),(c)</sup>	}} <sup>2(a),(c)</sup>
213	{{	}} <sup>2(a),(c)</sup>	213	{{	}} <sup>2(a),(c)</sup>	}} <sup>2(a),(c)</sup>
214	{{	}} <sup>2(a),(c)</sup>	-	{{	}} <sup>2(a),(c)</sup>	}} <sup>2(a),(c)</sup>
215	{{	}} <sup>2(a),(c)</sup>	215	{{	}} <sup>2(a),(c)</sup>	}} <sup>2(a),(c)</sup>
334	{{	}} <sup>2(a),(c)</sup>	-	{{	}} <sup>2(a),(c)</sup>	}} <sup>2(a),(c)</sup>
335	{{	}} <sup>2(a),(c)</sup>	-	{{	}} <sup>2(a),(c)</sup>	}} <sup>2(a),(c)</sup>
336	{{	}} <sup>2(a),(c)</sup>	-	{{	}} <sup>2(a),(c)</sup>	}} <sup>2(a),(c)</sup>
-	{{	}} <sup>2(a),(c)</sup>	337	{{	}} <sup>2(a),(c)</sup>	}} <sup>2(a),(c)</sup>
-	{{	}} <sup>2(a),(c)</sup>	338	{{	}} <sup>2(a),(c)</sup>	}} <sup>2(a),(c)</sup>
	{{					}} <sup>2(a),(c)</sup>

Table 5-29 Fine vs. coarse mesh modal results for pivot boundary conditions in z-direction

Fine Mesh - Col 13 Pivot, Z (horiz)			Coarse Mesh - Col 13 Pivot, Z (horiz)			
MODE	FREQ. (HZ)	MASS PARTIC. RATIO, Z	MODE	FREQ. (HZ)	MASS PARTIC. RATIO, Z	% CHANGE FREQ.
12	{{	}} <sup>2(a),(c)</sup>	12	{{	}} <sup>2(a),(c)</sup>	}} <sup>2(a),(c)</sup>
13	{{	}} <sup>2(a),(c)</sup>	13	{{	}} <sup>2(a),(c)</sup>	}} <sup>2(a),(c)</sup>
14	{{	}} <sup>2(a),(c)</sup>	14	{{	}} <sup>2(a),(c)</sup>	}} <sup>2(a),(c)</sup>
15	{{	}} <sup>2(a),(c)</sup>	15	{{	}} <sup>2(a),(c)</sup>	}} <sup>2(a),(c)</sup>
18	{{	}} <sup>2(a),(c)</sup>	18	{{	}} <sup>2(a),(c)</sup>	}} <sup>2(a),(c)</sup>
126	{{	}} <sup>2(a),(c)</sup>	126	{{	}} <sup>2(a),(c)</sup>	}} <sup>2(a),(c)</sup>
128	{{	}} <sup>2(a),(c)</sup>	128	{{	}} <sup>2(a),(c)</sup>	}} <sup>2(a),(c)</sup>
129	{{	}} <sup>2(a),(c)</sup>	129	{{	}} <sup>2(a),(c)</sup>	}} <sup>2(a),(c)</sup>
131	{{	}} <sup>2(a),(c)</sup>	131	{{	}} <sup>2(a),(c)</sup>	}} <sup>2(a),(c)</sup>
139	{{	}} <sup>2(a),(c)</sup>	139	{{	}} <sup>2(a),(c)</sup>	}} <sup>2(a),(c)</sup>
184	{{	}} <sup>2(a),(c)</sup>	184	{{	}} <sup>2(a),(c)</sup>	}} <sup>2(a),(c)</sup>
-	{{	}} <sup>2(a),(c)</sup>	185	{{	}} <sup>2(a),(c)</sup>	}} <sup>2(a),(c)</sup>
186	{{	}} <sup>2(a),(c)</sup>	186	{{	}} <sup>2(a),(c)</sup>	}} <sup>2(a),(c)</sup>
187	{{	}} <sup>2(a),(c)</sup>	187	{{	}} <sup>2(a),(c)</sup>	}} <sup>2(a),(c)</sup>
188	{{	}} <sup>2(a),(c)</sup>	188	{{	}} <sup>2(a),(c)</sup>	}} <sup>2(a),(c)</sup>
191	{{	}} <sup>2(a),(c)</sup>	191	{{	}} <sup>2(a),(c)</sup>	}} <sup>2(a),(c)</sup>
200	{{	}} <sup>2(a),(c)</sup>	200	{{	}} <sup>2(a),(c)</sup>	}} <sup>2(a),(c)</sup>
201	{{	}} <sup>2(a),(c)</sup>	201	{{	}} <sup>2(a),(c)</sup>	}} <sup>2(a),(c)</sup>
208	{{	}} <sup>2(a),(c)</sup>	-	{{	}} <sup>2(a),(c)</sup>	}} <sup>2(a),(c)</sup>
235	{{	}} <sup>2(a),(c)</sup>	-	{{	}} <sup>2(a),(c)</sup>	}} <sup>2(a),(c)</sup>
236	{{	}} <sup>2(a),(c)</sup>	-	{{	}} <sup>2(a),(c)</sup>	}} <sup>2(a),(c)</sup>
-	{{	}} <sup>2(a),(c)</sup>	237	{{	}} <sup>2(a),(c)</sup>	}} <sup>2(a),(c)</sup>
-	{{	}} <sup>2(a),(c)</sup>	238	{{	}} <sup>2(a),(c)</sup>	}} <sup>2(a),(c)</sup>
	{{					}} <sup>2(a),(c)</sup>

Table 5-30 Fine vs. coarse mesh modal results for fixed boundary conditions in x-direction

Fine Mesh - Col 13 Fixed, X (horiz)			Coarse Mesh - Col 13 Fixed, X (horiz)			
MODE	FREQ. (HZ)	MASS PARTIC. RATIO, X	MODE	FREQ. (HZ)	MASS PARTIC. RATIO, X	% CHANGE FREQ.
1	{{	}} <sup>2(a),(c)</sup>	1	{{	}} <sup>2(a),(c)</sup>	}} <sup>2(a),(c)</sup>
2	{{	}} <sup>2(a),(c)</sup>	2	{{	}} <sup>2(a),(c)</sup>	}} <sup>2(a),(c)</sup>
15	{{	}} <sup>2(a),(c)</sup>	15	{{	}} <sup>2(a),(c)</sup>	}} <sup>2(a),(c)</sup>
16	{{	}} <sup>2(a),(c)</sup>	16	{{	}} <sup>2(a),(c)</sup>	}} <sup>2(a),(c)</sup>
28	{{	}} <sup>2(a),(c)</sup>	28	{{	}} <sup>2(a),(c)</sup>	}} <sup>2(a),(c)</sup>
29	{{	}} <sup>2(a),(c)</sup>	29	{{	}} <sup>2(a),(c)</sup>	}} <sup>2(a),(c)</sup>
30	{{	}} <sup>2(a),(c)</sup>	30	{{	}} <sup>2(a),(c)</sup>	}} <sup>2(a),(c)</sup>
32	{{	}} <sup>2(a),(c)</sup>	32	{{	}} <sup>2(a),(c)</sup>	}} <sup>2(a),(c)</sup>
-	{{	}} <sup>2(a),(c)</sup>	33	{{	}} <sup>2(a),(c)</sup>	}} <sup>2(a),(c)</sup>
41	{{	}} <sup>2(a),(c)</sup>	41	{{	}} <sup>2(a),(c)</sup>	}} <sup>2(a),(c)</sup>
44	{{	}} <sup>2(a),(c)</sup>	44	{{	}} <sup>2(a),(c)</sup>	}} <sup>2(a),(c)</sup>
47	{{	}} <sup>2(a),(c)</sup>	47	{{	}} <sup>2(a),(c)</sup>	}} <sup>2(a),(c)</sup>
-	{{	}} <sup>2(a),(c)</sup>	48	{{	}} <sup>2(a),(c)</sup>	}} <sup>2(a),(c)</sup>
49	{{	}} <sup>2(a),(c)</sup>	49	{{	}} <sup>2(a),(c)</sup>	}} <sup>2(a),(c)</sup>
52	{{	}} <sup>2(a),(c)</sup>	52	{{	}} <sup>2(a),(c)</sup>	}} <sup>2(a),(c)</sup>
53	{{	}} <sup>2(a),(c)</sup>	-	{{	}} <sup>2(a),(c)</sup>	}} <sup>2(a),(c)</sup>
-	{{	}} <sup>2(a),(c)</sup>	54	{{	}} <sup>2(a),(c)</sup>	}} <sup>2(a),(c)</sup>
80	{{	}} <sup>2(a),(c)</sup>	80	{{	}} <sup>2(a),(c)</sup>	}} <sup>2(a),(c)</sup>
122	{{	}} <sup>2(a),(c)</sup>	122	{{	}} <sup>2(a),(c)</sup>	}} <sup>2(a),(c)</sup>
123	{{	}} <sup>2(a),(c)</sup>	-	{{	}} <sup>2(a),(c)</sup>	}} <sup>2(a),(c)</sup>
134	{{	}} <sup>2(a),(c)</sup>	134	{{	}} <sup>2(a),(c)</sup>	}} <sup>2(a),(c)</sup>
148	{{	}} <sup>2(a),(c)</sup>	-	{{	}} <sup>2(a),(c)</sup>	}} <sup>2(a),(c)</sup>
149	{{	}} <sup>2(a),(c)</sup>	-	{{	}} <sup>2(a),(c)</sup>	}} <sup>2(a),(c)</sup>
-	{{	}} <sup>2(a),(c)</sup>	150	{{	}} <sup>2(a),(c)</sup>	}} <sup>2(a),(c)</sup>
	{{	}} <sup>2(a),(c)</sup>				}} <sup>2(a),(c)</sup>

Table 5-31 Fine vs. coarse mesh modal results for fixed boundary conditions in y-direction

Fine Mesh - Col 13 Fixed, Y (vert)			Coarse Mesh - Col 13 Fixed, Y (vert)			
MODE	FREQ. (HZ)	MASS PARTIC. RATIO, Y	MODE	FREQ. (HZ)	MASS PARTIC. RATIO, Y	% CHANGE FREQ.
1	{{	}} <sup>2(a),(c)</sup>	1	{{	}} <sup>2(a),(c)</sup>	}} <sup>2(a),(c)</sup>
3	{{	}} <sup>2(a),(c)</sup>	3	{{	}} <sup>2(a),(c)</sup>	}} <sup>2(a),(c)</sup>
4	{{	}} <sup>2(a),(c)</sup>	4	{{	}} <sup>2(a),(c)</sup>	}} <sup>2(a),(c)</sup>
7	{{	}} <sup>2(a),(c)</sup>	7	{{	}} <sup>2(a),(c)</sup>	}} <sup>2(a),(c)</sup>
8	{{	}} <sup>2(a),(c)</sup>	8	{{	}} <sup>2(a),(c)</sup>	}} <sup>2(a),(c)</sup>
11	{{	}} <sup>2(a),(c)</sup>	11	{{	}} <sup>2(a),(c)</sup>	}} <sup>2(a),(c)</sup>
12	{{	}} <sup>2(a),(c)</sup>	12	{{	}} <sup>2(a),(c)</sup>	}} <sup>2(a),(c)</sup>
27	{{	}} <sup>2(a),(c)</sup>	27	{{	}} <sup>2(a),(c)</sup>	}} <sup>2(a),(c)</sup>
29	{{	}} <sup>2(a),(c)</sup>	29	{{	}} <sup>2(a),(c)</sup>	}} <sup>2(a),(c)</sup>
31	{{	}} <sup>2(a),(c)</sup>	31	{{	}} <sup>2(a),(c)</sup>	}} <sup>2(a),(c)</sup>
110	{{	}} <sup>2(a),(c)</sup>	110	{{	}} <sup>2(a),(c)</sup>	}} <sup>2(a),(c)</sup>
112	{{	}} <sup>2(a),(c)</sup>	-	{{	}} <sup>2(a),(c)</sup>	}} <sup>2(a),(c)</sup>
-	{{	}} <sup>2(a),(c)</sup>	113	{{	}} <sup>2(a),(c)</sup>	}} <sup>2(a),(c)</sup>
115	{{	}} <sup>2(a),(c)</sup>	-	{{	}} <sup>2(a),(c)</sup>	}} <sup>2(a),(c)</sup>
-	{{	}} <sup>2(a),(c)</sup>	135	{{	}} <sup>2(a),(c)</sup>	}} <sup>2(a),(c)</sup>
136	{{	}} <sup>2(a),(c)</sup>	-	{{	}} <sup>2(a),(c)</sup>	}} <sup>2(a),(c)</sup>
137	{{	}} <sup>2(a),(c)</sup>	-	{{	}} <sup>2(a),(c)</sup>	}} <sup>2(a),(c)</sup>
-	{{	}} <sup>2(a),(c)</sup>	138	{{	}} <sup>2(a),(c)</sup>	}} <sup>2(a),(c)</sup>
140	{{	}} <sup>2(a),(c)</sup>	140	{{	}} <sup>2(a),(c)</sup>	}} <sup>2(a),(c)</sup>
-	{{	}} <sup>2(a),(c)</sup>	143	{{	}} <sup>2(a),(c)</sup>	}} <sup>2(a),(c)</sup>
141	{{	}} <sup>2(a),(c)</sup>	-	{{	}} <sup>2(a),(c)</sup>	}} <sup>2(a),(c)</sup>
144	{{	}} <sup>2(a),(c)</sup>	144	{{	}} <sup>2(a),(c)</sup>	}} <sup>2(a),(c)</sup>
-	{{	}} <sup>2(a),(c)</sup>	147	{{	}} <sup>2(a),(c)</sup>	}} <sup>2(a),(c)</sup>
148	{{	}} <sup>2(a),(c)</sup>	-	{{	}} <sup>2(a),(c)</sup>	}} <sup>2(a),(c)</sup>
-	{{	}} <sup>2(a),(c)</sup>	156	{{	}} <sup>2(a),(c)</sup>	}} <sup>2(a),(c)</sup>
-	{{	}} <sup>2(a),(c)</sup>	160	{{	}} <sup>2(a),(c)</sup>	}} <sup>2(a),(c)</sup>
161	{{	}} <sup>2(a),(c)</sup>	-	{{	}} <sup>2(a),(c)</sup>	}} <sup>2(a),(c)</sup>
	{{					}} <sup>2(a),(c)</sup>

Table 5-32 Fine vs. coarse mesh modal results for fixed boundary conditions in z-direction

Fine Mesh - Col 13 Fixed, Z (horiz)			Coarse Mesh - Col 13 Fixed, Z (horiz)			
MODE	FREQ. (HZ)	MASS PARTIC. RATIO, Z	MODE	FREQ. (HZ)	MASS PARTIC. RATIO, Z	% CHANGE FREQ.
1	{{	}} <sup>2(a),(c)</sup>	1	{{	}} <sup>2(a),(c)</sup>	}} <sup>2(a),(c)</sup>
2	{{	}} <sup>2(a),(c)</sup>	2	{{	}} <sup>2(a),(c)</sup>	}} <sup>2(a),(c)</sup>
13	{{	}} <sup>2(a),(c)</sup>	13	{{	}} <sup>2(a),(c)</sup>	}} <sup>2(a),(c)</sup>
14	{{	}} <sup>2(a),(c)</sup>	14	{{	}} <sup>2(a),(c)</sup>	}} <sup>2(a),(c)</sup>
27	{{	}} <sup>2(a),(c)</sup>	27	{{	}} <sup>2(a),(c)</sup>	}} <sup>2(a),(c)</sup>
28	{{	}} <sup>2(a),(c)</sup>	28	{{	}} <sup>2(a),(c)</sup>	}} <sup>2(a),(c)</sup>
29	{{	}} <sup>2(a),(c)</sup>	-	{{	}} <sup>2(a),(c)</sup>	}} <sup>2(a),(c)</sup>
38	{{	}} <sup>2(a),(c)</sup>	38	{{	}} <sup>2(a),(c)</sup>	}} <sup>2(a),(c)</sup>
-	{{	}} <sup>2(a),(c)</sup>	40	{{	}} <sup>2(a),(c)</sup>	}} <sup>2(a),(c)</sup>
-	{{	}} <sup>2(a),(c)</sup>	41	{{	}} <sup>2(a),(c)</sup>	}} <sup>2(a),(c)</sup>
42	{{	}} <sup>2(a),(c)</sup>	42	{{	}} <sup>2(a),(c)</sup>	}} <sup>2(a),(c)</sup>
43	{{	}} <sup>2(a),(c)</sup>	43	{{	}} <sup>2(a),(c)</sup>	}} <sup>2(a),(c)</sup>
45	{{	}} <sup>2(a),(c)</sup>	-	{{	}} <sup>2(a),(c)</sup>	}} <sup>2(a),(c)</sup>
-	{{	}} <sup>2(a),(c)</sup>	53	{{	}} <sup>2(a),(c)</sup>	}} <sup>2(a),(c)</sup>
54	{{	}} <sup>2(a),(c)</sup>	-	{{	}} <sup>2(a),(c)</sup>	}} <sup>2(a),(c)</sup>
55	{{	}} <sup>2(a),(c)</sup>	55	{{	}} <sup>2(a),(c)</sup>	}} <sup>2(a),(c)</sup>
80	{{	}} <sup>2(a),(c)</sup>	80	{{	}} <sup>2(a),(c)</sup>	}} <sup>2(a),(c)</sup>
84	{{	}} <sup>2(a),(c)</sup>	84	{{	}} <sup>2(a),(c)</sup>	}} <sup>2(a),(c)</sup>
109	{{	}} <sup>2(a),(c)</sup>	109	{{	}} <sup>2(a),(c)</sup>	}} <sup>2(a),(c)</sup>
121	{{	}} <sup>2(a),(c)</sup>	121	{{	}} <sup>2(a),(c)</sup>	}} <sup>2(a),(c)</sup>
135	{{	}} <sup>2(a),(c)</sup>	-	{{	}} <sup>2(a),(c)</sup>	}} <sup>2(a),(c)</sup>
146	{{	}} <sup>2(a),(c)</sup>	146	{{	}} <sup>2(a),(c)</sup>	}} <sup>2(a),(c)</sup>
147	{{	}} <sup>2(a),(c)</sup>	-	{{	}} <sup>2(a),(c)</sup>	}} <sup>2(a),(c)</sup>
-	{{	}} <sup>2(a),(c)</sup>	149	{{	}} <sup>2(a),(c)</sup>	}} <sup>2(a),(c)</sup>
-	{{	}} <sup>2(a),(c)</sup>	161	{{	}} <sup>2(a),(c)</sup>	}} <sup>2(a),(c)</sup>
	{{					}} <sup>2(a),(c)</sup>

### 5.1.2.7 Strain Gauge Placement Recommendations

Modal analysis was performed on the two bounding tubes of the Column 11 individual tube model for the pivot and fixed boundary conditions. Strain gauge placement recommendations are provided for the top five mass participating modes in the vertical y-direction. These maximum strain locations are determined using the “EPELINT” (elastic strain intensity) user defined result in ANSYS Workbench Mechanical. Analysis was performed for the tubes in the dry condition.

Table 5-33 provides the top five mass participating modes in the y-directions for each of the two tubes for each of the boundary conditions. The strain gauge placement recommendations are shown in Figure 5-20 through Figure 5-23. The maximum strain for each mode occurs at the mid-span between boundary conditions, or at the boundary condition.

Table 5-33 Top 5 participating modes in y-direction for Column 11 tubes

Col 11 Tube 1 Pivot			Col 11 Tube 1 Fixed		
MODE	FREQ. (HZ)	MASS PARTIC. RATIO, Y	MODE	FREQ. (HZ)	MASS PARTIC. RATIO, Y
1	{{	}} <sup>2(a),(c)</sup>	2	{{	}} <sup>2(a),(c)</sup>
10	{{	}} <sup>2(a),(c)</sup>	4	{{	}} <sup>2(a),(c)</sup>
12	{{	}} <sup>2(a),(c)</sup>	16	{{	}} <sup>2(a),(c)</sup>
68	{{	}} <sup>2(a),(c)</sup>	65	{{	}} <sup>2(a),(c)</sup>
123	{{	}} <sup>2(a),(c)</sup>	79	{{	}} <sup>2(a),(c)</sup>

Col 11 Tube 16 Pivot			Col 11 Tube 16 Fixed		
MODE	FREQ. (HZ)	MASS PARTIC. RATIO, Y	MODE	FREQ. (HZ)	MASS PARTIC. RATIO, Y
1	{{	}} <sup>2(a),(c)</sup>	2	{{	}} <sup>2(a),(c)</sup>
10	{{	}} <sup>2(a),(c)</sup>	4	{{	}} <sup>2(a),(c)</sup>
69	{{	}} <sup>2(a),(c)</sup>	16	{{	}} <sup>2(a),(c)</sup>
122	{{	}} <sup>2(a),(c)</sup>	63	{{	}} <sup>2(a),(c)</sup>
194	{{	}} <sup>2(a),(c)</sup>	79	{{	}} <sup>2(a),(c)</sup>



{{

}}<sup>2(a),(c)</sup>

Figure 5-20 Maximum strain intensity locations for Column 11, tube 1, pivot case, dominant vertical modes

{{

}}<sup>2(a),(c)</sup>

Figure 5-21 Maximum strain intensity locations for Column 11, tube 1, fixed case, dominant vertical modes

{{

}}<sup>2(a),(c)</sup>

Figure 5-22 Maximum strain intensity locations for Column 11, tube 16, pivot case, dominant vertical modes

{{

}}<sup>2(a),(c)</sup>

Figure 5-23 Maximum strain intensity locations for Column 11, tube 16, fixed case, dominant vertical modes

### 5.1.2.8 Modal Analysis – TF-3 Full Bundle Model

Modal analysis is performed for the TF-3 full bundle model. The purpose of the full bundle analysis is to determine the full bundle modes, and also determine if the tube modes within the full bundle match those of the individual tube models. If the tube modes are similar, it validates the assumption of rigid supports in the individual tube models.

The full bundle model is run in both the pivot and fixed conditions for the tube-to-tube support connections. These are the same boundary condition cases used in the individual tube models.

An additional case is run with the fixed condition where the circumferential coupling between the tube supports and the inner and outer vessels is removed. This is done to determine a possible twisting mode of the tube bundle in case the circumferential restraints were removed. This third case is called “fixed, no circ.”

The full bundle analyses are run from 0 Hz to 55 Hz for the pivot case, and 0 Hz, to 80 Hz for the fixed case. These upper bounds were selected to capture the modes with highest vertical mass participation as seen in the individual tube models. The “fixed, no circ” case is run for the first 1,000 modes, which terminated at  $\{\{ \quad \} \}^{2(a),(c)}$ . This was done to capture the twisting mode, but not repeat other modes that are similar to the normal fixed case.

The modes of interest that are discussed in the in the following sections are summarized in Table 5-34.

Table 5-34 Summary of full bundle model results

Boundary Condition Case	Mode Freq. (Hz)	Mode Type	Notes
Pivot	{{ }} <sup>2(a),(c)</sup>	tube breathing	Similar frequency as breathing mode in column 13 individual tube model ({{ }} <sup>2(a),(c)</sup> Hz)
	{{ }} <sup>2(a),(c)</sup>	full specimen rocking	Full specimen rocking mode. Not seen in individual tube models
	{{ }} <sup>2(a),(c)</sup>	tube beam (long span between supports)	Highest y-mass participation. Matches frequencies for high y-mass participation modes in individual tube models (see below)
	{{ }} <sup>2(a),(c)</sup>	tube beam (long span between supports)	Top 38 y-mass participating modes. Matches frequencies for highest y-mass participating modes in individual tube models ({{ }} <sup>2(a),(c)</sup> Hz)
Fixed	{{ }} <sup>2(a),(c)</sup>	full specimen rocking	Full specimen rocking mode, similar to pivot case. Not seen in individual tube models
	{{ }} <sup>2(a),(c)</sup>	full specimen squeezing	Full specimen squeezing mode. Likely exists in pivot case, but difficult to discern due to overlapping tube modes. Not seen in individual tube models
	{{ }} <sup>2(a),(c)</sup>	tube beam (transition bend)	Beam mode of tube transition bend. Similar to transition bend beam mode of Column 13 individual tube model ({{ }} <sup>2(a),(c)</sup> Hz)
	{{ }} <sup>2(a),(c)</sup>	tube beam (long span between supports)	Highest y-mass participation. Matches frequency for highest y-mass participation mode in Column 13 individual tube model ({{ }} <sup>2(a),(c)</sup> Hz)
Fixed, No Circ	{{ }} <sup>2(a),(c)</sup>	tube bundle twisting	Twisting of the tube and tube support bundle relative to the vessels. Low mass participation (outside of top 240 participating modes in any direction). Not seen in individual tube models. Other modes similar to fixed case

The following sections contain several figures of mode shapes. In some figures, the cross-section shapes are shown, and some figures they are not. The option that showed the mode shape best was chosen.

The fundamental mode of the full bundle pivot case is at  $\omega_{(a),(c)}$ . This is about 5 percent lower than the fundamental mode of the Column 13 individual tube model of  $\omega_{(a),(c)}$ . Both modes correspond to breathing of the tubes. This tube breathing mode shape is shown in Figure 5-24.

$\omega_{(a),(c)}$

$\omega_{(a),(c)}$

Figure 5-24 Fundamental mode for full bundle pivot case (breathing mode)

The mode with highest x-direction mass participation is at  $\{\{ \quad \}\}^{2(a),(c)}$ . This mode is the entire specimen rocking back and forth, and thus there is no corresponding mode in the individual tube models. This mode shape is shown in Figure 5-25.

$\{\{$

—

$\}\}^{2(a),(c)}$

Figure 5-25 Mode with highest x-direction mass participation for full bundle pivot case (rocking mode)

The mode with highest y-direction mass participation is at  $\{\{ \quad \}\}^{2(a),(c)}$ . This is a tube beam mode and is shown in Figure 5-26. The vessels do not respond to this mode.



The top 38 y-participating modes are between  $\{\{ \dots \}^{2(a),(c)}$ . These are similar frequencies as seen in the individual tube models, which have dominant y-direction modes of  $\{\{ \dots \}^{2(a),(c)}$  for Column 13 and Column 9, respectively.

$\{\{$

$\}^{2(a),(c)}$

Figure 5-26 Mode with highest y-direction mass participation for full bundle pivot case (tube beam mode)

The fundamental mode of the full bundle fixed model is an  $\{\{ \dots \}^{2(a),(c)}$  rocking mode, similar to the one shown in Figure 5-25 for the pivot case.

An additional entire specimen mode becomes apparent in the fixed case, which is a squeezing mode at  $\{\{ \dots \}^{2(a),(c)}$ . It is less apparent in the pivot case because it

overlaps the lower frequency tube modes of that case. This mode shape is shown in Figure 5-27. Despite this being a full specimen mode, it has relatively low mass participation, with similar participation values to the closely spaced tube modes.

{{

}}<sup>2(a),(c)</sup>

Figure 5-27 Entire specimen squeezing mode for full bundle fixed case

The tube fundamental mode within the full bundle model is at  $\{\{ \quad \}\}^{2(a),(c)}$  and is a beam mode of the tube transition bend region. This is a similar mode shape as the individual tube model shown in Figure 5-18, which also has a similar frequency of  $\{\{ \quad \}\}^{2(a),(c)}$ . The full bundle mode is shown in Figure 5-28.

$\{\{$

$\}\}^{2(a),(c)}$

Figure 5-28 Tube fundamental mode for full bundle fixed case (beam mode of transition bend)

The overall mode with highest y-direction mass participation is at  $\{\{ \quad \}\}^{2(a),(c)}$ . It makes up  $\{\{ \quad \}\}^{2(a),(c)}$  of the vertical mass, indicating it is a vessel axial mode. It

is difficult to visualize the axial motion of the specimen because the axial displacement is very small compared to the tube displacements that also occur in this mode.

The mode with highest y-direction mass participation that is dominated by tube movement is at  $\{\{ \quad \} \}^{2(a),(c)}$ . This mode exhibits beam mode behavior for the long spans of many tubes, similar to that shown in the Column 13 individual tube model in Figure 5-19. It is also similar in frequency to the individual tube model  $\{\{ \quad \} \}^{2(a),(c)}$ . This full bundle mode is shown in Figure 5-29.

$\{\{$

$\} \}^{2(a),(c)}$

Figure 5-29 Tube mode with highest y-direction mass participation for full bundle fixed case (tube beam mode)

The fixed case model was repeated but the circumferential coupling between the tube supports and the inner and outer vessels was removed. This simulates a condition where the circumferential restraints welded to the inner and outer vessels are removed. This model was only analyzed for the first 1,000 modes.

This case introduces a tube bundle twisting mode at  $\omega_{2(a),(c)}$ . This mode shape is shown in Figure 5-30. Cross-section shapes are turned on to highlight the tube supports. The mode has low mass participation. It has the 798<sup>th</sup> highest x-mass participation, 248<sup>th</sup> highest y-mass participation, and 978<sup>th</sup> highest z-mass participation.

{{

$\omega_{2(a),(c)}$

Figure 5-30 Twisting mode for full tube bundle fixed (no circ) case

### 5.1.2.9 Conclusions

This calculation provides modal analysis of the TF-3 test specimen through the use of individual tube models and the full bundle model.

The modal analysis results show agreement between the full bundle model and the single tube models for modes involving the tubes (see Table 5-34). This validates the use of the rigid boundary conditions in the single tube models, because the inclusion of the explicitly modeled tube supports and vessels in the full bundle model did not significantly alter the tube modes. The full bundle analysis also provides the additional full bundle modes not captured in the individual tube models.

The individual tube models provide frequencies and mass participations for the bounding tubes in the bounding columns (Columns 9 and 13). The effects of different boundary conditions, added mass, and mesh size are evaluated. Mode shapes for modes below 300 Hz are written to text files for downstream analysis of Columns 9, 11, and 13.

Maximum strain intensity locations are provided for the Column 11 dominant vertical modes, as a recommendation for strain gauge placement.

### 5.1.3 TF-3 FEI Pre-Test Prediction

The purpose of this section is to document the pre-test prediction for the fluid elastic instability (FEI) flow test in the TF-3 test facility. This section contains an assessment of the best estimate FEI results, assessment of the TF-3 experimental biases, and analysis of input, measurement and numerical uncertainties that affect the validation of the design analysis using the TF-3 validation test results.

This calculation estimates the uncertainty in the design analysis safety margin for FEI and provides the expected and allowable range for measurements in the test to validate the design analysis, considering input, measurement and numerical uncertainties, as well as experimental biases due to test facility distortions.

#### 5.1.3.1 Methodology

##### 5.1.3.1.1 Input Uncertainties

Uncertainty evaluation is performed to determine the effect of input and measurement uncertainties on the validation range for the TF-3 testing. The results of the uncertainty evaluation are calculated in terms of the dimensionless safety margin parameter, and then converted to velocities and flow rates that correspond to the expected onset of FEI for the test specimen, and the range that would adequately validate the design analysis, considering input and measurement uncertainties as well as experimental biases. The TF-3 testing will provide information regarding the frequencies, mode shapes, and damping for the SG tubes. The best-estimate and uncertainty values for these parameters are used to calculate the expected velocity for FEI onset and range of validation velocities. Testing results will be used to confirm the values used in this analysis are appropriate.

Best-estimate or nominal values are provided for parameters that are biased in the design analysis. Removing conservatism results in a higher predicted velocity for the onset of FEI, which is important for validating that the TF-3 test is adequately designed to observe the phenomena. A summary of the nominal values are provided in the following bullet points:

- The mean gap velocity is calculated considering the range of best-estimate primary coolant flow rates in the upper region of the tube bundle and in the lower region of the tube bundle, and the pitch representing the diagonal distance between tubes. Uncertainty in the gap velocity is evaluated considering variability in flow from the steam to feedwater region of the tube bundle (due to density change), minimum to maximum design primary coolant flowrates, and steady-state versus transient flow conditions. The uncertainty is based on the sample variance in the distribution of velocity values.
- A modal multiplier value of 1.0 corresponds to a mode shape where the tube motion is bending in or out of plane relative to the tube axis. If FEI occurs, cross flow is expected to excite a bending mode with a high modal multiplier value, i.e. close to or equal to 1.0, since it's not likely that cross flow could excite a tangential mode. Based on this judgment, this pre-test prediction assessment does not specifically assess uncertainties in the modal multiplier value and assigns the frequencies for FEI as the lowest frequency that is a bending mode in the helical region. The results of the flow testing will validate this design approach.
- The linear mass includes the mass of the tube, fluid inside the tube, and the hydrodynamic mass. The design analysis value represents the conditions in the tube bundle near the steam plenum and the feedwater plenum, at full power maximum design flow rate conditions. The nominal value represents roughly the average conditions in the tube bundle, and also accounts for a mean added mass coefficient. There will be slight temperature and thus density changes in these regions based on the primary coolant flow rate conditions; however, these changes are small relative to the changes between the conditions at the top and bottom of the tube bundle. The input uncertainty is determined from the variation between the linear masses from the steam to feedwater regions of the tube bundle.
- The design analysis damping is  $\{\{ \quad \} \}^{2(a),(c)}$  is assumed in this calculation. Input uncertainty is based on the variation between the design analysis and build-out test results.
- In the design analysis, the hot region primary coolant density is used. For the best-estimate assessment, the hot and cold primary coolant densities are averaged to provide a mean density for the tube bundle, which is set as the nominal value. The input uncertainty is determined from the variation between the fluid densities from the steam to feedwater regions of the tube bundle.
- The design analysis and nominal value for the SG tube outer diameter is the same value. The input uncertainty considers a  $\{\{ \quad \} \}^{2(a),(c)}$  manufacturing tolerance.

- The design analysis assumes a Connors' constant a coefficient of  $\{\{ \}^{2(a),(c)}$ . These constants bound the straight and helical tube experimental data, and better match the shape of the test data in the low mass damping region. There are various constants which could be selected as the best-estimate values for this assessment. For this assessment the Connors' constant coefficient of  $\{\{ \}^{2(a),(c)}$  are selected. These bound most of the experimental results at low mass damping and are judged to be appropriate for use as the best-estimate values in the pre-test prediction.
- The design analysis value for frequency that produces the limiting reduced velocity is the same for both the sliding and fixed boundary conditions of column 21, which is the limiting column. The calculation of mean frequency considers a  $\{\{ \}^{2(a),(c)}$  frequency shift in the design analysis value based on mesh refinement, and a  $\{\{ \}^{2(a),(c)}$  frequency shift associated with the added mass factor for tubes in a bundle. Note that there are some differences between the mode shapes and frequencies for the tubes within a column. These differences are not specifically considered herein, but may be appropriate to assess in the post-test analysis.

The design analysis input parameters and nominal values are summarized in Table 5-35.

Table 5-35 Design and Nominal values for input uncertainty assessment

Parameter	Variable	Design Analysis Values	Nominal Value
Velocity	X <sub>1</sub>	$\{\{ \}$	
Modal multiplier	X <sub>2</sub>		
Linear mass density	X <sub>3</sub>		
Damping	X <sub>4</sub>		
Fluid density	X <sub>5</sub>		
SG tube OD	X <sub>6</sub>		
Connors' Constant 'C'	X <sub>7</sub>		
Connors' Constant 'a'	X <sub>8</sub>		
Frequency	X <sub>9</sub>		$\{\{ \}^{2(a),(c)}$

### 5.1.3.1.2 Measurement Uncertainties

Measurement uncertainties are assessed for input terms that will be directly or indirectly measured in the testing. Measurement uncertainties are largely based on engineering judgment at the time of the pre-test prediction, and will be validated in the post-test assessment. The measurement uncertainties used in this calculation are summarized in the following bullets and Table 5-36.

- The gap velocity in the test specimen is the same as in the design, since the geometry within the tube array is prototypic. While gap velocity is the parameter of interest for FEI, volumetric flow rate is what will be measured for the test. Errors in volumetric flow rate are directly proportional to the errors in gap velocity, so the volumetric flow rate measurement uncertainty of  $\{\{ \}^{2(a),(c)}$  is evaluated. Uncertainty in the tube OD and other test specimen dimensions, such as the riser OD and vessel ID, introduce uncertainty in the gap velocity measurements.



However, these uncertainties are expected to have a minimal effect on the local gap velocity at any specific cross section of the test specimen. Therefore, they are not evaluated in the pre-test prediction. However, once the final dimensions and measurement uncertainties throughout the test specimen are quantified in the test equipment error and accuracy report (TEEAR), evaluations can be performed to confirm the effect on the gap velocity uncertainty is small.

- Modes shapes will be measured and will have an uncertainty associated with their value based on interpolation of the mode shape between accelerometer locations. However, since the modes of interest are bending modes that produce a modal multiplier of 1, it is not necessary to factor mode shape measurement uncertainty into the total measurement uncertainty at this time.
- The linear mass is based on the mass of the tube, instrumentation and cables inside the instrumented tubes, and the hydrodynamic (added) mass. Uncertainties in the linear mass of the test specimen include uncertainties in the tube OD, the weight of the sensors and cables, the test fluid density, and the mass of the tube wall. The uncertainty is the sample variance between the linear mass value and the mean.
- The nominal value for damping in the test is  $\{\{ \quad \} \}^{2(a),(c)}$  based on  $\{\{ \quad \} \}^{2(a),(c)}$  nominal value minus  $\{\{ \quad \} \}^{2(a),(c)}$  bias due to the potential for movement of cables within the tubes. Measurement uncertainty is assumed to be  $\{\{ \quad \} \}^{2(a),(c)}$  of the measured damping value.
- The nominal value for the test fluid density is the mean of the density range based on the test temperature allowable range. The measurement uncertainty is based on an assumed  $\{\{ \quad \} \}^{2(a),(c)}$  of the mean value.
- The nominal value for the SG tube outer diameter is the same as the design value. The measurement uncertainty considers an uncertainty in the tube OD measurements of  $\{\{ \quad \} \}^{2(a),(c)}$ . The uncertainty is the standard deviation of the measurement values.
- No measurement uncertainties are applied to the Connors' constants.
- Evaluating column 13, the limiting frequency based on the highest reduced velocity value is for the pivot boundary conditions and a frequency of  $\{\{ \quad \} \}^{2(a),(c)}$  Hz. A  $\{\{ \quad \} \}^{2(a),(c)}$  uncertainty in the frequency measurement is evaluated.

Table 5-36 FEI Measurement Uncertainties

Parameter	Variable	Measurement Uncertainty	Test Value
Velocity	X <sub>1</sub>	{{	
Modal multiplier	X <sub>2</sub>		
Linear mass	X <sub>3</sub>		
Damping	X <sub>4</sub>		
Fluid density	X <sub>5</sub>		
SG tube OD	X <sub>6</sub>		
Frequency	X <sub>9</sub>		}} <sup>2(a),(c)</sup>

The effect of each of these uncertainty parameters on the safety margin and the flow rate for the onset of FEI is determined using the sensitivity coefficient method, which is described in Section 4.5.3.

### 5.1.3.1.3 Numerical Uncertainties

In the FEI analysis, the primary flow rates are not subject to numerical uncertainty. Although they are calculated with thermal hydraulic software, they can be validated with hand calculations. Therefore, numerical uncertainties are limited to the modal analysis.

The modal analysis results for the test specimen are documented in Section 5.1.2.

### 5.1.3.1.4 Best-Estimate Design Analysis and Pre-Test Prediction

FEI calculations are performed for the design using the nominal input conditions shown in Table 5-35, and a calculation is also performed for the test conditions shown in Table 5-40. The safety margin range is calculated and then it is converted to the main parameter that will be monitored during the testing. This provides the expected flow velocity for an FEI condition to occur corresponding to each calculated safety margin value.

$$v_{measure} = v_{assume} (1 + SM) \quad \text{Equation 5-1}$$

where:

- $v_{measure}$  = Velocity to be measured, corresponding to a safety margin (in/s)
- $v_{assume}$  = Velocity assumed in safety margin calculation (in/s)
- $SM$  = Safety margin (design analysis, best estimate, testing, upper or lower validation range) (%)

The velocities are converted to volumetric flow rates based on the characteristics of the TF-3 test facility. The validation range represents the upper and lower bound of the flow velocity (and flow rate) where FEI is expected to occur, considering the best-estimate results, the bias due to the test design, and the measurement and input uncertainties. The range is calculated by subtracting the distortion from the best-estimate results, which is equal to the safety margin value of the test. This accounts for bias in the test on the expected and validation range. To calculate the upper range for validation, the sum of the input and measurement uncertainties are added to the test value, and to calculate the lower value, the sum of the input and measurement uncertainties are subtracted from the test value. Note that the design analysis safety margin is not considered in the upper validation range value because the calculated range is judged to be sufficiently large.

### 5.1.3.1.5 Testing Distortions

If the test conditions exactly matched the nominal operating conditions, the test design would have no distortions and the expected experimental result would equal the nominal result for the onset of FEI. However, the TF-3 facility contains some distortions (also referred to as experimental biases) based on the test design. These biases are evaluated in the pre-test analysis to inform the expected test result since it will not exactly match the predicted results at nominal operating conditions.

Table 5-37 provides a summary of the testing conditions that are different from the design analysis that are relevant to the FEI flow testing. The difference between the best-estimate safety margin and the safety margin of the test condition is defined as the bias introduced by the test. The bias value is then used along with the input and measurement uncertainties to calculate the range of results that may be used to adequately validate the design analysis.

Table 5-37 Test Distortions for FEI

Parameter	FEI Variables	Limiting Design Analysis Condition	Test Condition
Frequency	X <sub>9</sub>	Column 21 for FEI	Column 13
Tube linear mass	X <sub>3</sub>	FEI: representative of a portion of the tube near the steam plenum region	Empty tube, plus mass of sensors and cables, and increased added (hydrodynamic) mass due to higher primary coolant density
Damping	X <sub>4</sub>	{{ }} <sup>2(a),(c)</sup>	Preliminary assessments show greater damping. There is also the possibility that the instrument cables add a small amount of damping to the system.
Primary coolant density	X <sub>5</sub>	FEI: Temperature of hot leg, near steam plenum region	Room temperature

### 5.1.3.2 TF-3 Pre-Test Prediction Results for FEI

Table 5-38 summarizes the values of input and measurement uncertainty and the “u<sub>θ</sub>” terms identify their magnitude for FEI. The results show that the velocity and Connors’

constant "C" terms have the largest input uncertainty, and the frequency and damping have the highest measurement uncertainty. Per the validation methodology, the "uθ" terms are combined via square root sum of squares to produce the total input and measurement uncertainty.

Table 5-38 FEI Input and Measurement Uncertainties

Parameter	Input Uncertainty	Measurement Uncertainty	$U_{xi}\theta_i$ Input	$U_{xi}\theta_i$ Measurement
Velocity	{{			
Modal multiplier				
Linear mass				
Damping				
Fluid density				
SG tube OD				
Connors' Constant 'C'				
Connors' Constant 'a'				
Frequency				
Total				$\}}^{2(a),(c)}$

The best-estimate safety margin for the onset of FEI is  $\}}^{2(a),(c)}$  at normal operating conditions, and it is about  $\}}^{2(a),(c)}$  using conservative design analysis inputs. The predicted safety margin for the test is  $\}}^{2(a),(c)}$ , which implies that the bias introduced by the test distortions is about  $\}}^{2(a),(c)}$ . Physically, this means that the combined effect of test distortions make the expected critical velocity for FEI slightly lower for the test specimen compared to the best-estimate (positive bias). A summary of the testing biases is provided in Table 5-39. The percentage differences in bias are provided for comparison to each other only; they are not directly comparable to the input and measurement uncertainties in Table 5-38 nor the effect on the safety margin.

Table 5-39 FEI Testing Biases

Parameter	Best-Estimate Value	Testing Value	Bias Percentage
Frequency	{{		
Linear Mass			
Damping			
Density			$\}}^{2(a),(c)}$

Accounting for the positive safety margin, as well as the input and measurement uncertainties and the experimental bias, the lower value of velocity for the validation range is significantly greater than the nominal velocity at normal operating conditions ( $\}}^{2(a),(c)}$ ). The predicted safety margin for the test represents the expected onset of FEI based on the design analysis method and corresponds to a flow velocity of  $\}}^{2(a),(c)}$ . Based on the input and measurement uncertainty values in Table 5-38, the validation range is calculated as  $\}}^{2(a),(c)}$ , which corresponds to gap velocities of  $\}}^{2(a),(c)}$ .

Additionally, the expected onset flow rate for FEI in the test facility is less than the capacity of the test facility, which is  $\{\{ \}^{2(a),(c)}$  gpm. This means that the test facility is expected to be adequate to confirm the lack of FEI at the design operating conditions, considering all relevant input and measurement uncertainties, and biases. This conclusion will be confirmed in the post-test analysis, based on the testing results, including the final measurement uncertainties in the TEEAR.

Because the test is performed in a test facility, the flow rate will be increased above the equivalent 100% power normal operating flow rate of  $\{\{ \}^{2(a),(c)}$  up to  $\{\{ \}^{2(a),(c)}$  to detect for vibration frequencies and amplitudes of FEI. Table 5-40 summarizes the calculated safety margins and the corresponding flow velocity and flow rate value and ranges for the onset of FEI conditions.

Table 5-40 Expected and Validation Range of Results for FEI

Parameter	Safety Margin	Validation Safety Margin Range for Test	Expected Velocity / Flow Rate	Validation Velocity / Flow Rate Range for Test
Design Analysis	$\{\{ \}$			
Best-Estimate				
Test Conditions				$\}\}^{2(a),(c)}$

### 5.1.3.3 Conclusions for TF-3 Pre-Test Prediction for FEI

Figure 5-31 demonstrates that the validation ranges for FEI are significantly above the full power normal operating flow rate, and below the flow capacity of the TF-3 test facility. Therefore, the test design is expected to adequately validate the design analysis conclusion that FEI does not occur at the limiting full power conditions for the NuScale SG design. The validation ranges shown in Figure 5-31 are based on the design analysis methodology and the sensitivity coefficient assessment of input, measurement and numerical uncertainties, and testing biases.

If the flow rate associated with the onset of FEI phenomena falls within the expected validation range, minimal post-test analysis is required to demonstrate that the test results adequately validate the design analysis predictions, since relevant input uncertainties, measurement uncertainties and experimental biases have been used to determine these validation ranges. Test results below the validation range may still be acceptable for validation, but will require additional assessment in the post-test analysis to verify their acceptability. For example, the final measurement accuracies provided in the TEEAR may need to be considered, or updated predictions of nominal frequencies and damping based on the experimental results may need to be used. Test results above the validation range indicate that FEI is not a concern for the NuScale SG design, and if desired, the design analysis methodologies can be improved to provide more accurate safety margins.

Figure 5-31 provides an overview of the calculated expected flow rates for the onset of the phenomena using the design analysis methods, and the validation ranges that

consider all input, measurement and numerical uncertainties, as well as the bias introduced by test facility distortions on the range of flow rates that are adequate to validate the design analysis and demonstrate that FEI and VS phenomena are beyond design basis phenomena for the NuScale steam generators.

Figure 5-32 plots the lower, expected and upper range for FEI onset described in Table 5-56 based on the expected test conditions. The maximum flow rate of the test facility is also plotted at a mass damping corresponding to the expected damping value  $\{\{\}^{2(a),(c)}$  and at a low damping value  $\{\{\}^{2(a),(c)}$  to demonstrate the mass damping range over which the critical velocity measurements may occur.

$\{\{\}$

$\}\}\}^{2(a),(c)}$

Figure 5-31 Flow Rates and Validation Ranges for TF-3

{

}}<sup>2(a),(c)</sup>

Figure 5-32 FEI Stability Map with TF-3 Test Conditions

If FEI occurs during the testing, the post-test analysis will characterize the vibration amplitudes that are observed and onset of the condition.

#### 5.1.4 TF-3 VS Pre-Test Prediction

The purpose of this section is to document the pre-test prediction for the vortex shedding (VS) flow test in the TF-3 test facility. This section contains an assessment of the best estimate VS results, assessment of the TF-3 experimental biases, and analysis of input, measurement and numerical uncertainties that affect the validation of the design analysis using the TF-3 validation test results.

This calculation estimates the uncertainty in the design analysis safety margin for VS and provides the expected and allowable range for measurements in the test to validate the design analysis, considering input, measurement and numerical uncertainties, as well as experimental biases due to test facility distortions.

### 5.1.4.1 Methodology

Subsection N-1324.1 of Reference 9.1.14 provides three acceptance criteria that can be used to demonstrate that a VS lock-in condition does not occur for the SG design. Subsection N-1324.1 is written such that if at least one criterion is met, VS lock-in is precluded. The acceptance criteria are based on the reduced velocity and reduced damping of the system. The reduced velocity is calculated using gap velocity and fundamental frequency, which both are parameters that will be validated during the testing. The reduced damping contains the in-air system damping term, but also contains the integral of the mode shape over the entire tube length divided by the integral of the mode shape of the tube length subject to lock-in cross flow. The planned testing is not expected to have sufficient sensors to accurately validate the ratio of these two mode shape integrals, nor will it validate the length subject to VS lock-in cross flow. The sensitivity coefficient method could be used to determine a validation range for the damping value, but because the mode shapes and integration length for cross flow have a greater effect on the reduced damping term and are not expected to be validated with the experimental design, predicting a range of damping values that validate the design analysis is not very informative. Instead, the sensitivity coefficient method is used for Method A, which is described in Section 4.5.2.

#### 5.1.4.1.1 Input Uncertainties

The design analysis values listed in Table 5-41. Best-estimate or nominal values are provided for all parameters that are biased in the design analysis. Removing conservatism results in a higher predicted velocity for the onset of VS, which is important for validating that the test is designed to actually observe the phenomena under the expected onset conditions. A summary of the nominal values are provided in the following bullet points:

- The mean gap velocity is calculated considering the range of primary coolant flow rates in the FW region of the tube bundle, where VS is applicable, and the pitch representing the diagonal distance between tubes. Uncertainty in the gap velocity is evaluated considering minimum to maximum design primary coolant flowrates, and steady-state versus transient flow conditions. The uncertainty is based on the sample variance of the distribution of velocity values.
- In the design analysis, the limiting reduced velocity is for the frequency of  $\omega_{2(a),(c)}$  associated with column 1, tube B with fixed boundary conditions. The nominal value considers a reduction in the frequency due to mesh sensitivity as well as added mass coefficient. The input uncertainty is based on the sample variance between the design analysis and nominal values.
- The design analysis and nominal value for the SG tube outer diameter are the same. The input uncertainty considers a  $\pm \Delta D$  manufacturing tolerance.
- Lastly, although the Strouhal number is assessed herein since the conservatism provided by the Reference 9.1.14 design analysis rule (a) results in under-prediction of the velocity needed to generate a lock-in condition during the testing. The expected Strouhal number for the tube bundle is  $St_{2(a),(c)}$ . Using a nominal Strouhal number provides an increase in velocity associated with the lock-in condition. The



nominal value is set as the mean of the staggered and design Strouhal number values. The uncertainty is the standard deviation of distribution.

Table 5-41 VS Design Analysis and Nominal Values – Method A

Parameter	Variable	Design Analysis Value	Nominal Value
Velocity	X <sub>8</sub>	{{	
Frequency	X <sub>9</sub>		
Tube outer diameter	X <sub>10</sub>		
Strouhal Number	X <sub>11</sub>		}} <sup>2(a),(c)</sup>

#### 5.1.4.1.2 Measurement Uncertainties

Measurement uncertainties are assessed for input terms that will be directly or indirectly measured in the testing. These include velocity, frequency and tube outer diameter.

Measurement uncertainties are largely based on engineering judgment at the time of the pre-test prediction, and will be validated in the post-test assessment. The measurement uncertainty values for VS are the same as for FEI (Section 5.1.3.1.2). The nominal value for frequency in the test is determined from the average of the first bending mode frequencies for columns 9, 11 and 13 in the test specimen. These are the first mode for the fixed boundary conditions, and have a mode shape in the FW transition span that is susceptible to VS lock-in. The ‘wet’ case is used, to correspond to the conditions associated with flow testing.

Table 5-42 VS Measurement Uncertainties

Parameter	Variable	Measurement Uncertainty	Test Value
Velocity	X <sub>8</sub>	0.5% velocity uncertainty	Same as nominal
SG tube OD	X <sub>10</sub>	±0.05 inch uncertainty	0.625 in
Frequency	X <sub>9</sub>	5% of frequency	33.1 Hz

#### 5.1.4.1.3 Numerical Uncertainties

Consistent with the FEI assessment, the primary flow rates used for VS are not subject to numerical uncertainty. Although they are calculated with thermal hydraulic software, they can be validated with hand calculations. Therefore, numerical uncertainties are limited to the modal analysis. The modal analysis results for the test specimen documents a frequency shift of less than 2% for the modes of interest for FEI. The 2% frequency shift is applied to the design analysis input value to account for an increased distribution of ranges associated with the input frequency.

#### 5.1.4.1.4 Best-Estimate Design Analysis and Pre-Test Prediction

Safety margins for VS are calculated using the nominal parameters in Table 5-41 and the test conditions for column 9.

The safety margin range is calculated and then it is converted to the main parameter that will be monitored during the testing. This provides the expected flow velocity for an VS condition to occur corresponding to each calculated safety margin value.

$$v_{measure} = v_{assume} (1 + SM) \quad \text{Equation 5-2}$$

where:

$v_{measure}$	=	Velocity to be measured, corresponding to a safety margin (in/s)
$v_{assume}$	=	Velocity assumed in safety margin calculation (in/s)
$SM$	=	Safety margin (design analysis, best estimate, testing, upper or lower validation range) (%)

The velocities are converted to volumetric flow rates based on the characteristics of the TF-3 test facility. The validation range represents the upper and lower bound of the flow velocity (and flow rate) where VS is expected to occur, considering the best-estimate results, the bias due to the test design, and the measurement and input uncertainties. The range is calculated by subtracting the distortion from the best-estimate results, which is equal to the safety margin value of the test. This accounts for bias in the test on the expected and validation range. To calculate the upper range for validation, the sum of the input and measurement uncertainties are added to the test value, and to calculate the lower value, the sum of the input and measurement uncertainties are subtracted from the test value. Note that the design analysis safety margin is not considered in the upper validation range value because the calculated range is judged to be sufficiently large.

#### 5.1.4.1.5 TF-3 Testing Experimental Bias Assessment

If the test conditions exactly matched the nominal operating conditions, the test design would have no distortions and the expected experimental result would equal the nominal result for the onset of VS. However, the TF-3 facility contains some distortions (also referred to as experimental biases) based on the test design. These biases are evaluated in the pre-test analysis to inform the expected test result since it will not exactly match the predicted results at nominal operating conditions.

Table 5-43 provides a summary of the testing conditions that are different from the design analysis that are relevant to the VS flow testing. The difference between the best-estimate safety margin and the safety margin of the test condition is defined as the bias introduced by the test. The bias value is then used along with the input and measurement uncertainties to calculate the range of results that may be used to adequately validate the design analysis.

Table 5-43 Test Distortions for VS

Parameter	VS Variables	Limiting Design Analysis Condition	Test Condition
Frequency	X <sub>9</sub>	Column 1 for VS	Column 9-13

5.1.4.2 TF-3 Pre-Test Prediction Results for VS

Table 5-44 summarizes the values of input and measurement uncertainty and the “uθ” terms identify their magnitude for VS. The results show that the Strouhal number has the largest input uncertainty, and the frequency has the highest measurement uncertainty. Per the analysis methodology, the “uθ” terms are combined via square root sum of squares to produce the total input and measurement uncertainty.

Table 5-44 VS Input and Measurement Uncertainties

Parameter	Input Uncertainty	Measurement Uncertainty	U <sub>xi</sub> θ <sub>i</sub> Input	U <sub>xi</sub> θ <sub>i</sub> Measurement
Velocity	{{			
Frequency				
SG tube OD				
Strouhal Number				
Total				}} <sup>2(a),(c)</sup>

Table 5-45 VS Testing Biases

Parameter	Best-Estimate Value	Testing Value	Bias Percentage
Frequency	{{		}} <sup>2(a),(c)</sup>

When nominal values are used the predicted safety margin under normal operating conditions is {{ }}<sup>2(a),(c)</sup>. For the conditions of the TF-3 test, the safety margin is {{ }}<sup>2(a),(c)</sup>. This implies that the bias introduced by the test distortion of testing the middle columns versus the inner columns is approximately {{ }}<sup>2(a),(c)</sup>. Physically, this means that the velocity to achieve VS lock-in conditions in the test design is higher than during normal operating conditions (negative bias). Table 5-46 summarizes the safety margins, velocities, and flow rates for the expected onset of VS in the test and the validation range considering experimental biases and input and measurement uncertainties. The range is also shown in Figure 5-31.

Table 5-46 Expected and Validation Range of Results for VS

Parameter	Safety Margin	Validation Safety Margin Range for Test	Expected Velocity / Flow Rate	Validation Velocity / Flow Rate Range for Test
Design Analysis using method A <sup>Note 1</sup>	{{			
Best-Estimate				
Test Conditions				}} <sup>2(a),(c)</sup>

Note 1: the design analysis safety margin for the SG tubes is based on acceptance criteria A and C, so this value (calculated using method A) differs from the design analysis results.

### 5.1.4.3 Conclusions for TF-3 Pre-Test Prediction for VS

During the flow testing, low levels of vibration are expected due to turbulence. The vibration amplitude typically increases at a rate proportional to the velocity raised to the power of 1.5, which is the nominal increase for tubes in cross flow due to turbulence. Increases greater than this rate may be due to strongly-coupled flow-induced vibration phenomena such as VS. If VS occurs, vibration amplitude will increase as the resonant condition is approached, and will decrease as flow velocity is increased further. These characteristics in the vibration versus flow rate will be monitored during the testing to identify a VS condition, and during post-processing the exact flow rate corresponding to the onset point can be more accurately determined.

### 5.1.5 TF-3 TB Pre-Test Prediction

This section defines the range of acceptable mean square response measurements that will validate the analytical method used in the design analysis of the NuScale SG accounting for input, numerical, and measurement uncertainties. The range of acceptable mean square responses is then converted into a range of safety margins for impact fatigue.

#### 5.1.5.1 Methodology

##### 5.1.5.1.1 Input Uncertainties

The four variables and the basis for each uncertainty are described below.

#### Effective Mass

The effective mass is typically defined as two thirds the mass of the spans on either side of the support where impact fatigue is being evaluated. The linear mass is a sum of the mass of the metal, the added mass for the primary fluid, and the added mass of the feedwater. As the location of the highest vibration amplitude is not known and could be in the liquid, vapor, or two phase regions of the tube, the effective mass uncertainty is based on the difference between the tube mass with feedwater added mass and with vapor added mass. The vapor added mass is approximated as zero as it is much smaller than

the feedwater added mass. The feedwater density is  $\{\{ \} \}^{2(a),(c)}$  slinch/in<sup>3</sup>. Using a uniform distribution between zero and the feedwater density, the input uncertainty in effective mass is  $\{\{ \} \}^{2(a),(c)}$  slinch.

### **Crossing Frequency**

Calculation of the impact stress typically uses the natural frequency when calculating the impact stress because it is a parameter that is generally known or can be calculated without significant effort. A frequency is needed along with the displacement response to quantify how fast the tube is moving upon impact with the support. Rather than the natural frequency, this calculation uses the crossing frequency as it is more representative of the actual frequency of vibration and impact. In many cases, the two frequencies are similar as the first mode tends to have the highest response. However, since the crossing frequency is available, it is used to be more accurate.

The input uncertainty in the crossing frequency is calculated using Latin Hypercube Sampling (LHS). The crossing frequency input uncertainty includes uncertainties in the damping, modal frequencies, and input pressure power spectral densities (PSDs).

### **Maximum Mean Square Response**

The input uncertainty in the maximum mean square response is calculated using LHS. The maximum mean square response input uncertainty includes uncertainties in the damping, modal frequencies, and input pressure PSDs.

### **Tube Outer Diameter**

The input uncertainty in the tube outer diameter is based on a manufacturing tolerance of  $\pm 0.005$  inches. Using a uniform distribution over the allowed range of diameters produces an input uncertainty of  $\{\{ \} \}^{2(a),(c)}$  inches. The standard deviation of a uniform distribution is the range of values divided by the square root of twelve.

## **5.1.5.1.2 Measurement Uncertainties**

The four variables and the basis for each uncertainty are described below.

### **Effective Mass**

The effective mass is a function of the tube linear density and the effective span of the tube. The effective span is defined as two thirds of the span on either side of the support of interest. In the test facility, the spans on either side of a support are one quarter of the helix circumference. The helix circumference is calculated from the helical radius. No uncertainty is attributed to the measurement of the span as it can be measured with enough precision to not significantly contribute to the overall uncertainty in the effective mass. The value of  $\{\{ \} \}^{2(a),(c)}$  lbm/in is multiplied by the effective span to produce the uncertainty in the effective mass.

### **Crossing Frequency**

The measurement uncertainty in the crossing frequency is  $\{\{ \quad \}^{2(a),(c)}$  percent. The best estimate test crossing frequency is used as the reference value for calculating  $\{\{ \quad \}^{2(a),(c)}$  percent.

### **Maximum Mean Square Response**

The total measurement uncertainty in the RMS response is assumed to be  $\{\{ \quad \}^{2(a),(c)}$  percent. The best estimate test RMS response is used as the reference value for calculating  $\{\{ \quad \}^{2(a),(c)}$  percent.

### **Tube Outer Diameter**

The measurement uncertainty in the tube outer diameter is based on a  $\{\{ \quad \}^{2(a),(c)}$  in range. Using a uniform distribution over the range of measured diameters produces a measurement uncertainty of  $\{\{ \quad \}^{2(a),(c)}$  inches.

#### **5.1.5.1.3 Numerical Uncertainties**

The numerical uncertainty in the ANSYS model of the SG is accounted for in the input uncertainty of the mean square response and the crossing frequency. An additional numerical uncertainty is included for the approximate solution of the acceptance integrals discussed. Sensitivity studies show that the results change less than a percent when the significance threshold was reduced by an order of magnitude. Therefore a percent of the design analysis RMS response is used as the numerical uncertainty associated with truncated summations in the acceptance integral solution.

#### **5.1.5.1.4 Nominal Design Analysis**

It is important that uncertainties be calculated using nominal conditions, if possible. The design analysis uses the primary side maximum design flow condition to provide bounding results. The design analysis is re-run using the primary side best estimate flow condition. Tube B of column 21 has the largest RMS vibration and is therefore selected to be re-run.

The mode shape information is used from the design analysis for column 21. To generate the nominal fluid conditions required for the TB analysis, the best estimate NRELAP5 input file for 100 percent power is used.

The TB response is calculated using the same methodology as in Section 3.2.2. The same primary side single phase, secondary side single phase, and secondary side two phase pressure PSDs are applied using the fluid conditions described above. The mode combination significance threshold and the mesh size for evaluating the acceptance integrals are used from Section 3.2.2.

#### **5.1.5.1.5 Best Estimate Pre-Test Prediction**

The best estimate pre-test prediction of the TB response in the TF-3 test facility is calculated for the two column 11 tubes included in a single tube model. Of the

instrumented columns in TF-3, column 11 is selected for evaluation as it represents the average geometry of the five columns. Confirmation that column 11 is an appropriately representative column for the test facility can be confirmed in the post-test analysis.

The TF-3 test facility is different from the NuScale SG in that it is unheated, has flow only on the primary side, and only contains the five middle columns. A comparison between the design analysis at nominal conditions and this best estimate pre-test prediction allows the test facility distortion to be quantified.

#### **5.1.5.1.5.1 TF-3 Fluid Conditions**

The fluid conditions used for the test should be scaled as much as possible to provide a direct comparison to the nominal design analysis. The test facility fluid temperature is set based on the ambient conditions. The fluid velocity is the only test facility parameter that can be used for scaling. The goal is to have the same primary side PSD in the design analysis and the test. The primary side velocity is selected to create the same scaling factor on the nondimensional PSD. For the same nondimensional frequency, the two cases use the same pressure PSD. There is a shift in frequency between the two PSDs, but this is unavoidable and contributes to the distortion in the test facility.

#### **5.1.5.1.5.2 TF-3 Modal Analysis**

Two boundary conditions are available in the ANSYS model, given the names fixed and pivot. The fixed boundary condition is consistent with the design analysis, all degrees of freedom at a support are fixed except for rotation along the tube axis. The pivot boundary condition does not fix any moments and only fixes two of the translational degrees of freedom. Sliding translation along the tube axis is allowed at the support. While the fixed boundary condition is appropriate for the NuScale SG due to thermal expansion forces, the TF-3 facility may not create the same type of contact. The pivot boundary condition is evaluated in this calculation to provide a range of results. Post-test analysis of the modal testing can be used to determine what type of boundary condition is most appropriate.

#### **5.1.5.1.6 Mean Square Response and Crossing Frequency Input Uncertainties**

The acceptance integral methodology does not lend itself to the analytical derivatives typically used in sensitivity analysis. Instead a Monte Carlo type method is used to assess the total uncertainty in the mean square response and crossing frequencies. The LHS method is used to determine the random instances of the properties of interest. The properties that are varied are described in the section below along with justification for their ranges.

With LHS, the range of possible values for each variable is divided in  $n$  equal probability bins where  $n$  is the number of samples. For each sample case, a value for each variable is selected from a unique bin. The selected value is assigned a random value within the bin. The uncertainties in RMS response and crossing frequency are equal to the sample standard deviation.

As LHS is a Monte Carlo type method, the number of samples used has an important effect on how well the sample statistics match the true statistics. To investigate the

sensitivity of the results to the number of samples used, three different sample sizes are used, 50, 100, and 150.

#### 5.1.5.1.6.1 Damping

The design analysis uses a damping value of  $\{\{ \quad \}^{2(a),(c)}$  percent. There is some uncertainty in what damping value is most appropriate. While  $\{\{ \quad \}^{2(a),(c)}$  percent is considered a reasonable estimate, higher damping values could exist. A uniform probability distribution is assumed between  $\{\{ \quad \}^{2(a),(c)}$  percent and  $\{\{ \quad \}^{2(a),(c)}$  percent.

#### 5.1.5.1.6.2 Pressure PSD

To assess the uncertainty in the PSD, the magnitude of the PSD is scaled by a factor distributed uniformly between  $\{\{ \quad \}^{2(a),(c)}$ . This range of uncertainties includes and bounds potential uncertainties in the velocity and density.

#### 5.1.5.1.6.3 Modal Frequency

The SG structural model includes a mesh refinement study that showed that the modal frequencies varied with mesh refinement by less than  $\{\{ \quad \}^{2(a),(c)}$  percent for modes below 200 Hz. Therefore, the modal frequencies are multiplied by a factor distributed uniformly between  $\{\{ \quad \}^{2(a),(c)}$ .

#### 5.1.5.1.7 TF-3 Test Distortion

The biases in the TF-3 test facility can be evaluated by comparing the nominal design results to the best estimate test results. This comparison includes the following distortions:

- Column 21 is the most limiting in the design analysis and column 11 is evaluated in the test best estimate case
- Differences in tube materials
- Differences in primary temperature and pressures
- No secondary side flow in TF-3
- Differences in tube to tube support boundary condition due to non-prototypic temperature and pressure

The effect of instrumentation and cabling is addressed in the effective mass uncertainty. The difference in support boundary condition is assessed by comparing the nominal design analysis results to results for two different boundary conditions. This produces two estimates of distortion based on the two boundary conditions, fixed and pivot.

For each boundary condition, two tubes from column 11 are evaluated. These tubes are the two end tubes from the tube sheet. For each tube, the largest response from the helical portion of the tube is used. The helical portion is used to coincide with the region of



maximum response in the design analysis. Of the two tubes, the smaller maximum response is used to maximize the difference.

#### 5.1.5.1.8 TF-3 Test Distortion and Fatigue Calculations

The distortion in the TF-3 test facility is evaluated by comparing the maximum mean square responses of the nominal design analysis to the best estimate pre-test predictions. The maximum response in the design analysis is in the helical portion of the tube, so the comparison excludes the response in the transition bends of the pre-test predictions.

The upper limit for the mean square response that validates the design analysis method is determined by adding the distortion plus uncertainty to the nominal design analysis result. Negative distortions indicate that the test distortions are nonconservative and vice versa.

The upper validation limits are then used to calculate equivalent alternating impact stresses in the design analysis by subtracting the test distortion and plugging the resulting mean square response into the impact stress equation. The uncertainty in the impact stress is added to the calculated result. This produces the upper limit alternating stress that would occur if the mean square response is measured at the upper limit. The alternating stresses are then used to calculate a fatigue usage over the life of the SG. Checking the fatigue is important to ensure that the uncertainties do not create a situation where test results are higher than the best estimate, low enough to validate the design analysis, and indicate that a more accurately calculated design analysis fatigue would produce unacceptable fatigue.

#### 5.1.5.2 TF-3 Pre-Test Prediction Results

##### 5.1.5.2.1 Nominal Design Analysis

The nominal design analysis RMS displacement response is shown in Figure 5-33. The maximum response is  $\{\{ \quad \}^{2(a),(c)}$  inches. The response spectra for the location with the maximum response is shown in Figure 5-34.

{{

}}<sup>2(a),(c)</sup>

Figure 5-33 Nominal design analysis column 21 tube B RMS displacement (in)

---

{{

}}<sup>2(a),(c)</sup>

Figure 5-34 Nominal design analysis column 21 tube B displacement response (in) at maximum location

#### 5.1.5.2.2 Best Estimate Pre-Test Predictions

The best estimate test analysis RMS displacement responses for the column 11 are shown in Figure 5-35 through Figure 5-38. The maximum responses in the helical region are shown in Figure 5-37. These responses show that the fixed boundary condition has test distortion in the nonconservative direction and the pivot boundary condition has distortion in the conservative direction. This result also shows that responses in the helical region do not vary drastically between tube A and B. The responses in the transition bends do vary between tubes due to the significantly different transition span lengths from tube A to tube B.

Table 5-47 Best estimate pre-test prediction response

Case	Maximum RMS Response (in) in the Helical Region	Minimum RMS Response (in) per Boundary Condition	Mean Square Response Distortion (in <sup>2</sup> )
Tube A, Fixed	}}		}}2(a),(c)
Tube B, Fixed			
Tube A, Pivot			}}2(a),(c)
Tube B, Pivot			

}}

}}2(a),(c)

Figure 5-35 Best estimate test column 11 tube A, fixed, RMS displacement (in)

{{

}}<sup>2(a),(c)</sup>

Figure 5-36 Best estimate test column 11 tube B, fixed, RMS displacement (in)

{{

}}<sup>2(a),(c)</sup>

Figure 5-37 Best estimate test column 11 tube A, pivot, RMS displacement (in)

{{

}}<sup>2(a),(c)</sup>

Figure 5-38 Best estimate test column 11 tube B, pivot, RMS displacement (in)

### 5.1.5.2.3 Mean Square Response and Crossing Frequency Input Uncertainties

The LHS methodology is executed for sample sizes of 50, 100, and 150. The results are shown in Table 5-48 below. The results are mostly independent of the sample size. The largest differences are in the standard deviation of the RMS response which varies by {{  
}}<sup>2(a),(c)</sup> percent from sample sizes of 100 and 150. This is an acceptably small variation. The uncertainties in RMS response and crossing frequency are used from the 150 sample case as the larger number of samples should provide the most representative statistics.

Table 5-49 summarizes the uncertainties that make up the total uncertainty in the mean square response. The input uncertainty dominates the total uncertainty, mostly due to the large range of PSD excitations used in the LHS method. Table 5-50 uses the nominal design analysis, the test distortion, and the total uncertainty to establish an upper limit on the measured mean square response that would validate the design analysis. Two values are provided to cover the possible tube to tube support boundary conditions in the test facility, fixed or pivot. If fixed boundary conditions are present, the upper limit is much lower as the test has a non-conservative distortion. A lower limit is not defined as the TB methodology has been shown to be conservative when compared to the TF-2 test data. Any measured mean square responses below the upper limit indicate that there is unrealized margin in the methodology which is acceptable for TB.

Table 5-48 LHS results

Sample Size	Mean RMS Response (in)	Standard Deviation of RMS Response (in)	Mean Crossing Frequency (Hz)	Standard Deviation of Crossing Frequency (Hz)
50	{{			
100				
150				}} <sup>2(a),(c)</sup>

Table 5-49 Total uncertainty in the mean square response

Input Uncertainty	
Input	{{
Measurement	
Numerical	
<b>Total</b>	}} <sup>2(a),(c)</sup>

Table 5-50 Upper limit in measured mean square response to validate design analysis

Boundary Condition	Design Analysis Mean Square Response (in <sup>2</sup> )	Test Distortion in Mean Square Response (in <sup>2</sup> )	Total Mean Square Response Uncertainty (in <sup>2</sup> )	Upper Limit for Test Results to Validate Analysis (in <sup>2</sup> )
Pivot	{{			
Fixed				}} <sup>2(a),(c)</sup>

#### 5.1.5.2.4 Total Uncertainty

Based on the methodology in Sections 5.1.5.1.1 and 5.1.5.1.2 the input and measurements uncertainties are calculated. Table 5-51, Table 5-52, and Table 5-53 summarize the uncertainties in the alternating impact stress.

Table 5-51 Summary of input uncertainties

Parameter	Input Uncertainty	U <sub>x</sub> θ <sub>x</sub>
Effective Mass	{{	
Crossing Frequency		
Mean Square Response		
SG Tube Diameter		
		}} <sup>2(a),(c)</sup>



Table 5-52 Summary of pivot boundary condition measurement uncertainties

Parameter	Measurement Uncertainty	$U_x \theta_x$
Effective Mass	{{	
Crossing Frequency		
Mean Square Response		
SG Tube Diameter		
		$\}}^{2(a),(c)}$

Table 5-53 Summary of fixed boundary condition measurement uncertainties

Parameter	Measurement Uncertainty	$U_x \theta_x$
Effective Mass	{{	
Crossing Frequency		
Mean Square Response		
SG Tube Diameter		
		$\}}^{2(a),(c)}$

Using the upper limits on measured mean square response from Table 5-50 and the test distortion values, an equivalent alternating impact stress is calculated for the design analysis column 21. The input and measurement uncertainties in alternating impact stress are added to get the upper limit on alternating impact stress that would validate the design analysis. The corresponding fatigue usage is also calculated to show that uncertainties added to the alternating impact stress do not allow unacceptable fatigue results to be within the range of acceptable test results.

Table 5-54 Fatigue usage due to impact stress

Boundary Condition	Equiv. Design Analysis Impact Stress for Column 21	Input Uncertainty	Meas. Uncertainty	Upper Limit for Test Results to Validate Analysis ( $in^2$ )	Fatigue Usage
Nominal DA	{{				
Pivot					
Fixed					$\}}^{2(a),(c)}$

### 5.1.5.3 TF-3 Pre-Test Prediction Conclusions

As there are two potential boundary conditions at the tube to tube support interfaces, two sets of results are generated, one for the pivot case and one for the fixed case. As there is expected to be boundary condition variability from tube to tube in the test, the post-test

analysis can determine which set of results is most appropriate based on the modal results of the tested tube.

Not including uncertainties, the column 11 maximum RMS responses in the helical region are estimated to be between  $\{\{ \quad \} \}^{2(a),(c)}$  in and  $\{\{ \quad \} \}^{2(a),(c)}$  in for the pivot boundary condition and between  $\{\{ \quad \} \}^{2(a),(c)}$  in and  $\{\{ \quad \} \}^{2(a),(c)}$  in for the fixed boundary condition. The range is based on which tube in the column is selected.

Including uncertainties, test results that show mean square responses less than  $\{\{ \quad \} \}^{2(a),(c)}$  in<sup>2</sup> for the pivot case or less than  $\{\{ \quad \} \}^{2(a),(c)}$  in<sup>2</sup> for the fixed case validate the design analysis methodology. No lower bound is used because lower values are more conservative and the TB analysis is expected to have unrealized conservatism. These upper limit mean square responses in the test correspond to impact fatigue usage in column 21 of the NuScale SG of  $\{\{ \quad \} \}^{2(a),(c)}$  and  $\{\{ \quad \} \}^{2(a),(c)}$  respectively including uncertainties.

## 5.2 CNTS Main Steam Line Branch Connections Validation Testing

Initial startup testing is performed on the first NPM after the first fuel load. Due to the natural circulation design of the NPM, it is not possible to obtain the limiting thermal hydraulic conditions that are necessary to verify the FIV inputs and results until the NPM is operating near full power conditions. Initial startup testing is performed for a sufficient duration to ensure one million vibration cycles for the component with the lowest structural natural frequency. It takes less than 2.5 days of operation to obtain one million cycles of vibration. This is a conservative estimate because the lowest natural frequency of any component evaluated in the CVAP is  $\{\{ \quad \} \}^{2(a),(c)}$  (outer column of the SG, conservatively assuming it is filled with subcooled liquid, which it will not be during full power conditions).

The initial startup test is performed with online vibration monitoring of the DHRS steam piping. In the event that an unacceptable vibration response develops any time during initial startup testing, the test conditions are adjusted to stop the vibration and the reason for the vibration anomaly investigated before continuing with the planned testing. Vibration amplitudes in the DHRS steam lines are measured to confirm the acoustic resonance (AR) analysis results.

### 5.2.1 CNTS Main Steam Line Branch Connections Test Design

The DHRS steam piping, MS drain valve branch, and MSIV upstream and downstream bypass lines were determined to be components susceptible to acoustic excitation with margins of less than 100 percent to the critical Strouhal number. These locations are branch lines where there is normally no flow during operation. As a group the DHRS steam piping tees, the MS drain valve branch, and the MSIV upstream and downstream bypass lines are referred to as the CNTS main steam line branch connections. This report develops an approach and testing requirements to perform in-situ measurements in the piping outside the containment vessel head.

Flow-excited ARs, where instabilities in the fluid flow excite acoustic modes within valves, stand pipes, or branch lines can play a significant role in producing mid- to high-frequency

pressure amplification and vibration. Flow separation and generation of unstable shear layers at closed branch lines can sometimes lead to AR. To determine if there is a concern for AR in the NuScale design, the piping locations where this source of flow excitation is possible were identified and the Strouhal number was calculated for each location. To determine the margin to AR, the calculated Strouhal number was compared to the critical Strouhal numbers based on geometry and flow parameters that could lead to the onset of AR. This analysis was applied to the CNTS main steam line branch connections, as described below, for full-power normal operating conditions when the secondary flow rate and steam velocity in the pipe is maximum. Full-power normal operating conditions produce the Strouhal numbers closest to the critical Strouhal number. At lower reactor power levels, velocities are reduced. This results in Strouhal numbers that are higher and therefore further from the critical limit.

Figure 5-39 shows the containment system (CNTS) MS line 2 from the CNV to the disconnect flange downstream of the main steam isolation valve (MSIV) and a portion of the DHRS steam lines up to the first bend after the DHRS actuation valves. The CNTS main steam line 1 is not shown. It has a very similar layout, but with different circumferential orientations of the tees around the steam piping. Each of the side branches and MS lines need instrumentation to measure flow parameters and pipe vibration during the initial start-up testing.

Acoustic resonance is considered a strongly coupled FIV mechanism that results in large vibration amplitudes. The design analysis approach is to preclude the onset of this mechanism.

The main objective of the test is to verify that AR is not active or causing detrimental vibration in the CNTS main steam lines, decay heat removal steam lines, bypass lines, and connected valves during tests that represent the full range of operating conditions. This includes testing for the detection of any acoustic excitation by a higher order shear layer mode during partial power operation. Another objective of the test is to validate the calculated AR safety margin. The test quantifies the measurement uncertainties of analysis input parameters such as the speed of sound in the fluid and the steam velocity in the CNTS main steam piping. The as-built component measurements are used to validate uncertainties on other analysis inputs, such as the DHRS side branch entrance diameter and side branch length.

Unlike monitoring mechanical vibration of a particular component, ARs are also detectable by monitoring the magnitude and frequencies of dynamic pressure pulsations in the fluid, which help identify the presence and excitation of a standing wave in a flow occluded region. Such measurements serve as additional evidence beyond the vibration data that are collected on the exterior of the pressure boundary.

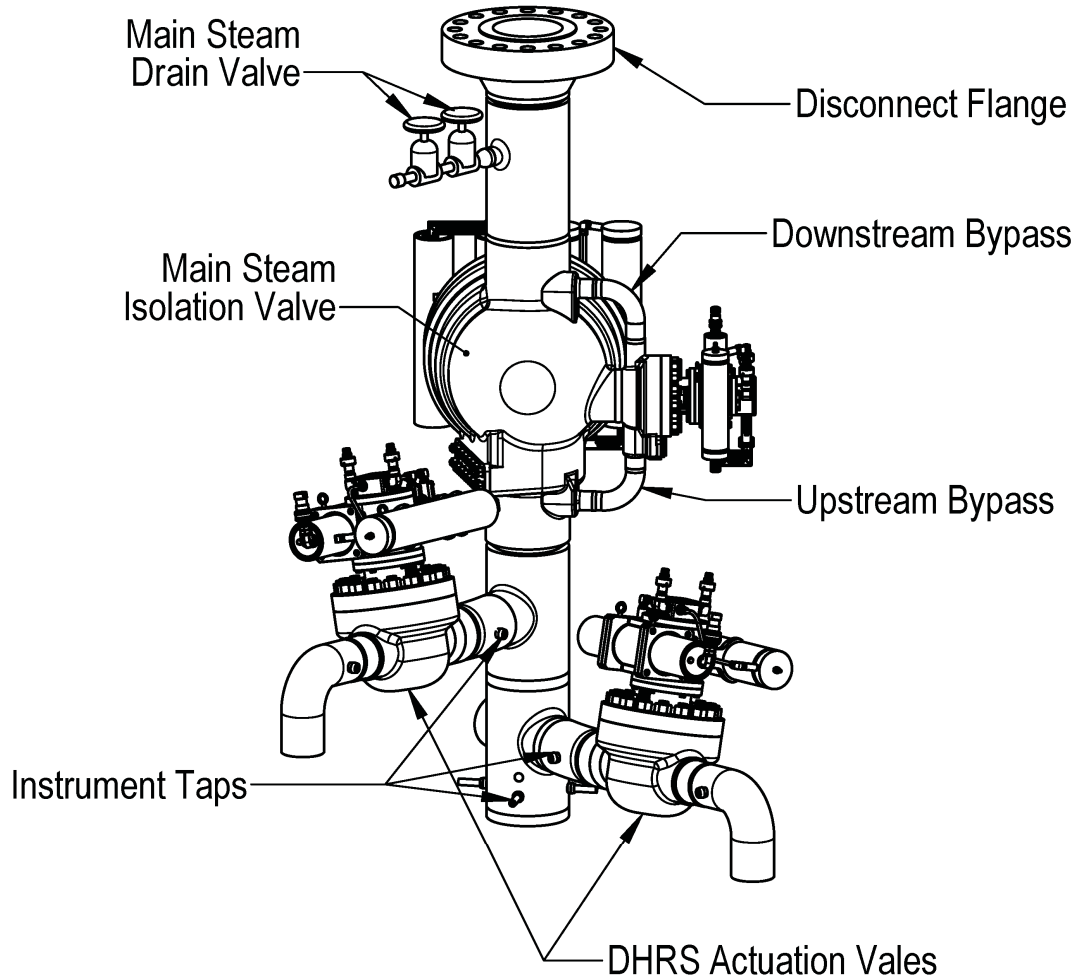


Figure 5-39 Containment system steam line 2 and CNTS main steam line branch connections

### 5.2.1.1 Vibration Testing Guidelines

The ASME Standard for Operation and Maintenance (OM) of Nuclear Power Plants (Reference 9.1.1) Part 3: “Vibration Testing of Piping Systems,” provides test methods and acceptance criteria for assessing the severity of piping vibration. Steady-state and transient vibration testing are addressed along with applicable instrumentation and measurement techniques, recommendations for corrective action, and discussions of potential vibration sources.

The test specification developed for the AR initial startup testing shall comply with the ASME Operations and Maintenance code requirements as follows:

- Reference 9.1.1 under “General Requirements,” stipulates that a test specification be prepared to ensure that the objectives of the tests are satisfied and that results obtained are accurate or conservative.

- The test specification shall include the minimum list of items in Reference 9.1.1 Section 3. Namely, (a) test objectives, (b) systems to be tested (including boundaries), (c) pretest requirements or conditions, (d) governing documents and drawings, (e) precautions, (f) quality control and assurance, (g) acceptance criteria, (h) test conditions and hold points, (i) measurements to be made and acceptable limits (including visual observations), (j) instrumentation to be used, (k) data handling and storage, and (l) system restoration.
- Classification of the piping is in accordance with the requirements and guidance of Reference 9.1.1, Section 3.1.1 (steady-state vibration) because transient operations such as pump actuation or rapid valve motion are not relevant for acoustic resonance. Due to operating experience and design analysis, the NuScale CNTS main steam line branch connections are classified as “Vibration Monitoring Group 2”.
- The test specification shall include deflection measurement of the CNTS main steam line branch connections as described in Reference 9.1.1, Section 5.1.1.4.
- The determination of an allowable deflection limit is to be developed based on the methodology defined in Reference 9.1.1, Section 5.1.1.5 and NuScale design inputs. The measurement technique and deflection limits are specific to the validation of the NuScale CNTS main steam line branch connections and AR phenomena.
- Instrumentation and the Vibration Monitoring System specifications comply with the requirements discussed in Section 7 of Reference 9.1.1.

#### 5.2.1.2 Instrumentation and Data Acquisition Requirements

A general description of the minimum measurements and sensors proposed to perform the testing is provided in Table 5-55. Sensor specifications, signal conditioning equipment, data conversion and storage procedures, and calibration procedures are to be accepted by NuScale.

Table 5-55 Measurements and sensors

Measurement	Minimum Number of Sensors	Description
Vibration amplitude	18	The accelerometers are mounted on the two MSIVs, two MS piping lines, four DHRS actuation valves, four DHRS branch piping legs, two MS drain valve branches, and four MSIV bypass lines in order to record their vibration response.
Dynamic pressure	10	The high frequency <sup>(b)</sup> dynamic pressure sensors probe the four branch lines to the DHRS actuation valves, two MS drain valves, and four MSIV upstream and downstream bypass lines and measure pressure fluctuations in the branch lines, and MS lines. Strain gauges may be substituted if dynamic pressure sensors cannot be accommodated <sup>(c)</sup> .
Temperature	2	These sensors are used to determine the superheated steam temperature inside the pipes. The main steam system (MSS) has these as part of its control and monitoring function.
Flow rate	2 <sup>(a)</sup>	The mass flow rate sensor in the MSS is used, along with pressure and temperature sensors in the MS line, to calculate the free stream flow velocity in the MS pipes at the DHRS branch lines. The uncertainties involved in this calculation are considered in the pre-test prediction. A velocity reading at the DHRS branch line location is not required because the analysis margin calculation is based on a free stream velocity upstream of the leading edge of the cavity.

(a) Quantity indicates a final datum of average velocity in each MS line. The velocity is calculated from the mass flow rate measurement in the downstream MSS line

(b) The frequency should be greater than the reciprocal of transit time for a fluid particle across the branch cavity, and the transit time of a sound wave traversing the length of the cavity and back to the MS pipe.

(c) If strain gauges are used, they would be installed in the DHRS branch, MS drain valve branch, and MSIV upstream and downstream bypass lines to transform strain oscillation readings into pressure amplitudes. Two sets of four symmetrically circumferential strain gauges placed at two axial locations in each branch pipe cancel out the shell modes of vibration such that the frequency range is well below the breathing shell mode of the pipe. Any deformation of the pipe as measured by strain gauges is caused by an acoustic pressure wave inside the pipe. The axial distance between the two measuring locations will be less than half the wavelength of the upper limit frequency.

Acceleration, velocity, and displacement are measured with the use of accelerometers. The accelerometer also provides the frequency signature of a vibration such that the vibration response can be correlated to a vibration source, i.e., from turbulence or from AR. Velocity and displacement readings are obtained through single and double integration, respectively. The advantage of accelerometers is they measure absolute acceleration and do not need to be referenced to a structure position. Each of the MSIVs and DHRS actuation valves are to be monitored with accelerometers mounted to the valve body to ensure that vibration amplitudes are acceptable. If AR is taking place in the DHRS cavity piping, high oscillating pressures develop and propagate through the entire piping system causing a vibration response in other nearby components. Also, if the instabilities in the stub piping resonate with the structural natural frequencies of the MS piping and MSIVs, dynamic loads could result in high cycle fatigue. Thus, it is important to also instrument nearby components such as the MSIVs.

The MS lines are not fully symmetric and a slight disparity in steam velocity between each line results from minor differences in flow resistance through the FW and MS piping. Although unlikely, with one MS line at a slightly higher velocity, resonance could occur in one MS line and not the other. Also, if resonance in a cavity were to propagate into the MS piping, there may be small differences in vibration response due to geometry, support locations, and damping, thus accelerometers are placed on both MS lines for this testing.

The branch piping exterior walls are also instrumented with accelerometers to ensure deflection is below the limits for the piping, as calculated using ASME OM Part 3 Section 5.1.1.5 (Reference 9.1.1). The amplitude measured on the branch pipe is expected to be larger than the process piping. As discussed in Section H-3.1.3 of Reference 9.1.1, measurement of true peak-to-peak displacement is preferred over RMS displacement because the displacement is proportional to the pipe mode shape and vibrational stress. RMS measurements cannot be readily converted to peak-to-peak measurements except for pure sinusoidal signals, so RMS displacements can only indicate averaged stress.

The count of two MSIVs, two MS line piping legs, four DHRS actuation valves, four MSIV upstream and downstream bypass lines, two MS drain valve and four DHRS branch piping legs requires 18 sensors, which is the minimum for accelerometers if tri-axial accelerometers are used. If biaxial accelerometers are used, then two accelerometers offset by 90 degrees are needed at each location. Consideration of additional sensors for redundancy in case some fail is assessed in the test plan based on review of vendor data, instrument specifications, and ease of installation.

Pressure data is best obtained through the use of dynamic pressure transducers directly in contact with the fluid, which requires tapping into the piping. This is feasible in the DHRS branches as indicated by the small-bore taps shown in Figure 5-39. These particular penetrations are used for sensors related to the nuclear steam supply system control, so additional ports are needed for the first prototype to accommodate using dynamic pressure transducers for this test.

Each of the four DHRS closed-end legs, two MS drain valve branches, and four MSIV bypass lines has dynamic pressure measurement in order to detect the presence of a standing wave in the branch piping and allow for the investigation of resonance. Because the acoustic transmission of pressure waves propagates in the MS lines, the remaining pressure sensors are installed in the flow path of the MS piping in order to compare to the branch measurements, and determine the strength of the reflected pulsation if it is active.

Alternatively, two sets of four strain gauges may be placed at two axial locations along a run of straight pipe to measure hoop strain in the pipe. This non-intrusive technique may be used to measure dynamic changes in pressure inside the pipe. At a given axial location, the four strain gauges will need to be placed around the circumference of the pipe every 90°. The axial distance between the measuring locations will be designed to avoid half-wavelengths of the acoustic pressure waves. The half-wavelength would be calculated as  $L = c/2f$ . In order to detect an excitation of a higher order acoustic mode by a higher order shear layer mode, the spacing should be less than the half wavelength based on the first and second mode acoustic frequencies. A third or higher acoustic mode is not expected to be excited because this requires higher flow velocities and the velocity is limited at full power operating flow rates during the initial startup testing. Strain gauges will be sensitive

to changes in hoop stress due to local pressure changes. A final method is selected in the test specification based on the accuracy and reliability of measurement (from field experience) with consideration of installation options.

Thermocouples are needed to measure the fluid temperature exiting the steam generators and flowing through the MS lines. Measurement uncertainties are quantified and provided. The plant has permanent instrumentation in the MS line for this purpose located upstream of the MSIV. The total loop uncertainty of the superheated steam measurement is  $\{\{ \} \}^{2(a),(c)}$ . The two MS flow venturies will have dual transmitters with dual temperature transmitters to support the flow measurement. These temperature sensors will also be used to allow for an assessment of the heat losses through the MS line, and the impact to the calculated velocity at the CNTS main steam line branch connections. The test plan will specify monitoring steam temperature at these locations and save their data during the test interval.

The pre-test prediction evaluates the uncertainty in the MS flow measurement, but the need to perform velocity measurement for this test is optional because the plant has permanent instrumentation to measure the mass flow rate in the downstream MSS piping outside of the NPM. Because the DHRS steam piping has the lowest margin to the critical Strouhal number, only the DHRS steam piping is considered in the pre-test prediction. The free stream velocity in the vicinity of the DHRS steam line tees can be back-calculated from the downstream steam flow rate measurement. Although the velocity profile at the DHRS steam line entrance may exhibit turbulence and swirl from the upstream pipe bends and tee junction (see Figure 5-39), this does not need to be measured explicitly because the AR analysis method is based on the free-stream velocity in the MS pipe upstream of the cavity, and not a local velocity at the cavity entrance. In addition, the back-to-back side openings to the DHRS lines may perturb the velocity profile at the downstream DHRS line tee and this would be seen as slight differences in the dynamic pressure transducer readings between the upstream and downstream DHRS cavities.

Design of the DAS is documented in test facility design documents submitted to NuScale for acceptance. The highest fundamental acoustic frequency of the pipe cavities is less than  $\{\{ \} \}^{2(a),(c)}$ . A time signal with a sampling rate five times the highest frequency of interest is sufficient to accurately record the expected pressure pulsations. Therefore, a DAS with a sampling rate of 3000 Hz or higher is used.

### 5.2.1.3 Description of Required Tests

This test includes gathering vibration, flow, and acoustic measurements at various power levels during the initial startup testing.

The test should gradually increase the FW pump flow rate such that the CNTS main steam line branch connections are exposed to a range of partial-power steam flow rates to detect any acoustic excitation by a higher order shear layer mode. When the flow velocity is ramped up from a low value a given resonance mode can be excited by a higher-order shear mode before it is excited by the first order shear mode. The shear-layer excitation is the strongest at the first shear layer mode, where the most severe pressure pulsations are developed. The test procedure specifies a range for the partial power flow rates and a time to hold at each flow rate for sufficient data collection. The partial power testing



exercises the test procedures and ensures that vibration levels are acceptable before increasing to the full 100 percent power conditions.

The test procedure also specifies a time to hold at full power for sufficient vibration and flow/acoustic measurement data collection. The plant performance parameters in terms of steam pressure, steam temperature, and flow rate are documented in the final test plan. The test procedure specifies a range for those values in order for data collection to be performed.

Variations in these secondary flow conditions affect steam velocity at the DHRS branch lines, but the reactor power level must remain at or below the maximum licensed power level during initial startup testing.

The accelerometers measure the acceleration on the valves, cavities, and piping while the plant is operating at each tested condition, which can be converted to a RMS velocity, or a peak displacement. Typically, vibration levels above a certain RMS velocity or displacement limit warrant corrective actions to reduce the vibrations. The test plan will need to establish these thresholds based on ASME OM Part 3 guidelines, and reviewing the vendor design limits for the valves. Stress limits on the piping/welds due to fatigue may also inform the point at which to stop testing and take corrective actions.

Vibration responses are manifested differently depending in their source, i.e., responses due to turbulence are typically random, low level spectral amplitudes along the same order of magnitude, whereas an AR source vibration is distinguished as large amplitude responses at distinct frequencies. Vibration signals usually consist of very many frequencies occurring simultaneously, such that a resonant frequency cannot immediately be seen by looking at the time history response. Therefore, a frequency analysis must be performed to break down the vibration time signals into individual frequency components such that a spectrogram is generated and analyzed to verify the presence or absence of AR. Online and offline frequency analysis are performed to determine the amplitude and frequency content of the vibration signals.

The dynamic pressure transducers are used for continuous monitoring of the pressure fluctuations in the DHRS branch lines MS drain valves branch lines, MSIV upstream and downstream bypass lines, and the MS lines. These measurements can be used to determine if resonance exists at acoustic source frequencies, and to understand the characteristics of the excitations if the piping or valve vibration amplitudes are excessive. Having pressure sensors in each MS line and each DHRS branch line helps determine if local velocity differences have an effect on the pressure fluctuations. The pressure measurements, along with temperature data, determine the uncertainty and bias in the design values for the speed of sound and velocity used in the AR calculation.

The inside diameters of the DHRS pipe at the tee connection, the MS drain valve tee entrance off the MS line, and the inside diameters of the MSIV upstream and downstream bypass lines and length of DHRS piping from CNTS steam tee to DHRS actuation valve seat, the length of the MS drain valve tee entrance to the first drain valve, and the length of the MSIV upstream and downstream bypass line entrances to the bypass valve are key inputs to the analysis.

The test procedure shall specify that as-built measurements of these variables are recorded to ensure that uncertainty in design inputs have been adequately accounted for in the analysis. Measurements need to be obtained for the inside diameter of MS lines at the flow sensor location and at the CNTS main steam line branch connections inside diameters. These measurements can be performed in the factory upon receipt inspection of the fitting or when it is welded as a piping assembly.

#### 5.2.1.4 Testing Activities Requirements

The testing to be performed follows at a minimum the sequence of activities specified in this section. Additional steps are included by the test supplier as needed to effectively and safely conduct the test.

For each test period, the vibration monitoring from the accelerometers and dynamic pressure transducers are recorded simultaneously to allow for data interpretation and decision making about test continuation. In the event that an unacceptable vibration response develops any time during initial startup testing, the test conditions are adjusted to stop the vibration and the reason for the vibration anomaly investigated before continuing with the planned testing.

Online and offline spectral analysis and time-history analysis are performed to determine the amplitude and frequency content of the vibration signals. Spectral analysis is used to detect large amplitude responses at distinct frequencies, which is indication of the acoustic frequency modes of the CNTS main steam line branch connections resonating with the MS line VS frequencies. The resulting vibration of the piping systems and DHRS MS drain valve, or MSIV valve bodies could cause dynamic loads and fatigue on the locations where maximum stress is expected. The measurements are compared to the established acceptance criteria for each location. The acceptance criteria are based on the allowable vibratory stress limits for the instrumented components.

Depending on the practical limitations of sensors placement, cable routing and DAS channels, the in-situ flow measurements (pressure, temperature, and flow rate) do not have to be performed at the same time as the accelerometer measurements, although the impact to overall test duration of sequential measurements should be considered in the test plan. The dynamic pressure transducers or accelerometers can independently indicate if there is an AR condition during operation.

The duration for data collection will need to be determined in the test specification and should be sufficiently long enough to allow for stabilized statistical averages in the data. If vibration levels are below the acceptance limit and the test is not stopped due to detection of resonance, a reasonable period for data collection is 1.5 hours for the full power test in order to achieve 1 million cycles of the CNTS main steam line branch connections natural frequencies, which is less than  $\{ \dots \}^{2(a)(c)}$  for the DHRS piping tees which have the lowest margin in the CNTS main steam line branch connections. For the second order shear layer test, it is not required to achieve 1 million cycles at each flow rate hold point, but the total test duration will depend on the heatup and power ascension rate limits.

A final test report is developed to summarize the testing activities and results. The content includes the following, at a minimum.

- 
- description of the testing infrastructure, such as
    - drawings, descriptions, and photographs of the NuScale NPM and instrumentation mounting
    - instrumentation diagrams
    - details of the DAS and instrumentation
    - dates of the testing
    - identification of tester or data recorder
  - discussion of testing methodology
  - actions taken as a result of any deviations
  - types of observations collected, for example
    - vibration amplitude
    - dynamic pressure or strain
    - temperature
    - mass flow rate/calculated velocity
  - test results and results evaluations
    - data files
    - data post processing (extent to be determined in the test specification)
    - identification of personnel evaluating test results
    - documentation of critical instrument channel total uncertainty in an official TEEAR
    - instrument calibration certificates
    - test readiness inspection report
    - completed and signed test procedures

## 5.2.2 Decay Heat Removal System Acoustic Resonance Pre-Test Prediction

Under normal power operating conditions of the NuScale plant, the steam generated in the SG tubes flows from the SG plenums to the CNTS main steam piping. The CNTS main steam piping contains tees that connect to the DHRS steam piping. The piping from the tee to the DHRS actuation valves normally does not have flow because the DHRS is isolated except when it is needed for decay heat removal. This cavity is potentially susceptible to AR (see Figure 5-40). At a critical Strouhal number, the shear layer departing the leading edge of the bifurcation becomes unstable and has the potential to excite acoustic standing waves. These acoustic waves are reflected in the cavity, and the oscillations of the shear layer become enhanced, which results in large fluctuating pressure in the cavity.

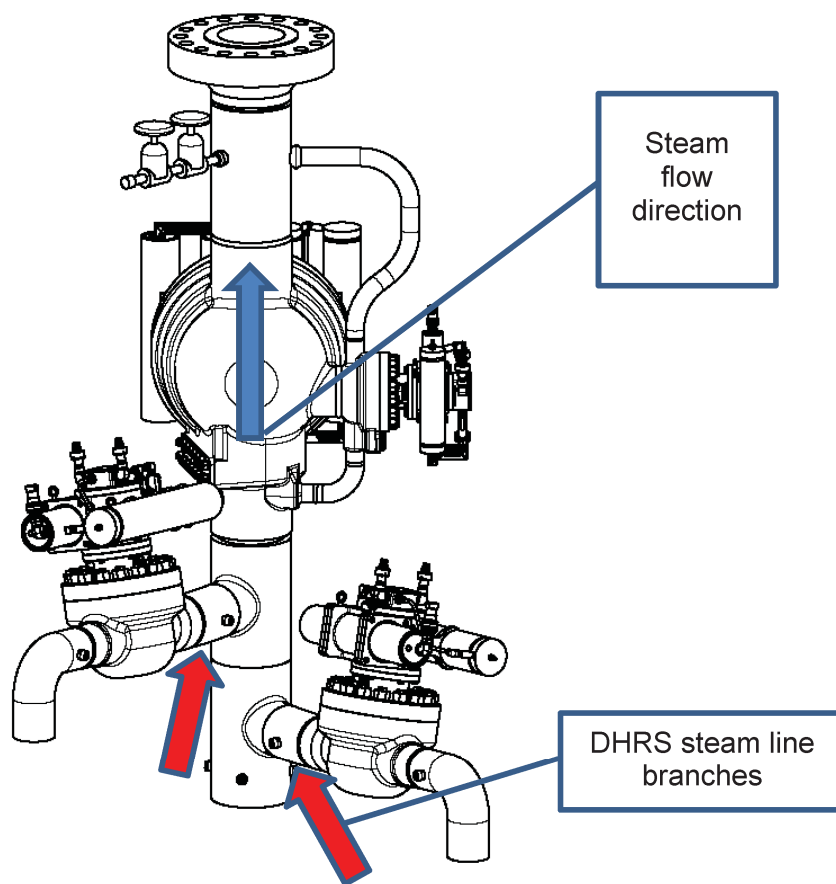


Figure 5-40 Drawing of decay heat removal system junctions to containment system main steam pipe

The design analysis demonstrates margin to the onset of an AR condition due to the first order shear layer associated with a Strouhal number range of 0.35 to 0.62 under all operating conditions. The most limiting operating condition occurs at full power conditions.

During the initial startup test, reactor power is increased to check for fluctuating pressure and vibration due to possible second order shear layers at lower flow rate conditions. Measurements are taken at the limiting full power conditions obtainable within the licensing basis to observe for an AR condition.

This calculation assesses input and numerical and measurement uncertainty to inform the range of possible test conditions at which an AR condition occurs. Because the test is performed during initial startup rather than in a test facility, it is not possible to increase flow until a resonance is observed. Further, because positive margin to the resonant condition is demonstrated in the design analysis, it is unlikely that a resonant condition is observed during the testing. This calculation quantifies the expected secondary flow velocity when the onset of AR is expected, and the effect of various uncertainties on the testing and validation of the predicted safety margin. The flow rate where a lower response due to possible second order shear layers is also calculated to inform the range of flow rates during the test when a smaller acoustic response might be observed.

### 5.2.2.1 Uncertainty Evaluation

Uncertainty evaluation is performed to determine the expected flow rate that AR is observed during testing, and the range of possible flow rates based on uncertainties. These parameters are also used to calculate a range of allowable flow rates that validate the design analysis results.

The length of the acoustic cavity and diameter of the tee are subject to variation due to manufacturing tolerances. The steam velocity in the CNTS steam piping and the speed of sound in the cavity are subject to uncertainty based on the operating conditions of steam pressure, temperature and flow rate obtained during the test and their associated measured uncertainties. Based on Section 6 of Reference 9.1.9, the Strouhal number at the onset of resonance varies as a function of the tee diameters and the distance from the nearest upstream elbow to the tee. These experimental results are used to inform the uncertainty in the Strouhal number. The effect of each of these uncertainty parameters on the safety margin and the predicted velocity for the onset of a resonant condition is determined using the sensitivity coefficient method.

Two input uncertainties that are not analyzed in this calculation are the potential for differences in flow between the two CNTS MS lines, and the effect of the fillet radius on the Strouhal number.

The design analysis estimates the effect of differences in flow losses on the safety margin for the two CNTS MS lines. The effect of this difference is  $\{ \{ \quad \} \}^{2(a),(c)}$  in terms of the predicted safety margin. Since both CNTS MS lines will be instrumented in this test, any effect of the flow loss differences to the onset of AR will be quantified in the testing and addressed in the post-test analysis.

Similarly, the transition to the DHRS branch in CNTS MS tee is specified with a fillet radius rather than a sharp corner that would create a discontinuity equal to the inner diameter of the DHRS steam piping. Use of a fillet radius in the design generates a larger effective diameter at the location where vortices are generated due to the discontinuity. This produces a higher Strouhal number and greater margin to the critical Strouhal number.

The dimension of the fillet radius has not yet been specified in the design, so the inner diameter of the DHRS branch piping is used in the Strouhal number calculation since it is bounding. The difference between the as-built fillet radius and tee branch inner diameter and its effect on the Strouhal number can be evaluated in the post-test analysis.

The acoustic frequency and the velocity design analysis values are calculated using methods that are not subject to numerical uncertainty. Therefore, the numerical uncertainty in these parameters is zero.

Uncertainty in the design analysis predicted safety margin and velocity for the onset of a resonant condition is calculated to inform the expected velocity that an AR condition could be reached during initial startup testing.

The uncertainty analysis for the DHRS steam tee is carried out in accordance with Section 4.5.4.

Because the testing has not been performed and experimental results are not available, a uniform distribution of uncertainties is estimated for the measurement and input terms to support the sensitivity coefficient method discussed above. The global uncertainty method of Equation 4-14 and Equation 4-15 are applied to the individual parameters relevant to AR. The equations provide the square root of the sample variance, also referred to as the standard deviation. This provides a method to estimate the interval or range of uncertainty in a parameter (i.e.,  $x \pm u$ ).

#### 5.2.2.2 Bias Considerations in the Test

This test is performed during initial startup testing on the first NPM at full power and flow conditions. Therefore, there are no experimental distortions between the design analyses and the test condition that affect the expected or allowable range for validating the design analysis.

There is analytical bias between the best-estimate and conservative design analysis results. Because the best-estimate predictions are used to define the expected results in Section 5.2.2.3, this result quantifies the value of the analytical bias.

#### 5.2.2.3 Expected and Validation Range of Experimental Results

The predicted, or expected, experimental result consists of the best-estimate safety margin, plus any test distortion adjustments. The range of experimental results is based on adding and subtracting the design analysis safety margin and the total uncertainty. The total uncertainty consists of both the design analysis input uncertainty and the measurement uncertainty.

As discussed in Section 5.2.2.2, the experimental bias for this test is zero, so only the design analysis uncertainties and the test uncertainties need to be considered, as shown in Equation 5-3 and Equation 5-4.

$$Range_{AR.High} = SM_{BE} + SM_{DA} + \Delta SM_{u.meas} + \Delta SM_{u.inp} \quad \text{Equation 5-3}$$

$$Range_{AR.Low} = SM_{BE} - \Delta SM_{u.meas} - \Delta SM_{u.inp} \quad \text{Equation 5-4}$$

Where,

$Range_{AR}$  = Range of safety margins for validation (%),

$SM_{BE}$  = Best-estimate safety margin (%),

$SM_{DA}$  = Safety margin from the design analysis (%),

$\Delta SM_{u.inp}$  = Safety margin adjustment from input uncertainty (%), and

$\Delta SM_{u.meas}$  = Safety margin adjustment from measurement uncertainty (%).

As this testing is performed during initial startup testing with the reactor critical in order to achieve full power secondary side flow rate conditions, flow rate cannot be increased any higher than the licensing design basis allows. Because the design analysis predicts a sufficiently positive safety margin to the onset of the phenomena, the expected onset of an AR condition and the allowable range are above the licensing design basis of the NuScale design. The allowable range of flow rates cannot be fully exercised in the test program. If an AR condition is not achieved during the testing, this impacts the ability to explicitly quantify the conservatism in the design analysis. The lack of AR onset during flow testing, covering the full range of operating conditions up to the limiting full power flow rates, confirms that the DHRS steam tee will not experience AR under any licensing basis operating condition for the NuScale design.

The safety margin range is calculated and then it is converted to the main parameter that will be monitored during the testing, which is the flow velocity. This provides the expected flow rate for an AR condition to occur corresponding to each calculated safety margin value.

$$v_{measure} = v_{assume} (1 + SM) \quad \text{Equation 5-5}$$

Where,

$v_{measure}$  = Velocity to be measured, corresponding to a safety margin (%),

$v_{assume}$  = Velocity assumed in safety margin calculation (%), and

$SM$  = Safety margin (design analysis, best estimate, upper or lower validation range) (%).

#### 5.2.2.4 Second Order Shear Layer

To investigate second order shear layers, testing occurs from ascending partial power flow rate to measure excitation of higher order shear layer modes. Acoustic pressures are lower for a second order shear layer mode compared to a first order shear layer mode (referred to herein as the AR condition). The second order shear layer is expected to occur at twice the Strouhal number range of the AR condition: 0.70 – 1.24.

The flow rate range that corresponds to the Strouhal number range is calculated and the associated reactor power levels are specified. Equation 5-6 solves for the flow velocity as a function of the Strouhal number. The velocity range for the second order shear layer is determined based on the Strouhal number range of 0.70 – 1.24. Due to the larger Strouhal number, most of the flow rates associated with this range are within the licensing design basis and can be achieved during initial startup testing operation.

$$v = \frac{cd_c}{4S(L+0.3d)} \quad \text{Equation 5-6}$$

Where,

- $v$  = Flow velocity (ft/s),
- $S$  = Strouhal number (-),
- $L$  = Length of acoustic cavity (ft),
- $d$  = Inner diameter of piping (ft),
- $c$  = Speed of sound (ft/s), and
- $d_c$  = Characteristic length of the discontinuity (ft).

#### 5.2.2.5 Expected Ranges for Test Variables

Section 5.2.1 discusses the scope of testing needs for the AR startup test. The permanently installed steam pressure and temperature sensors are used to record the pressure and temperatures during the flow test. Permanently installed steam flow rate measurement is also used. Temporary instrumentation consists of dynamic pressure sensors and accelerometers.

Signals from the dynamic pressure sensors and accelerometers are the primary means of identifying an AR condition during the test. If a resonant condition occurs, higher vibration amplitudes and dynamic pressures are measured. From these signals, the acoustic frequency can be identified. The presence of an acoustic frequency signature in the signals distinguishes a resonant condition compared to noise due to turbulence.

First- and second-order shear layers both excite the same acoustic mode. The magnitude of the dynamic pressure fluctuations and accelerations is the primary difference between whether a first or second order shear layer is excited. A second-order shear layer produces a response that is not significantly higher than from turbulence. Whereas if an AR condition



occurs, the accelerations and dynamic pressure fluctuations are significantly higher than from turbulence.

Pressure is a controlled process variable in the NuScale design, so significant variations in this parameter at the full power test condition is not expected. The actual pressure is subject to variability of  $\{\{ \quad \}^{2(a),(c)}$  psi. The effect of this variation on the safety margin and velocity where a resonance is expected has been accounted for in the measurement uncertainty assessment. There should be no observed difference between the expected (500 psia) and measured pressure during this test. If this occurs it requires assessment in the post-test analysis.

Steam temperature is subject to measurement uncertainty and design analysis uncertainty, based on limitations to accurately predict SG performance and natural circulation flow. Input uncertainty in the steam temperature is approximately  $\{\{ \quad \}^{2(a),(c)}$ . Temperature measurement uncertainty is  $\{\{ \quad \}^{2(a),(c)}$ . These uncertainties have been accounted for in the input and measurement uncertainty assessments. During this test, the observed steam temperature should be within about  $\{\{ \quad \}^{2(a),(c)}$  degrees Fahrenheit of the expected value (584.4 degrees Fahrenheit). Larger differences require assessment in the post-test analysis.

The flowmeter is located outside of the reactor building, so a small reduction in steam superheat temperature due to heat loss in the piping and a reduction in steam pressure due to flow losses are expected. This may produce a smaller velocity at the measured location compared to the location of interest for this test (the CNTS main steam piping at the DHRS steam tee). This difference is small and is not accounted for in the pre-test prediction but can be assessed in the post-test analysis. The assumed velocity measurement uncertainty based on the uncertainty of the venturi flowmeter, is  $\{\{ \quad \}^{2(a),(c)}$ . Additionally, because the flow rate measurement occurs in different size piping (NPS12 SCH160 versus NPS12 SCH80), the ratio of the measured versus the test location area uncertainty is accounted for in the velocity measurement uncertainty determination.

Based on the range of possible thermal hydraulic parameters, variations in the volumetric flow rate are quantified and combined with the uncertainties in the piping inner diameter at the measurement and test locations to determine the total input uncertainty for velocity. Measurement and input uncertainties are  $\{\{ \quad \}^{2(a),(c)}$ , respectively.

### 5.2.2.6 Results and Conclusions

This calculation provides the pre-test prediction results for AR testing of the DHRS steam line tee locations. The primary goal of the testing is to validate that AR does not occur at this location during limiting operating conditions. Additionally, the presence of second-order shear layers is investigated at lower flow rate conditions.

The results of this calculation show the effects of various input and measurement uncertainties on both the predicted safety margin and the velocity where an AR onset is possible. Table 5-56 summarizes the values of input and measurement uncertainty and the “ $u\theta$ ” terms identify their magnitude. The results show that the cavity length has the

largest input uncertainty, and the flow measurement has the highest measurement uncertainty. Per the analysis methodology, the “uθ” terms are combined by square root sum of squares to produce the total input and measurement uncertainty. Input uncertainty is  $\{\{ \dots \}^{2(a),(c)}$  and measurement uncertainty is  $\{\{ \dots \}^{2(a),(c)}$ .

Table 5-56 Input and measurement uncertainties

Parameter	Input Uncertainty	Measurement Uncertainty	$U_{xi}\theta_i$ Input	$U_{xi}\theta_i$ Measurement
Speed of Sound	$\{\{ \dots \}$			$\}^{2(a),(c)}$
Cavity Diameter	$\{\{ \dots \}$			$\}^{2(a),(c)}$
Cavity Length	$\{\{ \dots \}$			$\}^{2(a),(c)}$
Flow Velocity	$\{\{ \dots \}$			$\}^{2(a),(c)}$
Strouhal Number	$\{\{ \dots \}$			$\}^{2(a),(c)}$
Total	$\{\{ \dots \}$			$\}^{2(a),(c)}$

The best-estimate safety margin for the onset of AR is  $\{\{ \dots \}^{2(a),(c)}$  and considering the input uncertainty only, the safety margin range is  $\{\{ \dots \}^{2(a),(c)}$ . The design analysis safety margin is  $\{\{ \dots \}^{2(a),(c)}$ , below the input uncertainty range based on the overall conservatisms in the design analysis inputs and the use of square root sum of squares to calculate the total input uncertainty.

The test is performed on the NPM during initial startup testing so there are no distortions in the test. Therefore, the best-estimate safety margin of  $\{\{ \dots \}^{2(a),(c)}$  represents the expected test results, and the validation range is  $\{\{ \dots \}^{2(a),(c)}$ . This range corresponds to flow velocities of  $\{\{ \dots \}^{2(a),(c)}$  with an expected flow velocity for the onset of a resonant condition at  $\{\{ \dots \}^{2(a),(c)}$ . The nominal, full power flow velocity is  $\{\{ \dots \}^{2(a),(c)}$  including the 5 percent transient margin, and  $\{\{ \dots \}^{2(a),(c)}$  at steady-state conditions. This pre-test prediction quantifies the margin to the onset of the AR phenomenon, accounting for possible input and measurement uncertainties. These results are summarized in Table 5-57.

Because the test is performed during initial startup testing, flow rate cannot be increased to verify the onset of an AR condition.

Table 5-57 Expected and allowable results for acoustic resonance and second order shear layers

Parameter	Expected Safety Margin	Validation Safety Margin Range for Test	Expected Velocity	Validation Velocity Range for Test
Design Analysis	{{			}} <sup>2(a),(c)</sup>
Best-Estimate	{{			}} <sup>2(a),(c)</sup>
Initial Startup Test Nominal Flow Velocity	{{			}} <sup>2(a),(c)</sup>
2 <sup>nd</sup> Order Shear Layer	{{			}} <sup>2(a),(c)</sup>

Second-order shear layers occur at lower flow velocities. If this phenomenon occurs at the DHRS steam line tee locations, it is expected to be observed between {{  
}}<sup>2(a),(c)</sup> ft/s.

### 5.3 Steam Generator Inlet Flow Restrictor Validation Testing

Each individual SG tube of the HCSG tube bundle requires an inlet flow restriction device to maintain stability of the secondary side flow conditions. The flow restrictor fits into the tube inlet. Due to the design of the device, a small annular flow channel exists between the device and inner diameter of the tube. This narrow flow annulus and the flexibility of the IFR are design attributes that could make this device susceptible to LFI. The IFR also experiences vibration due to random turbulence but that response is much smaller than any potential excitation produced by LFI.

Leakage flow instability is a complex phenomenon and previous research has demonstrated that this source of flow excitation is sensitive to the flow and the structural details. As such, the industry has not developed general acceptance criteria to avoid LFI and there are no commonly used equations that predict the critical velocity associated with LFI. Therefore, an analysis of LFI of the SG tube IFR is not performed; instead, prototypical FIV tests are performed to fulfill the requirements of Regulatory Guide 1.20

To validate the final design of the SG IFR, follow-up testing supplements the benchmark testing discussed in Section 3.1. The purpose of this test is to demonstrate that the final design of the SG IFR does not experience unacceptable vibration. Due to the ability to gather higher quality and quantity test data, testing of the component is performed in advance of the startup test program, at a test facility. The specific objectives of this test are:

- Perform modal testing of the IFR to obtain the first two modal frequencies, both with the device in air and with the device submerged in water.
- Demonstrate that the design of the IFR does not experience unacceptable flow excitation due to LFI for the full range of operating conditions and expected manufacturing and installation tolerances. Showing 100 percent safety margin (i.e., no LFI at twice the full-power FW flow rate) is desirable.

- Acquire  $10^6$  cycles of vibration for IFR test specimens according to the recommendation of Regulatory Guide 1.20 (Reference 9.1.5), and examine wear resulting from vibration of the IFR during testing. This includes both wear on the IFR as well as wear on the model SG tube.

### 5.3.1 Test Facility General Arrangement, Accessibility, and Special Features

Due to the small size of the IFR, the design of the test facility allows multiple specimens to be tested concurrently and/or without draining the test loop between each test, if it is cost-effective to do so (i.e., if the savings in reducing the overall number of tests can offset the complexity and additional testing hardware and instrumentation required to run multiple simultaneous test cases). Testing more than one flow restrictor in a single plenum is acceptable because the effects of any geometrical differences between the test plenum and a prototypic one are negligible.

In order to test different IFR alignment and bolt compression conditions, the test facility either provides access to tighten the IFR bolt after installation in the tube or it allows the IFR to be placed in the tube after being aligned and bolted to a mounting fixture.

If concurrent testing is performed, the test specimen design ensures that any noise and structural vibration transmitted between specimens is consistent with (not exceeding) what would be expected from a fully prototypic operating environment.

### 5.3.2 Test Facility Fabrication Requirements

The SG IFR drawing specifies the dimensions and materials for the IFR and its mounting plate. The dimensions and materials of the flow restrictor, flow restrictor bolt, washer, and locknut are reproduced without modification. Figure 5-41, shows the configuration and flow path for the flow restrictor as installed in the NPM (this figure is not intended to control the design of the test fixture). Figure 5-42 gives dimensions of the two main IFR components: the flow restrictor and bolt.

The test specimens are fabricated within specified tolerances to ensure the test specimens are geometrically prototypic. Additionally, different test restrictors are fabricated with steps at the nominal and maximum step diameters. Leakage flow instability is a self-perpetuating phenomenon driven by fluctuating pressure differentials across constrictions. A variation in step diameter by the allowed tolerance has a higher relative effect on the constriction gap width, and thus constriction pressure drop, than a variation in step length or overall IFR length. Therefore, step diameter tolerance is specifically included as a test parameter.

{{

}}<sup>2(a),(c)</sup>

Figure 5-41 Steam generator tube inlet flow restrictor and mounting plate

{{

}}<sup>2(a),(c)</sup>

Figure 5-42 Dimensions of inlet flow restrictor and flow restrictor bolt

In the installed configuration, the IFR is contained within the portion of the SG tube that penetrates the FW plenum tubesheet. This length of tube is rigid compared to the IFR, which is replicated during testing to minimize experimental bias that could be introduced

by flexibility in this flow boundary. The method of providing stiffness is left to the testing services supplier and includes (but is not limited to) addition of supports along the length of tube inside the tubesheet or added tube wall thickness. The minimum length of the rigid section is equal to the depth of the tubesheet holes. For the in-water modal test, the wall stiffness design solution allows sufficient access to the flow restrictor to permit excitation while it is installed in the tube.

Instrument penetrations in the portion of the tube surrounding the flow restrictor are not permitted unless flush with the inside diameter of the tube such that no flow disturbance is generated.

The IFR mounting plate is altered because the full quantity of IFRs is not being tested. Modifications to the mounting plate maintain prototypic mechanical restraint without loss of rigidity.

The system for mounting the IFR allows some test specimens to be aligned eccentrically, that is, offset radially from the centerline of the tube. Eccentricities of 0 percent, 50 percent, and 100 percent shall be tested, where 0 percent is a centered IFR and 100 percent means the IFR is contacting the tube wall with negligible force. In addition, a method to install the test IFR with a specified contact load between it and the tube wall is provided.

Stack-up of tube geometric tolerances has the potential to result in a wide range of diametrical clearances between the IFR and tube wall (Table 5-58). A tube and IFR set for each of these three clearance conditions are created for the test, in order to gauge the effect of the relevant tolerances on the performance of the IFR. In the minimum clearance model, an IFR with the maximum allowed step diameter is used. The other two clearance conditions use a nominal-diameter IFR.

Table 5-58 Range of possible radial clearances between inlet flow restrictor and tube wall

Maximum clearance	{{ }} <sup>2(a),(c)</sup>
Nominal clearance	{{ }} <sup>2(a),(c)</sup>
Minimum clearance	{{ }} <sup>2(a),(c)</sup>

Material of construction for the tube(s) in the test facility is 304 or 316 stainless steel. Tubing for the test is acquired from NuScale's existing stock of Alloy 690 SG tubes. Another tube material may be proposed by the supplier and approved by NuScale; for instance, a nonmetallic tube that permits optical measurement of flow restrictor vibration. In general, the tube material is not a controlling parameter for this test and is selected for compatibility with test conditions and proposed measurement methods.

Unless specified above, other materials selected are at the discretion of the testing services supplier, subject to approval by NuScale design engineering. Materials selected should be of sufficient quality to meet any applicable facility design code requirements and to prevent the generation or accumulation of significant amounts of corrosion or wear products in the test fixture.

The test fixture design is in conformance with applicable pressure vessel and structural codes and standards in effect where pressurization and operation of the test specimen occurs. Construction and fabrication of the test fixture are in accordance with applicable design codes. Information concerning applicable codes and information demonstrating conformance of the test fixtures is to be provided to NuScale for information upon request.

### 5.3.3 Test Facility Operating Requirements

Table 5-59 provides the minimum and maximum pressures, temperatures, and flow rates required of the test facility. The values are given in ranges rather than as individual test conditions. The pressure and temperature for each volumetric flow rate are specified in Section 5.3.7.3.

Table 5-59 Range of flow conditions for steam generator inlet flow restrictor tests

Pressure (psia)	{{ }} <sup>2(a),(c)</sup>
Temperature (°F)	{{ }} <sup>2(a),(c)</sup>
Flow Rate (gpm)	{{ }} <sup>2(a),(c)</sup>

(1) Flow rate is on a per-IFR basis. Multiply by number of IFRs tested simultaneously to determine the total facility flow rate. This flow rate range represents conditions from zero reactor power to greater than three times the FW flow rate necessary to demonstrate 100% margin to LFI.

The test facility pump is selected so that the frequencies of pressure waves arising from pump operation do not coincide with major structural frequencies of the IFR or of the test fixture over the range of flowrates required to perform testing. Blade passing frequency is considered if a centrifugal pump is selected. If a positive displacement pump is used, the flow pulsation frequency is compared to the structural frequencies. Reciprocating positive displacement pumps are not be used.

### 5.3.4 Test Facility Control Requirements

The test facility shall have the ability to smoothly increase the flow rate between the minimum and maximum per-tube flow rates in Table 5-59, and to hold a steady-state flow at any point between the minimum and maximum. Controls on test facility flow rate shall maintain the flow rate within {{ }}<sup>2(a),(c)</sup> of the setpoint (considering uncertainty in the flow meter used for input to the control system) for steady-state flow test data collection when the total facility flow rate is {{ }}<sup>2(a),(c)</sup> or less, and within {{ }}<sup>2(a),(c)</sup> of the setpoint for total flow rates above {{ }}<sup>2(a),(c)</sup>. This provides reasonable control bands for facility designs where few IFR specimens are tested simultaneously and designs where several are tested simultaneously. If multiple IFR specimens are tested simultaneously, it is recommended that a separate flow instrument is used for flow control, rather than a summation of the individual IFR flow instruments.

Temperature shall be maintained {{ }}<sup>2(a),(c)</sup> degrees F from the nominal test case temperature (in addition to any relaxation in the temperature setpoint range). Considering the instrument uncertainty specified in Section 5.3.5, this keeps the temperature within {{ }}<sup>2(a),(c)</sup> degrees F of the target value. In turn, fluid properties of viscosity and density do not vary by more than {{ }}<sup>2(a),(c)</sup>.



Pressure variations do not exceed  $\{\{ \quad \}\}^{2(a),(c)}$ . Slow changes in pressure during a test are acceptable because properties of liquid water are not highly dependent on pressure. Fast pressure fluctuations (e.g., several times over a ten second span) are not acceptable.

Test facility water quality controls are proposed by the supplier and approved by NuScale. Water quality is adequate to prevent introduction of gross impurities and/or detrimental corrosion of the test facility.

Four parameters are of primary importance to measure in this test: modal frequencies, vibration amplitude, flow temperature, and flow rate. Additionally, plenum static pressure, dynamic pressure downstream of the IFR, and differential pressure across the IFR are recorded. The type and specifications of the instrumentation used to acquire the measurements are proposed by the testing services supplier and must be approved by NuScale before commencement of test facility construction or procurement of the instrumentation and DAS. The following subsections present needed attributes of the instrumentation for each measured parameter but do not select the type of instrumentation to be used to record the primary parameters.

All instrumentation discussed below, except for two, are considered critical instrumentation – the proper operation of which is necessary to accomplish the testing objectives. The two noncritical instruments are

- (1) the plenum static pressure instrument, because static pressure is not a controlling parameter for leakage flow instability.
- (2) the instrumentation used to measure differential pressure across the IFR, since validation of thermal-hydraulic analyses related to IFR pressure drop is not an objective of this test.

For the in-air and in-water frequency tests, the first two modal frequencies of the IFR shall be measured. This requires an instrumentation frequency range of at least  $\{\{ \quad \}\}^{2(a),(c)}$  Hz.

### 5.3.5 Flow Test Instrumentation

During the FIV testing, the IFR is mounted in a representation of the SG tube. IFR vibration amplitudes are measured during the FIV tests; however, the confined space presents a challenge for mounting instrumentation and routing cables. The method proposed by the testing services supplier may include (but is not limited to) directly-mounted accelerometers, strain gauges, or optical measurement.

The vibration instrumentation has a frequency range of at least  $\{\{ \quad \}\}^{2(a),(c)}$  Hz in order to measure vibration at the first two modal frequencies of the flow restrictor. It is capable of measuring a minimum displacement of  $\{\{ \quad \}\}^{2(a),(c)}$  inch, which is a quarter of the minimum IFR-tube radial clearance (Table 5-58). Total measurement uncertainty for the vibration instrumentation shall be  $\{\{ \quad \}\}^{2(a),(c)}$  percent of the minimum detectable displacement.

If practical, it is also desirable to obtain maximum IFR stress and strain data in both translational directions. This data is intended to verify that the IFR does not experience high cycle fatigue failure created by TB or LFI. The strain data is also processed to search for indication of LFI vibration.

Vibration measurements are taken at the outside of the tube downstream of the IFR as another method of monitoring for IFR vibration, and at the mounting plate in order to provide a reference signal for noise reduction in the IFR vibration data.

Pressure transducers are installed in the test apparatus for the FIV testing. One is located in the FW plenum to measure the static pressure upstream of the IFR. Two dynamic pressure transducers are installed on the tube immediately downstream of the IFR, within approximately an inch of the IFR tip. These sensors are installed opposing one another so that both can tap into the tube at the same axial location. This provides sensor redundancy while avoiding a situation where additional flow turbulence created by an upstream pressure tap affects data collected downstream. Finally, a differential pressure instrument is supplied to measure the pressure drop across the IFR. Its upstream tap is placed in the plenum and the downstream tap located to minimize measurement fluctuations due to flow disturbances created by the IFR.

The dynamic pressure transducers are used to monitor and record the pressure fluctuations associated with turbulence for the spectrum of frequencies that are measured. They provide an alternate method of monitoring for LFI through the ability to view pressure fluctuations at the discrete frequencies associated with the phenomenon. The dynamic pressure transducers have an amplitude range of  $\{\{ \quad \}^{2(a),(c)}$  psi and a minimum frequency range of  $\{\{ \quad \}^{2(a),(c)}$  Hz.

The sensor used to measure static pressure has a range of  $\{\{ \quad \}^{2(a),(c)}$  psia.

The differential pressure instrumentation has a range of  $\{\{ \quad \}^{2(a),(c)}$  psid. At 100 percent power, the flow restrictor generates a pressure drop of about  $\{\{ \quad \}^{2(a),(c)}$  psi.  $\{\{ \quad \}^{2(a),(c)}$  psid is specified in order to provide differential pressure measurement capability when testing at  $\{\{ \quad \}^{2(a),(c)}$ , because pressure drop increases by the square of the flow rate.

Total measurement uncertainty for pressure instrumentation shall be as follows: dynamic pressure instruments:  $\{\{ \quad \}^{2(a),(c)}$  percent of full scale, static pressure instrument:  $\{\{ \quad \}^{2(a),(c)}$  percent of full scale, differential pressure instrument:  $\{\{ \quad \}^{2(a),(c)}$  percent of range.

Instrumentation is provided to record the fluid temperature in the FW plenum. The instrument range shall be capable of measuring liquid water temperatures up to  $\{\{ \quad \}^{2(a),(c)}$  degrees F. In combination with the temperature control tolerance in Section 5.3.4, this keeps the recorded temperature variation to within  $\{\{ \quad \}^{2(a),(c)}$  degrees F of the true value. In turn, fluid properties of viscosity and density do not vary by more than  $\{\{ \quad \}^{2(a),(c)}$ .

The flow rate in the test facility shall be recorded individually for each flow restrictor undergoing testing. The flow instrumentation shall have a range of  $\{\{ \quad \}^{2(a),(c)}$  gpm to

encompass the range of test flow rates. If a separate flow instrument is used to control the overall test loop flow rate, its range shall be 3 gpm multiplied by the maximum number of simultaneously-tested IFR specimens. Flow rate measurement total uncertainty shall be  $\{\{ \quad \}^{2(a),(c)}$  gpm for each tube's flow instrument. This is better than  $\{\{ \quad \}^{2(a),(c)}$  percent of the full power FW flow on a per-tube basis. If a separate flow instrument is used to control the overall flow rate to multiple IFR specimens, its total uncertainty shall be  $\{\{ \quad \}^{2(a),(c)}$  of its range.

Critical instruments are within their manufacturer's recommended test service supplier calibration periodicity through the end of the testing period. Calibration and verification conform to the test service supplier's program requirements. For any instrumentation that is permanently installed, to the extent practical, calibration is performed just before installation.

Records of the results of calibration and verification are maintained.

### 5.3.6 Data Acquisition System Performance Requirements

Design of the DAS is documented and submitted to NuScale for acceptance. The specification for the transducers, the signal conditioning equipment, data conversion and storage procedures and the calibration procedures are accepted by NuScale before fabrication of the test facility.

The DAS for modal testing provides real-time frequency response display and recording. Real-time displays of frequency response are calculated using data from the beginning of the test run until the current display time. During the modal testing, the sampling rate is 3,000 Hz. An aliasing filter is provided to prevent frequencies above half the sampling frequency from appearing when the data is represented in the frequency domain.

Real-time frequency response is displayed during the FIV tests. The sampling rate for the FIV tests is 3,000 Hz; an aliasing filter again is used. Data is collected continuously for each FIV test beginning at the initiation of flow through the test loop and persisting until the upper limit of the flow rate ramp-up is reached. At each planned hold point, or unplanned hold for abnormal vibration, data shall be collected for 10 minutes after reaching steady-state conditions.

Applicable guidelines from Reference 9.1.1 are also considered.

Critical instrument channel total uncertainty is documented in an official TEEAR.

During testing, plots of various instrument values vs. time are displayed to assist in verifying the FIV performance of the IFR. Displacement, acceleration, and dynamic pressure time history plots of the IFR are included, as well as real-time display of frequency response.

### 5.3.7 Description of Required Tests

An overview of the required flow restrictor tests is provided in this section. These include in-air and in-water modal tests to obtain the first two IFR modal frequencies, and tests to evaluate FIV.

The test program is divided into three steps:

- In-air modal test: the first two modal frequencies are measured
- In-water (still) modal test: the first two modal frequencies are measured with the IFR submerged
- FIV testing: vibratory response is recorded while the IFR is subjected to various flow conditions.

#### 5.3.7.1 In-Air Modal Test

The in-air modal test determines the first two modal frequencies of the IFR without the hydrodynamic mass effects of the fluid that would be present during operation. For this test, the IFR is not tested inside the SG tube. However, the prototypical restraint of the IFR with its mounting plate is preserved with this test. This test is performed at room temperature for each of the two IFR compression (bolt tension) conditions described for the FIV testing. An IFR manufactured to nominal dimensions (including step diameter) shall be used.

Excitation is imparted to the IFR using a method proposed by the testing services supplier and accepted by NuScale that is compatible with the chosen instrumentation scheme and that is capable of exciting the first two modes of the IFR. In addition to the primary instrumentation used to record vibration results during the modal testing, data is collected from any additional instrumentation preinstalled for the FIV testing that can provide vibration data. The excitation input to the IFR is also recorded. For each modal frequency determined, a duplicate value is obtained. If divergent results are observed for the duplicate tests, additional test runs may be requested consistent results are observed.

#### 5.3.7.2 Static In-Water Modal Test

The in-water modal test determines the first two modal frequencies of the IFR while accounting for the damping effects of the fluid that would be present during operation. This test is performed two ways: with the IFR outside the SG tube and with the IFR installed centered in the tube. The prototypical restraint of the IFR with its mounting plate is preserved with this test and the test shall be performed for each of the three radial clearance conditions. The results are compared to gauge the hydrodynamic mass effects upon the fundamental frequency of the IFR resulting from the thin fluid-filled annulus. This test is performed at room temperature and without flow.

All other requirement for the in-water modal testing are the same as for the in-air test.

### 5.3.7.3 In-Water Flow Induced Vibration Test

The FIV test is to assess if LFI of the IFR occurs at any normally expected operating flow rate. The IFR is installed in the SG tube and mounted to preserve both the structural and thermal hydraulic boundary conditions.

Numerous test cases are required to cover the range of expected operating flow rates and temperatures and the various aspects of IFR installation.

Four general parameters are varied to execute the IFR FIV testing: flow conditions, and the compression, radial clearance, and alignment of the flow restrictor.

#### Flow Rate, Temperature, and Pressure

Flow rate testing of the IFR is by means of a flow ramp-up from no flow to an elevated flow rate much higher than expected for any operational mode, high enough to show 100 percent safety margin against LFI. After each IFR test specimen is installed, FW flow is initiated and ramped from  $\{\{ \quad \}\}^{2(a),(c)}$  gpm per tube at a maximum of  $\{\{ \quad \}\}^{2(a),(c)}$  gpm per minute, per tube. At discrete points during testing, the ramp is paused to allow steady-state data collection. These points are 33 percent, 66 percent, 99 percent, and 133 percent of the full power FW flow:  $\{\{ \quad \}\}^{2(a),(c)}$  gpm/tube,  $\{\{ \quad \}\}^{2(a),(c)}$  gpm/tube,  $\{\{ \quad \}\}^{2(a),(c)}$  gpm/tube, and  $\{\{ \quad \}\}^{2(a),(c)}$  gpm/tube. The flow ramp shall also be paused for steady-state data collection any time that abnormal vibration response is indicated by real-time monitoring. Data shall be collected for ten minutes following the establishment of steady-state conditions at each hold point, then the flow ramp shall resume.

If more than one IFR specimen is tested concurrently, a separate flow instrument is used to control the overall test loop flow rate. The measurements from this instrument should be used to determine when the steady-flow hold points and upper end of the flow ramp have been reached because individual tube flow rates are expected to be slightly dissimilar due to differing IFR installation conditions.

The IFR is tested at three different flow temperature-pressure combinations.

- **T1** represents low reactor power FW conditions:  $\{\{ \quad \}\}^{2(a),(c)}$  psia and  $\{\{ \quad \}\}^{2(a),(c)}$  degrees F. The test case pressure is lower, corresponding to a room temperature flow. Leakage flow instability is not expected to occur at or below the normal full-power FW flow rate; therefore, the low temperature test conditions are more approximate.
- **T2** simulates full-temperature FW flow:  $\{\{ \quad \}\}^{2(a),(c)}$  degrees F. Static pressure has a negligible influence on LFI; therefore,  $\{\{ \quad \}\}^{2(a),(c)}$  psia is chosen to ensure the flow remains subcooled and not require excessive design pressures for the test facility.
- **T3** tests above full-temperature FW flow:  $\{\{ \quad \}\}^{2(a),(c)}$  degrees F and  $\{\{ \quad \}\}^{2(a),(c)}$  psia. The pressure for this test case is selected identically to T2 above because pressure is not a controlling hydraulic variable for LFI. Condition **T3** provides 10% margin above the full-power feedwater temperature. This is conservative, as demonstrated by testing of boiling water reactor jet pumps that showed that increasing

fluid temperature decreased the differential pressure at which leakage flow instability developed (Reference 9.1.10, p. 4-2). In application to the IFR, this is equivalent to reducing the critical flow rate for onset of LFI.

### Compression

In its installed configuration, the IFR is compressed by the through-bolt that fastens it to the mounting plate. Varying amounts of compression affect the stiffness of the restrictor, so two different fastener conditions are investigated during testing. The test matrix abbreviations for the two states are defined below:

- **C1:** standard installation with all parts shown on the drawing.
- **C2:** IFR is installed with a second flat washer underneath the locknut and the locknut is tightened to the over-torque specification to place excess compression on the IFR.

The torque specifications for the IFR are provided in the test specification.

### Radial Clearance

Per Table 5-58, the range of radial clearances to be used in the test are as follows.

- Minimum (**min.**): {{

}}<sup>2(a),(c)</sup>

Only the nominal radial clearance is tested for off-normal compression condition C2. The as-designed configuration of the IFR is of primary interest in the testing, so fewer test cases are acceptable for scenarios that do not fully represent a design configuration installation.

### Eccentricity and Preload

Eccentricity is the radial distance off-center that the IFR is installed, given in the test matrix as a percentage of the width of the gap between the IFR and the tube wall. Three eccentricities are specified: {{}}<sup>2(a),(c)</sup>, where {{}}<sup>2(a),(c)</sup> percent represents the IFR touching the tube wall with insignificant contact force. The eccentricity tolerance is {{}}<sup>2(a),(c)</sup> percentage points, except at the 100 percent eccentricity condition which is {{}}<sup>2(a),(c)</sup> percentage points. The methods of setting and verifying eccentricity are sensitive enough to meet these requirements. The actual eccentricity for each test case, measured both before and after the test run, is recorded and included in the final test report (see Section 5.3.8).

It is possible that some flow restrictors are in contact with the SG tube wall after installation and that this will apply a load to the IFR. This is not the design configuration for the IFR, so it is not examined in every test case, but it is of interest because imperfections in installation or bowing of the tubesheet due to thermal and pressure effects could create the situation. Two preloads are tested by positioning the IFR in the tube such that a load is applied from pressing against the tube wall. These preloads are described below and depicted in Figure 5-43.

- **P1:** lower preload force applied to one side of the IFR that may deflect the IFR, but not to the extent that part of the IFR touches the SG tube wall opposite the location of the applied force
- **P2:** a higher preload force displaces the IFR enough that the base and tip are contacting opposite faces of the tube wall. The IFR vibrates similar to a fixed-pinned beam in this situation, if any LFI occurs. If IFR vibration is customarily measured at the tip, the location needs to be changed to a higher-displacement location on the IFR for P2 test cases. Note that if it is determined that preload P2 causes yielding of the flow restrictor material, the force is reduced to some multiple of the P1 force that does not cause the material to yield.

The two preload force values are determined before the test.

{{

}}<sup>2(a),(c)</sup>

Figure 5-43 Preload conditions (not to scale)

To optimize the test matrix, and because installation with a preload is not the design of the IFR, preload conditions are tested for a subset of flow and clearance states.

Table 5-60 provides the test matrix. It is recommended that the FIV tests are performed at temperatures in order from T1 to T3. Starting with the lowest temperature is more conducive to troubleshooting, if issues arise early during testing. As used in the matrix, the term “test specimen” is defined as a unique combination of installation parameters, thus a single physical IFR could fill the role of more than one test specimen upon removal and reinstallation in a different configuration.

In general, the test matrix is ordered so that conditions that are closer to the nominal design configuration are listed earlier. Aside from test temperature, the order of testing compression, radial clearance, and eccentricity or preload is of low importance. Four preload tests are included in the matrix, two each at compression states C1 and C2. Because the IFR is not intended to be installed with a contact force between itself and the tube wall, the preload conditions are not studied as extensively. The test matrix has not been screened from a design-of-experiments perspective, so the testing services supplier is encouraged to provide input on potential streamlining of the matrix.

If leakage FIV is encountered during the flow ramp, below the full-power flow rate ( $\{\{ \}^{2(a),(c)}$  gpm/tube), for any test specimen at compression C1 or C2, then the remainder of the testing may be postponed at the direction of the NuScale test engineer until a solution is produced.

During FIV testing of the IFR, test specimens  $\{\{ \}^{2(a),(c)}$  (listed in Table 5-60 shall be retested at the flow temperatures given in the right-hand column of Table 5-60 on a different day than the original tests to show consistency. More test cases may be specified for repeat if it is warranted based on the results of the first repeatability study. The test cases selected for the repeatability assessment are a sample of about 15 percent of the test matrix and cover the flow rates and include at least one example of each clearance and alignment condition for fastener conditions C1 and C2. These choices are open to modification if statistical analysis or experience of the testing services supplier indicate that it would be advisable.

The total duration of FIV testing for each IFR used in the test shall be enough to capture  $10^6$  cycles of vibration assuming the IFR is vibrating at the in-water fundamental frequency determined in the modal testing. At the predicted fundamental frequency of  $\{\{ \}^{2(a),(c)}$  Hz, this requires a total of at least  $\{\{ \}^{2(a),(c)}$  minutes of FIV testing for each restrictor. The  $10^6$  cycles are not required to be consecutive; they may be collected over the course of multiple test runs.

Table 5-60 SG IFR flow test matrix

Test Specimen #	IFR Compression	Radial Clearance	Eccentricity/Pre load	Repeat at Flow Temperature
Ramp flow from $\{\{ \}^{2(a),(c)}$ for flow temperature cases T1, T2, and T3				
1	$\{\{ \}$			$\}^{2(a),(c)}$
2	$\{\{ \}$			$\}^{2(a),(c)}$
3	$\{\{ \}$			$\}^{2(a),(c)}$
4	$\{\{ \}$			$\}^{2(a),(c)}$
5	$\{\{ \}$			$\}^{2(a),(c)}$
6	$\{\{ \}$			$\}^{2(a),(c)}$
7	$\{\{ \}$			$\}^{2(a),(c)}$
8	$\{\{ \}$			$\}^{2(a),(c)}$
9	$\{\{ \}$			$\}^{2(a),(c)}$
10	$\{\{ \}$			$\}^{2(a),(c)}$
11	$\{\{ \}$			$\}^{2(a),(c)}$
12	$\{\{ \}$			$\}^{2(a),(c)}$
13	$\{\{ \}$			$\}^{2(a),(c)}$
14	$\{\{ \}$			$\}^{2(a),(c)}$
15	$\{\{ \}$			$\}^{2(a),(c)}$
16	$\{\{ \}$			$\}^{2(a),(c)}$



After all FIV test cases are completed, the test specimens and SG tubes are visually inspected for wear caused by impact between the IFR and the tube wall and the results documented in the final test report. A unique identifier is created for each flow restrictor and tied to the corresponding data files in the DAS output to allow easier correlation of IFR wear to overall time in the flow. The same restrictor specimen is used for the preload test cases, if possible, because this may affect the wear on the device.

As part of the initial startup testing performed after NuScale power plant construction, the IFR is subject to a Section XI VT-3 visual examination (Reference 9.1.8, IWB-3520.2). It is therefore recommended that the wear examination conducted after the FIV testing outlined in this report inspects the test specimens and tubes for the applicable VT-3 relevant conditions listed in Section XI, IWB-3520.2. Alternatively, the testing services supplier may propose other inspection methods and criteria, to be agreed upon with NuScale before testing commences. Note that if a nonmetallic material is used to model the SG tubes (for instance, to allow optical measurement of IFR vibration amplitude), the ensuing wear will not be prototypic. However, the wear data is still collected for informational purposes.

The objective of the FIV tests is to demonstrate that leakage FIV does not occur for test cases that bound the expected operating conditions for the NPM. Individual test points have been established to provide for discrete periods of steady-state data to support sufficient evaluations. Because this test sweeps a range of flow rates, it is necessary to maintain continuous data recording, including during transitions that take place between identified discrete data collection periods. It is possible that abnormal vibration could occur during these transitions or at flow rates encompassed by these transition flows. Therefore, for FIV testing there are three types of testing data required:

- continuous data files for each time period the test facility is in operation, including all test runs for that time period and all recorded data during transitions between test runs
- discrete data files for each flow rate ramp test that can be referenced to the continuous data file
- discrete data files for each steady-flow hold point during a test run that can be referenced to the continuous data file

Data files include the record of vibration, dynamic pressure, flow rate, temperature, plenum static pressure, and differential pressure across the flow restrictor. A high resolution in temperature data is not required so the temperature data recording frequency may be decreased from the DAS sampling rate, though not below  $\{\{ \quad \}\}^{2(a),(c)}$  Hz.

Pump operating speed is recorded for the tests to allow for determination of blade passing frequency (for a centrifugal pump) or pulsation frequency (positive displacement pump). Pump operating speed is recorded as a parameter at the same data acquisition frequency as flow restrictor vibration. This data is necessary to allow determination of any correlation between observed FIV and pump-generated pressure waves.

### 5.3.8 Test Acceptance Criteria

Test steps from the test plan and procedures are performed as written; any deviations from test plan and procedures are reviewed and entered into the test log.

A final test report is developed to summarize the testing activities and results. The content includes the following, at a minimum.

- description of the testing infrastructure, such as
  - drawings, descriptions, and photographs of the test specimens and method of mounting
  - schematics and photographs of the test facility
  - instrumentation diagrams
  - details of the DAS and instrumentation
  - dates of the testing
  - identification of tester or data recorder
- discussion of testing methodology
- actions taken in connection with any deviations
- types of observations collected, for example
  - strain
  - displacement
  - pressure drop
  - wear inspection results
- test results and results evaluations
  - data files
  - data postprocessing (extent to be determined in the test specification)
  - identification of personnel evaluating test results

## 6.0 Initial Startup Measurement Testing

### 6.1 Regions of Interest and FIV Mechanisms

Table 6-1 summarizes the regions of interest for monitoring during initial startup testing and flow induced vibration (FIV) mechanisms for each region. Section 6.4 provides annotated figures to visually relate the regions and mechanisms of interest, which are referenced throughout the remaining text in this section.

Table 6-1 NPM initial startup test regions and susceptible FIV mechanisms

Region	FIV Mechanism
SG Assembly	Vortex shedding at bottom tube span
	Turbulence due to internal flow/boiling and external cross flow
	Fluid elastic instability throughout tube bundle
	Acoustic Resonance in hydraulically-connected MS/FW piping cavities
ICIGTs	Leakage flow between tube and support
	Vortex shedding above riser and below pressurizer baffle plate
	Turbulence due to primary flow
CRD shaft and shaft sleeve	Leakage flow between shaft, sleeve and support
	Vortex shedding above riser and below pressurizer baffle plate (sleeve only)
	Turbulence due to primary flow
Upper/Lower riser slip joint	Leakage flow instability

#### 6.1.1 Predicted Modal Responses

Sensing configurations are designed to capture the operating deflection shape due to various forcing/input functions. The operating deflection shape is a combination of mode shapes; therefore, the sensors should be selected to detect these modes by frequency, displacement resolution and orientation. For accelerometers and strain gauges, the lowest structural frequency is generally limiting for the selection process.

For some FIV mechanisms, structural modal frequencies may not represent the predominant spectral energy (e.g. LFI and the flutter frequency, excitation from any AR conditions); however, this non-structural spectral content contributes to overall RMS calculations if present within the bandwidth. Therefore, frequency ranges of interest are established for acceptance criteria that represents the proper unexpected response

grouping inclusive of all other mechanisms. The absence of these mechanisms represents the expected response.

VS and FEI primarily excite first mode structural frequencies; whereas LFI introduces combination resonance. Turbulent buffeting consists of random velocity perturbations spread over a wide range of frequencies. Predominant responses contributing to an overall RMS calculation are comprised of a combination of structural natural frequencies as opposed to VS which excites a single natural frequency (usually first mode). Historical FIV instrumentation programs have limited the general frequency range to 200 - 350 Hz, bounding the frequencies used for structural analysis. This range is consistent with appreciable stress ranges of NPM components, where higher frequencies do not result in displacements sufficient for high cycle fatigue due to vibration. Recognizing that the HCSG tubes have exhibited responses above this general range in TF-1 and TF-2 testing, the evaluation of unexpected responses entails analysis over two ranges: 1) a primary lower bound, consistent with historical CVAP applications and adjusted for TF results and 2) a secondary range inclusive of bounding higher frequency responses as observed during testing. Based on available analytical and empirical results for the as-designed NPM, the recommended primary range of responses is set to  $\{ \{ \dots \} \}^{2(a),(c)}$  and the secondary range is set to  $\{ \{ \dots \} \}^{2(a),(c)}$ . These ranges are to be adjusted to be consistent with future testing (TF-3) and/or structural analyses, if applicable.

### Steam Generator Tubes

The FE model used for FIV analysis couples the nodes near the top of each tube to the steam tube sheet and the nodes near the bottom of each tube to the feed tube sheets, simulating the inserted and welded tube in the tube sheet. Tube nodes are coupled in the tube support tabs at each interface. Two boundary conditions are simulated: 1) fixed (axial, lateral, and rotation, less rotation/twisting about tube axis which is left free) and 2) sliding, where the tube is constrained laterally (translation and rotation) but left free in displacement along the tube axis and rotation about the axis. Both cases are intended to envelop the range of possible combinations of modal behavior by simulating the potential support friction contributed by thermal expansion and manufacturing/assembly tolerance stack-up.

Simulating the varying boundary conditions demonstrates that the fixed case results in elevated modal frequencies and less mass participation in the horizontal directions due to increased stiffness. The modal results are similar in the vertical direction for both cases. Further, interior columns (lower numbers) have elevated frequencies when compared to the outer (longer, higher numbered columns). For individual tube models considering column 21 (fixed), the predominate axial mode is around  $\{ \{ \dots \} \}^{2(a),(c)}$ , the vertical modes are around  $\{ \{ \dots \} \}^{2(a),(c)}$  (most mass participation) and horizontal modes near  $\{ \{ \dots \} \}^{2(a),(c)}$  (most mass participation). For the sliding case, the predominant axial modes are near  $\{ \{ \dots \} \}^{2(a),(c)}$  with upper modes between  $\{ \{ \dots \} \}^{2(a),(c)}$ . The vertical modes remain similar to the fixed boundary condition case, plus the addition of an  $\{ \{ \dots \} \}^{2(a),(c)}$  mode. The horizontal predominant modes are around  $\{ \{ \dots \} \}^{2(a),(c)}$  (most mass participation).

The first mode response for the SG tube is predicted to occur at a maximum displacement mid- span followed by modes (n) with equally spaced nodes (n-1) along the span length. Previous mode shape testing indicated that predominant directional responses (vertical or horizontal) were detectable in both measurement directions allowing some redundancy in detection. However, shape characterization requires both measurement directions for relative phase and amplitude preservation.

### ICIGT

Of the 12 ICIGTs in the riser, eight are straight and four have a bend near the top of the riser. The bent ICIGTs do not pass through the uppermost support in the riser and therefore have a larger unsupported span.

For the supports within the riser area there are multiple spans between supports. The bent, longer span, configuration results in the lowest modes. The first mode response is predicted to occur at a maximum displacement mid- span followed by modes (n) with equally spaced nodes (n-1) along the span length. Furthermore, frequencies for the straight spans below the baffle plate will be much higher than those predicted for the bent ICIGTs in this region.

### CRD Shaft and Sleeves

The CRD shaft protective sleeve is a 2-inch schedule 40 pipe welded to the upper riser hanger ring and hangs  $\{\{ \quad \quad \quad \} \}^{2(a),(c)}$  down half way into the penetration of the top CRD shaft support. Modeling as a cantilever beam the pipe is fixed at the top and free at the top CRD shaft support where LFI regions are present. Modes 1 and 2 are acting in orthogonal directions at  $\{\{ \quad \quad \quad \} \}^{2(a),(c)}$  and Modes 3 and 4 also act in orthogonal directions at  $\{\{ \quad \quad \quad \} \}^{2(a),(c)}$ . These frequency ranges are applicable over the TB and VS mechanisms as the configuration is a single span with multi-mechanism boundary conditions. For the CRD Shaft (fixed supports), the first mode response is predicted to occur at a maximum displacement mid- span followed by modes (n) with equally spaced nodes (n-1) along the span length. For the CRD shaft sleeve the first mode response is predicted to occur at a maximum displacement near the end of the sleeve followed by modes (n) with equally spaced nodes (n-1) along the sleeve length.

## **6.1.2 Acoustic Resonance (AR)**

Pressure waves caused by flow disturbances can travel and reflect throughout the flow path of the NPM. As the waves encounter changes in cross-sectional area the waves are reflected and either reinforce or cancel out the original pressure pulsation. Whether the standing wave is amplified or attenuated is a function of the geometry of the flow path, wave speed and other acoustic considerations. The piping and vessel essentially act as a filter for the pressure pulsations: cavities like branch piping with an acoustic frequency near the pressure wave frequency will be amplified, and cavities with acoustic frequencies not in resonance will be attenuated. The amplified pressure pulsations can travel through the vessel and, if sufficiently aligned with a structural natural frequency, further amplify structure responses as a resonance. The waves can be fluid or structure born (i.e. in the vessel wall). Pulsations that do not align with structural natural frequencies will also

contribute to elevated vibration at these discrete standing wave frequencies but are filtered by damping encountered over the distance traveled.

For example, fluid flowing past a closed branch line will initiate a wave that is reflected back (from the closed valve / blind flange). For any given branch, there exists several acoustic modes corresponding to the length of the branch; when pressure excitation is imparted at these frequencies, the wave is reflected back in a manner that reinforces its amplitude, producing a standing wave. These acoustic modes can be excited by vortex shedding (VS), turbulent buffeting, or mechanically-imparted excitation (such as pump-induced pressure oscillations). The most common source of a pressure wave at the mouth of a branch line is vortex shedding; if the frequency of the vortex shedding matches the standing wave acoustic frequency of the branch, significant acoustic vibration may occur and propagate through the main piping run.

### 6.1.2.1 MS/FW Piping

Within the NPM containment system (CNTS), outside of the RPV, there are several components that are susceptible to AR, most notably lines branching off of the main steam (MS) lines, such as the DHRS steam lines, connections upstream and downstream of the MSIV bypass valves, and the MS drain valve branches. Due the safety margin being less than 100% for these regions, these branches will be instrumented during initial startup testing. This report includes prioritization of instrument locations to detect unexpected responses to standing waves generated in the CNTS on the SG Assembly.

### 6.1.3 Fluid-Elastic Instability

Fluid-elastic instability (FEI) is a phenomenon primarily associated with arrays of closely packed circular cylinders, such as a SG tube bundle. Instability occurs when during one vibration cycle, the energy absorbed from the fluid exceeds the energy dissipated by damping. Fundamentally, FEI is a strongly coupled fluid-structure interaction (FSI) mechanism, where the motions of individual cylinders result in fluid force components that are proportional to cylinder displacements and in-phase with the induced velocity of the cylinders. Based on the strong coupling, once the onset of FEI occurs (critical fluid velocity,  $V_{crit}$  is exceeded), Vibration amplitudes increase exponentially with any additional increase in fluid velocity. Vibration amplitudes are only limited by tube-to-tube or support contact.

#### 6.1.3.1 Steam Generator

The response from FEI is strongly coupled to the first bending mode of the tubes. For FEI, the limiting tube column is 21 based upon the longest possible span length and lowest corresponding first mode natural frequency. This location is represented in Figure 6-1. The interaction between Column 21 tubes (entire column) and adjacent column tubes provide the necessary feedback between the fluid and tube to excite FEI under proper flow conditions and onset could likely be detected from adjacent tubes. Specifically, only one limiting column would require instrumentation to detect unexpected responses.

### 6.1.4 Vortex Shedding (VS) and Turbulent Buffeting (TB)

#### Vortex Shedding (VS)

A fluid flowing over a bluff body will cause boundary layer separation and flow instabilities as downstream shedding vortices, commonly known as vortex shedding. A resonant condition will exist if the shedding frequency is close enough to a natural frequency of the structure component in the path of the flow. The shedding frequency is directly proportional to flow velocity (Reynolds number of the bulk fluid flow). The energy imparted upon a solid structure from vortex shedding can be reduced as the effective size of the bluff body is reduced, such as making the shape more aerodynamic, or by reducing the local Reynolds number.

#### Turbulent Buffeting (TB)

Components subject to turbulent flow are also excited by that flow causing turbulent buffeting. Coupling between a structure and the random pressure fluctuations induced by turbulent flow is typically weak. The amplitude of the structural response will be a function of several variables, including the turbulent forcing function and the frequency of the structure.

The turbulent forcing function is developed based on several components, including convective velocity, the correlation length (e.g. coherence of the forcing function between different points on the structure) and the power spectral density (PSD), which describes the turbulent energy distribution as a function of frequency. Based on greater coherence of the forcing function along a structure subject to cross flow, vibration amplitudes are greater for structures exposed to cross-flow as compared to axial flow geometries. Consequences of turbulence-induced structural vibrations are typically life time management issues due to the cumulative effect of these low amplitude vibrations, such as wear and fatigue.

Components that are subject to turbulent flow are susceptible to turbulent vibration. Additionally, a component interface location that may not be directly subject to turbulent flow but is in the load path of one or more components that are subject to turbulent flow is also susceptible to turbulent vibration.

#### **6.1.4.1 SG Assembly**

Turbulent buffeting is possible for the tube bundle. In addition, the random pressure fluctuations associated with boiling inside the tubes provides a secondary source of turbulent energy to the tubes in addition to the turbulent forces due to primary coolant cross flow outside the tubes. This region is shown in Figure 6-1.

Vortex shedding is assumed to be possible for all tube span locations where there are not tubes located directly downstream. This location is also shown in Figure 6-1, specifically locations A05 and A06.

#### **6.1.4.2 ICIGT**

Vortex shedding and turbulent buffeting are possible on the outside of the ICIGTs as the fluid first moves vertically parallel to the component routing and then turns in the upper plenum to move outward toward the steam plenums in a crossflow configuration. This location is shown in Figure 6-3.

### 6.1.4.3 CRD Shaft and Sleeve

Above the upper riser, the fluid changes direction and the CRD shaft would be a bluff body with respect to the flow direction; however, the addition of the protective sleeve results in only parallel flow for this component. Therefore, the CRD shaft is not susceptible to vortex shedding due to cross-flow. The protective shaft sleeve is susceptible to VS in the same area. This location of interest is shown in Figure 6-2 as points B03 and B04.

Similar to the ICIGT and CRD shaft sleeve, the upper riser hanger braces experience cross flow as the flow turns from the upper riser outlet into the SG region. Also, as the primary fluid moves around the CRD shaft supports located in the riser, vortex shedding, and turbulent buffeting may also occur. These locations are not the primary concern for this mechanism but are shown in Figure 6-2 and Figure 6-3.

### 6.1.5 Leakage Flow Instability (LFI)

Leakage flow instability is caused by fluid flow through a thin space with at least one flexible structural boundary, resulting in vibration of the flexible boundary due to the negative fluid damping becoming larger than the total structural/fluid damping. In this case, damping forces are converted to driving forces and transferred from the fluid to the structure through a fluid-structure interaction in an additive fashion (self-excited) which creates a dynamically unstable and non-linear system with both positive and negative damping forces.

For each of the areas of the NPM a primary and secondary component/location for LFI is identified corresponding to areas determined to have the least margin by evaluation. Primary modes of vibration are also used to determine maximum displacements and frequencies of interest.

#### 6.1.5.1 ICIGT

Two areas were assessed. The primary instrumentation location, ICIGT-LFI-1, includes the interior surface of the ICIGT to exterior surface of the lower ICIGT support. The radial gap between these surfaces is  $\{\{ \quad \}^{2(a),(c)}$ . The secondary location, ICIGT-LFI-2, includes the interior surface of the ICIGT to exterior surface of the ICIGT support within riser. The radial gap between these surfaces is  $\{\{ \quad \}^{2(a),(c)}$ .

#### 6.1.5.2 CRD Shaft and Sleeve

Seven areas were assessed. The primary instrumentation locations include the interior surface of the CRD shaft to exterior surface of the top CRD shaft support, and the interior surface of the CRD shaft sleeve to the exterior surface of the top CRD shaft support.

#### 6.1.5.3 Upper/Lower Riser Slip Joint

The upper and lower riser sections meet at the slip joint where the bellows is designed to handle the thermal expansion of the riser to ensure positive force at the interface. The slip joint is designed to be maintained in a closed condition and has a small pressure difference



with a convergent flow passage. LFI is not expected at this annular passage. This location, however, is monitored to confirm this conclusion.

The upper riser in the area of the transition is shown in Figure 6-3. A bellows allows for thermal expansion in the upper riser and is located just above the slip joint. The slip joint movement could occur in either the vertical or lateral directions.

## 6.2 FIV Detection Methodology

Characterization of FIV mechanisms for the SG are provided during the TF-3 testing. Validation testing is also planned for the SG inlet flow restrictor and for AR in the CNTS steam piping. The purpose of the startup testing measurements discussed here is not primarily for structural validation but to detect any unexpected FIV responses. In order to do so, the sensors and acquisition platform used for startup testing needs to be engineered to characterize expected FIV to distinguish it from unexpected. The only expected response is turbulent driven FIV.

Acceptance criteria can be defined in two ways 1) in terms of an unexpected response and 2) sustained vibration stress per the design life (such as an endurance limit based on ASME fatigue curves and/or ASME OM guidance). Using the location/magnitude of the highest peak stress intensity, the modal strains and displacements at sensor locations can be determined relative to the peak stress intensity on a normalized basis.

Although the measurements are not intended to be used for structural evaluation, acceptance criteria in terms of stresses is most readily related to measured strain or displacement amplitudes as these are directly proportional. During any unexpected events, it is also important to characterize the motion such that likely sources can be identified. For startup testing, this includes being able to distinguish modes of vibration related to FIV (generally first few modes) by both frequency and predominate direction of motion. To make this determination, test and analytical modes need to correlate with respect to the predominant modal direction and corresponding modal frequencies.

Response amplitudes are best trended in both RMS and peak units to capture the overall vibration energy trends and departures from expected trends (peaks) as flow increases. Unexpected wear caused by impacting; however remote of a possibility, should also be able to be characterized by the monitoring system. Impacting differs in characterization as it is not readily detectable through RMS or peak amplitudes alone. Rather, impacting is typically best characterized by the crest factor (ratio of peak to RMS), and is recommended to be measured over a frequency range (2,000+ Hz) considerably higher than is necessary to detect typical FIV phenomenon. Measuring to the higher range ensures that the full peak effect of any impulses are fully characterized (e.g. not attenuated by filtering). For components with strongly-coupled, single-mode responses, crest factors of 2 to 3 are typically observed. For piping and other components exposed to more variable excitation, values of 4 to 6 are common. Values of 10 or higher typically indicate presence of a non-linear input or response (i.e. impacting).

If an amplitude criterion is exceeded, the following vibration indicators are used to identify which FIV mechanisms can be attributed to the unexpected responses.

### 6.2.1 Turbulent Buffeting

At flow velocities below the critical value, turbulent buffeting is the dominant and expected excitation mechanism. Therefore, there is no onset, rather the response is present and largest in turbulent flow regimes. It excites a broad range of coupled frequencies.

RMS and/or peak values of component displacement and vibration velocity as a function of flow rate are used for detection. Vibration responses for TB should be proportional to  $\rho Q^{1.5}$  or  $\rho V^{1.5}$  and departures from this trend may indicate other active mechanisms or unexpected responses. In addition, power spectral density plots should be used to validate that the frequency domain response remains broadband (or associated with TB) and do not manifest in narrow bands, which would indicate other sources of FIV. Instrumentation for the locations need to be able to characterize expected TB responses and clearly identify any unexpected responses.

### 6.2.2 Vortex Shedding

Flow across a bluff body produces vortices. The vibration frequency of the wake is proportional to the flow velocity and results in a coupled force on the body/component. When the frequency of the vortex shedding coincides with a natural frequency of the component, higher levels of vibration and fatigue damage can occur.

A velocity range over which large amplitudes may occur is referred to as the lock-in range. The onset of vortex shedding vibration can be detected by trending the energy at component natural frequencies overtime and comparing to the flow velocity. The onset is depicted within the turbulent buffeting flow regime as a clear departure from the normal turbulent buffeting trend/response. The elevated response would also produce very narrow bands of energy at shedding frequencies and natural modes of vibration. Vortex shedding occurs only within the lock-in range and is not present for lower or higher flow velocities (unlike FEI) where the response is predominated by a turbulent/expected response.

### 6.2.3 Fluid Elastic Instability

The onset of FEI, specifically instability, manifests in different ways and therefore, multiple criteria are used. These can include:

- (a) High increase in the tube vibration response versus increase in flow rate
- (b) Change in frequency response
- (c) Change from random to well-defined tube trajectory (orbit).

#### Tube Response vs. Flow Rate

Rather than a clear indication of the critical velocity transition, the response can tend to exhibit undulating behavior. The response peaks near the transition velocity tend to occur when increasing the velocity (ramping up flow) and may not occur when decreasing flow (hysteresis may not be exhibited). In addition, if flow velocity is not continuously increased,

peaks or transitions may be mistaken for FEI. This is relevant for startup testing, as flow regimes are limited by the licensing basis flow rates when the reactor is critical. Therefore, trends in TF-3 testing, including transitions prior to reaching a critical velocity, if present, inform the startup testing procedures. Time history responses (RMS) in the flow direction and perpendicular to flow are capable of detecting the start of instability; therefore, both sensing directions are required for adequate detection of unexpected FEI responses.

To overcome the ambiguity in establishing the critical flow velocity for cases in which the RMS response versus flow curves exhibit “undulations,” a gradual rise, or both, several investigators have established a threshold displacement amplitude. Experience has shown that instability is more apparent (idealized response) for designs involving high damping. TF-3 testing will fully characterize damping and investigate the threshold displacement that is associated with the HCSG design including beyond design flow rates. In the absence of such data, this value is greater than the aforementioned TB threshold and therefore, exceedance of the TB threshold would indicate an unexpected response and an operative unexpected response for startup testing.

#### Change in Frequency Response

For in-water testing, coupling of the fluid and components (tubes) occurs. This is observed as a broad band of closely spaced frequencies centered about what would be the natural frequency of a tube. During the onset of instability, the response spectrum shifts to a well-defined single frequency. False indications for the onset of FEI can be detected by the following observations

- Significant narrowing of the broadband response and holding for flow rate increases before ultimately becoming extremely sharp single frequency.
- Amplitude and/or frequency responses change abruptly due to a change in the tube support configuration (i.e. changes in tube to tube-support coupling).
- Instability may begin very abruptly where impacting occurs immediately, and broadband responses remain present without a single distinct frequency.

If an unexpected response is detected the frequency and time domain can be used to evaluate potential sources or active mechanisms for FIV. Due to the potential risk of a false positive FEI indication (or other FIV mechanisms), the response spectrum should not solely be relied upon for an acceptance criterion but coupled with a known TB amplitude response and used to support conclusions regarding FIV sources. For the last observation in the list, the small window between the abrupt change in amplitude and impacting may not be sufficient to clearly identify the FEI onset; however, the impact signature would provide a positive indication of an unexpected response. Further post-processing and complimentary vibration indicators would be needed to attribute to a single mechanism/source. The sensors recommended in this report are sufficient in type/quantity to detect the vibration indicators (Table 6-6 and Table 6-7).

#### Tube Trajectory (Orbit)

A tube trajectory can be monitored using two orthogonal accelerometer axes (or inferred from strain directions) to detect changes in the pattern of motion. Without flow instability the shape of motion is random and very small amplitude. Upon the initial onset of

instability, the shape becomes elongated and the amplitude significantly increases about an order of magnitude. If the flow rate continues to increase, the tube begins to whirl and impact with motion limited by gaps/clearances. Similar to other response characteristics, the orbit is best used to supplement established amplitude acceptance criteria and support conclusions related to unexpected responses.

#### **6.2.4 Leakage Flow Instability**

The onset of LFI can be detected as a departure from normal turbulent buffeting during increases in flow velocity. When instability occurs, it is detected by trending RMS displacement/strain responses with flow rates to evaluate unexpected trends. Due to the difference in radial gaps, the smaller gap associated with ICIGTs may be influenced by alignment; and therefore, may not occur for all tubes uniformly (if present). In addition, it would be expected that the flutter frequency would be lower for the ICIGT when compared to the CRD shafts.

Detection is further supported by monitoring relative displacements between the inner and outer surfaces of the annulus and identifying the presence of a flutter frequency and its multiples (1x, 2x, etc.). The range of measurement frequencies is not limited to structural responses for this mechanism and therefore, additional bandwidth is required to capture the flutter frequency, if present. In addition, the onset of instability is detected using similar methods as for FEI, where random motion becomes elliptical. Both orthogonal directions must be measured to characterize this motion.

### **6.3 Sensor Considerations**

This section provides consideration of approaches used for historical CVAP qualification efforts as well as current/next generation sensor technologies. Consideration is provided for approaches successfully used for historical CVAP qualification efforts as well as current/next generation sensor technologies which may add value or limit the number of sensors needed to meet the testing objectives. The result is a preliminary instrumentation plan for NPM startup testing (Table 6-6), along with “optional” sensor locations (Table 6-7) which may provide additional redundancy and/or enhanced information on vibration conditions. Guidance is also provided pertaining to sensor installation and removal, signal conditioning considerations and limitations, pre-installation testing, and acquisition and analysis of the ensuing vibration data.

#### **6.3.1 Summary of Mechanisms and Detection Methods**

Table 6-2 summarizes the predicted frequency responses, displacements, and applicable onset detection methods for NPM components susceptible to FIV, which is used to inform sensor selection decisions. The displacements listed in Table 6-2 represent an upper range of unexpected responses where impacting would begin within a support, sleeve, or between adjacent components and offer a reasonable range for sensor selection in lieu of location and mechanism specific displacement values.

### 6.3.2 Historical CVAP Instrumentation

Historical CVAP testing has used a combination of strain gauges, displacement (LVDT), accelerometer, pressure transducers to characterize loads and responses. Testing of BWRs has traditionally measured control rod drive tubes, in-core guide tubes amongst other reactor internals. Tubes were generally measured from the ID or OD surface using axial strain gauges (vertically oriented) and separated by 90 degrees around the circumference. Accelerometers were used for relative movement of assemblies and to detect impacting. Relative motion between the vessel wall and various guides were measured by LVDTs. Orientation of sensors were specified to detect and differentiate between vibration modes.

Recent PWRs have used a combination of accelerometers, strain gauges, LVDTs, relative displacement (eddy current), and dynamic pressure transducers. Sensors were removed (or temporarily installed) as testing was completed for CVAP without fuel.

Historical CVAP testing differs from the NuScale startup testing. The primary difference is validation testing will be completed before startup testing for the SG assembly. In this regard, startup testing is limited to the detection of unexpected responses and the results and the final qualification is provided by a comprehensive inspection of NPM CVAP components following initial startup testing operation. This reduces the overall quantity of sensors needed for startup testing on the SG assembly and limits the number of similar components (IGICT and CRD shafts) that need to be instrumented.

Table 6-2 FIV Mechanisms, Predicted Responses, and Detection Methods for NPM

ID		General Characterization		Onset Detection (processing)				
Region	Mech.	Predicted Structural Modal Response Range (Hz)	Theoretical Displacement at Supports (inch)	RMS vs. Flow	Spectral Energy at Modes	Broadband Spectral Energy	Non-Structural Content	Relative Measurement
SG	VS	{{ [redacted] }}	[redacted]	◇	◇			
	FEI	[redacted]	[redacted]	◇		◇		
	TB	[redacted]	[redacted]	◇	◇			
	AR	[redacted]	[redacted]	◇				
ICIGT	LFI	[redacted]	[redacted]	◇			◇	◇
	VS	[redacted]	[redacted]	◇	◇			
	TB	[redacted]	[redacted]	◇		◇		
CRD Shaft/Sleeve	LFI	[redacted]	[redacted]	◇			◇	◇
	VS	[redacted]	[redacted]	◇	◇			
	TB	[redacted]	[redacted]	◇		◇	◇	
Slip Joint	LFI	[redacted]	[redacted] }} <sup>2(a),(c)</sup>	◇			◇	◇

### 6.3.3 Sensor Types

The following sensors are evaluated for startup testing.

1. Standard sensor types, including:
  - Uniaxial, weldable strain gauges
  - Uniaxial, piezoelectric accelerometers
  - Relative displacement sensor
  - Piezoelectric dynamic pressure transducers
2. Advanced sensor types, including:
  - Ultrasonic Testing
  - Fiber Optic Sensing
  - Vibro-acoustic sensors

#### 6.3.3.1 Standard Sensors

Standard sensors are those that have been installed previously in similar environments for CVAP or similar testing. Each sensor type is described including value differentiation and attachment.

##### Strain Gauges

Strain gauges measure a voltage change proportional to electrical changes in resistance, caused by tension, compression, or shear forces, on a filament such as a resistive wire or conductive foil. The filament acts as a resistor which is bonded to the component (chemically or mechanically). As the filament undergoes compression or tension, the resistance changes according to the amount of stress. The change in resistance is monitored as a change in voltage using a high accuracy instrument, usually a Wheatstone bridge. This change in voltage can then be converted to a measurement of applied strain. The gauges are not affected by radiation and can be specified for water and high temperature environments. Typical installations use a mechanical bond by welding the gauges to the component of interest.

The strain measurement is advantageous as it is directly proportional to stress. Therefore, the signal does not require filtering for stress/strain calculations. Measured frequency responses can include frequencies below 1 Hz and greater than 100 kilohertz. Calibration of signals is normally completed through a shunting routine where a known resistance is applied to the bridge and measured for an expected voltage/strain. Sensor selection is specific for dynamic or static strain measurements. FIV measurements are dynamic and gauges should reflect this response.

Strain gauge sensors are susceptible to Electromagnetic Interference (EMI) and other capacitive or leakage driven noise. A method for quantifying noise is to remove the bridge excitation and measure the signal. When this technique is employed, these measurements can be used to increase the signal-to-noise ratio (SNR) through compensation of the sensor signal when normally excited (similar to an algebraic subtraction). This method is employed prior to test plateaus for noise reduction.

## Accelerometers

Accelerometers for high-temperature applications generally greater than 325°F use high-impedance piezoelectric devices that require remote charge converters (isolating the electronics from elevated temperatures). Using an applied current, the piezoelectric crystal produces an electrical charge output proportional to the force applied.

The charge converters should be located as close as possible to the accelerometers to minimize electrical noise. The connections at charge converters are susceptible to signal degradation due to humidity and should be isolated from high humidity environments. For the NPM, the closest location for the charge converters within the measurement chain is directly outside the RPV instrument penetration and housed in a sealed box.

Accelerometers are normally stud mounted for permanent or semi-permanent applications using a mounting block that is welded or strapped to the component.

Accelerometers are suitable for the detection of metal-to-metal impacting. Strain gauges and displacement transducers provide better low frequency (less than 10 Hz) information than do accelerometers. Although lower frequency ranges can be measured in acceleration, the noise created during the application of high pass filters to integrate the signal into displacement (for use against acceptance criteria) generally limits the lower measurement range to 5-10 Hz. This means modal displacements using an accelerometer cannot be resolved as accurately as other sensors below 10 Hz.

High temperature radiation hardened accelerometers are commercially available for the NPM environment. These commercially available products are typically larger (too large to attach to the SG tubes, {{ }}<sup>2(a),(c)</sup> square) and uni-axial in design. If a radiation hardened accelerometer were mounted on SG tubes, the reduction in the available gap between tubes coupled with the increase in impact potential could influence measured motion which would not be acceptable for this testing.

## Displacement Sensors

Relative displacement sensors, such as a linear variable displacement transducers (LVDT), measure the movement of a target relative to the sensor mounting location. LVDTs operate on the principal of a transformer and consist of a cylindrical array of a primary and two secondary windings with a separate iron core which passes through the center. The coil assembly provides the reference from which the core is secured to the target that moves. The primary windings are energized with a constant amplitude alternating current supply at a frequency generally between 1 to 10 kHz. This produces an alternating magnetic field in the center of the transducer which induces a signal into the secondary windings depending on the position of the core.

These sensors are limited by the stroke distance or distance between the mounting location and target (on the order of 0.10 to 0.25 inches for radiation hardened versions, larger custom lengths are available) but are able to resolve accurate and direct displacements over a range of frequencies in the range of 2 to 200+ Hz. This range is acceptable to resolve gap distances and modal frequency ranges for NPM components. The size of the main body is dependent on stroke length. For a stroke length of 0.1 - 0.25



inches the body can vary from 2.5 to 3.8 inches and a width of 1 inch. This device could be mounted to CRD shaft supports by this size and used to measure the differential between CRD shaft supports and ICIGT.

These units are commercially available in radiation hardened assemblies (1011 rad) and elevated temperatures well above 600°F. The sensor is typically mounted to a bracket(s) which are welded to components. Mechanically nulling the sensor is required following the installation to ensure the documented measurement range is achieved. These sensors are susceptible to EMI (albeit relatively lower than other sensors mentioned).

If the response of CRD shafts is to be measured, a non-contact displacement probe would be needed. Eddy current non-contact sensors have been used in CVAP programs and are available over the gaps specified between the shaft and support. These sensors would require a bracket mount to fix the sensor and target path. Literature for commercially available sensors does not provide radiation hardening specifications and additional testing may be required to qualify the environmental exposure.

#### Pressure Transducers

Dynamic pressure measurement results can be used to measure pressure fluctuations in the fluid that could be attributed to vortex shedding, acoustic resonance, and leakage flow instability. These sensors are typically used for load definitions and mounted at various elevations in the RPV. However, they will be used in TF-3 testing and have also been used in TF-1 testing for load confirmation/definitions and should not be needed for the components inside the RPV during initial startup testing.

### **6.3.3.2 Advanced Sensors**

Three advanced sensor technologies have been evaluated in addition to traditional/historical approaches. These sensing methods are described using their respective technical merit to contrast from standard sensors and convey additional value during startup testing. In addition to the value differentiation, attachment, modifications for installation, and additional qualification testing is discussed for the following:

#### Ultrasonic Testing

Ultrasonic testing is used to detect signal anomalies of sound waves transmitted and received through various mediums (metal, fluid, etc.). The characterization of these anomalies can include static measurements such as fatigue crack sizing or dynamic measurements such as process fluid flow monitoring. The largest advantage of this method for FIV detection is the ability to characterize a dynamic response of a target, such as the upper/lower riser slip joint (SlipJoint-LFI-1) or hanger supports (CRDS-TB/VS-2), from the outer surface of the RPV (signal passes through RPV wall). This eliminates sensors in the flow path, foreign material exclusion risks, and modifications of internals for the attachment and routing of sensors and cables. The attachment of an ultrasonic sensor on the outside of the RPV would use a high temperature epoxy meeting chemistry and foreign material exclusion requirements.

The testing of this technology is in the development stage, with investigation using an ultrasound system to remotely monitor vibration from the exterior surface comprised of high-temperature and radiation-resistant ultrasonic transducers. The system was able to resolve 0.020-mm displacements through a 6-inch steel interface and 6-inch water column between the moving target and transducer.

Based upon this testing, the displacement accuracy of the measurement is a function of the length of the sound path (sensor to target), temperature of water, and temperature gradients present within the sound path. Locations that can minimize these errors offer the most suitable applications. Use of this technology to characterize FIV responses would require testing to approximate these variables and ensure the measurement resolution was sufficient to identify “unexpected” vibration in the ranges of possible motion similar to the listed gaps for LFI (Section 6.1.5).

Fiber optic sensing

Fiber optic sensing can use the fiber to transmit signals or the fiber itself can be used to measure temperature, pressure, strain, and similar/related parameters. The method measures the changes in light that are scattered in the fiber caused by physical changes in the sensors. These sensors offer a few strong advantages compared to standard sensors, as summarized in Table 6-3.

Table 6-3 Comparison of Standard Strain and Fiber Optic Sensors

Standard Strain	Fiber Optic Sensing
Individually wired (1 sensor = 1 cable)	Multi-point and sensor configuration using single cable
Single point measurement/direction	Full-field measurement profile and multi-sensor configuration (strain, temperature, and/or pressure)
Very limited mode shape resolution (direction and frequency only)	Full mode shape resolution, especially for elevated/complex modes
Limited mechanical cycle life and average SNR	Not prone to mechanical fatigue and very high SNR for static and dynamic measurements.

The sensors can be mounted by either welding, bonding, or embedding them into the structure. The latter is most commonly used for composite materials, but has been completed using powder laser deposition over machined grooves in steel components. For temperature compensation, a second fiber or an alternative is required for an unstrained but temperature influenced measurement. The local temperature gradients during startup testing would require assessment and the corresponding strain variance calculated to determine the full effect; however, dynamic measurements (such as those for FIV) do not require the same level of temperature compensation as a static strain measurement (i.e. absolute strain vs. relative strain).

The sensors are relatively equal in sensitivity to traditional sensors but offer less noise, thereby increasing SNR and improved resolution along the component. A known limitation

of these sensors is that they are influenced by radiation, primarily due to attenuation effects in a radiation field, but also due to changes to the refractive index and other material properties. Testing of different fiber materials has demonstrated the ability of commercially available fibers to tolerate the environment of the NPM including radiation exposure. In 2018, the Department of Energy (DOE) small business innovative research (SBIR) projects demonstrated various methods for fiber optic radiation hardening and new wave guides to reduce the cost of integrated measurements (multiple sensing types in one fiber). Research and development for fiber optics are continually being pushed to address instrumentation gaps for new advanced reactors.

Most locations to be measured during initial startup testing would be suitable for this technology but the top CRD support offers additional value with its use. By using a combined single sensor (pressure and strain), the fiber could be attached along the top CRD support, woven around multiple ICIGT and CRD shaft holes within the supports sensing local changes in the fluid pressure and strain and capturing responses using a single sensor. Other potential locations include along a SG tube span, riser slip joint, and inside ICIGTs. In all cases, these sensors allow for unprecedented resolution that could infer local and imparted loading from adjacent components and provide detailed stress profiles or precise fatigue usage for in-service inspection deferrals and crack growth analysis. The interior of the ICIGT tube may provide the most convenient location for a fiber (strained and unstrained) based upon all the location due to its inherent protection and perceived constraints for embedding or bonding.

The signal conditioning for fiber optic sensors is unique and requires a dedicated system that is not compatible with traditional sensing devices such as accelerometers and strain gauges. Strain systems (sensor and signal conditioner) are calibrated by the manufacturer to a NIST traceable standard. Signal conditioners offer gas cell references to calibrate optical frequencies before every measurement. Temperature sensitivity is the largest source of error for optical sensors and would apply to both the gauge factor and thermal strain. Compensation for these effects requires an unstrained length(s) of the fiber or an alternate fiber sensor. In addition, post-processing of the data would also require specialized software from the vendor.

#### Vibro-acoustic sensors

Vibro-acoustic responses differ from traditional vibration responses as they are detected at elevated frequencies typically above 10 kHz. These responses have been used for health monitoring of rotating machinery components such as motor operated valves (MOV). Many locations were instrumented including the valve stem, actuator and valve body. The testing program evaluated signature responses during stroke tests against a database of maintenance history/testing to identify key indicators of performance degradation. These responses helped inform maintenance schedules and early identification of anomalies during bench stroke tests before they are installed and tested in an outage. Advanced indications of component health is a key differentiator of this monitoring technology, this range of frequencies provide unique insight into components inferring material stress changes and extending the “detection horizon” for advanced indicators of performance degradation.

Stress waves are in the form of high frequency structure borne sounds caused by friction between moving parts. The analysis of the stress waves involves the detection and amplification of the high frequency sounds. In addition to the high frequency sounds, other noises and vibration signals are also present, which are not directly related to the stress waves. The amplitude of stress waves is relatively small as compared to low frequency sources of vibration and audible sound. As such, it is preferred to selectively amplify signals by designing the sensors resonance to coincide with the desired frequency range (i.e. 35-40 KHz) which are associated with stress wave signals. The chosen frequency range is preferably well above structural vibration frequencies and below high frequency acoustic emission sources. This provides the ability to quantitatively measure, and trend, low energy sources of friction in the presence of high background levels of vibration.

Heat dissipating mounts are used to monitor elevated temperature components (greater than 250°F) and the sensors are not capable of the temperatures specified in Table 6-4. Current radiation hardened vibration sensors are generally limited to 5 kHz in frequency resolution (well below the 35-40 kHz range) and insufficient for vibro-acoustic analysis. The vibro-acoustic sensor does not have published radiation tolerance but has been used for testing of in-service valves inside containment. Additional testing would be required to validate the performance of these high frequency sensors under high but limited duration exposure.

These sensors are attached using studs or epoxy directly to the components of interest. Mounting blocks may filter and further attenuate signals therefore direct attachment is preferred. This technology offers local diagnosis to specific components which could include SG tubes for wear to better predict the onset of degradation and inform maintenance strategies and schedules.

Since the monitoring evolution is relatively short, it is unclear how much value a baseline could be for establishing adverse trend indications. This sensor type provides an early indicator of wear and does not suit the near-term objectives of startup testing as wear will be confirmed by visual inspections. Sensing near the tube sheets may provide a signal to infer wear occurring on plenum tubes. Although the exact tube wearing could not readily be determined, a signature of wear may inform inspection frequencies. Additional testing would be needed to qualify the signature and its relation to wear.

### 6.3.3.3 Other Sensor Considerations

Historical startup testing has leveraged access to components outside the RPV as an “antenna” to evaluate a specific path through the reactor vessel (by attachment or proximity) to the component, which is accessed on the outside, especially for fuel components/assemblies. For example, in a boiling water reactor the local power/intermediate range monitor tubes are accessible outside. This could also be accomplished by loose part monitors (if active) in the NPM during startup testing.

### 6.3.3.4 Specifications and Models

#### Cabling

The cabling should be mineral insulated (MI) cable which is also used for other applications in the NPM. For this environment, the sensor and integral cable are hermetically sealed. The sensor and integral cable should be made of stainless steel or Inconel suitable for the desired water chemistry inside the reactor vessel.

#### Environmental

Table 6-4 summarizes the environmental conditions for the containment vessel (CNV). The radiation values bound those within the RPV. Operating riser temperatures are approximately 590°F with a pressure less than 2000 psia. Cable flow velocity for attachment are in the range of 26 inches/second.

Table 6-4 Environmental Conditions by Region

Region	Description	Pressure (psig)	Operating Temperature (F)	Radiation (Integrated Dose)			RH (%) (%)	Chemstry
				60 Year Neutron (Rads)	60 Year Gamma (rads)	Est. 30 Day Gamma (rads)		
	General Area							
B	Lower Riser Assembly/Core Plate	{{						}} <sup>2(a),(c)</sup>
C	Upper Riser Assembly							
D	Baffle Plate to Top of Pressurizer							
E	MS Piping							
F	upper CNV volume							
G	Outside Containment (below bioshield)							

#### Typical Sensitivity and Ranges

Table 6-5 summarizes the typical/suggested sensitivity and range parameters for the most-commonly-used vibration testing sensors, accelerometers and strain gauges. The detailed footnotes following the table convey additional considerations relevant to the NuScale startup instrumentation.

Table 6-5 Typical Parameters for Common Sensor Types

Accelerometers	Strain Gauges
Sensitivity {{  }} <sup>2(a),(c)</sup>	Gauge Factor {{  }} <sup>2(a),(c)</sup>

Notes: 1. Sensitivity should capture the smallest expected vibration to produce a signal 10x the noise floor (typical 50 μVrms) or 1.5 mV-Peak (3 rms/pk \* 10). For example, using a

sensitivity of 10 pC/g and a 1 mV/pC charge converter, the smallest signal for measurement would be 0.15 g peak.

2. Dynamic range should be at least 10x the expected turbulent motion. Note the upper end provides the maximum impact energy that can be resolved without saturating the signal.
3. Frequency range represents all structural modes and offers the ability to characterize impacting signatures. Note structure borne sound is typically high frequency between 2 and 7 kHz. However, the purpose of the testing is to detect a unexpected response but not fully characterize them resulting in only the lower end of the spectrum being covered.
4. Gauge factor is the change in resistance divided by measured strain  $(\Delta R/R)/\epsilon$  where a higher gauge factor produces higher SNR. Also note larger gauge resistances are preferred (generally 350 ohms) for lower bridge current and lead wire effects.
5. The dynamic measurement range represents at least three times the maximum expected stress (based on typical ASME modulus and fatigue curve values for high cycle fatigue of stainless steel).
6. Frequency response captures all predominate component modes and known structural responses.

#### 6.3.4 Proposed Sensor Types and Locations

Considering the regions and mechanisms of concern, including their predicted modal responses and maximum amplitudes (Table 6-2), historical precedence for similar testing (Section 6.3.2), and the state of sensing technology (Section 6.3.3), a detailed instrumentation plan is provided for the NPM components of interest for the purpose of monitoring for unexpectedly large vibrations during initial startup testing. Instrument locations and types are based on a combination of numerous factors, including: detectability of desired responses, prior applications/experience, performance characteristics, reliability/redundancy, physical constraints, and installation/removal considerations, among others. These determinations are summarized in Table 6-6, representing the minimum sensor arrangement sufficient to address the testing objectives. The locations in Table 6-6 are designated as the “recommended” sensor configuration hereinafter. The sensors are organized/grouped into “regions,” each of which is unique in component, elevation, and RPV azimuth. Each sensing direction/axis is labeled with a unique identifier, which are then used to indicate orientations and redundancy.

Additional locations (beyond those in Table 6-6) were identified as having the potential to improve characterization or address redundancy should unexpected responses be detected. These locations are not required to meet the intent of the testing, but summarized in Table 6-7 as optional locations for consideration in the detailed design of this test program. Both recommended and optional locations are depicted schematically in Figure 6-1 to Figure 6-3.

The following sections detail the engineering judgment leading to the recommended and optional sensor locations in Table 6-6 and Table 6-7.

##### Steam Generator (SG)

For the SG, detection of any of the mechanisms of interest (FEI, VB, TB) requires instrumentation of the tubing. The limited clearance between tubing/supports/riser and the

small physical size of the tubing itself limit the available sensing options. It is feasible to utilize axial strain gauges welded to the tubing; this approach was demonstrated during TF-2 testing. The planned TF-3 testing will largely rely on miniature accelerometers, but those sensors will be mounted inside of the tubing and not exposed to secondary flow nor high temperatures. It is not possible to obtain radiation-qualified, high-temperature, miniature accelerometers suitable for instrumenting the SG. Non-contacting sensors (proximity probes, ultrasonics) may be viable within the space and environmental constraints, but may have difficulty locating the small target (i.e. single SG tube). Fiber optic measurement of the SG tubes appears to be another viable option, but the current state of the technology is not sufficiently developed to provide confidence in its resolution and reliability (see Section 6.3.3.2 for additional discussion). For these reasons, strain gauges are selected as the primary means for instrumenting the SG.

Given the applicable mechanisms (FEI and TB globally; VS for the bottom/FW portion; AR if imparted from the MS/FW piping external to the RPV), multiple sensor locations are warranted. The strain gauges will be placed on the outermost (Column-21) tubes, as these exhibit the longest unsupported spans and thus the lowest margin to onset of the applicable phenomena. Given the potential for VS susceptibility, the bottom-most long spans (e.g. Span-3) should be instrumented (Regions A05/A06 in Table 6-6). Instrumentation of the corresponding top-most long span (e.g. Span-21) is also warranted, given that location will be exposed to the highest primary flow rates (Regions A01/A02 in Table 6-6). Note: instruments located on these “start” and “end” spans (close to the MS and FW plenums) have the added potential benefit of detecting any AR pulsations generated in the MS/FW piping external to the RPV. A third elevation is also recommended, corresponding to the point mid-way up the SG where the maximum secondary-side excitation is predicted (Regions A03/A04 in Table 6-6). For each identified elevation (Qty=3), redundant locations are recommended at adjacent azimuths in order to bound variability in the data and mitigate the effect of any sensor failures (resulting in Qty=6 total locations/regions).

It is possible for the tubing to vibrate radially and vertically; for this reason, TF-2 was instrumented with gauges on the outer (radial) and top (vertical-up) sides of select tubes. This same configuration will be applied for startup testing, although the position of the sensors will be adjusted such that they are closer to either the upstream or downstream support plates (location of maximum strain response across the frequency range of interest). This results in Qty=12 total recommended strain gauges, installed at six different locations/regions.

The recommended strain gauge model is identical to that used during TF-2 measurements. The sensors will be adhered to the SG tubing via capacitive discharge welding. The integral hardline cables will need to be routed to an instrument penetration, using one of the following options:

1. Affix cables to the side of the nearest tube supports (using welded shim covers or similar), which provide an interference-free path to progress up through the SG. This approach is beneficial in that it provides the most-secure cable routing, with no exposure to cross-flow. The downside is that the cable will be inaccessible after initial installation, and will thus need to be retired in place.

2. Route cables to the RPV wall or riser, and run vertically-up that surface (can be secured using welded shims or conduit). This approach is beneficial in that it may allow for component removal following initial testing. The downside is that the cables and/or conduits will be exposed to crossflow at some point in the routing, and will need to be evaluated for FIV concerns.

### In-Core Instrument Guide Tubes (ICIGT)

There are two different configurations of the ICIGTs, defined by the tubing geometry between the upper riser hanger ring (URHR) and the first/second CRD shaft support plate. Eight (8) tubes are “straight,” with rigid (welded) attachment at the URHR and the 1<sup>st</sup> CRD shaft support. The four (4) remaining tubes are “bent,” and are free-floating (unrestrained) at the 1<sup>st</sup> CRD shaft support (welded at the URHR and 2<sup>nd</sup> CRD shaft support). The NuScale CVAP analysis demonstrates that the bent ICIGTs have the lowest margin to onset of VS and greatest vibratory amplitude due to TB. Thus, two of the bent ICIGTs were selected for monitoring to provide measurement redundancy.

The configuration of the ICIGTs is well suited to measurement via accelerometers or strain gauges. Given the multi-plane routing of the bent ICIGTs through the fluid-turning region (multiple exposures to cross-flow), it is not clear which portion will be subject to the greatest level of excitation altering the predominate response. Conversely, strain gauges are the preferred sensor in this region (B01/B02 in Table 6-6), as they can be installed near a known point (welded anchor) where measured responses can be directly correlated with analytical predictions. Use of strain gauges also has the benefit of minimizing the exposure of sensor/cable at sections with high cross flow.

Within the riser section, the ICIGTs are also subject to potential LFI and TB at CRD shaft support plates. The support plates provide a bound on radial movement, but the designed clearance of  $\{\{ \}^{2(a),(c)}\}$  (see Table 6-2) is such that impacting could occur if vibrations are of sufficient amplitude. For these locations, accelerometers mounted directly to the ICIGT are recommended (Regions C01/C02 in Table 6-6). These sensors will facilitate characterization of ICIGT motion, and facilitate an assessment of whether localized impacting is present/absent. The sensors will be placed either just above or just below the 3<sup>rd</sup> CRD shaft support plate, as at that location all ICIGTs are unrestrained (not welded). This location also corresponds with the sensors to be installed on the CRD shaft support plate itself (see next section), allowing for cross-correlation should impacting be observed.

### Control Rod Drive Shafts and Sleeves

The portion of the CRD shaft between the URHR and 1<sup>st</sup> CRD shaft support plate has been designed with an external sleeve. Similar to the ICIGTs in this region, the recommended monitoring approach is via strain gauges installed at the top of the sleeve, near the attachment point (Region B03 in Table 6-6). However, unlike the ICIGTs, the point of maximum expected displacement is known (bottom of the sleeve), and the potential exists for impacting if VS or TB of the sleeve, or LFI of the CRD shaft itself, exceeds analytical predictions. Thus, an additional location is recommended (Region B04), with an accelerometer located near the bottom of the sleeve.



At the remaining CRD shaft support plates, the radial gap between the CRD shaft and the outer ring/guide is larger than that of the ICIGTs ({{ }}<sup>2(a),(c)</sup>, per Table 6-2). Thus, significant vibratory motion is not expected, and would likely be bounded by the ICIGT-mounted accelerometers (Regions C01/C02 in Table 6-6). However, the CRD shaft support plate itself is subject to TB/VS due to cross flow, and monitoring is desired. Either strain gauges or accelerometers could be used for this purpose; the accelerometers have an added benefit of being able to better detect impacting if occurring. Thus, two additional accelerometer locations (Regions C03/C04 in Table 6-6) are recommended.

#### Upper/Lower Riser Slip Joint

The mechanism of interest at this location (LFI) would manifest itself as impacting between the two friction-fit structural elements. Accelerometers are ideally suited for assessing the presence of impacting, and thus are the recommended sensor for this location. To simplify installation and routing considerations, the sensors will be placed on the inside of the upper riser, just above the point at which the lower riser interfaces/intersects, just below the bottom-most CRD shaft support plate (Regions D01/D02 in Table 6-6). The integral cable will be routed up the inner wall of the riser, and exit through the same penetration as the ICIGT and CRD shaft sensors.

#### Fiber Optic Sensors

In the course of finalizing the NPM prototype design and associated considerations for the instrumentation plan herein, fiber optic technology may be incorporated into the measurement plan if demonstrated and qualified for the environmental conditions. This technology could replace or augment a majority of the recommended strain gauge sensors and potentially accelerometers, with the added benefit of providing near continuous mode shapes over the installed length. Obtaining this data would expand the effective coverage of the instrumentation with minimal additional complexity.

Table 6-6 Recommended Sensor Locations

Location Information				Sensor Information				Target Mechanisms		Notes
ID	Component	Elevation	Azim.	ID	Type	Orientation	Redundancy	Primary	Secondary	
A01	}}									4
A02										
A03										4,5
A04										
A05										4
A06										
B01										4
B02										
B03										6
B04										
C01										7, 8
C02										
C03										7, 8
C04										
D01										7
D02										

- Notes:
1. Sensors are numbered sequentially by type (i.e. ACC-01, ACC-02, etc.; STR-01, STR-02, etc.).
  2. Refer to the annotated drawings/sketches in Figure 6-1 to Figure 6-3 for additional detail on sensing regions/locations.
  3. Location azimuths are suggested based on overall RPV orientation within referenced drawings, and may be changed/modified to accommodate optimal cable routing, available electrical penetrations, etc. Where multiple region IDs are grouped at the same elevation, the relative azimuthal spacing should be maintained.
  4. For SG locations, strain gauges are to be installed in pairs at radial/outside and top/vertical point on designated tube spans, close to a tube support. This location is the most strain-sensitive. The location at the top elevation also provides a first response to AR standing waves if present in the downstream MS piping, before being attenuated through transmission down the structure/assembly. The location at the bottom elevation provides a similar screening for AR excitation imparted from the upstream FW piping. Spans are designated between supports starting at the FW plenum.

5. Elevation of mid-span SG location (Locations A03/A04) to be determined based on predicted location of maximum secondary-side excitation due to phase change. Spans are designated between supports starting at the FW plenum.
6. For Locations B03/B04, identical sets of sensors are not planned; redundancy may be partially achieved via the alternate sensor located on the other end of the sleeve (e.g. for the top-mounted strain gauges, the bottom-mounted accelerometer should provide complementary data).
7. Accelerometer locations are denoted as having a sensor oriented in the vertical (Z-direction) axis. This sensing direction is optional but included in the table in the event tri-axial accelerometers are used for testing, per the discussion in Section 6.3.5. If uni-axial sensors are to be used instead, the vertical sensors (Z-direction) can be eschewed, such that only RPV-radial sensors (X- and Y-directions) are installed/monitored.
8. The C01-C02 locations provide redundancy in ICIGT measurement locations for LFI in addition to C03-C04 which offer additional grouped sensing along the CRD shaft support to detect vibration from adjacent ICIGT and CRD shafts through the interface. Note that actual limiting ICIGT and CRD shaft sleeve selection could consider post-fabrication alignment (i.e. uniform gaps). It is unlikely that each of the ICIGT and CRD shaft sleeves are equally susceptible to LFI based upon the as-fabricated/assembled tolerances.

Table 6-7 Optional Sensor Locations

Location Information				Sensor Information				Target Mechanisms		Notes	
ID	Component	Elevation	Azim.	ID	Type	Orientation	Redundancy	Primary	Secondary		
A11	SG Tubing Supports	}}								2	
A12											
B11	CRD Sleeve									3	
B12											
C11	CRD Shaft									5	
C12											

- Notes:
1. Sensors are numbered sequentially by type, similar to Table 6-6, with numbers starting in the 100-series to differentiate them from the recommended locations.
  2. Strain gauges on SG tubing supports could be used to infer compression due to thermal expansion.
  3. CRD shaft monitoring locations (B03/B04 in Table 6-6) are the only recommended sensors without direct redundancy; locations B11/B12 are suggested herein to address that potential gap.
  4. The Z-direction sensor is optional (triaxial accelerometers only) and may be excluded if uniaxial sensors are selected.
  5. Sensor installation on the CRD shafts themselves is limited due to the need to maintain the required safety function of insertion/extraction. Thus, if direct measurement of CRD shaft motion is necessary (to address concerns over LFI and/or TB), non-contacting sensors should be used. Without this measurement, there exists a remote possibility for the CRD shafts to vibrate at fatigue-deleterious levels without detection (i.e. above the endurance limit, but below the point where impacting will occur on the CRD shaft support plates).

### 6.3.5 Installation and Removal

Most transducers are welded to the components using capacitive discharge welders (strain gauges) or in the case of accelerometers affixed to welded mounting blocks by studs. Welding to internal components is governed by ASME B&PV Code, Section III, sub-sections NB-4430 (attachments) and NB-4311.2 (capacitive discharge welding). The method of attachment should be designed to function in the environment and operating loads between installation and removal. Methods for attachment of other sensor types, including advanced sensors, are provided in Section 6.3.2. Embedded sensors such, as fiber, have not been previously qualified for nuclear design and this installation method may require additional qualification. Component design specifications address temporary attachment requirements in accordance with NB-4000 and NG-4000 for CVAP instrumentation on the prototype design.

Integral cables from the sensors should be routed to minimize exposure to elevated flow velocities. For the NPM, this would include minimizing crossflow paths for the cable by selecting inner or outer components within an annulus (SG or riser assembly) and sensor elevations near existing instrument penetrations minimizing the overall cable run. Temporary installations have used stainless-steel straps and brackets to restrain the cabling while monitoring RVI. The spans and hardware should be designed to reduce susceptibility to FIV, including vortex shedding, in cross-flow areas. Based upon the relatively lower flow velocities in the NPM, conduit is not anticipated to be needed for the cable runs. Previous CVAP instrumentation programs have used conduit in elevated flow regimes. Conduit generally allows for easier temporary removal as the installation is contained.

Cables could be routed up through the pressurizer and out existing instrument penetrations in the RPV head. There also may be additional capacity for cabling inside the ICGTs as an option.

The installation process is the first opportunity to identify grounding or short issues that could render the sensor data unusable. Methods to reduce noise include individually shielded cable pairs (excitation/signal), conductor pairs separately twisted, and controlling the voltage difference between the shield and ground. In addition, as a diagnostic tool, resistance measurements including sensor to the component (should be greater than 10 megaohm) and measurements at the data acquisition system (DAS)-end including conductor to ground, shield to ground, and conductor to shield can be used to infer noise sources. These measurements should be similar to the sensor to component resistance and values that differ (lower) indicate a noise problem. Installations typically perform these measurements through various stages of the sensor installation for early identification of noise problems. Between test points these resistances should also be measured and compared to pre-testing (at-temperature) resistances (Section 6.3.6).

Presuming the attachment method for sensors is welding, the removal of the welded attachments is governed by NB-4435.

### 6.3.6 Pre-Installation Testing

To reduce the potential for instrument failures, the sensors used for testing should be tested in a similar environment prior to installation. This testing is separate from startup testing and would include validating the sensor performance through submersion and temperature exposure including resistance readings and followed lastly by post-calibration. Strain gauges and accelerometers have been utilized the most in these applications and the entire sensing population need not be tested, a statistically significant number can be used to infer results over a controlled material lot (strain gauges) or accelerometer model. Since strain gauges are destructively tested, they will not be reused but the accelerometers may be reused.

Each sensor is procured calibrated and certified through manufacturer acceptance to an appropriate NIST (NAS-942) or equivalent standard. The sensors should be exposed to one-time bounding transient test condition and a bounding (by duration) submersed test at a nominal startup testing conditions. During these environmental tests, the insulation resistance should be measured and compared with an acceptance criterion (nominally  $10^9$  ohms at nominal temperatures and  $10^7$  ohms at  $\sim 550^\circ\text{F}$ ) and the noise floor validated. The insulation resistance is inversely proportional to temperature. The performance during these tests establish the survivability of the sampled sensors.

Following these tests, the accelerometers (not strain gauges since they are destructively tested) are re-calibrated/checked, certified and any differences recorded from the original calibration. Sensor sensitivity at elevated temperatures should be recorded and incorporated into the calibration or post-processing to improve measurement accuracy. In addition, end-to-end calibration across all data acquisition channels can be used in lieu of manufacturer maximum possible values reducing the overall measurement uncertainty. This step should be performed prior to installation during the environmental testing to accommodate temperature effects using a calibrated input such as a shaker or induced strain.

Due to the relatively short duration of expected startup testing, the sensors will be exposed to acute radiation; however, most sensor specifications are provided for either no exposure or continuous exposure. For example, radiation hardened accelerometers offer hardening of  $6\text{E}10$  (integrated gamma flux) and  $3.7\text{E}18$  (integrated neutron flux) which bounds all NPM exposure expected over 60 years. Manufacturers recognize that limited exposure is possible from standard models; however, specific radiation testing is required to qualify and document this exact exposure. This provides a considerable number of options for sensors when compared to the relatively few radiation hardened sensors including triaxial designs (one cable for multiple sensing directions), smaller sizes, and greater ranges for sensitivity. It is recommended that the actual sensor chosen (if not specifically radiation hardened) be tested for expected exposure similar to the pressure, temperature and water chemistry environmental testing provided in Section 6.3.3.4. The testing for radiation exposure is typically governed by an irradiation plan which specifies the dosimetry and irradiation considerations under ISO 17025 or similar standard.

### 6.3.7 Signal Conditioning

Accelerometers require charge converters for high temperature applications (greater than 325°F). To minimize electromagnetic interference the distance between the sensor and charge converter should be minimized to the shortest distance practical to reduce capacitive load. Amplifier gain should be sufficient to resolve the displacements (through double integration) in Table 6-2 to a suitable analytical resolution – a detection floor of 0.1 mils zero-to-peak at any particular frequency is suggested. Filters, such as high and low pass should consider artificial amplification of low responses and potential impact signatures. Frequency responses in acceleration should include at least 2-3500 Hz.

Strain gauges require bridge excitation sufficient to measure the expected range of strain (see Table 6-2) and should be configured for a suitable analytical resolution considering the gauge factor, nominal gauge resistance, and bridge voltage. Bridge voltage should be maximized to increase the SNR but minimize drift caused by heating of the strain gauge element. Since the nominal gauge resistance changes following attachment and again during heatup, it is beneficial to provide a temperature cycle prior to collecting measurements on the gauges for static strain; however, dynamic strain measurement for startup testing should employ a bridge balancing routine between test plateaus. Generally, a bridge balance provides this compensation and a shunt routine verifies it. The desired frequency domain measurement range of 0-750 Hz captures all expected responses for the RVI and SG Assembly components.

### 6.3.8 Data Acquisition and Analysis during Flow Testing

The data acquisition system should provide the signal conditioning, recording and analysis. Analyses should be completed in real-time sufficient to compare with acceptance criteria. It may be desirable to trend other indicators as discussed in this report and listed in Table 6-2. These could be trended real-time to clearly and quickly characterize unexpected vibration and operative FIV mechanisms.

The sensors should be recorded synchronously for all test conditions. The duration of acquisition should be continuous if possible; however, reductions in the amount of data processed can be advantageous and generally five minutes of data over a test ramp or plateau is sufficient. Acquisitions during flow transients should be captured and include the time directly before and after the transient as a buffer (one minute). Operational parameters should be recorded synchronously with the FIV sensing package including flow rates, primary/secondary temperature, and pressure. The testing evolution will include hot shutdown to full power conditions (to the license basis) and a duration to achieve a million vibration cycles or approximately 2.5 days.

Acceptance criteria and a lower level established as a warning (typically 80% of the acceptance criteria) should be utilized for online processing. The data acquisition system should be sampling each sensor at a minimum of twice the desired frequency response. Hardware and software can be configured to offer sensor specific acquisition rates.

Noise present in a signal will elevate the overall values computed for trending (including RMS). Noise adjustments can also be made through filtering or subtracting known noise signals, reducing the overall RMS trends. For strain gauges and accelerometers, a

measurement without excitation can provide these values and should be computed prior to test plateaus. For sensors, a noise floor should be measured at a minimum to clearly delineate between true peaks (motion) and noise.



6.4 Annotated Drawings

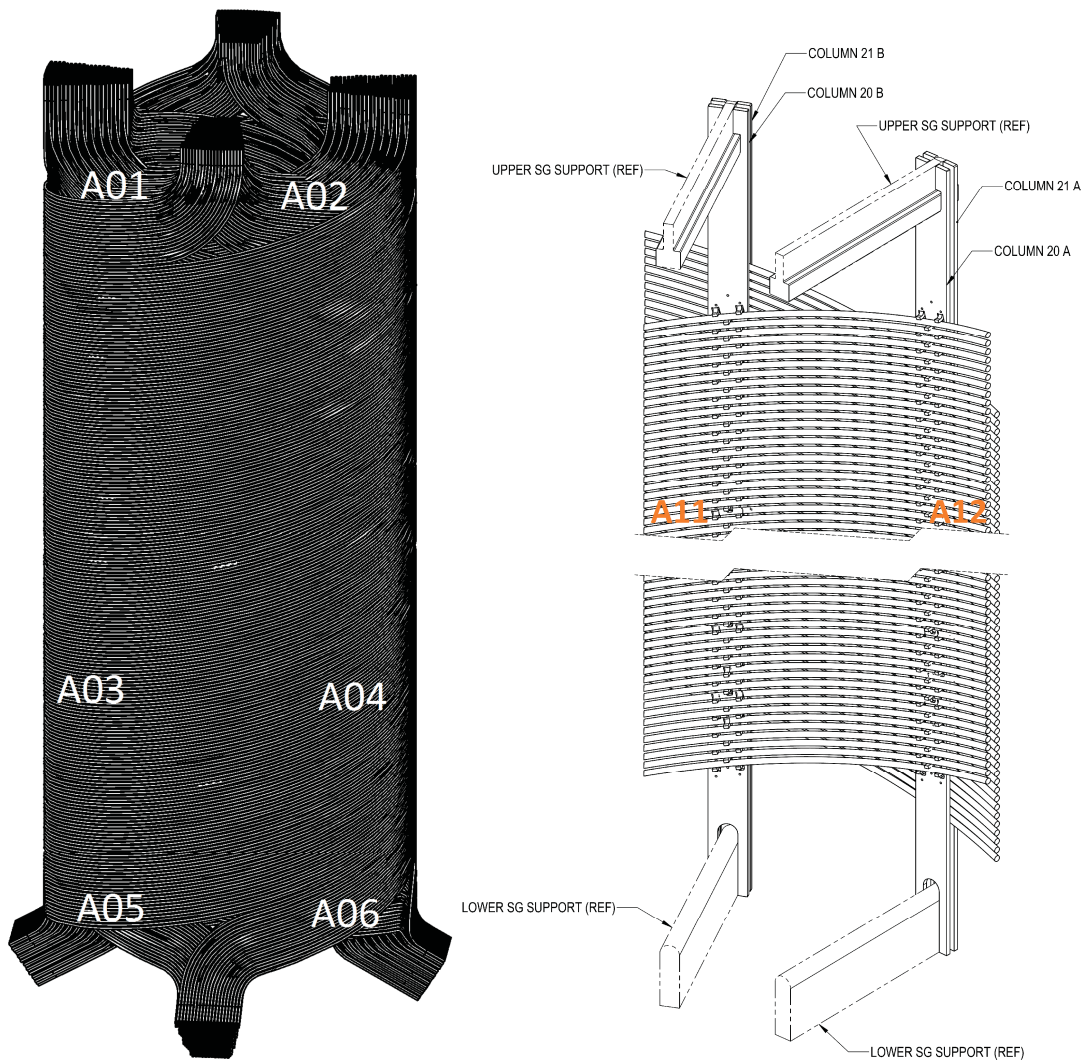


Figure 6-1 Recommended and Optional Measurement Locations (Table 4-5, Table 4-6)

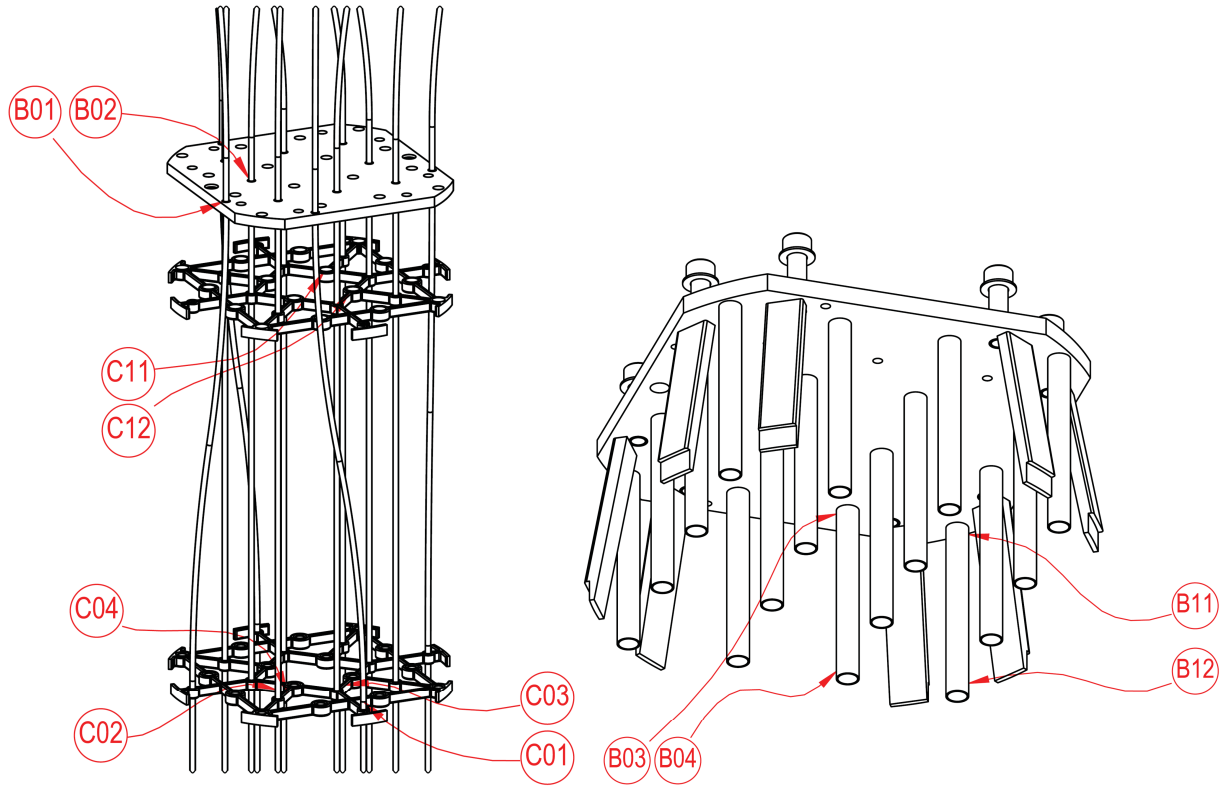


Figure 6-2 Recommended and Optional Measurement Locations (Table 4-5, Table 4-6)

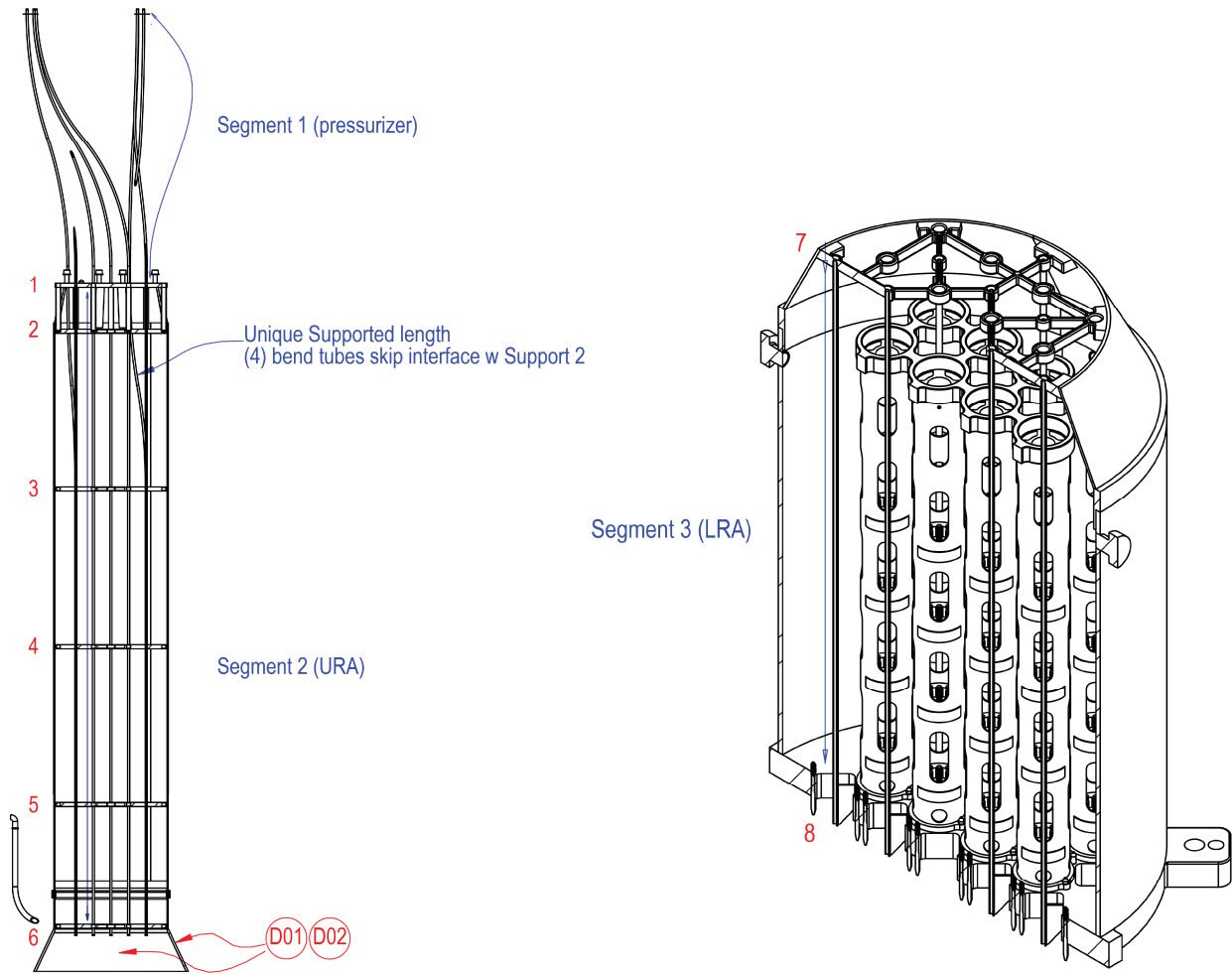


Figure 6-3 Recommended and Optional Measurement Locations (Table 4-5, Table 4-6)

## 7.0 Inspection Program

This section identifies the prototype components that require inspection before and after the CVAP measurement program. Because the measurement program focuses on the limiting components, inspection is used to confirm the assumptions regarding which components are limiting. For the components that are instrumented to support the measurement program, inspection provides a secondary confirmation of the FIV performance and integrity of these structures.

Before and after initial startup testing, components are inspected for mechanical wear and signs of vibration induced damage. Initial startup testing provides a sufficient duration for the limiting NPM component to experience a minimum of one million cycles of vibration. Components that are evaluated in the analysis program undergo inspection. For the components validated in the measurement program via testing, the inspection provides a secondary confirmation of the FIV integrity of the NPM components. For components that do not require testing due to large safety margins, the inspection confirms that the testing performed on more limiting components sufficiently bounds the performance of the non-tested components.

### 7.1 Inspection Methodology

The components most susceptible to FIV are examined in limiting and representative locations to demonstrate acceptable performance. Inspection areas include:

- a) Major load-bearing elements of the reactor vessel internals that position the core support structure
- b) Lateral, vertical, and torsional restraints inside the RPV
- c) Locking and bolting components whose failure could impact reactor vessel internals integrity
- d) Contact surfaces and potential contact surfaces
- e) Critical locations identified by the analysis program
- f) RPV interior for loose parts or foreign material

Components may be removed and inspected outside of the pressure vessel, but many NPM components cannot be removed from their installed locations. For those components, or when practical, an in-situ inspection is performed. Components like the SG tubes and SG tube supports that are too long to examine their entire surface and have inaccessible areas are inspected at least at the accessible ends of their length.

Initial startup testing provides for 1 million cycles of the most limiting (lowest fundamental frequency) component. This testing duration provides a reasonable number of cycles so that if rapid degradation is occurring due to FIV, there is evidence detectable by inspection.

## 7.2 Inspection Procedure

The NPM components are inspected following the guidelines and requirements provided in ASME Section III (Reference 9.1.6), Paragraph NG-5111, Paragraph NB-5111 and using the methods defined in the ASME Section V (Reference 9.1.7), Article 9.

The visual inspections are performed using VT-1 and VT-3, as defined by ASME Section XI, Subarticle IWB-2500, Tables IWB-2500-1 B-N-1, B-N-2, and B-N-3 (Reference 9.1.8). These nondestructive surface examinations are used to inspect the surfaces and welds of the components identified for inspection. Visual examinations are performed on the NPM components to satisfy the following objectives:

- On critical surfaces to see if there are any cracks, defects, or abnormal distortion
- On welds to see evidence of cracks
- On interface surfaces to see evidence of wear, distress, or abnormal corrosion
- On fittings to see if they are tight
- At reasonable locations to see if loose parts or debris have collected

The inspection results are documented in the CVAP Measurement and Inspection Program Results report. Any inspection findings and repairs/modifications are documented along with a complete record of the pre- and post- initial startup testing inspections including notes, photographs, and video.

## 7.3 Pre- and Post-Initial Startup Testing Inspection

The inspection and documentation for the NPM components are completed in two stages. The baseline inspection stage (pre-initial startup testing) takes place as the NPM components are assembled. The post-initial startup testing inspection stage takes place after the completion of the initial startup testing. During post-initial startup testing inspection, the core support structure and lower riser assembly are examined in the pool while other internals are examined in the dry dock.

The post-initial startup testing inspection results are compared with the baseline inspection data. The comparison provides an independent method of corroborating the conclusions of the CVAP analysis program, that no severe FIV related degradation is occurring.

The CVAP inspection locations are listed in Table 7-1 and depicted in Figure 7-1, Figure 7-2, Figure 7-3, and Figure 7-4. These locations include all inspection elements required to cover the six inspection areas listed in Section 7.1. The inspection examination methods defined in Table 7-1 are based on and consistent with the methods specified for in-service inspections of the NPM to meet ASME Code Section XI requirements. VT-1 inspections are specified for welded core support structures, attachments to the RPV, or identified areas of low margin. VT-3 inspections are specified for the majority of the remaining features except for locations that are mainly inspected for loose parts using a general visual exam.

Table 7-1 Pre- and post-initial startup testing inspection locations

Location ID	Feature to be Inspected	Exam. Method with Notes <sup>4</sup>	Inspection Req. Category (Section 7.1) <sup>8</sup>
<b>Core Supports and Flow Diverter</b>			
1	Core Support Block Gussets to RPV Bottom Head Welds	VT-1 <sup>1</sup>	a, b
2	Core Support Block Exterior Surfaces	VT-3 <sup>1,2</sup>	a, b, c
3	Lower Core Plate Surfaces	VT-3	a, b, c, d
4	Lower Core Plate to Core Barrel Weld	VT-1 <sup>1</sup>	a, b
5	Reflector Blocks	General Visual <sup>5</sup>	f
6	Core Barrel Exterior Surface	VT-3 <sup>6</sup>	a
7	Upper Support Block Weld and Fittings	VT-1 <sup>1,2</sup>	a, b, c, d
8	Core Barrel to Upper Core Plate Interface	VT-3	a, b, d
9	Shared Fuel Pins	VT-3 <sup>3</sup>	d
10	Flow Diverter	General Visual	f
<b>Lower Riser</b>			
11	Upper Core Plate to Lower Riser Section Weld	VT-3 <sup>1</sup>	a, b
12	Upper Core Plate Surfaces	VT-3 <sup>2,5</sup>	a, b, c, d, f
13	Lower Riser Section Surfaces	VT-3 <sup>5,6</sup>	a, b
14	Lower Riser Spacer Surfaces	VT-3	a, b
15	Lower Riser Transition Surfaces	VT-3	a, b
16	ICIGT Flag to Upper Core Plate Welds	VT-1 <sup>1</sup>	f
17	Fuel Pin	VT-1 <sup>3</sup>	d
18	CRA Lower Flange Surfaces	VT-3	b, c
19	CRA GT Interior and Exterior Surfaces	VT-3	b
20	CRA Card to CRA Rodlet Interface	VT-3 <sup>3</sup>	d
21	CRD shaft Alignment Cone to CRD shaft Interface	VT-3 <sup>3</sup>	d
22	CRD shaft Alignment Cone to CRA GT Support Plate Interface	VT-3	b, d
<b>Upper Riser and Pressurizer Spray Nozzle</b>			
23	Upper Riser Transition Surfaces	VT-3 <sup>6</sup>	b, d
24	Upper Riser Bellows	VT-3	b
25	Upper Riser Section Surfaces	VT-3 <sup>6</sup>	b
26	Injection Line Pipe	VT-3	-
27	CRD shaft Support Surfaces	VT-3	b
28	CRD shaft Supports to CRDS Interface	VT-3 <sup>3</sup>	d
29	CRD shaft Supports to ICIGT Interface	VT-3 <sup>3</sup>	d
30	Upper Riser Hanger Brace Surfaces	VT-3	b
31	CRD shaft Sleeve Surfaces	VT-3	-
32	Upper Riser Hanger Ring Surfaces	VT-3 <sup>2</sup>	b, c
33	Hot Temperature Thermowell External Surfaces	VT-3	-
34	Pressurizer Spray Nozzle Surfaces	VT-3 <sup>1</sup>	-
<b>SG and Downcomer</b>			
35	SG Inlet Flow Restrictors	VT-3 <sup>3,7</sup>	c, e, f
36	SG Inlet Flow Restrictor to SG Tube Interface	VT-3 <sup>3,7</sup>	d, e
37	SG Flow Restrictor Mounting Plate	VT-3 <sup>2</sup>	f
38	SG Lower Tube Support Cantilever Surfaces	VT-3	b, d

Location ID	Feature to be Inspected	Exam. Method with Notes <sup>4</sup>	Inspection Req. Category (Section 7.1) <sup>8</sup>
39	SG Tube to Tube Support Interface	VT-3 <sup>3, 6</sup>	b, d, e
40	Tube Support to Upper Riser Section Interface	VT-3 <sup>6</sup>	b, d
41	Injection Line Pipe Surfaces	VT-3	-
42	Cold Temperature Thermowells External Surfaces	VT-3	-
43	RRV Nozzles	VT-3	-
<b>Secondary Side Components</b>			
44	Steam Plenum	VT-3	-
45	Steam Plenum Nozzle	VT-3	-
46	SGS Piping	VT-3 <sup>6</sup>	-
47	Steam Temperature Thermowells, External Surface	VT-3	-
48	MSIVs, Interior Surfaces	VT-3 <sup>5</sup>	e
49	DHRS Steam Piping, Actuation Valve to Steam Line Tee	VT-1 <sup>3</sup>	e
50	DHRS Condensate Piping Inside Containment	VT-1	-
Notes:			
<ol style="list-style-type: none"> <li>1) Visually examine welds</li> <li>2) Verify that fittings are tight</li> <li>3) Visually examine for evidence of vibration wear</li> <li>4) Visual examinations include checking for loose parts</li> <li>5) Inspection limited to accessible surfaces exposed while assembled</li> <li>6) Inspection limited to the accessible ends of the feature due to the large surface area</li> <li>7) Inspection limited to a sampling of components due to the large quantity</li> <li>8) Rows with a - indicate that the feature to be inspected does not fall within one of the six categories identified in Section 3.0</li> </ol>			

{{

}}<sup>2(a),(c)</sup>

Figure 7-1 Lower reactor pressure vessel comprehensive vibration assessment program inspection locations



{{

}}<sup>2(a),(c)</sup>

Figure 7-2 Upper reactor pressure vessel comprehensive vibration assessment program inspection locations

{{

}}<sup>2(a),(c)</sup>

Figure 7-3 Steam generator and downcomer comprehensive vibration assessment program inspection locations

{{

}}<sup>2(a),(c)</sup>

Figure 7-4 Steam line comprehensive vibration assessment program inspection locations

---

## 8.0 Summary and Conclusions

This report provides the details of the NuScale CVAP measurement and inspection program. This program consists of benchmark testing and analysis, validation analysis and testing, an instrumentation plan to detect large amplitude vibration during initial startup testing, and inspection of components screened as susceptible to FIV before and after initial startup testing.

Following the completion of each test, post-test analysis is performed to complete the validation effort. Assessments are also performed based on the initial startup testing and inspection observations. Combined with the benchmarking efforts, the measurement and inspection work scope validate the FIV screening and predictive analyses in Reference 9.1.4.

## 9.0 References

### 9.1 Referenced Documents

- 9.1.1 American Society of Mechanical Engineers, *Operation and Maintenance of Nuclear Power Plants, Division 3: OM Guides*, ASME OM-2012, Part 11, Vibration Testing and Assessment of Heat Exchangers, New York, NY.
- 9.1.2 American Society of Mechanical Engineers, *Standard for Verification and Validation in Computational Fluid Dynamics and Heat Transfer*, ASME V&V 20-2009, New York, NY.
- 9.1.3 Au-Yang, M.K., *Flow-Induced Vibration of Power and Process Plant Components, A Practical Workbook*, ASME Press, New York, NY, 2001.
- 9.1.4 NuScale Comprehensive Vibration Assessment Program Analysis Technical Report, TR-0716-50439.
- 9.1.5 U.S. Nuclear Regulatory Commission, "Comprehensive Vibration Assessment Program for Reactor Internals during Preoperational and Initial Startup Testing," Regulatory Guide 1.20, Revision 3, March 2007.
- 9.1.6 American Society of Mechanical Engineers, Boiler and Pressure Vessel Code, 2013 Edition, Section III, "Rules for Construction of Nuclear Facility Components," New York, NY.
- 9.1.7 American Society of Mechanical Engineers, Boiler and Pressure Vessel Code, 2013 Edition, Section V, Nondestructive Examination, New York, NY.
- 9.1.8 American Society of Mechanical Engineers, Boiler and Pressure Vessel Code, 2013 Edition, "Rules for Inservice Inspection of Nuclear Power Plant Components," New York, NY.
- 9.1.9 Ziada, S. and Shine, S., Shrouhal Number of Flow-Excited Acoustic Resonance of Closed Side Branches, *Journal of Fluids and Structures*, Volume 13 (1999), pg. 127-142.
- 9.1.10 Schardt, J.F., "Flow-Induced Vibration Characteristics of BWR/6-238 Jet Pumps," GEAP-22201, UC-78, General Electric Company, September 1982.
- 9.1.11 Au-Yang, M.K. and Jordan, K.B., Dynamic Pressure Inside a PWR – A Study Based on Laboratory and Field Test Data. *Nuclear Engineering and Design* 58, pg 113-125, 1980.
- 9.1.12 Chen, Shoen-Sheng. *Flow-Induced Vibration of Circular Cylindrical Structures*. ANL-85-51, June 1985.
- 9.1.13 Giraudeau, M., et al. *Two-Phase Flow-Induced Forces on Piping in Vertical Upward Flow: Excitation Mechanisms and Correlation Models*. *Journal of Pressure Vessel Technology*, Vol. 135, p. 030907, 2013.

9.1.14 ASME Boiler and Pressure Vessel Code, Section III, Division 1 – Appendix N, Dynamic Analysis Methods, 2013 Edition, no Addenda. New York, NY.

---

**Appendix A. TF-3 Instrumentation Plan**

{{

}}<sup>2(a),(c)</sup>

Figure A-1 Column 11 tube 1 instrumented tube

{{

}}<sup>2(a),(c)</sup>

Figure A-2 Column 11 tube 16 instrumented tube



{{

}}<sup>2(a),(c)</sup>

Figure A-3 Column 9 tube 15 instrumented tube

{{

}}<sup>2(a),(c)</sup>

Figure A-4 Column 9 tube 16 instrumented tube

{{

}}<sup>2(a),(c)</sup>

Figure A-5 Column 12 tube 1 instrumented tube

{{

}}<sup>2(a),(c)</sup>

Figure A-6 Column 12 tube 2 instrumented tube

{{

}}<sup>2(a),(c)</sup>

Figure A-7 Column 11 tube 2 instrumented tube

{{

}}<sup>2(a),(c)</sup>

Figure A-8 Column 11 tube 15 instrumented tube

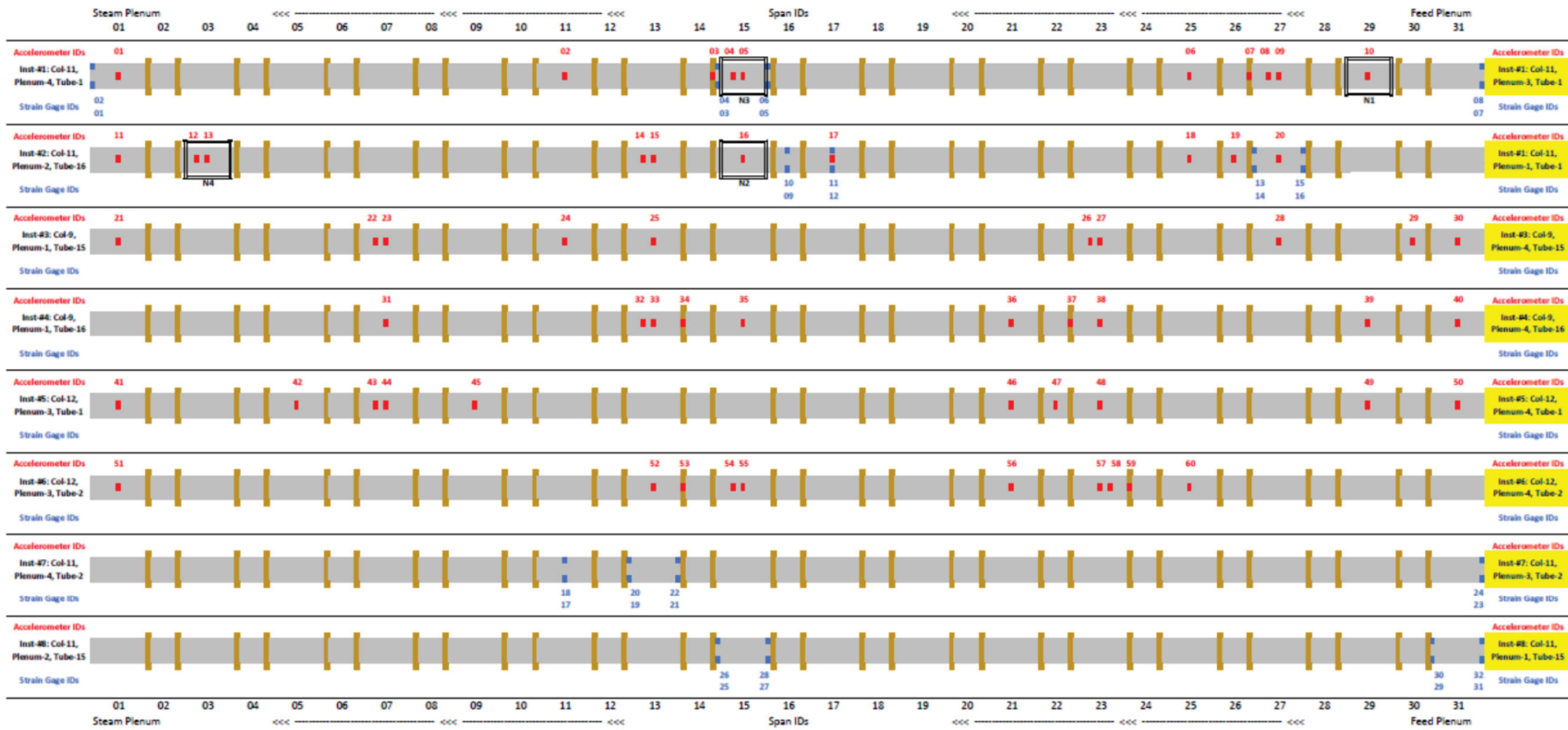


Figure A-9 Instrumentation summary

## **Appendix B. TF-2 FEI Spectral Plots by Test Series (0 - 300 Hz)**



{

}}<sup>2(a),(c)</sup>

Figure B-1 Test condition A, channel set 1

{

}}<sup>2(a),(c)</sup>

Figure B-2 Test condition A, channel set 2

{

}}<sup>2(a),(c)</sup>

Figure B-3 Test condition B, channel set 1

{

}}<sup>2(a),(c)</sup>

Figure B-4 Test condition B, channel set 2

{

}}<sup>2(a),(c)</sup>

Figure B-5 Test condition C, channel set 1

{

}}<sup>2(a),(c)</sup>

Figure B-6 Test condition C, channel set 2

{

}}<sup>2(a),(c)</sup>

Figure B-7 Test condition D, channel set 1

{

}}<sup>2(a),(c)</sup>

Figure B-8 Test condition D, channel set 2



{

}}<sup>2(a),(c)</sup>

Figure B-9 Test condition G, channel set 1

{

}}<sup>2(a),(c)</sup>

Figure B-10 Test condition G, channel set 2

## Appendix C. TF-2 FEI Spectral Plots by Flow Rate (0 - 300 Hz)

{

Figure C-1 Nominal primary-side flow rate of 114 kg/s, channel set 1

}}<sup>2(a),(c)</sup>

{

Figure C-2 Nominal primary-side flow rate of 114 kg/s, channel set 2

}}<sup>2(a),(c)</sup>

{

Figure C-3 Nominal primary-side flow rate of 143 kg/s, channel set 1

}}<sup>2(a),(c)</sup>

{

Figure C-4 Nominal primary-side flow rate of 143 kg/s, channel set 2

}}<sup>2(a),(c)</sup>

{

Figure C-5 Nominal primary-side flow rate of 173 kg/s, channel set 1

}}<sup>2(a),(c)</sup>



{

Figure C-6 Nominal primary-side flow rate of 173 kg/s, channel set 2

}}<sup>2(a),(c)</sup>

{

Figure C-7 Nominal primary-side flow rate of 201 kg/s, channel set 1

}}<sup>2(a),(c)</sup>

{

Figure C-8 Nominal primary-side flow rate of 201 kg/s, channel set 2

}}<sup>2(a),(c)</sup>

{

Figure C-9 Nominal primary-side flow rate of 230 kg/s, channel set 1

}}<sup>2(a),(c)</sup>

{

Figure C-10 Nominal primary-side flow rate of 230 kg/s, channel set 2

}}<sup>2(a),(c)</sup>

{

Figure C-11 Nominal primary-side flow rate of 263 kg/s, channel set 1

}}<sup>2(a),(c)</sup>

{

Figure C-12 Nominal primary-side flow rate of 263 kg/s, channel set 2

}}<sup>2(a),(c)</sup>

**Appendix D. TF-2 FEI Spectral Plots by Test Series (0 - 1000 Hz)**



{

Figure D-1 Test condition A, channel set 1

}}<sup>2(a),(c)</sup>

{

Figure D-2 Test condition A, channel set 2

}}<sup>2(a),(c)</sup>

{

Figure D-3 Test condition B, channel set 1

}}<sup>2(a),(c)</sup>

{

Figure D-4 Test condition B, channel set 2

}}<sup>2(a),(c)</sup>

{

Figure D-5 Test condition C, channel set 1

}}<sup>2(a),(c)</sup>

{

Figure D-6 Test condition C, channel set 2

}}<sup>2(a),(c)</sup>

{

Figure D-7 Test condition D, channel set 1

}}<sup>2(a),(c)</sup>

{

Figure D-8 Test condition D, channel set 2

}}<sup>2(a),(c)</sup>



{

Figure D-9 Test condition G, channel set 1

}}<sup>2(a),(c)</sup>

{

Figure D-10 Test condition G, channel set 2

}}<sup>2(a),(c)</sup>

**Appendix E. TF-2 FEI Spectral Plots by Flow Rate (0 - 1000 Hz)**

{

Figure E-1 Nominal primary-side flow rate of 114 kg/s, channel set 1

}}<sup>2(a),(c)</sup>

{

Figure E-2 Nominal primary-side flow rate of 114 kg/s, channel set 2

}}<sup>2(a),(c)</sup>

{

Figure E-3 Nominal primary-side flow rate of 143 kg/s, channel set 1

}}<sup>2(a),(c)</sup>

{

Figure E-4 Nominal primary-side flow rate of 143 kg/s, channel set 2

}}<sup>2(a),(c)</sup>

{

Figure E-5 Nominal primary-side flow rate of 173 kg/s, channel set 1

}}<sup>2(a),(c)</sup>



{

Figure E-6 Nominal primary-side flow rate of 173 kg/s, channel set 2

}}<sup>2(a),(c)</sup>

{

Figure E-7 Nominal primary-side flow rate of 201 kg/s, channel set 1

}}<sup>2(a),(c)</sup>

{

Figure E-8 Nominal primary-side flow rate of 201 kg/s, channel set 2

}}<sup>2(a),(c)</sup>

{

Figure E-9 Nominal primary-side flow rate of 230 kg/s, channel set 1

}}<sup>2(a),(c)</sup>

{

Figure E-10 Nominal primary-side flow rate of 230 kg/s, channel set 2

}}<sup>2(a),(c)</sup>

{

Figure E-11 Nominal primary-side flow rate of 260 kg/s, channel set 1

}}<sup>2(a),(c)</sup>

{

Figure E-12 Nominal primary-side flow rate of 260 kg/s, channel set 2

}}<sup>2(a),(c)</sup>

## **Appendix F. TF-2 FEI Content within Frequency Ranges of Interest**



Table F-1 Amplitude of spectral content between 0 – 10 Hz

{{

}}<sup>2(a),(c)</sup>

Table F-2 Amplitude of spectral content between 0-10 Hz (excluding test series G)

{{

}}<sup>2(a),(c)</sup>

Table F-3 Amplitude of spectral content between 16-28 Hz

{{

}}<sup>2(a),(c)</sup>

Table F-4 Amplitude of spectral content between 35-55 Hz

{{

}}<sup>2(a),(c)</sup>

Table F-5 Amplitude of spectral content between 70-85 Hz

{{

}}<sup>2(a),(c)</sup>

Table F-6 Amplitude of spectral content between 140-160 Hz

{{

}}<sup>2(a),(c)</sup>

Table F-7 Amplitude of spectral content between 10-300 Hz

{{

}}<sup>2(a),(c)</sup>

## Appendix G. TF-2 FEI Frequency-Specific Amplitudes versus Flow Rate



{{

}}<sup>2(a),(c)</sup>

Figure G-1 Dynamic strain, 0-10 Hz versus flow rate

{{

}}<sup>2(a),(c)</sup>

Figure G-2 Dynamic strain, 16-28 Hz versus flow rate

{{

}}<sup>2(a),(c)</sup>

Figure G-3 Dynamic strain, 35-55 Hz versus flow rate

{{

}}<sup>2(a),(c)</sup>

Figure G-4 Dynamic strain, 70-85 Hz versus flow rate

{{

}}<sup>2(a),(c)</sup>

Figure G-5 Dynamic strain, 140-160 Hz versus flow rate

{{

}}<sup>2(a),(c)</sup>

Figure G-6 Dynamic strain, 10-300 Hz versus flow rate

## **Appendix H. TF-3 Build-out Testing Frequency Response Function Calculations**

Table H-1 Testing matrix

{{

}}<sup>2(a),(c)</sup>



{{

Figure H-1 315-12-1-C-5 (5y)  
{{

}}<sup>2(a),(c)</sup>

Figure H-2 zSgle tube 1sec

}}<sup>2(a),(c)</sup>

{{

Figure H-3 1A-1Y  
{{

}}<sup>2(a),(c)</sup>

Figure H-4 1A-1Z

}}<sup>2(a),(c)</sup>

{{

Figure H-5 1A-3Z  
{{

}}<sup>2(a),(c)</sup>

Figure H-6 1A-5Z

}}<sup>2(a),(c)</sup>

{{

Figure H-7 1C-1Y  
{{

}}<sup>2(a),(c)</sup>

Figure H-8 1C-1Z

}}<sup>2(a),(c)</sup>

{{

Figure H-9 1C-5Z  
{{

}}<sup>2(a),(c)</sup>

Figure H-10 1E-1Y

}}<sup>2(a),(c)</sup>

{{

Figure H-11 1E-1Z  
{{

}}<sup>2(a),(c)</sup>

Figure H-12 1E-5Z

}}<sup>2(a),(c)</sup>

{{

Figure H-13 2A-CmsZ

{{

}}<sup>2(a),(c)</sup>

Figure H-14 2A-EfwZ

}}<sup>2(a),(c)</sup>

{{

Figure H-15 2A-EmsZ  
{{

}}<sup>2(a),(c)</sup>

Figure H-16 2A-GfwZ

}}<sup>2(a),(c)</sup>



{{

Figure H-17 2C-CmsZ

{{

}}<sup>2(a),(c)</sup>

Figure H-18 2C-EfwZ

}}<sup>2(a),(c)</sup>

{{

Figure H-19 2C-EmsZ  
{{

}}<sup>2(a),(c)</sup>

Figure H-20 2C-GfwZ

}}<sup>2(a),(c)</sup>

{

Figure H-21 3C-EmsZ

}}<sup>2(a),(c)</sup>

{{

Figure H-22 4A-2Z  
{{

}}<sup>2(a),(c)</sup>

Figure H-23 4A-3Z

}}<sup>2(a),(c)</sup>

{{

Figure H-24 5A-2Z  
{{

}}<sup>2(a),(c)</sup>

Figure H-25 5A-4Y

}}<sup>2(a),(c)</sup>

{{

Figure H-26 5A-5Z  
{{

}}<sup>2(a),(c)</sup>

Figure H-27 5A-Support Z

}}<sup>2(a),(c)</sup>

{{

Figure H-28 Sup-103+col-12 span E, Tube 1, 5, 9 impact 1x  
{{

}}<sup>2(a),(c)</sup>

Figure H-29 Sup-103+col-12 span E, Tube 1, 5, 9 impact 1Z

}}<sup>2(a),(c)</sup>

{{

Figure H-30 Supp-to-tube 103 span-E FW-X  
{{

}}<sup>2(a),(c)</sup>

Figure H-31 Supp-to-tube 103 span-E FW-X on plate

}}<sup>2(a),(c)</sup>





**Enclosure 3:**

Affidavit of Thomas A. Bergman, AF-0719-66346

## NuScale Power, LLC

### AFFIDAVIT of Thomas A. Bergman

I, Thomas A. Bergman, state as follows:

- (1) I am the Vice President of Regulatory Affairs of NuScale Power, LLC (NuScale), and as such, I have been specifically delegated the function of reviewing the information described in this Affidavit that NuScale seeks to have withheld from public disclosure, and am authorized to apply for its withholding on behalf of NuScale
- (2) I am knowledgeable of the criteria and procedures used by NuScale in designating information as a trade secret, privileged, or as confidential commercial or financial information. This request to withhold information from public disclosure is driven by one or more of the following:
  - (a) The information requested to be withheld reveals distinguishing aspects of a process (or component, structure, tool, method, etc.) whose use by NuScale competitors, without a license from NuScale, would constitute a competitive economic disadvantage to NuScale.
  - (b) The information requested to be withheld consists of supporting data, including test data, relative to a process (or component, structure, tool, method, etc.), and the application of the data secures a competitive economic advantage, as described more fully in paragraph 3 of this Affidavit.
  - (c) Use by a competitor of the information requested to be withheld would reduce the competitor's expenditure of resources, or improve its competitive position, in the design, manufacture, shipment, installation, assurance of quality, or licensing of a similar product.
  - (d) The information requested to be withheld reveals cost or price information, production capabilities, budget levels, or commercial strategies of NuScale.
  - (e) The information requested to be withheld consists of patentable ideas.
- (3) Public disclosure of the information sought to be withheld is likely to cause substantial harm to NuScale's competitive position and foreclose or reduce the availability of profit-making opportunities. The accompanying report reveals distinguishing aspects about the methodology by which NuScale has developed its CVAP Measurement and Inspection Plan.

NuScale has performed significant research and evaluation to develop a basis for this CVAP Measurement and Inspection Plan technical report and has invested significant resources, including the expenditure of a considerable sum of money.

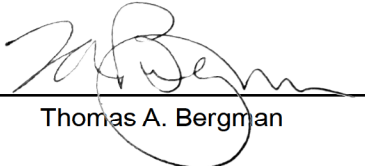
The precise financial value of the information is difficult to quantify, but it is a key element of the design basis for a NuScale plant and, therefore, has substantial value to NuScale.

If the information were disclosed to the public, NuScale's competitors would have access to the information without purchasing the right to use it or having been required to undertake a similar expenditure of resources. Such disclosure would constitute a misappropriation of NuScale's intellectual property, and would deprive NuScale of the opportunity to exercise its competitive advantage to seek an adequate return on its investment.

- (4) The information sought to be withheld is in the enclosed report titled "NuScale Comprehensive Vibration Assessment Program Measurement and Inspection Plan Technical Report." The enclosure contains the designation "Proprietary" at the top of each page containing proprietary information. The information considered by NuScale to be proprietary is identified within double braces, "{{ }}" in the document.

- (5) The basis for proposing that the information be withheld is that NuScale treats the information as a trade secret, privileged, or as confidential commercial or financial information. NuScale relies upon the exemption from disclosure set forth in the Freedom of Information Act ("FOIA"), 5 USC § 552(b)(4), as well as exemptions applicable to the NRC under 10 CFR §§ 2.390(a)(4) and 9.17(a)(4).
- (6) Pursuant to the provisions set forth in 10 CFR § 2.390(b)(4), the following is provided for consideration by the Commission in determining whether the information sought to be withheld from public disclosure should be withheld:
- (a) The information sought to be withheld is owned and has been held in confidence by NuScale.
  - (b) The information is of a sort customarily held in confidence by NuScale and, to the best of my knowledge and belief, consistently has been held in confidence by NuScale. The procedure for approval of external release of such information typically requires review by the staff manager, project manager, chief technology officer or other equivalent authority, or the manager of the cognizant marketing function (or his delegate), for technical content, competitive effect, and determination of the accuracy of the proprietary designation. Disclosures outside NuScale are limited to regulatory bodies, customers and potential customers and their agents, suppliers, licensees, and others with a legitimate need for the information, and then only in accordance with appropriate regulatory provisions or contractual agreements to maintain confidentiality.
  - (c) The information is being transmitted to and received by the NRC in confidence.
  - (d) No public disclosure of the information has been made, and it is not available in public sources. All disclosures to third parties, including any required transmittals to NRC, have been made, or must be made, pursuant to regulatory provisions or contractual agreements that provide for maintenance of the information in confidence.
  - (e) Public disclosure of the information is likely to cause substantial harm to the competitive position of NuScale, taking into account the value of the information to NuScale, the amount of effort and money expended by NuScale in developing the information, and the difficulty others would have in acquiring or duplicating the information. The information sought to be withheld is part of NuScale's technology that provides NuScale with a competitive advantage over other firms in the industry. NuScale has invested significant human and financial capital in developing this technology and NuScale believes it would be difficult for others to duplicate the technology without access to the information sought to be withheld.

I declare under penalty of perjury that the foregoing is true and correct. Executed on August 2, 2019.



Thomas A. Bergman